
Investigations of radiation shielding, diagnostic methods and imaging for conventional and laser-driven radiation sources

Franz Siegfried Englbrecht



München 2022

Investigations of radiation shielding, diagnostic methods and imaging for conventional and laser-driven radiation sources

Franz Siegfried Englbrecht

Dissertation
der Fakultät für Physik
der Ludwig-Maximilians-Universität
München

vorgelegt von
Franz Siegfried Englbrecht
aus München

München, den 09.05.2022

Erstgutachter: Prof. Dr. Katia Parodi
Zweitgutachter: Prof. Dr. Jörg Schreiber
Tag der mündlichen Prüfung: 15.06.2022

*Wenn es überhaupt eine gute Idee gibt,
dann die Idee der Skepsis gegenüber allen guten Ideen.
Gerhard Polt, Bayerischer Satiriker*

Zusammenfassung

Die Wechselwirkung von hochintensiven *Petawatt* (PW) Laserpulsen mit Materie kann die Emission einer großen Anzahl hochenergetischer Sekundärteilchen bewirken. In den letzten Jahren haben zahlreiche Entwicklungen den Übergang von Machbarkeitsstudien, bei denen ein Spray von Protonen, Neutronen, Ionen, Elektronen und Röntgenstrahlen erzeugt wurde, zu laserbasierten Teilchenquellen von biomedizinischer Relevanz ermöglicht. Protonenbündel mit breitbandigen Energiespektren, Bündelladungen jenseits von 1 nC und Maximalenergien nahe 100 MeV bei Fluenzen von 10^7 p/cm^2 innerhalb von Nanosekunden und im 1 Hz Betrieb werden ebenso in naher Zukunft realisiert werden wie Elektronenbündel jenseits von 8 GeV und Röntgen- und Protonenquellen im μm Bereich. Die treibenden Kräfte sind neue Technologien auf der Laser- und Targetebene, aber auch angepasster Strahlenschutz und Detektoren sowie die Aussicht auf neue Anwendungen in der Strahlentherapie und der ultraschnellen Biologie.

Das inhärent artengemischte Strahlungsfeld von großer Divergenz und der intensive, sich gemeinsam ausbreitende breitbandige elektromagnetische Puls (EMP) ermöglichen nicht nur neue Anwendungen, die diese besonderen Merkmale nutzen. Sie stellen auch Herausforderungen dar indem Sie die direkte Übernahme etablierter Konzepte aus konventionellen Elektronen-, Photonen-, Protonen- oder Ionenstrahl-Beschleunigeranlagen behindern. Die vorliegende Arbeit widmet sich der Identifizierung von Grenzen sowie der Entwicklung von Berechnungswerkzeugen, um einige dieser Herausforderungen zu überwinden.

Die Kenntnis über die Existenz des sekundären Strahlungsfeldes in der Umgebung von Beschleunigern ist von zentraler Bedeutung für den Strahlenschutz und kann neuartige Strahlüberwachung sowohl für konventionelle als auch für lasergetriebene Beschleunigungsanlagen ermöglichen. Die systematische Korrelation zwischen 75-250 MeV magnetisch abgelenkten therapeutischen Protonenstrahlen und den Neutronen im sekundären Strahlungsfeld als Funktion des Beobachtungswinkels wurde für einer konventionellen Protonenbehandlungsanlage untersucht. FLUKA *Monte Carlo* (MC)-Simulationen der Neutronenspektren im Energiebereich 10^{-9} - 10^2 MeV wurden mit bereitgestellten GEANT4-Simulationen und Messdaten eines *Extended-Range Bonner Sphere Spectrometer* (ERBSS) verglichen. Die Modellierung der Behandlungsgantry und des Behandlungsraums ist essentiell um die ERBSS-Daten insbesondere im Bereich der thermischen Neutronenenergie zu reproduzieren. Diese thermischen Energien (10^{-2} - 10^1 MeV) sind von erhöhter biologischer Wirksamkeit. Zusätzlich wurde das *Centre for Advanced Laser Applications* (CALA) in FLUKA modelliert. Die Energiespektren, Dosisleistungen und räumlichen Verteilungen von sekundären Elektronen, Neutronen, Pionen, Röntgen und Gammastrahlen, die durch laserbeschleunigte Protonen-, Elektronen-, Kohlenstoff- und Goldionenbündel erzeugt werden, wurden ausgewertet. Die Dosisleistungen der primären und sekundären Strahlung wurden mit den gesetzlichen Grenzwerten in Einklang gebracht. Die Strahlplätzen verwendeten Laserpulse (2,5 PW, 800 nm, 25 fs) des *ATLAS*-Lasers bei 1 Hz Wiederholfrequenz mit. Für nicht klassifizierte Bereiche konnten Dosisleistungen im Schussbetrieb $< 0,5 \mu\text{Sv/h}$ erreicht werden, für Überwachungsgebiete $< 2,5 \mu\text{Sv/h}$. Dies war nötig, da die Einrichtung von Kontrollbereichen mangels geeigneter Personendosis-Monitore für die Nanosekunden kurzen Strahlungspakete nicht möglich ist. Die sekundären Neutronenenergiespektren, hervorgerufen durch 10-75 MeV-Protonen, welche in Kürze am *Laser-driven Ion Acceleration* (LION)-Experiment zur Verfügung stehen werden, wurden simuliert. Die Daten ermöglichen die Abschätzung der Korrelation zwischen den primären laserbasierten Protonen- und Elektronenbündeln mit dem sekundären Neutronenstrahlungsfeld.

Die verwendeten Offline-Detektoren, welche zum Nachweis von laserbeschleunigten Teilchenbündeln verwendet werden, werden zunehmend durch elektronische Systeme mit Wiederholraten von wenigen Hz verdrängt. Die Messung des Energiespektrums, der Teilchenzahl und der Divergenz der Bündel sind der Schlüssel zur Eingrenzung der optimalen Quellenparameter und zur Entwicklung einer stabilen Protonenquelle für Anwendungen. Die Steuerungssoftware des $5\text{ cm} \times 10\text{ cm}$ RadEye CMOS-Sensor mit $48\text{ }\mu\text{m}$ Pixelgröße wurde weiterentwickelt. Dadurch wurden solche Detektoren unter anderem in der getriggerten Hauptdiagnostik des LION-Experiments, einem kombinierten Elektronen- und Protonenmagnetspektrometer, eingesetzt. Des Weiteren fanden Sie Anwendung zur Auslese eines Szintillatorenstapels und konnten mit Softwareseitig erweiterten Dynamikumfang eingesetzt werden. FLUKA-Simulationen von therapeutischen Elektronenfeldern wurden verwendet, um Tiefendosisverteilungen und laterale Feldprofile des medizinischen Elektronen-Linearbeschleunigers Siemens ONCOR zu reproduzieren. Diese gut definierte Elektronenquelle half, zusammen mit Messungen der Elektronenfelder dabei, das strahleninduzierten Hintergrundsignal im Magnetspektrometer zu identifizieren. In einem weiteren Schritt wurde ein MC-basierter Algorithmus zur Rekonstruktion von Elektronenspektren am Laser entwickelt und getestet. Im Hinblick auf zukünftige Entwicklungen wurde der CM49 CMOS-Sensor als Nachfolgekandidat des RadEye für das LION-Experiment getestet.

Zuletzt wurde die Anwendung der lasergetriebenen Teilchenquellen für die Bildgebung untersucht. FLUKA-Simulationen wurden mit Messdaten aus Strahlzeiten am *Laboratory for extreme Photonics* (LEX) und dem *Texas Petawatt Laser* (TPW) kombiniert. Ziel der Experimente waren Grundlagenexperimente zur Bildgebung sowohl mit Protonen allein als auch mit Röntgenstrahlen und Protonen. Die Ergebnisse ermöglichen eine Bewertung der Lücke, die geschlossen werden muss, um die Vorteile der neuen Quellen für die Bildgebung voll auszuschöpfen.

Zusammenfassend lässt sich sagen, dass in dieser Arbeit mehrere Entwicklungen bearbeitet wurden, die den Weg für den Einsatz von lasergetriebener Strahlung für ein breiteres Spektrum von Anwendungen ebnen.

Abstract

The interaction of highly intense *petawatt-class* (PW) laser pulses with matter can cause the emission of a large number of secondary particles with large kinetic energy. Over the past years, many developments enabled the transition from proof-of-principle studies generating a spray of particles such as protons, neutrons, light-ions, electrons and X-rays towards laser-based particle sources of biomedical relevance. Bunch-charges beyond 1 nC, broadband proton bunch energy spectra with maximum energies up to 100 MeV and electron bunches beyond 8 GeV are soon to be realized. The whole bunches are impinging onto experiments at shot repetition rates of 1 Hz within a few ns and present a fluence of 10^7 p/cm², originating from μ m source sizes of X-rays and protons.

The named source parameters, together with the intrinsically mixed radiation field of large divergence and the intense co-propagating broadband *electromagnetic pulse* (EMP), enable not only novel applications exploiting these distinct features, but also pose challenges. They hinder the direct transfer of established experimental concepts from conventional electron-, photon-, proton- or light ion-beam accelerator facilities. This work is dedicated to identify limits as well as to develop computational tools to overcome some of these transfer challenges.

Knowledge of the secondary radiation field around accelerators is of key relevance for radiation protection and can enable novel beam monitoring in both conventional and laser-driven acceleration facilities. The systematic correlation between 75-250 MeV scanned therapeutic proton beams and the neutrons in the secondary radiation field as function of the angle of observation at a conventional proton treatment facility has been studied. FLUKA *Monte Carlo* (MC) simulations were compared to GEANT4 simulations and *Extended-Range Bonner Sphere Spectrometer* (ERBSS) neutron spectra between 10^{-9} - 10^2 MeV. The modelling of the gantry and the treatment room are relevant to reproduce the ERBSS data, especially in the thermal energy region (10^{-2} - 10^1 MeV) of increased biological effectiveness. Additionally, the *Centre for Advanced Laser Applications* (CALA) was modelled in FLUKA to evaluate the energy spectra, dose rates and spatial distributions of secondary electrons, neutrons, pions, X-rays and γ -ray photons generated by laser-accelerated bunches of protons, electrons, carbon and gold ions. The dose rates from the intense radiation bunches, most caused by beamlines using the 2.5 PW, 800 nm, 25 fs laser pulses from the ATLAS laser at 1 Hz repetition frequency were brought into agreement with the regulatory limits. Dose rates for unclassified zones could be kept < 0.5 μ Sv/h, while supervised zones below < 2.5 μ Sv/h were successfully realized, as the existence of controlled zones was not possible due the lack of adequate personal dose monitors for the ns short radiation bunches. Neutron energy spectra from 10-75 MeV protons from the near-future operation of the *Laser-driven Ion Acceleration* (LION) experiment were simulated to provide an estimate on the correlation of the laser-based proton and electron bunches to the secondary neutron radiation field.

The detection of laser-accelerated ion bunches is transitioning from offline towards online electronic systems with a few Hz repetition rates. The characterisation of the energy spectrum, particle number and divergence of the bunches is key to the exploration of the optimal source parameters and the development of a stable proton source for applications. Control software development for the 5 cm \times 10 cm RadEye CMOS sensor with 48 μ m pixel size successfully enabled several applications: the triggered main diagnostic of the LION experiment in a combined electron and proton magnet spectrometer, as readout of a stack of scintillators, as well as a dynamic range extension by stacking multiple consecutive frames of a single bunch impact. FLUKA

simulations of large electron fields were used to accurately reproduce depth-dose distributions and lateral field profiles of a Siemens ONCOR medical electron linac. This well defined electron source together with measurements of the electron fields helped to identify the radiation-induced measurement background in the magnetic spectrometer. In a following step, a MC based electron spectra reconstruction algorithm was developed and tested. Finally, in view of future developments, the CM49 CMOS sensor was tested as a successor candidate of the RadEye for the LION experiment.

As last challenge the envisioned application of the laser-driven sources for imaging was investigated. FLUKA simulations were combined with data from experimental campaigns at the *Laboratory for Extreme Photonics* (LEX) and *Texas Petawatt laser* (TPW), where basic imaging experiments were performed using protons alone as well as simultaneous X-rays and protons. The results allow to assess the gap that needs to be bridged in order to take full advantage of the novel sources for imaging.

Summarizing, this thesis work addresses several developments which help pave the way towards the use of laser-driven radiation for a broader set of applications.

Contents

1	Introduction	1
1.1	Development of Accelerators stimulates Medical Physics	1
1.2	High Power Lasers as Sources of Ionizing Radiation	2
1.3	Outline of the thesis	3
2	Interaction of radiation with matter	5
2.1	Photons	6
2.2	Protons and light ions	8
2.3	Electrons	14
2.4	Neutrons	15
2.5	Dose and biological considerations	17
3	Fundamentals of radiotherapy-, laser-acceleration- and detector technologies	23
3.1	Accelerator research from a radiotherapy point of view	23
3.2	Electron-, photon-, proton- and light ion-beam radiotherapy technology .	25
3.3	High-power laser systems as particle sources	35
3.4	Particle detector technology at laser facilities	50
4	Simulation studies of secondary radiation in modern acceleration facilities	57
4.1	Secondary neutrons in scanned proton therapy at RPTC	59
4.2	Radiation protection studies for novel laser particle sources at the Centre for Advanced Laser Applications	88
4.3	Study of secondary neutrons at the Centre for Advanced Laser Applications	113
5	Investigation of pixel detectors for applications at laser-driven particle beams	117
5.1	RadEye CMOS sensor	118
5.2	CM49 CMOS sensor	132
6	Detector application 1: Development of MC based reconstruction of secondary electrons in Laser-ion acceleration	139
6.1	Combined electron proton spectrometer	141

CONTENTS

6.2	MC model of electron linac Siemens ONCOR	143
6.3	Modelling the spectrometer as linear system	153
6.4	Reconstruction of ONCOR measurements and simulations	155
6.5	Limitations of system matrix reconstruction and WASP	159
7	Detector application 2: Concepts for laser-driven proton radiography	161
7.1	Introduction	162
7.2	Experiments	165
8	Summary and Outlook	175
A	Further RadEye and CM49 characterisation and HDR experiments	179
A.1	RadEye HDR proton detection at MLL and LION	179
A.2	Initial CM49 proton characterisation and HDR photon and proton detection	183
	List of abbreviations	186
	List of scientific contributions	189
	Bibliography	199

Chapter 1

Introduction

1.1 Development of Accelerators stimulates Medical Physics

According to the 2016 evaluation of the *German federal institute for infectious and non-infectious diseases* (Robert-Koch-Institut), cancer is, after cardiovascular diseases, the second most frequent cause of death in Germany [14]. In a prediction for 2020, 519.000 newly diagnosed cancer cases for a total population of 83.2 Mio were expected [216].

As an alternative to surgery and chemotherapy, radiation can be used to treat cancer by killing the tumour cells and stop tumour growth. Shortly after the discovery of X-rays by Wilhelm Conrad Röntgen in 1895, Stenbeck and Sjögren in 1899 reported the first successful image of a tumour using a X-ray tube. In the decade of 1920, industrial manufacturing of X-ray tubes with an energy spectrum around 150 kV for radiotherapy treatments was started by the Reiniger-Gebbert & Schall AG in Germany. The *linear accelerator* (linac), invented by Wideroe in 1930, was first used in 1953 to perform the first patient treatment using a 8 MV photon beam. Following the invention of the cyclotron by Ernest Lawrence in 1929 and the proposal by Robert Wilson in 1946 to medically use fast high energetic protons for radiotherapy, proton therapy was established at the Lawrence-Berkley National laboratory in 1954 [246, 233]. A similar time lapse was the parallel independent invention of the synchrotron by McMillan and Veksler in 1945, leading to the start of heavy ion therapy using Argon, Silicon and Neon ions in Berkley in 1975.

The technological complexity and cost makes modern hadron therapy using protons or heavier ions nowadays still a less spread teletherapy option compared to the established photon and electron therapy using small linac machines. In 2020, only 113 treatment centers were in operation and the total amount of patients treated worldwide with protons or light ions until 2020 summed up to ≈ 230.000 patients, while in 2014, a total of 434 photon and electron linacs were in operation in Germany [176, 86].

The history of radiotherapy and medical imaging can be summarized as progressive development of **novel accelerator technologies** applying unconventional physics in the field of medical physics, allowing to exploit a new regime of ionizing radiation. This

always is accompanied by the translation of the new and complex technologies into the related **computational models, beam application methods and detector instrumentation**.

1.2 High Power Lasers as Sources of Ionizing Radiation

Since the theoretical prediction of GeV electron acceleration in short distances, driven by high peak power laser pulses in 1979 by Tajima et al., the development of techniques to rise the peak power of lasers, most important of all the invention of *chirped pulse amplification* (CPA) by Strickland and Mourou in 1985, has enabled to overcome the limited laser peak power of the used mode-locked laser systems [220, 43]. CPA allowed to increase the peak powers to reach focused laser intensities above 10^{15} W/cm².

Laser-driven ion acceleration for example becomes feasible above 10^{18} W/cm², but was inaccessible before the CPA invention, since the laser amplifier medium is damaged by excessive spatio-temporal fluences. A similar problem is the desire to operate the amplifier medium close to the damage threshold in order to achieve maximum pulse energies, whereby the pulse repetition frequency of high-power laser systems is, depending on the cooling system and gain medium, restricted to a few shots per hour. Using *titanium:sapphire* (Ti:Sa) crystals, TW-class laser systems with 1 Hz shot frequency were realized in the past decade [115].

This upgrade in repetition frequency, together with automated target positioning, shifts the experimental challenge to the availability of electronic online diagnostics. The ongoing evolution of laser-ion acceleration experiments as *complicated basic-research experiments* towards stable *Integrated Laser-driven Ion Accelerator Systems* (ILDIAS) as reliable and application friendly particle sources of biomedical interest also calls for detectors to probe the laser-target interaction and the emitted particle bunches [116].

In addition to the demand for **proper instrumentation**, adequate **radiation shielding** is necessary to establish high-power lasers as **particle sources with distinct properties**. For laser-driven proton bunches with kinetic energy spectra close to 100 MeV and electron bunches beyond 8 GeV, together with bunch durations which are challenging for established dose monitors, proper radiation shielding of staff, other experiments and the public has to be designed a-priori using simulations.

Further developments of the source properties and beam transport techniques will be **driven by the demand of novel applications**. Due to the unique source features, the concepts of experiments not only in radiobiology and biological imaging, but also material research have to be extended. **Reproducible experiments** with large sample numbers and the transfer, for radiobiology applications, of in vitro-cell culture experiments towards small-animal experiments with associated higher necessary proton beam energies will be essential.

1.3 Outline of the thesis

This thesis work realized several contributions to address the mentioned radiation protection, instrumentation and application challenges:

Chapter 2 lists the basic laws of physics for electromagnetic and nuclear interactions and their mechanisms. Emphasis is given to both elementary particles such as photons and electrons, as well as the nucleons, proton and neutron or heavier nucleon compounds such as alpha particles or carbon ions and non-ionizing particles such as optical photons.

Chapter 3 motivates and summarizes several types of medical accelerator technologies and the related Monte Carlo simulation technique used in this thesis. The technology of using lasers as novel particle sources is presented alongside with detector techniques used for conventional accelerator and laser-based particle beams.

Chapter 4 discusses the energy spectra of secondary neutrons, generated by monoenergetic protons at a proton therapy facility and the distribution of secondary electrons, neutrons, pions, X-ray and γ photons generated by primary proton, electron, carbon and gold ion beams, which are accelerated by an electrical field gradient, generated by optical photons at a laser acceleration facility.

Chapter 5 describes a CMOS pixel detector used to detect the direct impact of proton and gold ions, the detection of proton-induced scintillation photons as well as the usage of the wave and particle nature of optical photons to characterize silicon based CMOS detectors. Many technical steps taken in order to use a new commercial CMOS detector for the detection of particles at laser-driven ion acceleration experiments.

Chapter 6 discusses the characterisation of an electron and proton spectrometer at an electron linear accelerator, also used for X-ray generation. The spectrometer is in routine use for characterisation of electron, proton and carbon ion bunches accelerated by laser-driven sources.

Chapter 7 shows the preliminary work for quantitative radiography using laser-driven proton and X-ray sources.

Chapter 8 concludes the thesis. The achieved results are summarized and suggestions for future experiments are given, based on the lessons learned.

Chapter 2

Interaction of radiation with matter

An understanding of the occurring electromagnetic and nuclear interactions and their mechanisms with regard to the listed non-ionizing particles such as optical photons or neutrons and the ionizing types of radiation is the purpose of chapter 2. The described set of interactions is limited to the particle types and energies relevant to projects dealt with in this thesis. The general comprehension of the physical processes governing the particle specific energy/dose deposition patterns in matter (figure 2.1) are of medical relevance in radiation therapy and for particle detection.

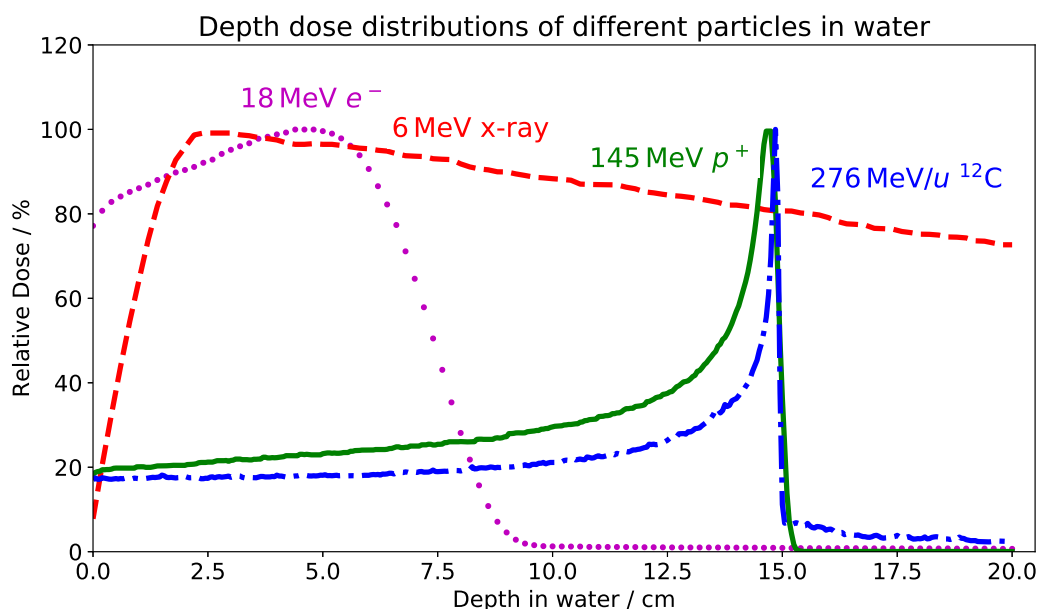


Figure 2.1: FLUKA Monte Carlo (MC) simulations of laterally integrated *depth dose distributions* (DDD) by electron, X-ray, proton and carbon ion beams in water. The different particle interaction mechanisms lead to a very particle specific DDD and hence behavior in radiotherapy, particle detection, particle acceleration and shielding. The DDDs have been normalized to the maximum dose for comparability in shape.

2.1 Photons

The photon is an electrically neutral, massless elementary particle fundamental to the standard model of elementary particle physics. Like all elementary particles, its properties and interaction behaviors are nowadays best explained using quantum mechanics by wave-particle duality. The explanation of the photoelectric absorption interaction (section 2.1.2) relies on the behavior as a particle (section 2.1.2), while the wave-like nature is used to explain the diffraction pattern behind a single slit (used in detector characterisation experiments in section 5.1.5).

2.1.1 Classification of photons

The photon is the discrete energy quantum of the electromagnetic radiation and can be classified based on frequency ν or wavelength λ .

$$(2.1) \quad E_\gamma = h\nu = \frac{hc}{\lambda}$$

In equation 2.1, Planck's constant $h \approx 6.266 \times 10^{-34}$ Js and the speed of light in vacuum $c \approx 2.997 \times 10^8$ m/s are used as the conversion factors. A photon of $\lambda = 800$ nm as generated by a titanium:sapphire (Ti:Sa) crystal-based laser system¹ can hence be attributed an energy of $E_\gamma = 1.5$ eV. The wavelength of optical photons ranges between 380 nm and 740 nm. Scintillators such as *Caesium-Iodide* (CsI), *Lanex* or *Polysiloxane* as used for X-ray and particle detection emit photons in the visible range, which can be collected using silicon semiconductor detectors (applied in chapter 5).

Ultraviolet photons of shorter wavelengths down to $\lambda \approx 10$ nm are followed by the class of X-ray photons ($\lambda \approx 3 - 0.03$ nm), where each X-ray photon has accordingly higher energies (equation 2.1) of keV to MeV. X-rays can either originate as bremsstrahlung from electron deceleration, as characteristic X-rays from atomic processes or as γ -rays from nuclear level transitions. X-rays of $E_\gamma = 6 - 21$ MeV are generated through bremsstrahlung from electron linear accelerators for external beam radiation therapy.

The near-infrared and infrared band of longer wavelength above $\lambda = 740$ nm is followed by the microwave band of λ in the range of several cm. Such microwaves are employed in the resonators of linear accelerators for electron acceleration (used in chapter 6). As mentioned above, such electrons can then be converted into X-rays using a target (described in section 3.2).

Such classification is useful, since the energy of a photon beam determines the interaction behavior of the photon beam with matter.

¹For example the ATLAS laser system used in this thesis as driver of particle acceleration.

2.1.2 Interaction of photons

A photon beam interacting with a material is attenuated during the penetration following the Beer-Lambert Law (equation 2.2). The initial intensity of the photon beam I_0 is reduced to an intensity $I(x)$ after traversing a homogeneous material of thickness x . So the actual number of photons in the beam is reduced by the exponential attenuation law.

$$(2.2) \quad I(x) = I_0 \cdot e^{-(\mu x)}$$

The energy and material dependent linear mass attenuation coefficient $\mu(Z, E)/\rho_a$ reflects the energy dependence of the total photon interaction cross section σ_{tot} , which can be calculated using μ/ρ_a , the atomic molar mass m_a of the material, its density ρ and Avogadro's number N_A via

$$(2.3) \quad \sigma_{tot} = \frac{\mu}{\rho_a} \cdot \frac{m_a}{N_A}$$

The total interaction cross section σ_{tot} is the sum of the constituent interaction cross sections (equation 2.4). The interactions in the photon energy range relevant for this work (eV to MeV) are: Photoelectric absorption ($\sigma_{p.e.}$), Rayleigh scattering ($\sigma_{Rayleigh}$) and Compton scattering ($\sigma_{Compton}$).

$$(2.4) \quad \sigma_{tot} = \sigma_{p.e.} + \sigma_{Rayleigh} + \sigma_{Compton}$$

Far below photon energies of 1.022 MeV, the threshold for necessary for pair production, photoelectric absorption is the dominant photon interaction mechanism (figure 2.2b). The incoming photon interacts with an electron from the shell of a target atom and is absorbed. If the photon energy E_γ exceeds the binding energy E_b of the electron, the electron with the kinetic energy $E_{kin} = E_\gamma - E_b$ is emitted and called *photoelectron*. A photocurrent can be measured by collection of these ionisations. This photocurrent may be collected by a pixelized detector and gives a spatially resolved, quantitative measure of the incoming photon flux (section 3.4). The probability for the occurrence of the photoelectric effect is $\sigma_{p.e.} \propto Z^5/E_\gamma^{3.5}$ (figure 2.2b). The strong $\approx Z^5$ dependence can explain why lead ($Z = 82$) is an excellent shielding material for photons, e.g. compared to aluminum ($Z = 13$). It also explains why X-ray absorption ($\sim 80 - 120$ keV) imaging shows a good bone, but a weak soft-tissue contrast.

For intermediate photon energies between 1.022 MeV and a few MeV, elastic Rayleigh and later Compton scattering are dominant. Since Rayleigh scattering is an elastic scattering process and does not transfer energy to the material, Compton scattering with loosely bound atomic electrons is the dominant energy loss mechanism (figure 2.2b).

2 INTERACTION OF RADIATION WITH MATTER

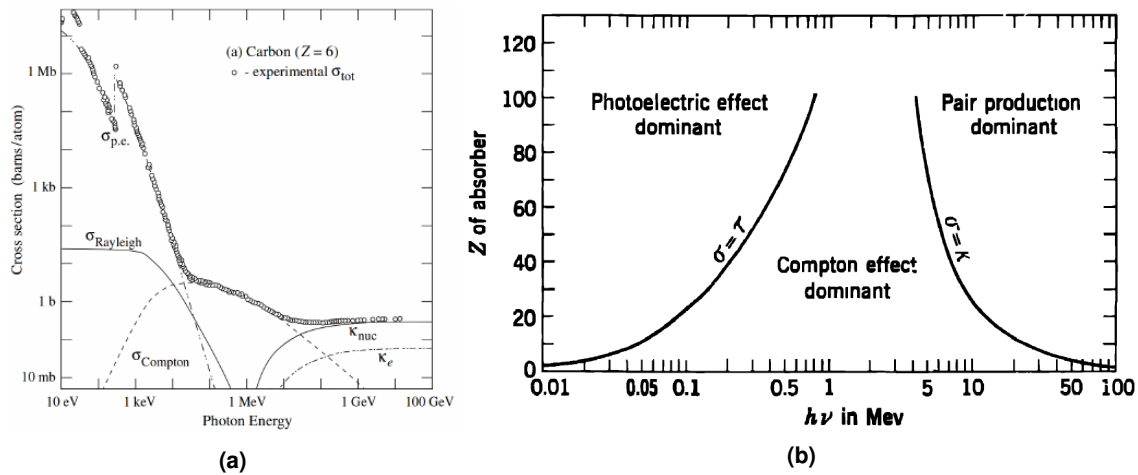


Figure 2.2: Cross sections of photon-matter interactions. **(a)** Total interaction cross section σ_{tot} and underlying contributions of interaction cross sections in solid carbon. **(b)** Relative importance of interaction cross sections relevant to energy loss, plotted as function of photon energy and atomic number Z [172, 223, 60].

For higher photon energies above a few MeV, the pair production cross section in the nuclear field κ_{nuc} mainly contributes to σ_{tot} (figure 2.2a). The photon threshold energy for pair production in the field of a single nucleus is $2 \times m_e c^2 \approx 2 \times 511 \text{ keV}$, where $m_e \approx 0.511 \text{ MeV}/c^2$ is the rest mass of an electron / positron. Pair production is only kinematically possible in the vicinity of the electric field of a nucleus (of atomic number Z), which allows for the necessary conservation of the momentum. The process can also happen with electrons of the atomic shell (triplet production), presenting a higher energy threshold, but is of lower importance (figure 2.2a). Figure 2.2b shows the dependence on Z . The materialisation of a photon into an electron - positron pair depends on the atomic number of the material ($Z \propto Z^2$) and is of less importance for biological tissue ($Z_{eff,water} = 7.2$) or the detector material silicon ($Z_{Si} = 14$).

2.2 Protons and light ions

2.2.1 Electromagnetic interactions

Stopping power Charged particles other than electrons, often referred to as *light ions* or *heavy charged particles*, release their energy in different interactions with the traversed material. Each one of those interactions can change the direction and the energy of the original particle. The average rate at which ions lose the amount of energy E per unit path length x due to Coulomb interactions is given by the linear stopping power S :

$$(2.5) \quad S = - \frac{\Delta E}{\Delta x}$$

The stopping power can be expressed in units of mass thickness. Equation 2.5 has to be divided by the density of the medium resulting in the *mass stopping power* $((dE/dx)/\rho)$. For ion beam therapy treatment planning, the mass stopping power is obtained from stoichiometric calibration curves, which link the X-ray based CT imaging *Hounsfield units* (HU) in each voxel to mass stopping power values [201].

The dominant effect for proton energy loss in the therapeutic energy regime results from inelastic interactions with electrons via electromagnetic Coulomb forces and is summarized in the electronic stopping power. This mechanism, compared to the nuclear and radiative contributions, contributes most to the total energy loss.

The following analytical expression describes the electronic mass stopping power of ions with kinetic energy higher than 1 MeV, charge number Z_p and velocity $\beta = v/c$. The so-called Bethe-Bloch equation (equation 2.6) is also referred to as mean ionisation energy loss rate [20, 23]:

$$(2.6) \quad -\frac{dE}{dx} = 4\pi r_e^2 m_e c^2 \times n_e \frac{Z_p^2}{\beta^2} \left[\ln \left(\frac{2m_e c^2 \beta^2}{1 - \beta^2} \right) - \beta^2 - \ln \langle I_e \rangle - \frac{\delta}{2} - \frac{C}{Z_t} \right]$$

The medium in which the ion is moving is, in this formulation, characterized by the mean ionisation potential $\langle I_e \rangle$ and the density of electrons $n_e = N_A \rho \frac{Z_t}{A}$, in which Z_t is the atomic number of the target medium and ρ the mass density of the medium. The further proportionality constants are N_A as the Avogadro number, r_e is the classical electron radius and m_e is the electron mass. Furthermore, δ and C are higher order correction terms in order to extend the energy range for which equation 2.6 is valid. The shell correction C accounts for the invalid assumption that the orbital electrons of the absorber are at rest (relative to the projectile ion), being a prerequisite of the Bethe-Bloch theory [65]. This effect can be up to 6% for protons in the energy regime of 1-100 MeV. The density correction δ includes the stopping power reduction due to polarisation effects in the medium, which reaches the 1% level only above 500 MeV [114].

In general, equation 2.6 is valid for velocities β much higher than the orbital velocity of the electrons.

At high velocities, heavy ions are fully stripped from electrons. Coming down from kinetic energies used in radiotherapy (250 MeV for protons, corresponding to semi-relativistic relativistic velocity of $\beta = 0.6$) to energies of around 10 MeV, the projectile velocity becomes comparable to the orbital electron velocity ($\beta \approx 0.008$). This causes a reduction of the mean charge state, since the ions get partly neutralized by recombining with electrons from the target material as they slow down. Thus, the projectile charge Z_p in equation 2.6 is reduced and must be replaced by an effective charge Z_{eff} , which can be calculated from the empirical formula of Barkas (equation 2.7) [13].

$$(2.7) \quad Z_{p,eff} = Z_p \times \left(1 - e^{-125\beta Z_p^{\frac{2}{3}}} \right)$$

For intermediate energies preceding the Bethe-Bloch region (< 1 MeV), energy losses can be described by the model of Anderson and Ziegler [258].

For very low energies, β becomes comparable to the velocity of the orbital electrons and equation 2.6 is no longer valid. For this so-called Lindhard region, the energy loss is proportional to β [137].

The electronic stopping power as a function of the kinetic energy of protons impinging on a water target is depicted in figure 2.3. The Bethe-Bloch equation is responsible for the finite range and, together with range straggling due to the stochastic nature of the interactions, for the characteristic depth dose along the beam direction with a low entrance plateau, ending with a steep Bragg peak (figure 2.1) [30]. The plateau height for a clinical 200 MeV proton Bragg-peak can be approximated as $\approx 30\%$ of the Bragg-peak maximum dose.

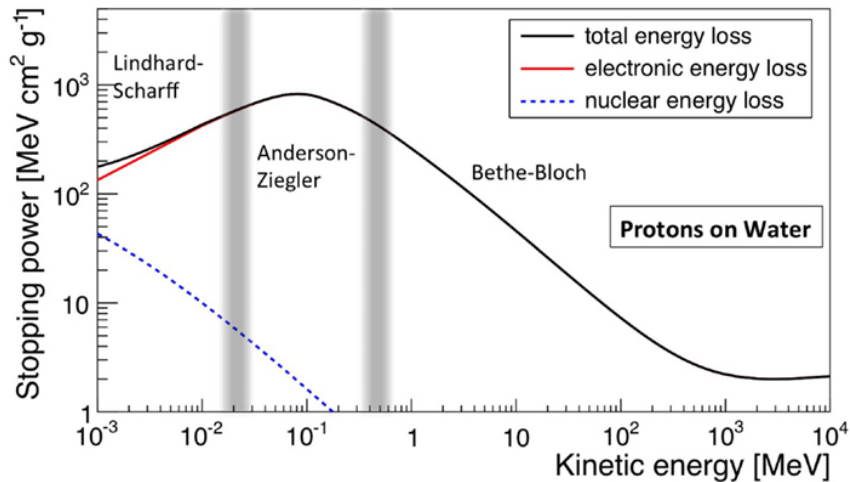


Figure 2.3: Total stopping power of protons in water. The data shows the proton energies relevant to radiation therapy. Over the important four orders of magnitude, the energy loss is exclusively dominated by electronic energy loss [128].

Range R The range R of a charged particle beam is a phenomenological expression used to quantify the average depth of penetration in an absorber material. The range in *continuous slow down approximation* (CSDA) R_{CSDA} represents the average path length traveled by a proton beam when slowing down to rest $E_f = 0$ from an initial energy E_0 [212]:

$$(2.8) \quad R_{CSDA}(E_0) = - \int_{E_0}^0 \frac{dE}{S_{tot}(E)}$$

The stopping power as presented in equation (equation 2.6) expresses the mean energy loss for a beam consisting of a large number of particles having an identical initial kinetic energy. Each beam particle will experience a slightly different energy loss throughout the passage due to the stochastic nature of the collisions. Consequently, the energy distribution of an initially monoenergetic particle beam widens with increasing absorber depth. The corresponding path length fluctuations are referred to as *range straggling* and are in the range of a few percent [157]. A visible consequence is a longitudinal widening of the proton dose distribution peak that becomes broader for high beam energies (figure 2.1). The energy loss distribution for a thick target can be described by a Gaussian function, but for a lower number of collisions with energy loss, i.e. for thin targets and high-energy beams, a description by a Landau function is more precise [157].

The beam from an accelerator is never perfectly monoenergetic. For modern medical proton accelerators (section 4.1), the spread is smaller than 1% of the energy. For electron linacs (chapter 6) or laser-driven accelerators (section 4.2), the spread can be $10\times$ to $100\times$ higher.

But since it is impractical to directly measure the 50% fluence or energy of a charged particle beam, usually the dose delivered by the beam is measured and the distal 80% of the dose of the Bragg peak (figure 2.1) is referred to as eighty percent range R_{80} .

The R_{80} of interest in external beam radiotherapy using protons is between a few cm and around 30 cm in water, corresponding to 50 MeV and 230 MeV initial beam energy. For the tandem accelerator used in this thesis, the mostly used 22 MeV corresponds to a proton range in water at room temperature of 4.2 mm, according to a MC simulations using the *FLUKA* code (section 3.2.5).

2.2.2 Electromagnetic Coulomb scattering and lateral broadening of an ion beam

When passing through matter, beam particles (projectiles) will be deflected laterally from the original straight path. The most dominant cause is a large number of elastic and semi-elastic Coulomb scattering events with atomic nuclei, leading to an accumulated effect called *Multiple Coulomb Scattering* (MCS). The net energy loss due to MCS is negligible. Lateral scattering due to projectile - electron interactions can be neglected, as the mass of protons or heavier projectile ions is at least three orders of magnitude higher compared to the atomic electrons.

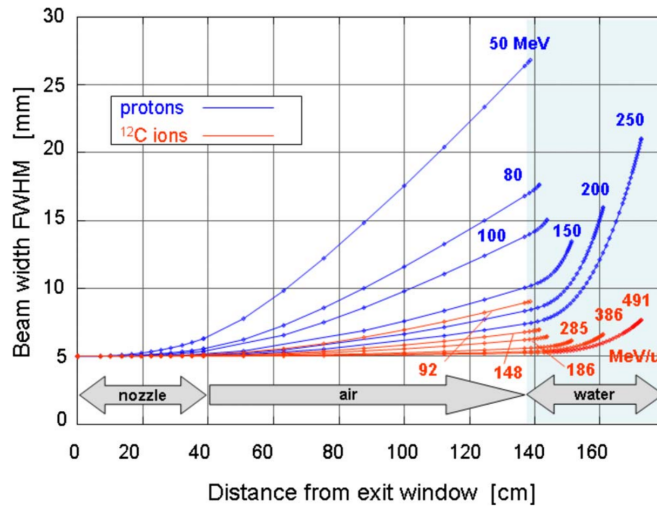


Figure 2.4: Lateral deflection of clinical proton and carbon ion beams in the GSI treatment facility propagating towards the patient [128]. The carbon beam scatters less at the same depth in air / water compared to protons. Scattering in water is higher as in air due to the Z^{-2} dependence in equation 2.9. Beam broadening increases towards the end of the range, i.e. for lower energy.

The average deflection angle θ relative to the original straight path was calculated in an analytical solution by Molière [154]. The sophisticated analytical solution due to the Molière theory can be approximated as a Gaussian distribution using the *central limit theorem*, summarized in the Highland formula [102]. The probability distribution of the net angle of deflection of a particle traversing a thick material then is close to be of Gaussian shape, as a result of being the sum of many small random deflections. The net angle quantifies the beam broadening of an initially parallel and pencil-like beam. A modern approximation to the root mean squared error of scattering angles θ_0 is [142]:

$$(2.9) \quad \theta_0 = \frac{13.6 \text{ MeV}}{\beta c p} Z_p \sqrt{\frac{x}{X_0}} \left[1 + 0.038 \times \ln \left(\frac{x}{X_0} \right) \right]$$

where p is the projectile momentum and x the straight connection of the start and the end point of the particle trajectory in the medium. X_0 is the radiation length of the material and it is defined as the mean length to reduce the energy of a beam of relativistic electrons, losing mostly energy by bremsstrahlung, to $1/e$. The radiation length X_0 depends on Z_t^{-2} of the target material atomic number Z_t . Typical values, normalized by the material density, are 21.82 g/cm^2 for silicon and 36 g/cm^2 for water. The denominator $\beta \cdot c$ dependence leads to increased scattering towards the end of the particle range and low deflections at high particle energy, i.e. for example at the trajectory start (figure 2.4).

Since the Gaussian approximation of the probability distribution of the net angle is not perfect, low magnitude large-angle tails exist for particle beams, originating from single large-angle scattering events in the target [247]. Although this inaccuracy is often ne-

glected, e.g. in analytical proton therapy treatment planning systems, modern proton spot scanning therapy consisting of many spots can accumulate the inaccuracy and lead to discrepancies to measurements. In previous work, the author contributed to absolute dosimetry simulations investigating this effect [249].

2.2.3 Nuclear reactions of ions in matter

Besides the electromagnetic interactions, nucleons in heavy ions or individual protons and neutrons can interact with target nuclei via the strong nuclear force. Nuclear interactions contribute significantly less to the kinetic energy losses than the aforementioned electromagnetic processes. To interact via the strong force, the kinetic ion energy needs to be high enough to overcome the Coulomb barrier of the target atoms.

These nuclear interactions can be *elastic* or *inelastic*. In case of *elastic interactions*, the kinetic energy of the projectile-target system is conserved, but the momentum vector may have changed orientation. The involved nucleus / ion stays intact.

In *inelastic interactions*, the kinetic energy is not conserved and the projectile nucleus (in case of ions heavier than protons) may fragment and eject secondary particles such as protons, neutrons, deuterons or heavier ions. Such *inelastic nuclear reactions* exponentially reduce the particle fluence ϕ as function of depth x inside the traversed material. Inside a material of atomic density N , the initial particle fluence ϕ_0 is reduced as:

$$(2.10) \quad \phi(x) = \phi_0 \cdot e^{-N\sigma x}$$

The total nuclear reaction cross section σ quantifies the probability of a general nuclear reaction to occur per unit path length. It contains the dependencies on the mass number of the projectile and target, the nuclear radius and the impact factor of projectile and target and is measured in barn, where $1 \text{ barn} = 100 \text{ fm}^2 = 10^{-28} \text{ m}^2$.

The type of interaction, namely *elastic* or *inelastic*, the exact reaction called *reaction channel*, which is dependent on the projectile and ejectile type, the energies and the target material, are collected in nuclear databases such as the *Evaluated Nuclear Data File* (ENDF) [32].

Microscopically speaking, a proton, ion or neutron hitting an atomic nucleus initiates a series of nucleon-nucleon collisions, which can lead to the emission of protons, neutrons, light fragments, and to equilibration of the remnant nucleus [128]: (*Generalized Intra-nuclear cascade* (INC) ($> 50 \text{ MeV}$ projectile nucleon energy, 10^{-23} - 10^{-22} s , emission of high energy nucleons or light ions), pre-equilibrium ($< 50 \text{ MeV}$ projectile nucleon energy, mainly nucleon-nucleon collisions leaving a certain excitation energy shared among the target-nucleus nucleons) and disexcitation step. The disexcitation step, dependent on the mass of the target and the remaining energy, dissipates the excitation energy either via

the fast processes of evaporation and fission (fission for heavy nuclei, both 10^{-22} s) or by the slow processes (10^{-18} - 10^{-16} s) of Fermi-breakup and γ -ray emission.

Since the kinetic energy of therapeutic protons (< 300 MeV) is high enough, the patient itself, beam delivery or surrounding material has to be regarded as potential source of neutrons, protons, ions, electrons, positrons or, to a lesser extend, other particles (section 4.1). Laser-accelerated ions may in the next years be available in Munich in this energy regime (section 4.2). The main reduction of beam fluence (equation 2.10) is caused by the inelastic nuclear reaction cross section entering the total reaction cross section σ . For an initially 160 MeV proton beam in water, the fluence reduction at the Bragg peak depth are only $\phi(16 \text{ cm}) = 0.8 \times \phi_0$ [84].

The secondary particles originating in these fragmentation reactions may be as high-energy as the incoming projectile and light and carry the kinetic energy away from the incoming beam direction or beyond the range of the initial ion beam Bragg peak (figure 2.1). High-energy secondary fragments, especially secondary neutrons are of concern, since they may themselves cause further nuclear reactions without being decelerated by the Coulomb barriers (section 4.1.1).

2.3 Electrons

Electrons lose their energy while traversing matter mainly through radiation-less collisions and radiative losses. Moderately relativistic electrons predominantly interact by the Coulomb force and lose their kinetic energy primarily by inelastic collisions with the atomic electrons, resulting in ionisation and atomic excitation. These energy losses are continuous. When the ejected electron is of such high kinetic energy that it can cause secondary ionisation itself, it is called *delta-ray* electron. The amount of energy lost in Coulomb interactions with the target nuclei of atomic number Z is very small. For electrons of higher energy $E_{kin} > 500$ keV (equation 2.12), the contributions to the total stopping power $S_{tot} = S_{col} + S_{rad}$ hold the approximation:

$$(2.11) \quad \frac{S_{rad}}{S_{col}} \approx \frac{Z \cdot E}{800}$$

The relationship can be used to calculate the critical energy E_c at which the radiative losses are equal to the radiation-less losses. For energies above E_c , electromagnetic showers, in which electrons, positrons and photons continuously transform into each other and lose energy while interacting with the medium, are the dominant energy loss. The critical energy for electrons in water ($Z_{eff} = 7.2$) is 110 MeV, whereas for lead ($Z=82$) it is already $E_c = 9.76$ MeV [129].

The emitted photon radiation caused by the deceleration in the Coulomb field is called bremsstrahlung. The energy loss due to radiative losses can be quantified as:

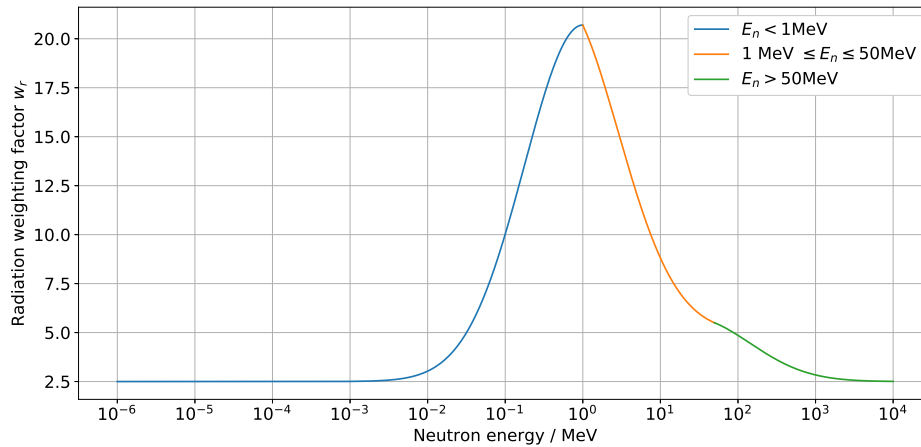


Figure 2.5: Radiation weighting factor w_R for epithermal, fast and high-energy neutrons used to calculate equivalent dose for the purpose of radiation protection, i.e. in low-dose exposition regions [112].

$$(2.12) \quad S_{rad} = \left(\frac{dE}{dx} \right)_{rad} \propto \rho \times \left(\frac{e}{m} \right)^2 Z^2 E$$

For electron energies above 1 MeV, the emitted bremsstrahlung is forward peaked within $\pm 10^\circ$. For radiation protection purposes, the usage of high-Z material can hence be problematic for high energy electrons. The caused secondary bremsstrahlung shower can be penetrating itself and also cause the emission of even more penetrating secondary neutrons due to photo-nuclear reactions above a certain threshold of usually 6 to 8 MeV [129].

2.4 Neutrons

The kinetic energy spectra of secondary neutrons in a treatment room can span up to 12 orders of magnitude. In order to allow for evaluation of the physical processes in dependence of the neutron kinetic energies, neutrons are typically binned in four energy intervals:

- Thermal neutrons ($1 \text{ meV} \leq E < 0.4 \text{ eV}$)
- Epithermal neutrons ($0.4 \text{ eV} \leq E < 100 \text{ keV}$)
- Fast neutrons ($100 \text{ keV} \leq E < 19.4 \text{ MeV}$)
- High-energy neutrons ($E \geq 19.4 \text{ MeV}$)

2 INTERACTION OF RADIATION WITH MATTER

The term *evaporation neutrons* refers to a special type of neutrons in the fast energy range, which were emitted from excited nuclei via the fast evaporation process (section 2.2.3).

Since neutrons are electrically neutral hadrons, the interaction mechanisms differ from the charged particle beams such as electrons (section 2.3), protons or ions (section 2.2). Neutrons do not interact and deliver their kinetic energy to the traversed material via electrons but directly interact with the nuclei. Apart from the inelastic generation of secondary nuclear fragments or nucleons, of which the different stages were described in section 2.2.3 and are valid for all incoming nucleons, neutrons may also scatter elastically and lose kinetic energy and/or change direction (equation 2.13).

Neutrons are of concern in medical physics. Neutrons are used in *Boron-Neutron capture therapy* (BNCT) for a small number of < 100 patients per year worldwide in palliative treatments. Recently, investments in the technology are rapidly growing. In BNCT, short-ranged and biologically effective α particles are used for tumour control and are emitted in the $^{10}\text{B}(n, \alpha)^7\text{Li} + 2.4 \text{ MeV}$ reaction, since the corresponding neutron capture cross section for thermal neutrons (e.g. $E_n = 0.0252 \text{ eV}$) is as high as $\sigma_{nc}(^{10}\text{B}) = 3838 \text{ b}$ [48]. Other than that are neutrons the main constituents to out-of-field dose in radiotherapy: in megavoltage X-ray radiotherapy, the physical effect generating such secondary neutrons is the photonuclear absorption of $E > 8 \text{ MeV}$ photons in collimators and the linear accelerator beam delivery system (section 2.3) [107].

The kinetic energy of a neutron after a collision with a target nucleus of mass M_t for an initial energy E_0 and mass m_n can be calculated for a scattering angle δ in the relative system using simple two-body collision kinematics:

$$(2.13) \quad E_n = E_0 \times \frac{M_t^2 + m_n^2 + 2M_t m_n \cos \delta}{(M_t + m_n)^2}$$

For radiation protection of neutron radiation, a maximum energy loss is desirable. The energy loss is maximal for backscattering ($\delta = \pi, \cos \delta = -1$), as equation 2.13 can be rewritten:

$$(2.14) \quad E_n = E_0 \times \frac{(M_t - m_n)^2}{(M_t + m_n)^2}$$

From equation 2.14, it is clear that the energy transfer is high for light materials of comparable mass ($M_t \approx m_n$), which is exploited in the usage of proton-rich paraffin neutron moderators.

In addition to a maximal energy loss, reduction of the neutron fluence is possible and realized using neutron capture reactions, leading to the absorption of neutrons and the emission of protons or γ rays, which are easier to shield. Further notable cross sections

for thermal neutron capture ($E_n = 0.0252$ eV) are for example $\sigma_{nc}(^{113}\text{Cd}) = 20.600$ b and $\sigma_{nc}(^{157}\text{Gd}) = 254.000$ b [129].

Neutron spectral fluence can be used to calculate effective doses for a given incident neutron field by applying *fluence to equivalent dose* conversion coefficients that vary with neutron energy [112]. The radiation weighting factor w_R is used in radiation protection and so far a valid concept in low dose regions to convert absorbed physical dose to equivalent dose (section 2.5.1). It has been reported that w_R of neutrons is highest for epithermal, fast, and high-energy neutrons in the interval 10^{-2} MeV to 10^2 MeV, which shows a 10 times higher w_R compared to $w_R \sim 2 - 3$ elsewhere or $w_R = 1$ for photon radiation (figure 2.5) [202, 112].

2.5 Dose and biological considerations

2.5.1 Dose

Absorbed dose The absorbed dose in a medium is of central interest for evaluation of the quantitative interaction of radiation with matter. The dose as a macroscopic is microscopically defined as the mean energy $d\epsilon$ imparted to a small mass element dm of matter [113]:

$$(2.15) \quad D = \frac{d\epsilon}{dm}$$

For example for a monoenergetic beam of charged ions, the stopping power, describing the energy deposition pattern in a microscopic way (equation 2.6), can be linked to the macroscopic absorbed dose [84]:

$$(2.16) \quad D = 1.602 \times 10^{-10} \times \phi \times \frac{dE}{dx} \frac{1}{\rho}$$

In order to get the dose in its natural unit *Gray* ($1 \text{ Gy} = 1 \text{ J/kg}$), the particle fluence $\phi = dN/da$ [cm^{-2}] for dN ions impinging upon a small sphere of cross-sectional area da , target density ρ [g/cm^3] and stopping power (dE/dx [MeV/cm]) from equation 2.6 are used.

In the direct measurement of several mGy high absorbed doses, e.g. for detector tests at accelerators (or in external beam radiation therapy), the direct and quantitative measurement of the amount of energy that the incident radiation is imparting is linked quantitatively to deterministic effects like the number of generated electron-hole pairs, which can be measured as a current.

2 INTERACTION OF RADIATION WITH MATTER

In radiation protection, the absorbed doses usually are lower than several mGy (mSv) and the direct effect may not be macroscopically visible. The absorbed dose in Gray is in radiation protection therefore only used for the description of the immediate health effects due to high levels of acute dose. These exposures are for example tissue effects like inflammation, vomiting or bleeding, summarized as *acute radiation syndrome*. These medical effects are deterministically linked to levels of e.g. 10 Gray and are certain to happen after a short amount of time.

Equivalent dose While the high doses above ≈ 500 mSv are linked to *deterministic* effects in the absorbing materials or tissues, the low-doses, e.g. in radiological protection, try to quantify the *stochastic* health risk to the whole body. Examples are the probability of cancer induction and genetic effects of low levels of ionizing radiation [112]. Two types of quantities are defined for use in radiological protection: *protection quantities* and *operational quantities*:

- Protection quantities are defined by the *International Commission on the Radiological Protection* (ICRP) and are used for the formulation of the radiation limits that living organisms should be exposed to. They are not measurable but are calculated via anthropomorphic phantoms and are used to compare observed stochastic health effects after exposure to lower radiation doses. Stochastic radiation damage does not have any threshold dose in contrast to the *deterministic effects*. Physical quantities like fluence ϕ and absorbed dose D (equation 2.16) are weighted using the radiation weighting factor w_R and the tissue weighting factor w_T to account for the observed biological effects. Examples are the *organ equivalent dose* H_T and *effective Dose* E explained in the following.
- Operational quantities are defined by the *International Commission on Radiation Units and Measurements* (ICRU) and are intended to provide an estimate for the *protection quantities*. They are measurable and can be calculated using simple phantoms like spheres or slabs and used for the practical evaluation of doses. An example is the *ambient dose equivalent* $H^*(d)$, also explained in the following.

Equation 2.17 calculates the *organ equivalent dose*, where the energy dependent w_R accounts for the biological effectiveness of a radiation of type R and $D_{T,R}$ is the mean *absorbed dose* in a tissue or organ T . w_R is necessary, since high-LET radiation like low energy protons and ions, as well as fast neutrons and lower energy X-rays, are of higher biological effectiveness compared with low-LET radiation (X-ray photons) (section 2.5.3).

$$(2.17) \quad H_T = \sum_R D_{T,R} \cdot w_R$$

Since w_R is dimensionless, the unit for organ equivalent dose is the same as for absorbed dose, J/kg . Differentiation is done by the special name *Sievert* (Sv) [237].

The operational quantity *ambient dose equivalent* $H^*(d)$ is used in radiation protection to estimate the organ equivalent dose at a point of interest. Typically for radiation, which is more penetrating than low-energy X-rays, electrons or alpha particles, $H^*(10)$ is used, as it can be experimentally measured in 10 mm depth of the standardized ICRU-sphere, a human tissue equivalent phantom [129].

Although most of the kinetic energy of a clinical proton beam is deposited in tissue via electromagnetic interactions with atomic electrons, proton induced nuclear reactions can generate unwanted secondary radiation like stray neutrons within the beamline elements, the structures of the gantry room, and even within the patients themselves [157, 156, 94].

Although the stray neutron dose is much lower in magnitude compared to the therapeutic proton doses, it penetrates the whole body of the patient. The ambient dose equivalent $H^*(10)$ of stray neutrons was found to be up to $25 \mu\text{Sv}/\text{Gy}$ for a proton therapy treatment fraction dose of 2 Gy [234]. Although conceived for radiation protection purposes, w_R has been already used as a reasonable approximation for the estimation of biological effectiveness for organ equivalent dose calculations in proton therapy, e.g., Rechner et al. and Zheng et al. [183, 255]. The stray neutron dose may therefore be approximated using w_R to be possibly up to 20-times more biologically effective [202].

In order to make quantitative assessments in calculating the prompt dose rates for shielding design of treatment rooms, the systematic knowledge of the neutron fluence spectrum is hence essential. Chapter 4 presents a Monte Carlo study of the neutron spectra encountered inside a pencil beam scanning proton therapy treatment room.

Effective dose Apart from the varying biological effectiveness of different types of radiation as considered in H_T , the *effective dose* also accounts for the individual radiosensitivity of different tissues and organs of the human body. It is calculated as the tissue-weighted sum of the equivalent doses in all specified tissues and organs T of the body [237]:

$$(2.18) \quad E = \sum_T H_T \times w_T$$

For a partial body irradiation, the effective dose E is the sum of the organ doses H_{T1} , H_{T2} , etc. of the irradiated parts, which had been weighted with the corresponding tissue weighting factor w_T . The factor w_T is weighted such that for a whole body irradiation of all organs T : $\sum_T w_T = 1$ [237]. The *whole body equivalent dose* is the effective dose. The unit for the effective dose is the same as for absorbed dose, J/kg , and its special name is again *Sievert* (Sv). Dose limits in the regulatory German law are expressed as effective dose limits per year [33].

2.5.2 Relative biological effectiveness

Although the interaction mechanisms for photons and charged particles differ, it is desirable to have a measure to compare the doses of different types of radiation needed to provoke the same biological effect in the therapeutic high-dose regime. Such intercomparison allows to build on the radiation oncology experience of doses needed for local tumour control, which was gained in the past decades of photon therapy using e.g. ^{60}Co γ -radiation or linear accelerator generated X-ray beams.

The comparison factor *Relative Biological Effectiveness* (RBE) is defined as the ratio of the physical dose by a reference radiation, typically ^{60}Co γ -radiation, and the physical dose by the ion radiation, which causes the same biological effect in typical cell irradiation experiments [119].

By weighting the physically deposited dose (measured in Gy) with RBE, the so-called biological dose (denoted as $\text{Gy}(\text{RBE})$) of the ion radiation can be obtained and directly compared to the equivalent photon dose requested to produce the same biological effect.

$$(2.19) \quad \text{RBE} = \frac{D_{\text{Reference}}}{D_{\text{Ion}}}|_{\text{isoeffect}}$$

2.5.3 Linear Energy transfer

The value of RBE microscopically depends in a complex manner on several parameters: The biological endpoint under evaluation (e.g. cell death), the cell-type under investigation (e.g. tumour cell type), the charge Z of the heavy ion radiation and the linear energy transfer (LET) of the radiation [143]. LET is the local concentration of average energy that an ionizing particle transfers to the material per unit distance and typically expressed in $\text{keV}/\mu\text{m}$.

$$(2.20) \quad \text{LET}_{\Delta} = \frac{dE_{\Delta}}{dx}$$

In this definition, dE_{Δ} is the kinetic energy, which is locally transferred to charged secondary particles of the propagation medium. Secondary particles above the energy threshold Δ are excluded, since these have the a range high enough that their kinetic energy is not absorbed locally.

For protons, a constant RBE of 1.1 is used clinically. This value is under discussion in the community and observed to increase up to 1.6 towards the last μm of the proton range inside the Bragg peak [163].

RBE is dependent on LET, i.e. on the local energy deposition pattern, since the goal of ionizing radiation is to induce complex, i.e. in close vicinity to each other, DNA double

strand breaks. Closer damages to the DNA double helix may be less probable to be repaired by the repair proteins of the tumour.

2.5.4 FLASH

Not only is the RBE dependent on the local spatial dose deposition pattern. Since years, fractionation is used to exploit the differing response to radiation of tumour and healthy tissue. Fractionation splits the therapeutic tumour control dose prescribed by the physician into a number of individual fractions, e.g. 21 fractions. The 21 fractions are then consecutively irradiated to the tumour in the progress of 21 days, each fraction containing 1/21 of the total tumour control dose. Since healthy tissue is able to repair better the damage caused by the ionizing radiation more easily than tumour tissue, a differential effect sparing the healthy tissue is observed with fractionation.

New research shows hints that the time delivery structure towards short time scales may also be important to consider. Pre-clinical results from so called FLASH irradiation using commercial spot scanning proton therapy systems at dose rates of 40 Gy/min are encouraging in terms of improved healthy tissue sparing [238]. The typically used dose rate of a clinical system is one order of magnitude lower at about 2 Gy/min. As of today, the biological mechanism is still unclear but subject of very vivid investigations. Estimates towards even higher dose rates would be desirable.

Laser accelerated protons may deliver the whole dose of a treatment fraction of e.g. 1 Gy not as usual with a dose rate of 2 Gy/min, but orders of magnitude shorter in bunches of nanosecond length. The biological effectiveness of ultrashort-bunches with nanosecond ion bunches of high charge were previously studied using protons accelerated using the an early version (10 TW) of the ATLAS-laser system, which is, in an upgraded version, also used in LEX and CALA [21]. In 2012, the group was not able to find new radiobiological effects of the nanosecond proton delivery Using 7 Gy/ns bunches of up to 5.2 MeV.

Reliable statistics with large sample numbers and the transfer of the in vitro-cell culture experiments towards small-animal experiments with associated higher necessary proton beam energies will be essential. The LION experiment in LEX and CALA is continuing the research after laser power upgrades to 300 TW in LEX and 3 PW in CALA, as well as other experiments in Dresden and Berkley [22, 131].

Chapter 3

Fundamentals of radiotherapy-, laser-acceleration- and detector technologies

This chapter motivates and summarizes several types of medical accelerator technologies and the related Monte Carlo simulation technique used in this thesis (section 3.2), the technology of using lasers as novel particle sources (section 3.3) and detector techniques used for conventional accelerator and laser-based particle beams (section 3.4).

3.1 Accelerator research from a radiotherapy point of view

Radiation therapy for tumour treatment is mainly divided into brachytherapy and teletherapy:

Brachytherapy For brachytherapy, clinicians place short-range radiation sources inside the patient body or in direct contact with it, which are made of radioactive isotopes emitting electrons or low energy (kV) γ -rays, so called seeds.

Teletherapy For teletherapy, the therapeutic beams are delivered using accelerators or radioactive cobalt sources from the outside into the patient. An ideal treatment would place 100% of the radiation dose inside the tumour volume and no dose in the surrounding tissue (figure 3.1a). The used beams hence have to have sufficient energy to penetrate the patient body. Clinically the employed energies today are 6-21 MeV for photon and electron beams, 75-250 MeV of kinetic energy for proton beams, 430 MeV/u for carbon ions and even more for heavier ion beams or less than several MeV for nuclear reactor originated neutrons. It is hence evident that the ideal treatment situation of 100% dose

3 FUNDAMENTALS OF RADIOTHERAPY-, LASER-ACCELERATION- AND DETECTOR TECHNOLOGIES

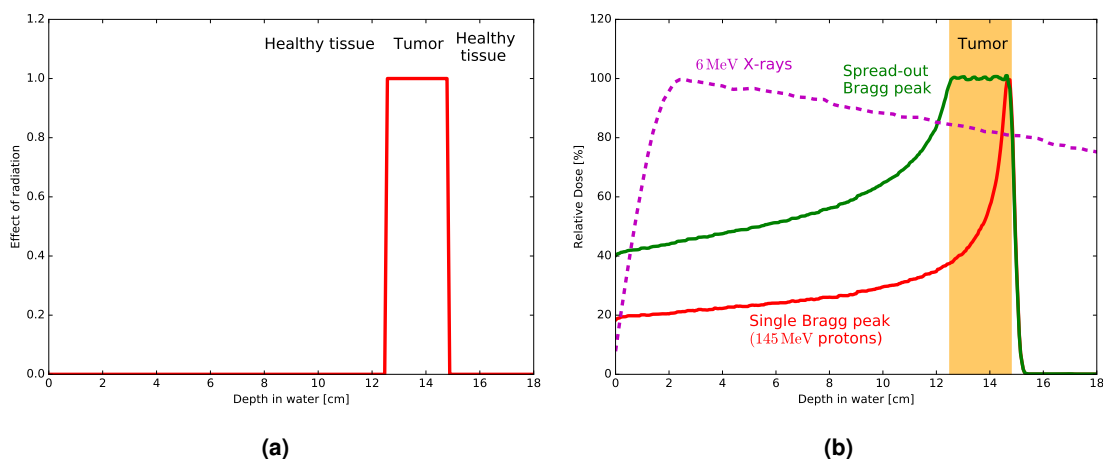


Figure 3.1: Targeted delivery of radiation to a deep seated tumour. **(a)** Idealized irradiation only depositing energy in tumour. **(b)** Simulated X-ray and proton (single beam and SOBP) depth-dose distributions. A fraction of dose is deposited outside the tumour volume.

in the target volume and no *out-of-field* dose cannot be realized. The task is realistically to tailor the type and spatial shape of the radiation field to maximize a biologically effective in the tumour dose and minimize out-of-field dose (figure 3.1b). The accelerator and shielding structures for the operational personnel can be additionally challenging this task by generating out-of-field radiation in the treatment head or scattering radiation back on the patient (chapter 4).

The usage of different ionizing beams of photons and particles (electrons, protons, light ions and neutrons) in teletherapy is mainly motivated by their different physical energy deposition mechanisms of ionizing particle beams inside matter (figure 2.1). The increasing demands to provide such high-energy radiation beams at sufficient dose rates of at least the clinically used values of few Gy per minute with, sharp spatial dose confinements motivated and still motivate the development of modern particle accelerators for (not only) medical applications.

In order to understand the challenges addressed in the presented thesis, namely radiation protection at modern accelerators (chapter 4), online detector technology for beam diagnostic (chapter 5, chapter 6) and novel applications (chapter 7), an understanding of features of the used accelerator, the radiation field characteristics, the simulation tools and the employed detector technology is crucial.

3.2 Electron-, photon-, proton- and light ion-beam radiotherapy technology

3.2.1 Electron and photon therapy

Teletherapy using photon and electron beams is since decades an established tumour treatment modality and uses industrialized accelerator technology. The cost of single *turn-key* machine is approximately 2 Mio. € and fits in a compact bunker of $8\text{ m} \times 8\text{ m}$. The central functionality of the linac is the acceleration of an electron beam to the desired clinical energies of 6-21 MeV.

A linac consists of a klystron and a magnetron as power generators for the accelerating *radiofrequency* (RF) waveguide cavity structure. An *electron gun* is used to generate the electrons by thermo-electric emission from a cathode heated by a high-current filament. The electron gun is used to inject electrons ($\approx 20\text{ keV}$) into the $\approx 1\text{ m}$ long accelerating waveguide, which is evacuated to vacuum (figure 3.2a). There, the Klystron-fed electric field gradients of typically 6-21 MV cause the acceleration of the injected electrons up to 9-21 MeV. The resonance frequency of employed cavities is in the 3 GHz regime, causing the time structure of the electron bunches to be pulsed in the ps scale, separated by ms breaks. Already this ms bunch duration causes some electronic personal dosimeters as required by law for radiation protection in *controlled areas* to fail [110]. Usually, a 135° achromatic bending magnet is used to bend the beam towards the X-ray target where the first electron-matter interaction happens.

The X-ray target is sometimes aluminium or a high-Z material such as lead or tungsten. The deceleration of electrons in such materials causes $\approx 95\%$ of the kinetic energy of the beam to be converted into heat and $\approx 5\%$ into a forward peaked spectrum of bremsstrahlung photons. The process has a strong Z dependence (section 2.3). In order to obtain a spatially flat field, a photon beam *flattening filter* (FF) follows the X-ray target (figure 3.2b).

Some modern linacs are designed and operated to generate and apply therapeutic X-ray beams and can additionally be configured to produce therapeutic electron beams. An example is the Siemens ONCOR as used in chapter 6.

Removal of the X-ray generating metal target and replacement of the FF with an electron scattering foil allows for the transmission of the initial electron beam from the bending magnet to the patient (figure 3.2b). The $\approx 1\text{ mm}$ thick scattering foil made of aluminium or copper also broadens the initially narrow electron beam into a spatially broad radiation field of typically $40\text{ cm} \times 40\text{ cm}$ at the patient position (called *Isocenter*). For patient treatment, so called *electron applicators* can be mounted to the gantry and can be used to shape the broad radiation field to the desired tumour geometry.

The measurement of the dose deposition pattern in three dimensions inside a water phantom is an *indirect* measurement of the accelerator performance, but clinically only the spatial distribution of the dose to water is of interest. The quality assurance, i.e. whether the

3 FUNDAMENTALS OF RADIOTHERAPY-, LASER-ACCELERATION- AND DETECTOR TECHNOLOGIES

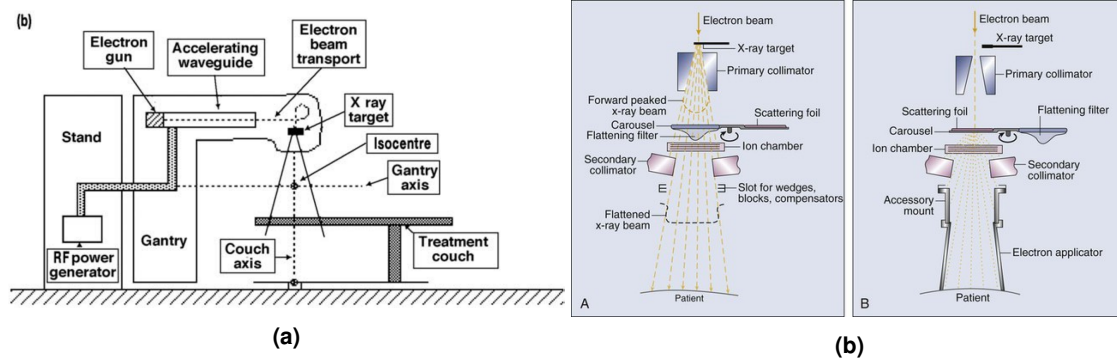


Figure 3.2: Conventional RF-based linear accelerator for electron and photon therapy. **(a)** Schematic depiction of the main linac components. **(b)** Accelerator head in photon and electron application mode needed for conventional photon and electron teletherapy [230, 254].

linac correctly delivers the lateral beam / treatment field shape and depth-dose deposition pattern as desired, is hence experimentally measured point-wise using an ionisation chamber on a motor controlled stage. Such measurements were simulated in chapter 6 as basis for *direct* measurements of the electron spectra using a magnetic spectrometer.

3.2.2 Proton therapy

The characteristics of the primary proton beam and the secondary radiation field are highly dependent on the proton delivery technique that is used. A conventional research tandem accelerator and two different ways in which protons can be delivered for treatment are compared in the following, as relevant to this work:

Maier Leibnitz Laboratory (MLL) The MLL was a 22 MV Tandem accelerator for ion acceleration in Garching near Munich and was operated from 1970 until 2018. With specialized settings, the beam characteristics could be tailored to mimic the 100% broad proton spectra, high flux ($10^{10} p/cm^2$ in 5 ns bunches) and down to 1.5 ns short bunch duration as encountered for laser-driven proton beams [250, 193, 194, 77]. This characteristics made it a viable test-bench for detector tests, especially the *RadEye* (section 5.1) and *CM49* sensor (section 5.2). Furthermore electron and proton scintillators were thoroughly characterized (chapter 6) and setups for proton radiography tested under laser-like conditions (chapter 7).

The MLL used a *Tandem-van de Graaff* accelerator. For the presented experiments, protons are negatively overcharged and extracted from a gas. A built-in chopper and buncher system using *radiofrequency* (RF) cavities are used to generate down to 1.5 ns short proton bunches, which are then pre-accelerated using 80-150 keV before being injected in the 25 m main acceleration pressure tank. The ion source can achieve high injection currents of up to $100 \mu A$ [77]. The tank is filled with insulating SF_6 gas. After being accelerated

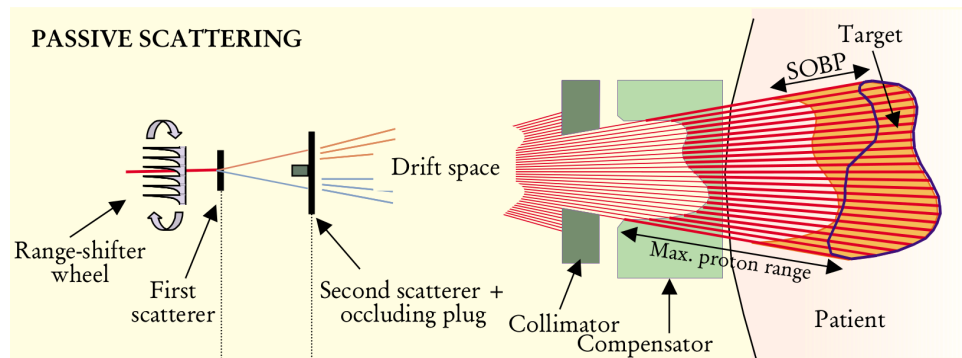


Figure 3.3: Scheme of passive proton therapy [82].

towards the accelerator terminal, which is held at the static potential +11 MV relative to the injection and exit site, a stripper foil removes the electrons. The 11 MV potential difference is then used a second time and the protons arrive at the tank exit at $E_{kin} = 22$ MeV. The accelerator allowed for acceleration of all types of ions and to change the terminal voltage for stable operation between 3 MV and 11 MV. Unfortunately, a change of the terminal voltage also requires readjustment of the beam-guiding magnets, which makes such energy-change a process of several hours.

A set of dipole and quadrupole magnets analyses, trims, guides, focuses and energy filters the bunches towards the experimental port. A narrow energy bandwidth of $\Delta E/E \approx 10^{-4}$ is reached at the experimental setups, which were placed inside of different vacuum chambers. These chambers were located ≈ 60 m downstream of the accelerator tank.

Several beam attenuators (two $1000\times$ and one $33\times$ attenuators) made of $50\ \mu\text{m}$ tungsten foils with a structured hole pattern can be inserted into the beam before it passes an energy-dispersive filter magnet. They allow a reduction of the beam current up to a factor of 3×10^{-8} .

Cesium-Iodine (CsI) scintillators can be inserted to intersect the beam ≈ 40 cm before the bunches enter the experimental vacuum chambers to check the beam position and shape. Remote controlled *Faraday cups* can be inserted to absorb the beam and provide a measurement of the beam current before entering the experiment. The bunch duration at the experimental position cannot be measured online, but with a dedicated setup, as it has been done in separate experimental campaigns using scintillator coupled *photomultiplier tubes* (PMT) and novel semiconductor time-of-flight detectors [250, 248].

Passive degraders were designed, simulated, 3D printed and experimentally verified in order to passively degrade the beam energies and use the range straggling in a engineered way to generate broadband, laser-like proton spectra from monoenergetic proton bunches (section 7) [249, 250, 248]. The *PolyJet* UV-lithography technique was used in order to achieve vacuum compatible, relatively radiation hard and tens of μm fine detailed absorbers.

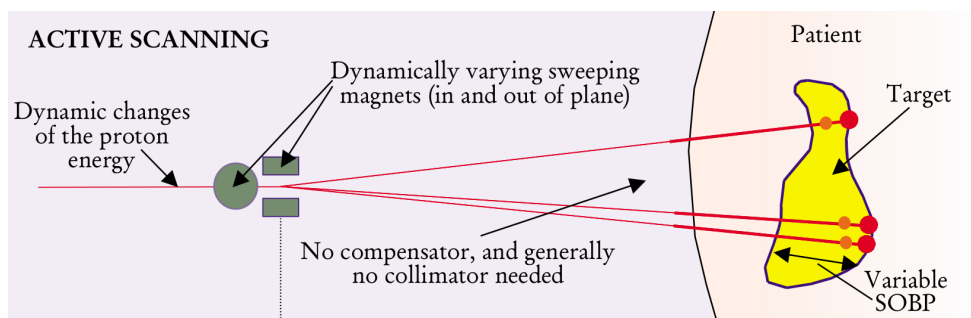


Figure 3.4: Scheme of active proton therapy using the pencil beam scanning technique. Narrow proton beams of a selected energy, corresponding to the desired penetration depth are magnetically deflected to spots of predefined dose to laterally cover the target [82].

Passive Proton therapy In clinical proton beam therapy, passive scattering technology does not use active elements such as quadrupole or dipole magnets to shape the beam for treatment, but places material directly into the proton beam path [125]. The initially monoenergetic proton pencil beam, e.g. a 250 MeV beam generated by a cyclotron, is broadened laterally and spread out longitudinally (i.e. passively generating a broad proton spectrum) in order to produce a homogeneous dose distribution throughout the solid angle covering the tumour (figure 3.3)

A different series of absorbers of variable thickness mounted on a rotating wheel is used for range modulation and generates a *Spread-Out Bragg Peak* (SOBP) (figure 3.1b). Laterally, the beam is typically broadened by two scatterers and tailored to the lateral target extension using a field-specific collimator. A field-specific range compensator is able to conform the SOBP dose distal fall-off to the the distal edge. The volume of healthy tissue proximal to the tumour gets unwanted high plateau dose (orange in figure 3.3). Since the proton fields can be directed from 360° using an isocentric gantry, being able to rotate around the patient, the out-of-field dose to critical radiosensitive structures may be reduced by combination of multiple fields from different beam angles.

The out-of-field dose to healthy tissue due to secondary neutrons originating in the patient and additional materials along the beam path and the poor dose conformation in the proximal part of the target are clear dosimetric disadvantages of the passive scattering technique [103, 157]. Until a few years ago, most experience in clinical trials for proton therapy had been gained using scattering facilities. The possible sparing of healthy tissue, motivated by the physical beam properties, has motivated the wider adoption of active beam scanning proton therapy and is rapidly replacing the passive facilities.

Active beam scanning proton therapy While for passively scattered proton beam therapy a treatment field is consisting of one single pencil beam, which is passively broadened in energy and space, the active beam scanning proton therapy uses multiple pencil beams to form the treatment field [82].

The energy of each individual beam is dynamically adjusted at the accelerator level (syn-

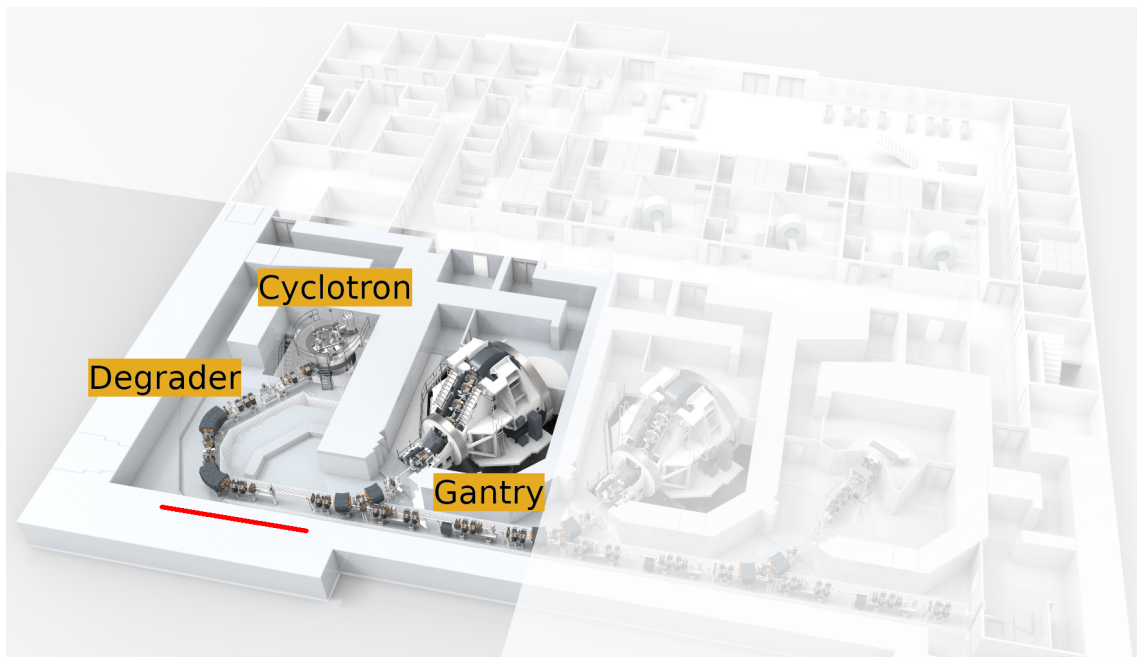


Figure 3.5: Layout of the RPTC proton therapy center. The red bar is depicting 10 m. Image adapted from the vendor [239].

chrotron) or immediately after extraction with a degrader (cyclotron). The different monoenergetic beams are deflected to predefined spots inside the target volume using dipole magnets (figure 3.4). Apart from the plateau before the Bragg peak (figure 3.1b), the dose maximum of the individual monoenergetic pencil beams is deposited in and restricted to a some mm small area (Bragg peak), resulting in a homogeneous dose coverage of the target when combined. By ramping the currents of two scanning electromagnets, the beams are magnetically deflected in the two lateral dimensions without the need for field specific scatterer, absorber and compensator hardware [141]. Compared to photon and scattered proton therapy, the out-of-field dose as well as the integral dose can be reduced, especially the former in the proximal target volume edge.

Quadrupole magnets are used to focus the beams to $\sigma \approx 2 - 3$ mm at the isocenter position in air. The beam application is continuously monitored by transmission ionisation chambers measuring the beam current to measure fluence and spot position and rough size. The chambers are mounted in the nozzle of the gantry, similar to passive proton therapy.

Different from passive proton or photon therapy, a single field is not delivered as a broad field but in a consecutive sequence of individual spots. The treatment field delivery is less robust with regard to the interplay effects of the tumour motion and the scanning sequence [197].

An example of a modern spot scanning proton therapy facility was the *Rinecker Proton Therapy Center* (RPTC), where secondary neutrons are studied in chapter 4.1.1.

RPTC Munich - A technology leading spot scanning facility The RPTC Munich was the first hospital based institution Europe-wide that used the spot scanning technique for patient treatment when it started operation in 2009. Exceptional, especially compared to photon therapy linacs, are the investment of 150 Mio. € and the weight and size of the accelerator (90 tons) and each gantry (150 tons) [88, 24].

A superconducting proton isochron cyclotron accelerates the protons from a hydrogen gas to the fixed kinetic extraction energy of 250 MeV. A set of carbon degrader wedges inside a specially shielded shelter is used to moderate the energies to the clinically used energy range of 75-245 MeV, from where the beam is transported to the patient treatment room (figure 3.5). The treatment room houses the 360° gantry and is shielded by concrete walls towards the outside, the cyclotron area and the other gantry rooms. The intensity of each irradiation spot can be modulated using variable proton currents of 1-500 nA [130]. The installed pencil beam spot scanning gantries for patient treatment are the first four prototypes of the Varian *ProBeam* nozzle system (Varian Medical Systems, Palo Alto, USA) [198]. Previously, the proton beam lateral shapes around the isocenter along with the R_{80} beam ranges in water had been modelled to a satisfactory dosimetric accuracy in the FLUKA Monte Carlo code by the author [53]. To this end, the explicit model of the ProBeam nozzle includes the vacuum window and the *Multi Strip Ionisation Chamber* (MSIC). The ability to calculate absolute doses in Gy has been implemented by a *Monitor Unit* (MU) calibration [249]. PMMA range shifters of 1-5 cm thickness can be included in the simulation model, as used to treat tumours in shallow depths inside the patients.

At RPTC, energy spectra of secondary neutrons from proton irradiation have been simulated using the nozzle model and previously measured in absolute dose using the created MU calibration (section 4.1) [55, 234].

The *CM49* detector, which has been characterized as position sensitive pixel detector in this work (section 5.2) was used for quantitative proton radiography at RPTC and is among the considered candidates for a proton radiography system in the *Small Animal Proton Irradiator For Research In Molecular Image-Guided Radiation-Oncology* (SIRMIO) project [169, 151, 152, 132].

3.2.3 Heavy ion therapy

Even ions heavier than protons are clinically used for external beam radiotherapy. The 1946 article of Wilson already mentioned the possibility to further increase the target conformity and biological effectiveness by using high-energy carbon ion beams, since heavier ions also form a Bragg peak as depth-dose distribution but with a narrower peak width and a fragmentation tail (figure 2.1). Therapeutic treatment was first realized later in 1975. First irradiations with He ions were performed in 1957, in 1975 followed C and Ne ions [36]. The beams show reduced beam broadening and allow for improved lateral target conformity, due to the heavier projectile mass (equation 2.9, figure 2.4). Additionally, their *relative-biological effectiveness* (RBE) is further increased compared to protons (section 2.5.1) [244]. Radiotherapy with ions has, in Germany, mostly been used to treat

patients with radioresistant tumours in the skull-base and brain and is internationally under exploration for many more tumour entities [46, 210, 39, 59].

A burden to the widespread of the technique is again the employed technological footprint. HIT uses a synchrotron of 10 m radius as proton and ion accelerator ($E_p = 48\text{-}221\text{ MeV/u}$, $E_{12C} = 88\text{-}430\text{ MeV/u}$) [122]. The treatment beam is microstructured into bunches (called *spills*) due to the synchrotron accelerator [59]. Spills are phases of a few seconds of beam extraction, separated by second pulses. The bunches are 20 – 100 ns long with a period duration of hundreds of ns. The HIT gantry weights 600 tons and exceeds the proton gantries in size by a factor of two [89, 90]. New accelerator and delivery concepts such as laser acceleration and the easily interchangeable targets may in future be subject to research in order to produce similar beams

3.2.4 Charged particle imaging for radiotherapy

Clinical proton imaging Due to the higher conformity of charged particle beams, the sensitivity to uncertainties in the dose delivery is higher than for X-ray treatments. An accurate knowledge of the ion beam range in tissue is crucial for maximal conformity and a reduction of the safety margins around the tumour. Limitations of the dose calculation models in analytical treatment planning algorithms, day-to-day patient positioning errors in the treatment room and anatomical changes during the course of the radiation treatments over several days with respect to the incorrect calibration of X-ray images used for treatment planning cause uncertainties of the in-vivo proton or ion beam range.

Patient positioning errors on the treatment table and anatomical changes are up to now minimized by co-planar 2D X-ray tubes and detectors, typically mounted to the Gantry and, more recently, integration of volumetric X-ray imaging via cone beam CT setups or CT on rails [135]. Directly acquiring these radiographies with proton beams may serve as a more dose efficient patient position verification compared to daily X-ray radiographies or tomographies [151].

Several methods to perform online proton beam range verification in tissue are under development: ionoacoustic imaging uses an acoustic transducer for direct detection of the localized energy deposition in the Bragg peak, which is followed by a thermal expansion. It profits from short proton bunches, as present in the μs range in synchro cyclotron accelerators for example used by the PROTEUS proton therapy system by IBA (Ion Beam Applications, Ottignies-Louvain-la-Neuve, Belgium) or the laser-based ion source LION (section 3.3.4, section 3.3.5), which generates ns short bunches. Additionally, ion-beam induced prompt gamma disexcitation from excited nuclei in the MeV range or the detection of 511 keV annihilation photons from the β^+ decay of irradiation induced positron emitters have been extensively tested in clinical environments [185, 167]. These techniques are not limited to pulsed beams.

Monte Carlo simulations using e.g. FLUKA (section 3.2.5), reflecting the actual physics processes happening in tissue, are one approach to reduce the treatment planning related

uncertainties. Simulations can provide accurate beam data for facility startup and TPS commissioning, as well as in the validation of treatment plans or even a Monte Carlo-based treatment planning system [170, 145, 17].

Another approach to reduce treatment planning related uncertainties experimentally is the direct measurement of the *stopping power ratio relative to water* (RSP). For clinical proton treatment planning, a stoichiometric calibration is used to convert the linear attenuation coefficients from the *single energy spectrum X-ray CT* (SECT) into RSP. This calibration contributes with 3.5% to the total delivery uncertainty of proton therapy of $4.6\% \pm 1.2$ mm [253, 164].

Prototype proton CT scanners for quantitative 3D mapping of the RSP are under development [15, 168]. These scanners measure the residual range or energy of a monoenergetic proton beam behind the patient. Such scanners could also enable imaging at a lower dose than X-rays, since the beam completely traverses the object and places only the plateau region of the Bragg peak in the patient [41, 15, 109]. The spatial resolution of proton radiography and tomography is mainly limited by MCS (section 2.2.2) inside the object [259]. The most advanced scanners rely on single-particle tracking at MHz (counting rates of 10^6 p/s) to detect the proton positions and directions before and after the patient, to make the most likely estimation of the individual proton paths within the patient for image reconstruction [151, 152, 41]. Single-particle tracking at MHz-rates is possible and further improvements in detector technologies and data acquisition are ongoing [29, 169].

Historical proton radiography The first proton radiographies with biomedical motivation were using a single proton energy and so called *contact-radiographies*. Steward and Koehler used a monoenergetic 160 MeV proton beam and assessed the fraction of transmitted ions behind biological samples by placing a photographic film in contact with the object backside (figure 3.6c) [124, 218, 217]. Such *proton-absorption-imaging* is very sensitive to thickness or density variations along the path (figure 3.6a). It shows a binary contrast like a shadow of an object, making clear why energy resolving detectors or multiple energy stacking is used today (chapter 7).

The object thickness had to be matched to the beam energy. In this historical contact-radiography method, Bragg peaks of non-exiting protons are placed inside the object at the cost of a high given dose [217]. Additionally the imaging contrast when using a single proton energy is only produced. For a small range of object thickness or density [218]. Due to MCS, the spatial resolution is reduced, especially as the highest contrast is caused by particles at the end of their range, just able to exit the imaged object [124, 56].

Proton imaging with a broad beam Experiments using a broad cone beam with multiple single proton energies, which are modulated and used to create a monotonically decreasing signal versus penetration depth in a planar 2D detector after the object have

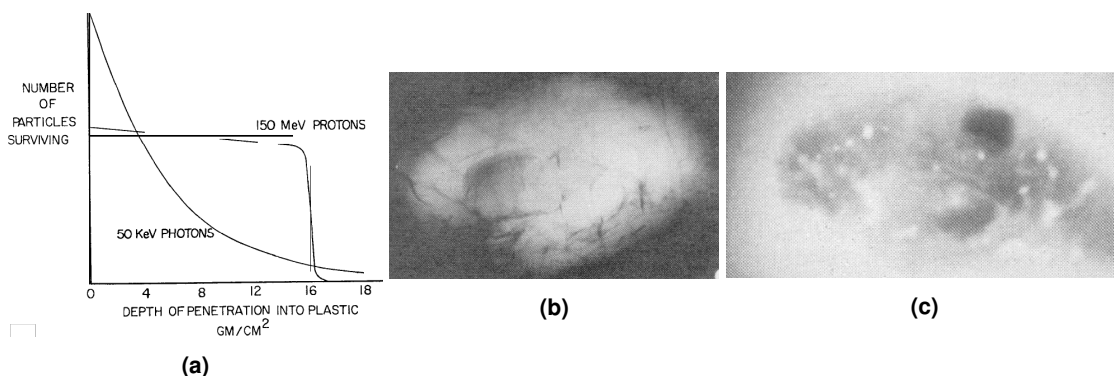


Figure 3.6: Contact-radiography with protons. **(a)** X-ray attenuation curve and proton stopping in depth from the Nobel lecture by A. Comack motivating the usage for protons for tomography [40]. **(b)** X-ray image of a human brain hemisphere [217]. **(c)** Corresponding proton radiography with clear tumour to tissue contrast [217].

been investigated [259, 189]. The experimental setup is measuring the 2D fluence after the object using scintillators instead of single-particle tracking and residual range or proton energy detectors. The concept could be entitled *beam-integrating* and is similar to the counting-experiment nature of X-ray absorption radiography.

In order to image a mouse-sized object at the SIRMIO project, several candidates of pixelated CMOS sensors such as the CM49, presented in section 5.2, are investigated as 2D detectors using the beam-integrating concept [208, 169]. First results show that the spatial resolution is acceptable when no tracking is used as long as the distance to the detector is kept as short as possible (few mm).

There are obvious disadvantages of the beam-integrating concepts: the dose to the imaged object is high [208, 205, 207, 206, 203, 204]. Additionally, the generated proton radiographies are of poor spatial resolution compared to X-rays since the concepts do not rely on individual particle tracking with residual energy measurement after the object but rather on the integral energy loss of a given number of particles.

Beam-integrating can be beneficial for higher particle rates than the 10^6 p/s (table 3.1) from therapeutic proton accelerators, especially at laser-based proton sources, for which single particle tracking with current technology is not possible. For such imaging concept, the name proposed in this thesis is *bunch-integrating* (chapter 7) [56, 248]. Such concept and measurements are discussed in chapter 7.

3.2.5 The *FLUktuierende KAskade* Monte Carlo code

The *FLUktuierende KAskade* (FLUKA) MC code was used throughout this work. FLUKA is a general purpose particle transport and interaction code, allowing the simulation of about 60 different projectile particles, their interactions and propagation in matter with energies between 1 keV up to PeV (10^3 eV – 10^{15} eV) for the case of photons and electrons and between several keV and 20 TeV for hadrons. Neutrons can be handled even

3 FUNDAMENTALS OF RADIOTHERAPY-, LASER-ACCELERATION- AND DETECTOR TECHNOLOGIES

down to 10^{-5} meV (= thermal neutrons) [67, 68, 72]. The code was originally developed by the *European Organization for Nuclear Research* (Conseil Européen pour la Recherche Nucleaire - CERN) for high energy physics. With help from *Istituto Nazionale di Fisica Nucleare* (INFN), FLUKA was further extended and since 1991 covers a wider range of kinetic energies to enable related general purpose applications. When employed in medical physics, FLUKA simulations are able to overcome shortcomings of the clinical standard of analytical dose calculation algorithms in the *treatment planning systems* (TPS), which typically fail to properly reproduce radiation transport in heterogeneous tissues and only approximate the patient as water of various thickness. Moreover Monte Carlo simulations allow the prediction of irradiation-induced radioactivity in the patient and treatment verification [171, 170]. The analytical dose calculation algorithms, which lack the explicit simulation of physical effects, benefit from orders of magnitude shorter calculation times than full-blown MC simulations. FLUKA finds also use in many other applications in high energy experimental physics and engineering, radiation shielding, detector and telescope design, cosmic ray studies, dosimetry and radiobiology [2, 128].

From a broader view, the Monte Carlo method is a numerical approach to approximate the solution of analytically unsolvable or only very difficult to solve problems. MC utilizes repeated random sampling from *Probability Density Functions* (PDF) describing the investigated problem to compute a result. After first unpublished studies using the MC method by Enrico Fermi in the 1930s, John von Neumann and Stanislaw Ulam in the 1940s addressed physical problems arising while working on nuclear weapon projects at the Los Alamos National Laboratory. The MC method has helped answering many questions not only in the field of physics but also mathematics, chemistry, economy, social science and engineering [150, 69, 149].

As the MC method is a numerical method, the results are only reliable for sufficiently high number of repeated samples. Following the *law of large numbers*, the simulation results converge for a sufficiently high sample number towards a steady state.

The role of Monte Carlo techniques as gold standard for radiation transport problems such as radiotherapy treatment planning and recalculation, especially for the case of particle therapy, originates from the fact that such general purpose Monte Carlo packages such as FLUKA or GEANT4 include a large number of modern theoretical physics models [34, 72, 5].

FLUKA models To describe the passage of hadrons through matter in FLUKA, the lateral scattering theory of Moliere is used for the simulation of multiple Coulomb scattering (section 2.2.2). For electronic energy-loss, the Bethe-Bloch theory is used in a formulation extended to the relativistic regime and combined with the Bloch-correction (Z^4) and Barka-correction (Z^3) (equation 2.6).

Besides the electromagnetic interactions, FLUKA uses experimental cross section data files (e.g. ENDF) as well as modern theoretical models to simulate hadron-hadron, hadron-nucleus and nucleus-nucleus interactions over the energy range of 0- 10^5 TeV.

Used theories are the *Pre-Equilibrium-Approach-to-Nuclear-Thermalization* (PEANUT) model for hadron-nucleus interactions, which features the simulation of *intranuclear cascades* (INC), pre-equilibrium, evaporation and disexcitation, the Fermi breakup model for light nuclei, the relativistic *Quantum Molecular Dynamics* (QMD) model and the *Dual Parton Model* (DPM) event generator DPMjet-III [2, 9, 182, 192, 67, 68]. By explicit simulation of all relevant quantum and nuclear physics interactions, as well as their explicit consequences such as the generation of secondary δ -electrons, positrons, excited nuclei and γ -ray disexcitations, FLUKA simulations can serve as a *mathematical experiment* and save experimental beamtime. Besides replicating real experiments, the simulations give access to experimentally not measurable quantities without disturbing an experiment.

FLUKA features The simulation is controlled by providing a plain text parameter file *input.inp*. The provided information has to include the primary beam particle, the initial energy spectrum, definition of single elements or compound materials making up the geometrical bodies along with their main properties (e.g. density and optionally ionisation potentials). Primary and secondary particles are tracked throughout the geometry following the chosen settings for the physical interaction models and above defined transport parameters and transport cut-offs. Information on simulation results is extracted by the definition of the physical quantities of interest and their scoring grid (e.g. differential fluence as a function of energy using *USRTRACK* or *USRBDX* scorers, spatially resolved fluence, energy deposition and interaction density using the *USRBIN* card).

By using the *DOSE-EQ* command, FLUKA not only calculates physical absorbed dose in a *USRBIN* scoring volume, but can convolve the particle fluence spectra with the particle-specific and energy-dependent conversion coefficients, by default from the AMB74-dataset, to calculate ambient dose equivalent $H^*(10)$ [173, 186].

FLUKA also allows for a deeper level of control by providing several programming interfaces to the transport and interaction processes via *user routines* [2]. During run-time, the user-written *FORTRAN77* are interpreted and allow for every transport step particle property dumping, as well as individual particle labelling and weighting as used in the neutron spectrometry studies of this work, presented in section 4.1.1.

3.3 High-power laser systems as particle sources

The interaction of highly intense *terawatt-* (TW) and *petawatt-class* (PW) laser pulses with matter can cause the emission of high-energy secondary particles such as protons, neutrons, light-ions, electrons [4, 87].

The development of techniques to rise the peak power of lasers, especially the invention of *chirped pulse amplification* (CPA), has enabled to overcome the limited laser peak power of the previously used mode-locked laser systems [220, 43]. CPA allowed to increase the peak powers in focus to laser intensities above 10^{15} W/cm².

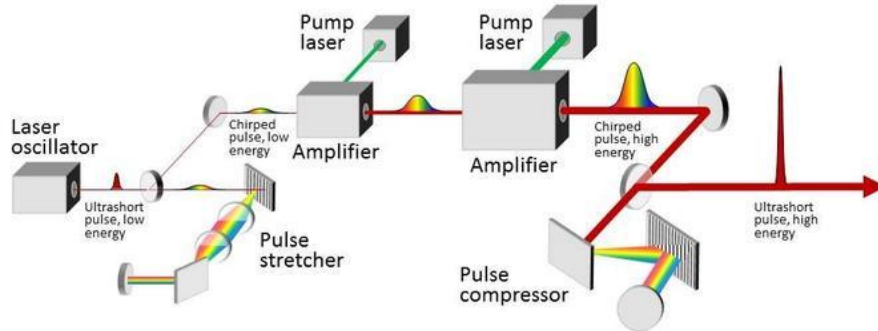


Figure 3.7: Schematic overview of chirped pulse amplification (CPA). The beam diameter is enlarged along the amplification stages, in order to operate the amplifiers below the damage threshold [236].

Laser-driven ion acceleration for example becomes feasible above 10^{18} W/cm^2 , but was inaccessible before the CPA invention, since the laser amplifier medium is damaged by excessive spatio-temporal fluences. As it is desirable to operate the amplifier medium close to the damage threshold in order to achieve a maximum pulse energy, the pulse repetition frequency of high-power laser systems is, depending on the cooling system and gain medium, restricted to a few shots per hour (table 3.2). Using *titanium:sapphire* (Ti:Sa) crystals, TW-class laser systems with 1 Hz shot frequency were realized [115]. This upgrade in repetition frequency, together with automated target positioning, raises interest for electronic online diagnostics (chapter 5).

One possible but limited and expensive strategy to reduce the spatial fluence is the beam expansion to larger beam diameters at the cost of demand for large amplifier crystals and mirrors. Several orders of magnitude in pulse energy can be gained by CPA: the different wavelengths contained in the broadband and *femtosecond* (fs) short laser pulse from the oscillator are delayed by path differences, which are caused by dispersive gratings. The initially short laser pulse is stretched in the time domain to hundreds of ps. Stretched, the pulse enters the gain medium and hence the peak fluence within the amplifier can remain below the amplified medium damage threshold (figure 3.7). After nonlinear gain of up to 10^8 , the stretched pulse is re-compressed using a dispersive grating compressor to obtain a pulse duration of typically $< 100 \text{ fs}$ (table 3.2).

Due to the high energy density and the pumping used to populate the excited states in seeded laser amplifiers, fs laser pulses are framed by a broad temporal *pedestal* before and after the main pulse (e.g. 2 ns in figure 3.9 bottom). This pedestal is the consequence of spontaneous disexcitations in the laser crystals, which are amplified along the beam-path with the main pulse and called *amplified spontaneous emission* (ASE).

The ratio of pedestal-height to the main pulse intensity is called *pulse contrast* and important for experiments generating particle bunches. The energy imparted by the photons from the pedestal may cause unwanted pre-heating or expansion of the experimental targets or change the optical properties of mirrors and gain media or even damage them.

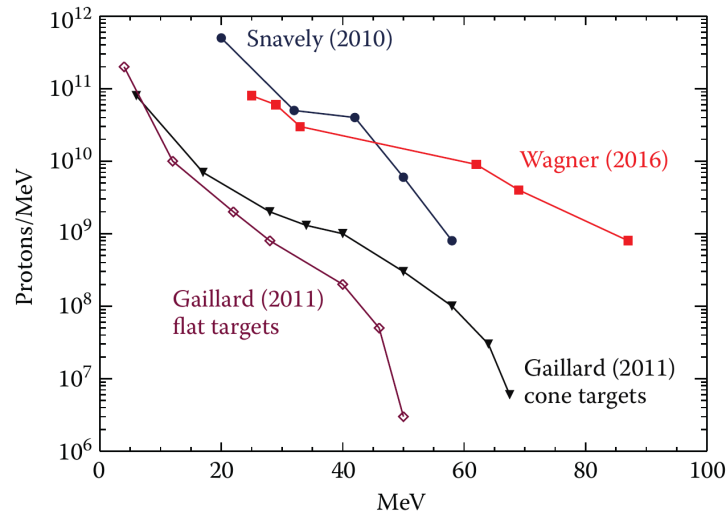


Figure 3.8: Reported world records of proton energies achieved in laser-driven ion source experiments (2016). The proton spectrum typically is broad and of high particle number. The recently obtained energies approach energies, which are of biomedical interest, since e.g. 75 MeV have a range of 4.6 cm in water [213, 195, 241, 116].

The target seen by the main pulse is a preformed plasma and can therefore be seen as a *dynamic* and *complex* target.

Another unwanted consequence of the amplification process are isolated pre-pulses, which can be present above the ASE level at ps or more before arrival of the main pulse (figure 7.1). Such pre-pulses are caused by imperfections of optical elements such as mirrors. Since the transitivity and reflectivity of the several hundred optical elements in the beam path is $< 100\%$, a fraction of the pulse could be multiply reflected inside the optical element and be delayed and be further susceptible to dispersion in the glass substrate.

Due to the different mechanisms and experiments used for ion and electron acceleration, a brief introduction is given separately in the following sections.

3.3.1 Lasers as ion sources

By focusing fs-short laser pulses from contemporary laser systems of tens of Joules pulse energy down to a few micrometers on the front side upstream of a solid target in vacuum, controlled conversion of the laser energy to kinetic ion energy and their emission from the downstream side is possible. The localized energy density of a short pulse generates a high power density at the front side of the target, which can cause laser field ionisation of the atoms in the surface layer of the target foil above 10^{13} W/cm^2 . In a simplistic picture, the laser field initiates heating and motion of the formerly bound electrons, which propagate as a plasma in the target. Due to the favourable charge-to-mass ratio of nuclei, e.g. $m_p/m_e \approx 2000$, the remaining ions can be approximated as at rest, while the plasma dynamic gives induces charge separation fields responsible for the ion accelera-

tion. The acceleration of ions for currently achievable laser intensities below 10^{24} W/cm² is therefore an indirect process, i.e. mediated by a plasma field associated with charge separation, and not the laser field itself [87].

The target material, target geometry, the electron density in the target, the pulse shape, the laser wavelength and spatio-temporal laser intensity influence the different nonlinear ionisation processes, the laser absorption, the plasma formation and plasma dynamics [4, 87]. An energy conversion efficiency from the laser pulse to the ion kinetic energy of 10% is estimated for a petawatt driving laser [213]. The parameters influencing the dynamics and their optimisation are subject to hydrodynamic *Particle-in-Cell* (PIC) simulations, which are used for an analytical understanding and for laser and source term optimisation, dependent on the application [115]. Experimentally, measurements of the electrons driving the acceleration can give insight into the ion acceleration performance. Based on this knowledge, a combined online diagnostic of the electron bunch, together with the resulting proton bunch was developed and tested in this work (chapter 6) [138, 139].

Experimentally, thin metallic, plastic or *Diamond Like Carbon* (DLC) foils of several μm (*Target Normal Sheath Acceleration TNSA*) or nm (*Radiation Pressure Acceleration RPA*) thickness are typically used as targets (chapter 7), although target thickness does not necessarily suggest the mechanism [144, 211]. Modern experiments also study the spatial confinement of the plasma dynamics to plastic and metal spheres or needles (section 7.2.1) [104, 160]. Tungsten needles were used in this work in the experiments at the Texas Petawatt Laser (section 7.2.2).

Regardless of the target material, which is hit by the laser pulse, the most abundant ion species in the accelerated ion bunches are protons. These protons originate from water and hydrocarbons surface contamination layers on the target foils [100]. If laser-acceleration of heavier ions is of main interest, the proton acceleration can be suppressed by dedicated heating of the target foil (e.g. a gold foil) as done in the *High-Field* (HF) experiment by a heating laser for acceleration of gold ions in CALA (section 3.3.5) [61].

In the case of high pre-pulse intensities, plasma expansion and even ion acceleration can already occur before the arrival of the main pulse and the high peak intensity itself is not exploited. Such conditions were the case for experiments described in section 7.2.1. Fast *Pockels cells* acting as optical switches and plasma mirrors can be used to partially clean the short laser pulses by pre-pulse removal. Double plasma mirrors are two single-use glass mirrors, which are damaged due to the pre-pulses, but the pre-pulses ignite a reflective plasma at the glass surface and reflect the main pulse, and can thereby improve the contrast by two orders of magnitude [99]. Novel and cheap inline plasma mirrors are plastic foils individually mounted close to each target and are able to improve the contrast by three orders of magnitude [215].

A variety of ion acceleration mechanisms from solid targets have been reported, depending on laser pulse and also target parameters [87, 4]. Here, the explanations are restricted to the two acceleration regimes accessible with the laser systems used for the presented

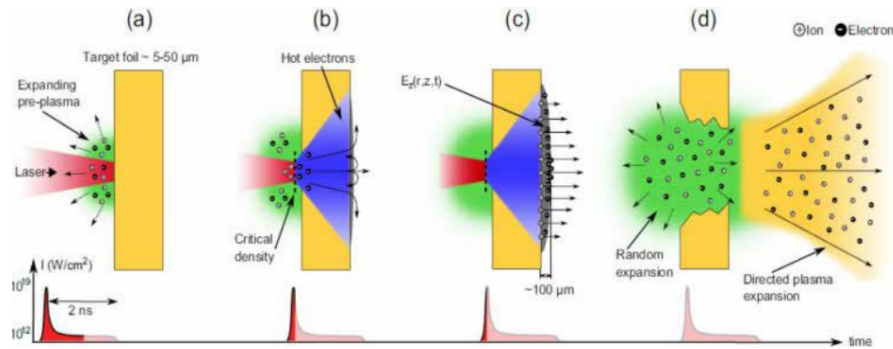


Figure 3.9: Scheme for TNSA based acceleration of particle bunches [121].

work, namely *target normal sheath acceleration* (TNSA) and *radiation pressure acceleration* (RPA):

TNSA The microscopic acceleration dynamic for TNSA can be described as a multi-stage process.

The low intensity pedestal of a laser pulse (red graph in figure 3.9 a) strikes the front side of nm to μm thin plastic or metal target (yellow) and causes ionisation. When reaching the critical plasma density at the front side, the laser main pulse is absorbed in the plasma which drives hot electrons (blue) through the target to the rear side (figure 3.9 b). The motion of the dispersing electron forms an acceleration sheath at the rear side, which locally causes a high field gradient normal to the target backside (figure 3.9 c), leading to the emission of a broadband particle bunches containing e.g. protons, ions, electrons, X-rays, muons and neutrons (figure 3.9 d). The bunches are ejected as a spray from the target back side, as well as with larger angular spread and lower energies from the front side.

Due to the short acceleration distance and the high energy density imparted by the short pulse, which causes an rapid electron displacement, the accelerating field gradients reach TV/m ($= MV/\mu m$), which is four to five orders of magnitude above the conventionally $\approx 10 - 100 MV/m$ used field gradients for linear accelerators. Due to the rapid and dynamic electron displacement, part of the target is left positively charged.

The TNSA mechanism is the central explanation for the laser-ion acceleration experiments in laser facilities exceeding $10^{20} W/cm^2$, although already at $10^{18} W/cm^2$ TNSA is relevant [245]. First experimental results for proton spectra typical for TNSA were measured by Snavely et al. in 2000 [213]. The kinetic proton energies accessible by TNSA in TW and PW class laser facilities are recently high enough for biomedical experiments an can penetrate cell samples, small animals and superficial tumours (figure 3.8).

In the TNSA acceleration regime, the resulting ion kinetic energy spectrum scales with the laser pulse energy and requires an efficient energy transfer from the laser pulse to the solid target. Up to 50% of the laser pulse energy can be transferred to the electrons

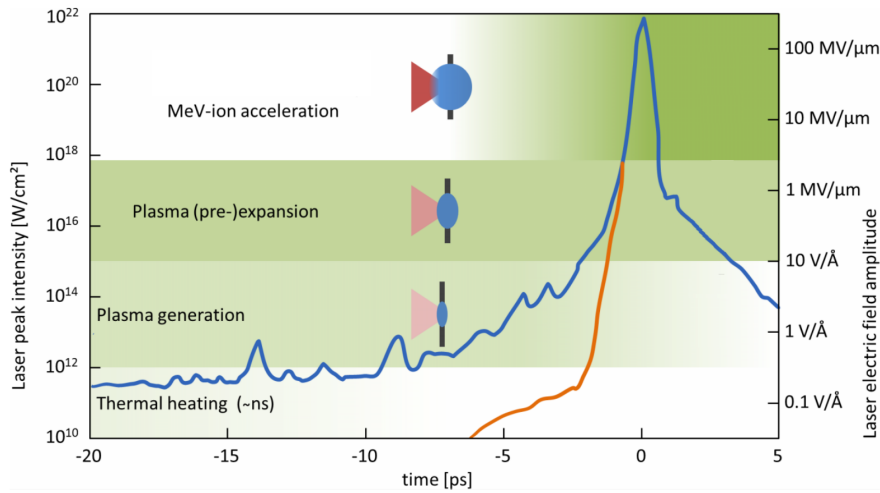


Figure 3.10: Temporal profile of laser peak intensity and electric field amplitude in logarithmic representation. The target (black) is ionized and the plasma (blue ellipse) starts expanding long before the laser intensity (blue curve) exceeds 10^{18} W/cm^2 . For RPA, a high laser contrast (orange curve) is desirable in order to minimize this pre-expansion [115].

[97]. The ion bunch, which is emitted from the target backside has a broad energy spread and a cone shape with a typically large divergence angle of a few tens of degrees [116]. Figure 3.8 shows typical spectra of exponentially tapering slope with a high energy cut-off ϵ_{co} , where proton numbers at the high energies are typically three orders of magnitude lower than for the lowest energies.

RPA The incoming laser pulse does exert a physical pressure to the target backside, which can be visualized using the picture of the quantum mechanical wave–particle duality. The RPA mechanism relies on the energy transfer from the laser field to the particles via radiation pressure due to favorable plasma dynamics [4].

The RPA mechanism could be a more efficient way to transfer energy from the laser field to the kinetic energy of the emitted particles [4]. Simulations predict RPA to be dominant over the TNSA mechanism for laser intensities above 10^{23} W/cm^2 , a regime however inaccessible for current laser systems. The dominance of RPA over TNSA is there possible since the first half cycle of the incoming laser pulse already is sufficient for protons to gain relativistic energies by compressing and pushing the target electrons into a piston-like plasma slab, building up a confined and ultra-high charge separation field [58]. Recent studies show that circular polarized laser pulses can enable the RPA mechanism at contemporary laser intensities $> 10^{20} \text{ W/cm}^2$, because circular polarisation suppresses electron heating which is key to the TNSA mechanism [80, 188, 101].

Efficient RPA requires nm thin targets, which thereby requires an excellent laser contrast, in order to avoid damage to the target by pre-pulses before arrival of the main pulse [58]. The laser contrast should not exceed 10^{12} W/cm^2 at 2 ps before the main pulse of 10^{22} W/cm^2 [115]. For such targets, nearly all pulse energy may theoretically be trans-

	Medical cyclotron facility [53, 88, 130]	300 TW Laser proton source [79, 87, 4]	3 PW Laser proton source [87, 4]
Example facility	RPTC Munich	LION@LEX	LION@CALA
Proton bandwidth $\Delta E/E$	$\approx 0.4\%$	$\approx 100\%$	$\approx 100\%$
Proton spectrum	Monoenergetic	Exponential slope	Exponential slope
Energy spectrum fluctuation	stable	shot-to-shot	shot-to-shot
Proton bunch length [s]	cw / 10^{-3}	10^{-9}	10^{-9}
Proton fluence [10^9 protons/s]	1 – 10	10^9 - 10^{10}	10^9 - 10^{10}
Max. proton energies [MeV]	< 250	$\epsilon_{co} < 20$	$\epsilon_{co} < 100$
Proton range in water [cm]	37.9 cm	0.4 cm	7.7 cm

Table 3.1: Beam characteristics for a conventional accelerator and two laser-based proton sources. Originating from the basic physics of the acceleration mechanisms, the beam characteristics from laser and cyclotron accelerators strongly differ, mandating redesign of used measurement methods, detectors and applications.

ferred to the kinetic ion energy directly [87]. Monoenergetic ion spectra ($\Delta E/E < 100\%$ for the field of laser-ion acceleration) may be realized using RPA, which would allow to have reasonable particle numbers at high energies for specific applications such as *laser-based ion beam radiation therapy* (LIBRT).

For a pulse of 60J energy, RPA could theoretically allow to accelerate 10^{12} protons to $\epsilon_{co} = 235$ MeV with one laser pulse (table 3.1) [184].

3.3.2 Distinctive features of laser-generated ion bunches

Due to the plasma dynamics, the properties of laser-accelerated ion bunches differ substantially from those of conventionally accelerated ions from conventional electrostatic accelerators or radiofrequency-driven cyclotrons and synchrotrons (table 3.1). Several differences and distinct features are listed here, since they drive new applications or the redesign of conventional applications of radiation beams, but also demand for adaption of the detector systems:

- In contrast to usually single species electron, proton- or carbon ion beams from therapy and research accelerators, the radiation field emerging from laser acceleration experiments is **mixed** and consists of photons, electrons, protons, neutrons, ions and muons in parallel [87].
- The **energy spread** of accelerated ions is usually broad and of exponentially tapered slope in a single shot (chapter 7). Conventional monoenergetic RF-accelerators such as RPTC or MLL (section 3.2) may need several seconds (RPTC) or hours (MLL) to deliver two beam energies consecutively.

- **Shot-to-shot fluctuations** in the energy spectrum can make it necessary to monitor the spectrum of ions, for example by only using part of the beam for the application (chapter 7). As surrogate diagnostic, the driver-electrons may be analysed in order to make predictions on the corresponding ion spectrum (chapter 6). From 85 consecutive and automated laser shots on 85 identical targets for LION@LEX Photonics, the proton energy spectra indicated strong fluctuations in the maximum energy and particle number. The maximum cut-off energy ϵ_{co} of up to 10 MeV fluctuated by 27%, while the particle number at 4 MeV fluctuated by 86% [79].
- The radiation field emerging from the laser-plasma interaction is pulsed. Particle bunches with **bunch duration of several nanoseconds** are present at the position of the ion-experiments some meters downstream the target due to the bunch dispersion, caused by the energy dependent particle velocity [250]. LIBRT could possibly, like for FLASH, benefit radiobiologically from the short bunch duration (section 2.5.4) [235].
- A laser-driven proton bunch is of extraordinary **high flux** of up to 10^7 protons / cm^2 per bunch. Together, with the ns bunch duration, the flux poses high demands in terms of spatial resolution, dynamic range and radiation hardness on spatially resolving detectors [87].
- The **high bunch charges** can be as high as ≈ 1 nC (table 4.5), which allows for a average beam current of several nA, since e.g. the LION experiment can deliver bunches in a 1 Hz repetition.
- An intense **electromagnetic pulse** (EMP) is caused by the interaction of the laser pulse with the target. The EMP is prompt, broadband and consisting of a broad frequency band in the GHz to THz regime. It interferes with electronic equipment such as detectors the vicinity of the experiment and can easily cause failure. The high intensity makes shielding using Faraday cages difficult [92].
- A potential benefit of the laser accelerator principle is how easily **different types of radiation beams** can be produced. By changing the target foil or target and converter material (for neutron generation), different ion species can be accelerated. In this way, different ion species can be combined in one experimental campaign. The laser itself serves just as an energy source. Conventional accelerators are on the other side very specialized in their infrastructure and usually optimized in their beam guidance [116].
- Beam splitters may be used to separate a fraction of the driving laser pulse before hitting the target. That way, a second laser pulse is generated, which is **synchronized to the accelerated ion bunch at a fs level**, which is several orders of magnitude more precise than using electronic signal synchronisation. In this way, experience from optical *pump-probe* methods can be used to probe the ion beam or the interaction of the ion beam with matter.

- The bunches originate from a laser focus of a few μm diameter. A tiny source size enables imaging applications with high spatial resolution and magnification (point projection) [160]. The **low source size and high beam divergence** (up to several tens of degrees) are also a key point in the chain towards applications, since the divergence either demands for refocusing to exploit the high particle numbers or enables illumination of a larger sample area (section 7). Permanent magnetic quadrupole lenses can be employed for this beam preparation [219]. These lenses also enable the spectral modification of the broad, exponentially decaying proton spectrum.
- The interaction of laser pulse and target is performed in **vacuum**, since the laser pulse power density is several orders of magnitude above the ionisation threshold of air, which would hinder the generation of ultrashort pulses of high power density. Also can the presence of air be a problem for the generated particle sources by stopping and scattering the bunches.

However, laser-accelerated ion beams are still not mature enough for several applications in which additional features are essential, such as low divergence, a monoenergetic beam with sufficient beam energy to penetrate a human body, a spatially uniform profile or shot-to-shot stability. Ideally, applications should make use of the features which are distinct from laser-ion sources, rather than trying to imitate beams which can be produced more easily using conventional accelerators, as studied in the last decade for radiotherapy [235].

3.3.3 Lasers as electron accelerators

High power laser systems can be used as designated sources of mono or polyenergetic electron bunches of high bunch charge (table 4.5). Due to the high charge to mass ratio, electron beams easily reach GeV level kinetic energies when accelerated in laser-induced plasma wakefields [3, 83]. Due to the high field gradients, the conventionally several meters long RF-accelerator cavity is replaced by a several cm long plasma cavity. By guiding the electron bunches through large magnetic undulators, the kinetic energy of the electrons can be converted into collimated, coherent, and femtosecond short pulses of X-ray radiation [50, 3, 240]. Using the Thomson scattering mechanism, the bunches can be overlain by a fraction of the initial laser pulse and use the laser field instead of the magnetic field to generate X-rays (section 3.3.5) [120]. The electrons may even be used for neutron generation using dedicated converter materials [118].

Laser-originated electron bunches have successfully been employed in X-ray and γ -ray secondary sources generation for a variety of basic research, ultrafast radiation biology and imaging experiments [87, 4, 243, 242].

Laser-accelerated electrons are in the framework of this thesis of interest from a radiation protection point of view (chapter 4.2). Although the acceleration physics, plasma

dynamics and interaction technology is of high interest, the most relevant point for the presented thesis is the fact that the electron beams have ranges of several meters in concrete and slow down using secondary showers of electrons and bremsstrahlung photons.

3.3.4 The experimental facility LEX Photonics

The *Laboratory for Extreme Photonics* (LEX Photonics) in its form described here was located at the Ludwig-Maximilians-Universität München as a laser-based ion and electron acceleration facility.

The first stage experiments to accelerate ions (Prof. Schreiber Group) and electrons (Prof. Karsch Group) were performed here. In the following, the driving laser and the ion acceleration experiment is described, since detector tests (chapter 5) and proton radiography experiments (chapter 7) were performed there.

ATLAS-300 laser system The *Advanced Titanium-Sapphire Laser* (ATLAS-300) system employing Ti:Sa crystals for pulse generation and the CPA technique for pulse amplification [43]. The system was designed to generate individual infrared pulses (central wavelength $\lambda = 800$ nm) containing 7.5 J of energy. The pulses of ≈ 25 fs pulse duration, hence theoretically generating a peak power of up to 300 TW were used for electron and ion acceleration experiments (table 3.2). Theoretical pulse repetition frequency was 80 MHz from the oscillator, but practically 1 Hz was used, although the final amplifier in the amplifier chain could theoretically be used at 5 Hz.

Laser-driven Ion Acceleration (LION) experiment at LEX The LION@LEX experiment used pulses from ATLAS-300, which were guided through a double floor into vacuum chambers¹. Since the aim was generation of ionizing radiation, the chambers were placed in a temporary bunker shielding the outside from the generated radiation bunches.

In the bunker, the pulses were focused onto the targets using a 90° off-axis parabolic mirror. The achieved laser focus of $2.7\mu\text{m}$ resulted in an intensity of 3.3×10^{20} W/cm² on target [79, 92]. Below laser intensities of 10^{22} W/cm², the *target normal sheath acceleration mechanism* (TNSA) is dominating the laser-plasma interaction and was hence probed in LEX [245, 87].

Target foils such as several thin (≈ 10 nm- $5\mu\text{m}$) plastic foils and gold foils, mounted on 18 target holders with theoretically 99 target foils each, were positioned in the focal plane by an automated positioning system [215, 79]. This 0.5 Hz system enabled, together with the RadEye-based spectrometer system (section 5.1, section 6.1), more than 8000 shots for ion acceleration in 1.5 years, especially ≈ 1000 in a row within a few hours [61, 95, 92]. Such high shot numbers are outperforming other laser-proton acceleration

¹Chambers were reused in CALA and are described in chapter 4.2

experiments by several orders of magnitude. For example, the Texas Petawatt Laser used for radiography experiments allowed only for 5-10 shots per day (section 7.2.2).

A adjustable doublet of permanent magnetic quadrupoles (PMQs) was used optionally to focus the laser-accelerated proton bunches to a target-focus-distance of interest in the range of 0.4-1.5 m. Since both, the focal position and the kinetic energy of the focused ion beam depend on the position of the PMQs, this doublet was used to generate focused quasi-monoenergetic bunches for design energies ranging from 6-10 MeV [190].

Based on experience at a lower power laser system at the *Max-Planck Institute of Quantum Optics* (MPQ) in Garching, the goal of LION@LEX was to accelerate protons up to 20 MeV and to explore various applications. Successful applications of this to which the author contributed include:

1. Development of integrated double-plasma-mirror targets for laser contrast enhancement to enable acceleration experiments [215]
2. Detectors for *Time-Of-Flight* (TOF) spectrometry from laser-proton bunches [250]
3. Zebrafish irradiation and observation of developmental malformations using focused bunches with permanent magnetic quadrupole lenses [219, 191]
4. Development of a reliable *wide-angle spectrometer* (WASP) for detection of laser-driven electrons and protons (chapter 5, section 6.1, [61])
5. Development of a radiatively resistant scintillator detector for protons (chapter 5.1.4)
6. Monte-Carlo-based reconstruction of secondary electrons from the laser-target interaction (section 6)
7. Laser-driven proton radiography of thin samples (chapter 7)

Other performed experimental demonstrations are:

1. Development of diagnostics to probe the plasma dynamics on target (*Time Resolved Intensity Contouring* TRIC) [44]
2. Detection system for protons using acoustic waves in water (*Ion-beam energy acoustic tracing* I-BEAT) [93]

After the period of 1.5 years of operation, the system was disassembled and has been relocated and upgraded to 3 PW peak power as ATLAS-3000 (section 3.3.5).

3 FUNDAMENTALS OF RADIO THERAPY-, LASER-ACCELERATION- AND DETECTOR TECHNOLOGIES

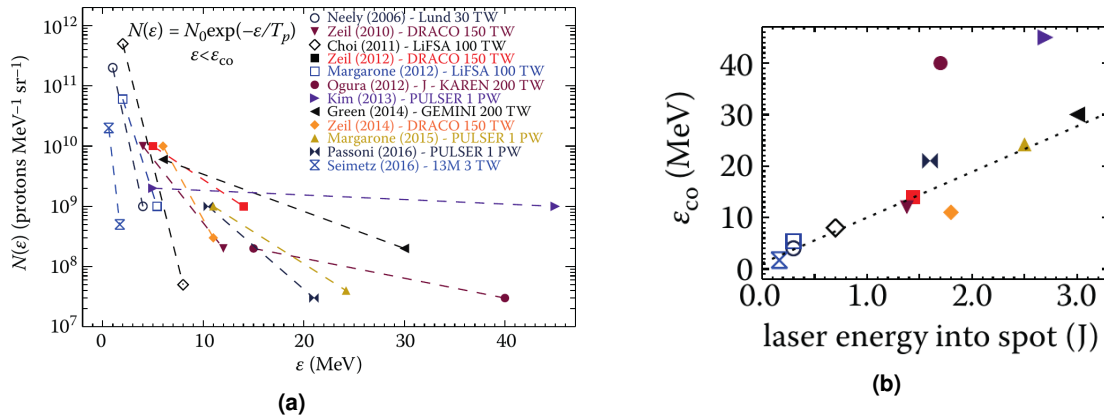


Figure 3.11: (a) Proton energy spectra spectra from sub-10 J, 25-40 fs laser systems using $0.05 - 4.0 \mu\text{m}$ solid targets, shown as simple exponential interpolations (dashed lines) of the high-energy tail using $N_p(\epsilon) = N_0 \times \exp(-\epsilon/T_p)$ (with ϵ_{co} , the cut-off energy). (b) ϵ_{co} as function of pulse energy in the focus [116].

3.3.5 The experimental facility CALA

The *Centre for Advanced Laser Applications* (CALA) is a new research institute for laser-based acceleration of electron beams for brilliant X-ray generation, as well as laser-driven sub-nanosecond bunches of protons and heavy ions for biomedical applications such as imaging, tumour therapy and nuclear physics [190, 139].

The radiation bunches emerging from experiments using the up to 2.5 PW laser pulses with 20 fs duration will be mixed particle-species of high flux, high energy and bunched. Recent results of the laser performance suggest 2.5 PW of laser power in 25 fs pulse duration and possibly a intensity of $1.2 \times 10^{20} \text{ W/cm}^2$. Envisioned proton bunch energies ($< 100 \text{ MeV}$) will enable cell or small animal (generalized as pre-clinical) experiments and come within range of conventional proton acceleration facilities. Also new challenges compared to conventional radiation protection are emerging, since such high-repetition rate generation of deeply penetrating beams using lasers is not yet common and the facility hence had to be carefully designed and examined from a radiation protection perspective (chapter 4).

The five main experimental areas and their components and infrastructure are described in more detail in section 4.2. The experimental motivation is described in the following.

ATLAS-3000 laser system The ATLAS-3000 is the petawatt upgrade of the ATLAS-300 system after relocation from LEX to CALA and one of the two laser systems driving experiments there. Table 3.2 lists the expected performance upgrades. The pulse energy is expected to rise from 7.5 J to 60 J and hence enable intensities exceeding 10^{22} W/cm^2 [139]. The optical power increase from 300 TW to 2.5 PW is realized by additional amplifiers and will, due to scaling of proton kinetic energies with the laser pulse energy,

	ATLAS-300	ATLAS-3000	PFS-pro	TPW
Facility	LEX	CALA	CALA	TPW
System	Ti:Sa	Ti:Sa	Yb:YAG	Nd:Glass
Power [10^{12} W]	300	3000	10	333
λ [nm]	750-850	750-850	700-1400	1058
Pulse Energy [J]	7.5	60	0.1	100
Pulse length [fs]	25	20	30	150
Shot frequency f [Hz]	1	1	1000	$1/(90 \times 60)$
Focal radius σ [μm]	25	25	tbd	2.5
Power density [W/cm^2]	1.5×10^{19}	1.5×10^{20}	tba	1.7×10^{21}

Table 3.2: Design parameters of the laser systems installed in CALA. The ATLAS-3000 and PFS-pro laser systems generate the pulses needed to accelerate particles to the described bunch energies (table 4.5). Measured ATLAS-300 and TPW parameters are shown for comparison along with the experimentally achieved focii and power densities [160].

allow to further increase the accessible proton energies and may allow the exploration of acceleration mechanisms beyond TNSA (figure 3.11).

The 2.5 PW peak power made it (in 2020) the strongest laser system operated by a university in Europe. ATLAS is used to seed experiments in the caves LION, HF, ETTF, LUX and SPECTRE. Even more powerful will be the lasers systems of the *European Light Infrastructure* (ELI), which aims to generate 1-50 GeV electron bunches and 100-3700 MeV proton bunches using 10-50 PW [70].

Petawatt Field Synthesizer light source (PFS-pro) The PFS-pro experiment is the second laser system under development at CALA with distinct broadband laser characteristics (table 3.2). Once completed, PFS-pro will seed the SPECTRE experiment. []

Using a repetition frequency of up to 1 kHz, the SPECTRE experiment will use the high-energy photons (50-200 keV) to generate X-rays by acceleration of electrons up to 70 MeV (table 4.5). The X-rays will be used for medical imaging, among other applications.

LION@CALA The LION@CALA experiment is the upgrade of LION@LEX for higher laser peak power, resulting in higher expected proton energies. Possibly exceeding laser intensities of $10^{22} \text{ W}/\text{cm}^2$, LION@CALA will be able to probe the radiation pressure acceleration mechanism (RPA), which promises different plasma dynamics and consequently reduced energy bandwidth, higher kinetic energies and a more efficient conversion of laser pulse energy to ion bunch kinetic energies [87].

The expected up to 100 MeV proton bunch energies increase the proton range in water, compared to LEX, by at least one order of magnitude² (table 3.1). The generation of

²27.7 cm for 100 MeV protons

to answer questions in astrophysical nucleosynthesis of heavy elements such as gold and uranium by experimentally realizing the fission-fusion reaction mechanism, which remains yet inaccessible using conventional particle accelerators [91].

Electron Thomson Test Facility (ETTF) The ETTF experiment is a basic research experiment to generate brilliant hard X-rays through Thomson-backscattering and betatron radiation from ATLAS-3000 pulses. Up to 5 GeV laser-accelerated electrons and their characteristics such as charge, space charge, timing and acceleration mechanism are probed experimentally, in order to provide X-rays best suited for biomedical experiments such as phase contrast imaging or ultrafast phenomena in solids and matter in the plasma state [243, 242]. The layout of the ETTF cave is visible in the FLUKA model in figure 4.20.

Laser-undulator X-ray source (LUX) The LUX experiment is set up to generate brilliant photon synchrotron radiation using a magnetic undulator seeded by up to 5 GeV laser-accelerated electrons. In full operation, it may serve as a prototype laser-plasma-accelerator based free-electron laser (FEL) for biomedical X-ray imaging experiments. Highly brilliant X-ray beams are desirable for phase contrast imaging of biological specimen and have been demonstrated in LEX [243].

A distinct feature of such laser-based X-ray-beams is the possibility of *fs* synchronized pump-probe experiments enabling highest time resolutions. The primary ATLAS pulse is divided optically into an excitation or pump pulse along with a synchronous probe pulse, probing the sample at different time delays using the brilliant X-rays generated using the probe pulse. The layout of the LUX cave is visible in the FLUKA model in figure 4.20.

Source for Powerful Energetic Compact Thomson Radiation Experiments (SPECTRE) The SPECTRE experiment uses both ATLAS and PFS-pro as the driving laser. Using ATLAS, SPECTRE aims to accelerate electron bunches of 0.25 – 0.5 nC up to 500 MeV for X-ray generation. At the PFS-pro repetition rate of up to 1 kHz, a tuneable source of X-rays for biomedical experiments using up to 70 MeV electron beam will be established. The layout of the SPECTRE cave is visible in the FLUKA model in figure 4.23.

3.3.6 The experimental facility TPW

The *Texas Petawatt laser* (TPW) at the University of Texas at Austin is a laser system using flash lamp pumped Nd:glass amplifiers. The amplifiers need cool down to avoid thermal damage for ≈ 1.5 h, allowing therefore only five shots per day. The low shot frequency gives the results of the experiments using the generated proton bunch a single-shot characteristic without the ability to collect multi-shot statistics, resulting in the experiments totally differing from the experiments using LION@LEX and LION@CALA.

The laser photons have a wavelength of $\lambda = 1058\text{ nm}$ and are compressed to 140 fs (FWHM) long pulse, carrying $\approx 100\text{ J}$ in a single pulse [160]. A contrast ratio of 10^{-10} up to 100 ps before the main pulse is achieved by a plasma mirror. The increased pulse duration compared to Ti:Sa lasers gives rise to different particle spectra due to the plasma expansion.

At TPW, imaging experiments using higher-energy protons than from LEX or CALA have been performed and are outlined in section 7.2.2.

3.4 Particle detector technology at laser facilities

The ongoing evolution from laser-ion acceleration experiments as complicated basic-research experiments towards stable *Integrated Laser-driven Ion Accelerator Systems* (ILDIAS) as reliable, stable and application friendly accelerator systems calls for reliable diagnostics of the laser-target interaction and the emitted particles [116]. The following section will focus on the detection of the emitted particles as indirect measure for the accelerator performance, whereas the large field of direct plasma diagnostics is separately covered, e.g. by Macchi et al. [4]. To provide such performance measure, the detectors are employed for detection of particle type, spatial distribution and kinetic energy.

3.4.1 Experimental challenges for detectors

The list of distinctive features of laser-generated ion bunches in section 3.3.2 can be used to derive a list of challenges for detectors to be used as bunch diagnostics and for applications relying on spatially resolved detection.

The presence of a mixed radiation field of charged and uncharged particles and the intense laser light itself can cause an **overlay background** over the signal of the particles of interest. Unfiltered cameras and detectors sensitive to energy deposition are **blinded**. The exponential energy spread and the shot-to-shot fluctuations make it difficult to choose a detection system with sensitivity to a **certain signal level**. The possible high intensity of 10^{10} p/ns and high fluences of 10^7 p/cm^2 , caused by the ns short bunch duration and the nC high bunch charges can generate **saturation** or **pileup**. The fact that the laser-plasma interaction has to take place in vacuum can cause damage by **out-gassing** and hence **material degradation**. The removal of offline detectors from vacuum, **venting** of the experimental **vacuum chamber** and replacement by new detectors is time consuming, **prone to setup-errors** and nowadays hindered by the few Hz shot repetition frequencies. The **induced radioactivity** can additionally be at dangerous levels. The high beam divergence can cause the detectors to be **placed close to the source** or **to lose a significant fraction of the beam**. The **debris** from destroyed laser targets is scattered inside the chamber and can be deposited on the detectors.

Especially detector systems relying on electronic components suffer various disturbances. The experiences from a variety of detector development and characterisation

experiments is summarized here and further discussed for electronic pixel detectors in chapter 5.

The intense and broadband EMP pulse with GHz to THz frequencies causes **electronic failure**, since modern chips operate in the same frequency band. The usage of **bulky housings for shielding** is difficult due to the limited space inside the vacuum chamber and since they possibly intersect a large fraction of the beam. The transport of the detector signals from the sensor to the readout electronics needs **shielded cables** in order not to catch up the EMP-like antennas. Cables themselves are **expensive** due to the needed vacuum compatibility and have to be placed outside the potential beam direction in order to avoid **direct irradiation**. The signals have to be fed outside the vacuum chamber using feed-through flanges, which can cause chamber **leakage** and **catch up disturbing signals** from other detectors. Additionally, the vacuum hinders the dissipation of heat from the electronic components via air-convection or heat conduction and can cause **overheating** and **increased dark current** due to a lack of efficient cooling capabilities.

Most laser-ion acceleration experiments to date use non-electronic detectors, and the adoption of established ion detection and beam monitoring devices, which are widely available for clinical accelerators, is therefore limited. Especially the high instantaneous flux due to the quasi-instantaneous ion acceleration using fs short pulses is a challenge for conventionally used beam monitoring systems.

3.4.2 Desired features for detectors

The list of challenges can be used to derive a list of desired or necessary features.

Since the radiation field from the interaction of laser pulse and target is of **mixed** particle types, a **particle selectivity** for e.g. protons, electrons or photons only can be desirable. Such selectivity can be achieved by the nature of the detector sensitive material (CR-39) or using magnetic deflection. The **energy spread** and the exponential proton spectrum can be detected if detectors are **energy selective** (e.g. by using magnets). Since single particle tracking is nearly impossible for such high particle rates, **linearity** with the deposited energy is desirable for particle counting. **Vacuum compatibility**, **radiation hardness**, **online readout** and retained functionality after exposure to the **laser-light** as well as **EMP hardness** are furthermore desirable.

For biomedical radiation research experiments with laser accelerators of ion beams in the context of particle therapy, detectors should provide quantitative real-time beam monitoring with accuracy better than 3-4 % of the dose level.

3.4.3 Contemporary detector technology

Up to present, mostly offline information on bunch intensity and position is available. No prompt, quantitative information is provided by from this kind of detectors, additionally

3 FUNDAMENTALS OF RADIOTHERAPY-, LASER-ACCELERATION- AND DETECTOR TECHNOLOGIES

	Online	Photon-sensitive	Energy resolving	Drawbacks
CR-39	No	No	stacked	Chemistry & Microscope
Image plates	No	Yes	No	minutes of scanning
Dosimetric film	No	Yes	stacked	hours of scanning
Scintillator	Yes	Yes	No	Alignment, Light-shielding
I-BEAT	Yes	No	Yes	under development
TOF	Yes	No	Yes	under development
WASP & CMOS Sensor	Yes	No	Yes	Alignment, B-field

Table 3.3: Listing of the detectors currently used in laser-driven ion acceleration [87].

mostly requiring replacement from laser shot to laser shot. Minutes to hours of careful processing time is often needed in order to achieve quantitative results (table 3.3).

Non-electronic and hence offline detectors such as films, phosphor screens or nuclear track detectors represent the detector techniques mostly used in laser-ion acceleration (figure 3.13). They are able to withstand the intense electromagnetic pulse (EMP) from the laser-plasma interaction, have spatial resolution of $< 100 \mu\text{m}$ and show a very high dynamic range ($10^2 - 10^6$) [87]. The photon sensitivity can be seen as good or bad, since the laser light has to be shielded.

Since laser system repetition rates can reach the few Hz range nowadays (section 3.3), the transition from offline to online techniques is highly desirable. Especially, ion radiography experiments performed at the LEX photonics laboratory (chapter 7) and experiments currently set up at CALA can exceed a 1 Hz shot repetition frequency.

Radiochromic films (RCFs) measure qualitatively, and after calibration quantitatively the two-dimensional distribution of ionizing radiation. RCFs are two dimensional detectors made of up to $30 \text{ cm} \times 30 \text{ cm}$ plastic sheets and have been established since decades for dosimetry or medical imaging.

Due to radiation induced polymerisation of organic monomers, dose deposition in the active layer causes a change in the *optical density* (OD) (figure 3.13a). The functional principle is, like the darkening in photographic films, offline and non-electronic. Although no chemical developing is needed, irradiated sheets need to self-develop over several hours, to be manually removed from the laser-ion experiment and digitized using flat-bed scanners.

RCFs are inexpensive, easy to handle and of linear response for dose levels of 10^{-3} - $4 \cdot 10^3 \text{ Gy}$, which allows to stack multiple sheets in order to measure a coarsely sampled depth-dose profile of the radiation beam (called RCF-stack) [116]. The 22 MeV proton

beam from MLL penetrates 13 RCFs of the type EBT-3, according to a FLUKA simulation, giving rise to only thirteen sample points for the Bragg curve.

Image Plates (IP) also measure qualitatively, and after calibration quantitatively the two-dimensional distribution of ionizing radiation, like RCFs. They are re-usable, since the radiation sensitive material is a photosensitive phosphor screen, which returns back to the original state after read-out and erasure using a Helium-Neon (He-Ne) laser (figure 3.13b). The He-Ne laser light externally stimulates the de-excitation of radiation-induced electrons, which remain trapped in energetically meta-stable states of the screen material over several hours, resulting in the emission of *ultraviolet* (UV) photons. By a lateral scan of the He-Ne laser across the IP after irradiation and measurement of the stimulated emission of the UV luminescence, IPs can be digitized and provide an up to 20 cm × 20 cm large beam profile with 25 μm resolution.

IPs have an even higher dynamic range than RCFs, are very sensitive to all types of ionizing radiation and have to be shielded from visible light using a 15 μm aluminium foil. They were used as X-ray detectors in ion radiography experiments at the TPW (chapter 7).

The Columbia Resin 39 (CR-39) is a *solid state nuclear track detector* based on plastic polymer chains of *Polyallyldiglycolcarbonate*. CR-39 is insensitive to visible light. It is used in sheets of up to 30 cm × 30 cm and is typically fabricated as offline non-electronic detector in thickness of 500 μm or 1 mm (figure 3.13c).

During the propagation and deceleration of a high-energy particle through the CR-39 layer, the deposited energy above a material-specific threshold causes localized cracks in the polymer chains, leaving a track throughout the sheet. Densely ionizing particles such as protons or heavier ions deposit, compared to electrons and photons, enough energy locally to create the cracks.

The tracks can be made macroscopically visible by etching the irradiated CR-39 in a NaOH solution. 60 min in 6-molar NaOH were for example used for the TPW experiments (chapter 7). Due to different etching rates for the cracked polymers and the intact ones, the entry and exit positions of individual particles become visible as μm-small pits at the front and back-surface.

Using an optical microscope, the individual pits can then be counted. The pit-density is an estimate of the absolute number of ions that hit the front- / back-surface. If pits overlap, i.e. for fluxes above 10^8 protons / cm², the CR-39 start to saturate.

Scintillators have started to be introduced as particle diagnostics in laser-ion acceleration experiment several years ago. Similar to IPs, the scintillators store the energy deposited by the particles generated in the interaction and release the energy as visible light. The scintillator material determines the electronic excitation and de-excitation levels and

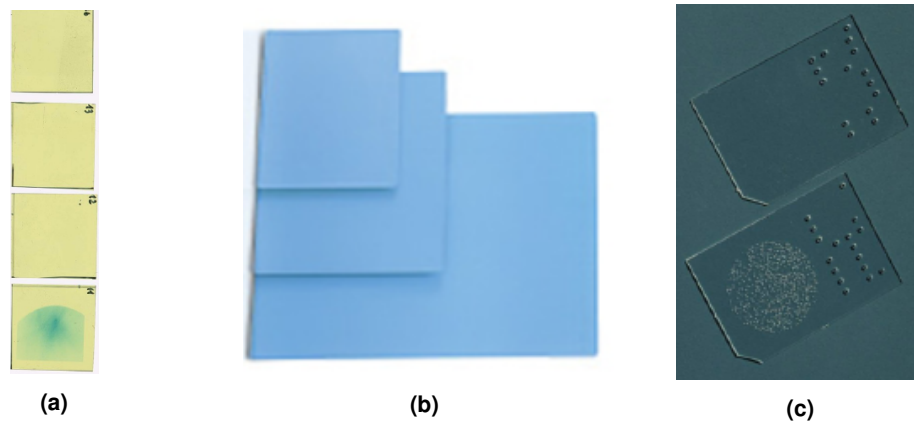


Figure 3.13: Offline detectors used at laser-driven ion acceleration experiments. (a) Four sheet stack of radiochromic films. (b) Three sheets of image plates. (c) Two CR-39 plastics. Clearly visible is the change in optical density after irradiation for the lowest film, as well as the pits on the CR-39 after the etching of the radiation-induced polymer damages.

can be chosen for best light yield, dependent on the application for electron, photon or ion detection.

Scintillators made of inorganic crystals such as *Sodium-* or *Cesium-Iodine* (NaI, CsI) or embedded in plastics such as *Lanex*, *MinR* or *Polysiloxane*, are available and vacuum compatible and were used as position diagnostics in the presented thesis at all conventional and laser facilities.

Due to the formerly low particle energies at LION experiments, the scintillators were mostly mounted close to the target inside the experimental vacuum chamber and read out using cumbersome and fragile *micro-channel plates* (MCPs), *charge-coupled device* (CCD) cameras with objectives or *photomultiplier tubes* (PMTs). The mentioned readouts however can provide digital online information. As light sensitive and electronic devices, these were usually placed outside the vacuum chamber by using mirrors, demanding for bulky shielding, error-prone alignment and possible image degradation from mirrors and flanges. MCP, CCD and PMT needed to be shielded using aluminium foils or housings against the neutron, X-ray, EMP, electron and laser light background.

3.4.4 Emerging detector technologies employed at laser accelerators

Micromegas are low material budget and radiation hard detectors offering a position resolution $< 100 \mu\text{m}$ even reasonable for proton radiography [37, 152]. Charged particles traversing the sensitive detector volume ionize a gas mixture and the generated electron-ion pairs drift towards charge-sensitive readout strips [28]. The radiation hardness comes from the usage of light materials such as Kapton (a polyimide film), aluminium and copper and by using air as ionisation medium [37, 29]. They are cheap and can be built in large areas, making them reasonable transmission detectors [123]. The list of features,

combined with a high rate-capability for tracking individual particles or working in integration mode makes them interesting for the beam profile monitoring at LION, however the need for high-voltage and gases makes them vacuum incompatible.

Time of flight (TOF) detectors such as the *Bridge-microdosimeter* are under investigation as bunch energy spectrum diagnostic at LION [250]. Since the bunch generation is only a few ps short, the investigated semiconductor or diamond detectors can use the time of arrival of different kinetic proton energies, which show dispersion at the nanosecond level, at the detector position for a spectroscopic measurement [248]. The need of several meters of drift space, the required small sensitive volume allowing for a fast detector response time and the lack of position resolution makes TOF useful but sometimes difficult to implement.

Pixelated semiconductors such as CCD or *Complementary metal-oxide-semiconductors* (CMOS) sensors can replace IPs, films or CR-39 as position sensitive detectors and have been introduced to medical imaging and dosimetry, as well as for non-laser based radiation research. The small pixel sizes of several μm practically allow to spatially spread the high particle flux of up to 10^8 p/cm^2 per bunch at laser-ion acceleration experiments over the detector surface, such that the individual pixels are irradiated by statistically a single particle per μm^2 . An online readout of up to 3 Hz can be realized for the RadEye sensor used in the presented thesis (section 5.1).

Bonner sphere spectrometers (BSS) are detector systems used for neutron detection (section 4.1). BSS use multiple counting detectors filled with ^3He gas, each one having a mantle of a different and a few cm thick lead shell, in order to be sensitive to a different energy range of neutrons. The performance at pulsed neutron sources will be in future investigated, since such systems could be used to monitor the neutron spectra generated at LION experiments. After a relationship between neutron and proton energy spectrum will be established, BSS could thereby serve as out-of-field passive proton detectors (section 3.3.2).

Chapter 4

Simulation studies of secondary radiation in modern acceleration facilities

The author has published the work presented in section 4.1 as a journal paper to *Zeitschrift für Medizinische Physik* and presented the results orally at the *DGMP 2016* conference and as poster at the *AAPM 2016*:

- Paper: **F Englbrecht** et al: A Comprehensive Monte Carlo Study of Out-Of-Field Secondary Neutron Spectra in a Scanned-Beam Proton Therapy Treatment Room, *Journal of Medical Physics*, 31(2):215-228 2021
- Oral Presentation: **F Englbrecht** et al: Monte Carlo Studie der Energiespektren sekundärer Neutronen außerhalb des Bestrahlungsfeldes in einem mit der Scanning Technik und Gantry ausgestatteten Protonentherapie Behandlungsraum, *Annual conference of the German Society for Medical Physics, DGMP 2016, Würzburg, Germany, Abstractband p. 290-291, ISBN: 978-3-9816508-2-2*
- Poster: **F Englbrecht** et al: SU-F-T-84: A Comprehensive Monte Carlo Study of Out-Of-Field Secondary Neutron Spectra in a Scanned-Beam Proton Therapy Treatment Room, *Annual Meeting of the American Association of Physicists in medicine, AAPM 2016, Washington DC, USA , Med. Phys. 43, 3512 (2016)*

The author has published the work presented in section 4.2 as a journal paper in the *Journal of Radiological Protection* and presented the results orally at the *DGMP 2018* conference and at the *Ffs 2019* conference:

- Paper: **F Englbrecht** et al: Radiation protection modeling for 2.5 petawatt laser production of ultrashort X-ray, proton and ion bunches: Monte Carlo model of the Munich CALA facility, *Journal Of Radiological Protection* 40, 1048–1073, 2020

4 SIMULATION STUDIES OF SECONDARY RADIATION IN MODERN ACCELERATION FACILITIES

- Oral Presentation: **F Englbrecht** et al: Monte Carlo simulations for radio protection shielding design of 3 petawatt laser based production of ultrashort x-ray, proton and ion bunches for biomedical applications, *Annual conference of the German Society for Medical Physics, DGMP 2018, Nürnberg, Germany*
 - Oral Presentation: **F Englbrecht** et al: Erzeugung ultrakurzer Röntgen-, Protonen- und Ionenstrahlen mittels Petawatt-Laser: Monte Carlo Simulationen für den baulichen Strahlenschutz, *Jahrestagung Fachverband für Strahlenschutz 2019, Würzburg, Germany*
-

Knowledge of the secondary radiation field around novel accelerators is of key relevance for patient and staff safety and generally speaking controlled operation.

The transition from established keV imaging- and MeV treatment energies of photons and electrons to photons, protons, electrons and ions of up to three orders of magnitude higher energies (250 MeV protons) drastically changes the possible nuclear reaction channels, the kinetic energies and the particle types present in the secondary radiation field. Common concepts of radiation protection have to be studied and some developed further:

- Section 4.1 studies the systematic correlation between therapeutic proton beams and secondary neutrons at the state-of-the-art proton treatment facility *Rinecker Proton Therapy Center (RPTC)*. Neutrons in the scanned beam treatment modality are of interest for a systematic investigation by Monte Carlo simulations, since not only the treatment head (3.2.2) but also the patient himself is main source of neutrons. Tests of detectors from chapter 5 have been performed at RPTC.
- Section 4.2 describes the studies performed for the safe operation of the novel laser-based particle source *Centre for Advanced Laser Applications (CALA)*. The high spatiotemporal laser-power density at 1 Hz repetition frequency, resulting particle energy, multi-species radiation field and short pulse duration complicates dosimetric measurements and makes detailed calculations necessary. Detector tests for CALA are reported in chapter 5 and chapter 6. Imaging studies using protons and X-rays from another laser-emulating accelerator or a different laser-particle source are reported in chapter 7.
- Section 4.3 starts to combine the concepts of section 4.1 and section 4.2. As measurements of the secondary neutrons at CALA will be difficult due to the ns particle bunch duration and broad proton energy distribution, simulations can provide an estimate on the correlation of the laser-based proton and electron bunches to the secondary neutron radiation field. If established, such correlation would even

allow a non-invasive monitoring of the laser-proton accelerator performance by on-line secondary neutron spectrometry.

4.1 Secondary neutrons in scanned proton therapy at RPTC

4.1.1 Introduction

It has been suggested that proton therapy could enable better tumour control probabilities and demonstrated to do so in treatment of cancers of the central nervous system, for head and neck cancers, and tumours inside the eye [6]. Recently, data from ion therapy irradiation of prostate cancer suggesting lower risk of subsequent secondary cancer for ion therapy have been reported [153]. Compared with conventional radiation treatments employing photons, proton beam therapy enables to spatially confine the therapeutic radiation dose to the targeted tumour volume and reduce the integral out-of-field to healthy tissue.

Despite these advantages, which are rooted in the physical nature of the interactions of protons with tissue, proton therapy still carries the problem of creating secondary charged particles and stray neutrons that expose the patient to undesired dose outside the tumour target. Being especially relevant for pediatric or re-irradiation patients, such unwanted neutrons can deposit their kinetic energy inside the patient far outside the desired treatment volume and increase the risk of secondary cancer [103, 156, 162]. However, an extensive knowledge review on neutron dose in proton therapy by Hälgl and Schneider recently summarized that it is unlikely that the neutron dose has a high impact on the secondary cancer risk of proton therapy patients [111]. Although neutron contribution is typically neglected in current treatment planning systems, there are efforts ongoing to integrate the information of risk estimation in the planning process, which will require also the treatment room to be modelled [200, 111, 126, 127, 183].

Similarly to the system used in this study, most modern active spot scanning proton therapy systems employ an isochronous cyclotron with a fixed extraction energy of 230-250 MeV and an energy degrading system several meters upstream of the treatment nozzle [198, 24]. By placing this strongest source of secondary neutrons (the proton energy degrader) in a separately shielded area, actively scanned proton therapy has been reported to reduce the secondary neutron ambient dose exposure to patients by up to one order of magnitude in comparison to delivery techniques based on passive scattering devices placed in the treatment nozzle for beam shaping [177, 199, 73].

Detailed room models were used in MC simulations to study the out-of-field dose and optimisation of the treatment room design [200, 147, 232, 221]. To a lesser extent and mostly modelling passively scattered proton beam facilities, the spectra and number of secondary neutrons were studied. The spectra and number of secondary neutrons were studied to a lesser extent and mostly modelling passively scattered proton beam facilities

4 SIMULATION STUDIES OF SECONDARY RADIATION IN MODERN ACCELERATION FACILITIES

[224, 42, 177, 38]. Some of the published works used models of the gantry and treatment room, but the mostly vague description of used materials and the treatment field specific collimators and compensators have so far hindered generalisation of the results. Recently, literature is starting to provide more detailed simulation models along with thorough predictions of neutron spectra coupled to measurements for the *Mevion S250* gentry-mounted passively scattered proton system [108, 11, 12]. Modeling the PBS treatment room *Gantry 1* at PSI, Schneider et al. reported the usage of a detailed MC room model and characteristics of the proton beam in order to have accurate neutron spectra for integration into the treatment planning system [200].

Because active beam scanning has begun to replace passive beam delivery techniques, and literature on secondary neutrons from active treatment facilities is still sparse, a detailed Monte Carlo analysis was performed for simple monoenergetic treatment fields. The goal was to enable comparative studies of the contributions of the gantry and treatment room elements on the secondary neutron generation [31, 221, 252, 18]. Spot scanning facilities can be expected to be more uniform in design and the present neutron spectra to be better inter-comparable, because the spot scanning technique does not place field-specific material into the beam path [7]. In this beam delivery approach, the patient will therefore be the main source of secondary neutrons and a detailed study of the spot scanning room and gantry elements is desirable [146, 106, 196]. Of the modelled Varian ProBeam therapy system, 17 rooms were in operation and 20 were under construction in 2019 [81, 176].

Although the purpose of the previously published studies on ambient dose equivalent from neutrons did not include the detailed validation of the Monte Carlo simulation models of the respective treatment facilities, the obtained measurement and simulation data showed that large differences may occur [199, 147]. For a scattering facility which causes neutrons to be mostly generated in the passive range modulators and field shaping apertures and not in the room itself. Farah et al. already reported that elements as the modelling of the bending magnet and mechanical gantry structure should be adjusted to minimize such discrepancies between measurement and simulation [147]. Other studies reported differences of a factor of 2-4 in ambient dose equivalent, also originating from approximations in the beamline and room modelling [18, 256]. In order to investigate the reasons for such differences, the influence of room components on the neutron spectra measured by Trinkl et al. was simulated systematically.

4.1.2 Material and Methods

For the measurements underlying the presented simulation study, a physically accessible basic quantity, the energy resolved neutron fluence $\phi(E)$ was chosen. Nuclear reaction cross sections needed for MC simulations are strongly dependent on neutron energy as is the simulated secondary radiation field [234, 257]. The energy resolved neutron fluence is also referred to as *neutron spectrum*.

The use of monoenergetic proton fields facilitated a quantitative and objective evaluation

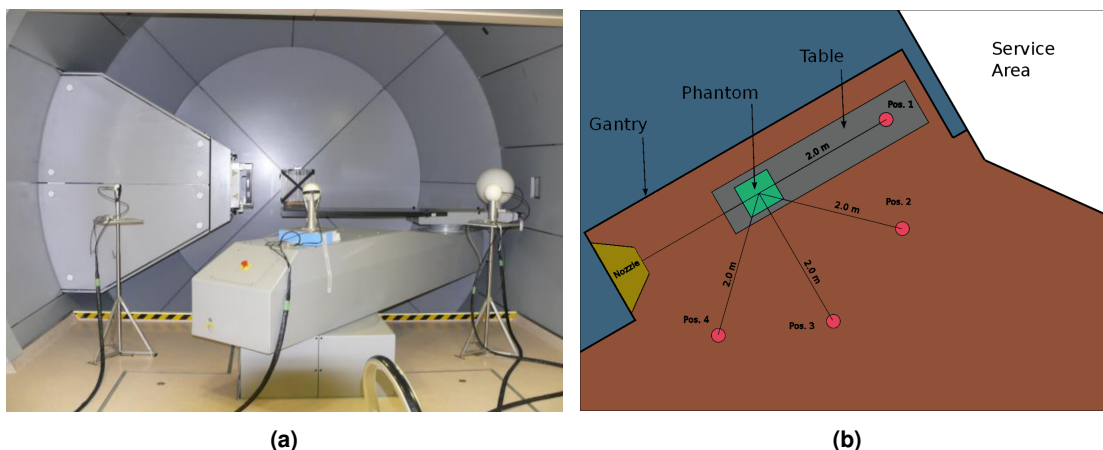


Figure 4.1: (a) Measurement setup by Trinkl et al., placing the ERBSS around the PMMA phantom. (b) Scheme of measurement and simulation setup [234].

of the angular resolved secondary neutron spectra as well as their dependence on the proton beam energy and the specific setting of the treatment room geometry. Monoenergetic proton fields were chosen in the measurement campaign in order to disentangle the influence of proton beam energy, as well as the influence of the individual treatment room components and the phantom itself on the secondary radiation field. In fact, nuclear reaction channels become enabled energetically when the neutron energy changes due to scattering or resonances of neutron production in material cross sections, influencing the field of secondary particles.

As a first step, the FLUKA MC code was used to reproduce published neutron spectra at the *Rinecker Proton Therapy Center* (RPTC) facility [16, 72]. Simulated FLUKA spectra were cross-checked using GEANT4 MC simulations starting from the same FLUKA-generated phase spaces of the proton fields [5]. As a second step, the validated FLUKA room model was used to study the contributions of the included treatment room elements and shielding to the full neutron fluence spectrum.

Previously measured secondary neutron spectra Neutron spectra had been measured using an *Extended-Range Bonner Sphere Spectrometer* (ERBSS) inside a gantry treatment room at RPTC [234]. As described in section 3.2.2, RPTC uses a Varian ProBeam nozzle for pencil beam spot scanning delivery [24, 136]. The used ERBSS uses a higher number and special material shells in order to reliably measure neutron spectra for the high-energy neutron range (> 20 MeV), which historically made a full range spectral measurement at proton therapy facilities difficult [146]. The measurement spheres had been placed concentrically at 0° , 45° , 90° and 135° relative to the beam axis at 2 m distance from isocenter. Square fields of $11\text{ cm} \times 11\text{ cm}$ size at an initial energy of 200 MeV, 140 MeV, 75 MeV and 118 MeV using a 5 cm PMMA range shifter were delivered to a polymethyl methacrylate (PMMA) slab phantom ($30\text{ cm} \times 30\text{ cm} \times 30\text{ cm}$). For each energy, Trinkl et al. unfolded neutron spectra for the four angle positions in the possible energy range

4 SIMULATION STUDIES OF SECONDARY RADIATION IN MODERN ACCELERATION FACILITIES

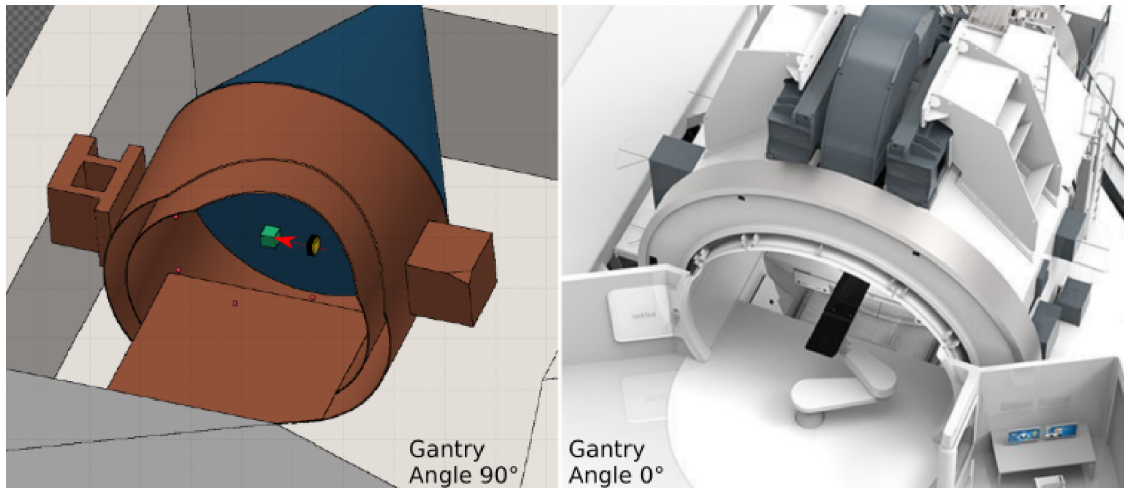
from 10^{-9} MeV- 10^4 MeV.

The results showed a strong dependence of the secondary neutron field on the angular measurement position and initial proton beam energy. Comparison of the neutron spectra from simple bare phantom simulations without room model, which are used as input for the ERBSS unfolding, to the measurement results, showed severe differences. Especially in the thermal energy region (10^{-2} MeV- 10^1 MeV) of increased biological effectiveness (figure 2.5), it is evident that the influence of the treatment room dominated the characteristics of the secondary stray neutron field (figure 3 and figure 4 by Trinkl et al. [234]). In order to clarify the origin of the secondary neutrons and systematically understand the room influence on the different components of the neutron spectrum, the RPTC treatment room was modelled and the experiments were re-simulated.

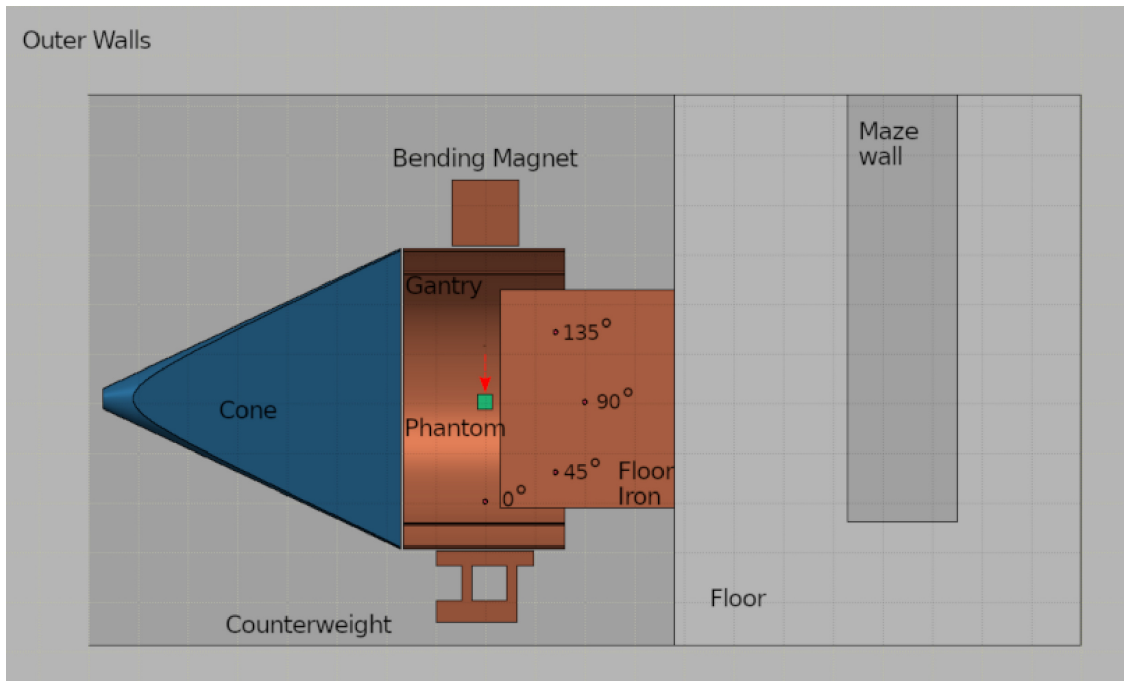
Detailed treatment room model In contrast to a previous Monte Carlo study by Hofmann et al. modelling the cyclotron and energy selection system area of the facility [105], the interior of a clinical gantry room (figure 4.2) was modelled. In addition to the literature, information was also provided by the local medical physics team [198, 24, 249].

In the FLUKA simulation model, walls of two meters thickness, enclosing the treatment room ($11 \times 11 \times 20 \text{ m}^3$) and made of standard concrete from the FLUKA material database, formed the outer mantle (figure 4.2 bottom). Standard air was used to fill the shelter. The entrance maze included the concrete floor. The gantry was split into two main model components: a gantry wheel and a gantry cone. The section of the floor accommodating the patient table and its support structure were included as a 1 cm plate of standard iron in FLUKA, extending 130 cm into the inner gantry wheel. The wheel consists of two concentric 2 cm thick iron cylinder shells of 5.08 m radius (inner shell) and 6 m radius (outer shell) (figure 4.2 top). The modelled size of the gantry cone matched the installed, cone shaped, complex back support structure of the gantry. For simplification, the cone model reproduced just the outer dimension with no internal structure. It was modelled as solid iron of reduced density $\rho_{cone} = 2 \text{ g/cm}^3$ in order to reproduce the actual weight [24]. The 135° bending magnet of the gantry was included as a massive cube of iron. On the opposite site of the outer gantry wheel, the counterweight of the bending magnet was modelled based on the exact geometrical drawing by the manufacturer. The geometry of the counterweight was used to calculate a mass of 18.7 tons of massive iron when using a density of $\rho_{Fe} = 7.874 \text{ g/cm}^3$. The bending magnet edge length was hence set to 133 cm to match the counterweight mass.

The primary protons were sampled inside a small vacuum region 3 cm upstream of the vacuum window and the beam monitor chambers using the previously published nozzle model [249]. After 86 cm of travel, the protons and generated secondary particles hit the front surface of a PMMA phantom, consistent with the phantom position as used for the ERBSS measurements [234]. The density of the slab phantom at the isocenter, made of PMMA, was the default value as used by the local medical physics staff for quality



(a)



(b)

Figure 4.2: (a) 3D FLUKA model of the treatment room (Gantry position 90° , beam direction along arrow) containing the most important elements of the manufacturer representation (shown at gantry position 0°) [239]. (b) Horizontal cut at floor level (gantry position 90°). The four points of the neutron spectrum-scoring are marked as circles.

4 SIMULATION STUDIES OF SECONDARY RADIATION IN MODERN ACCELERATION FACILITIES

assurance procedures. The density of $\rho_{PMMA} = 1.2 \text{ g/cm}^3$ was dosimetrically verified to produce the realistic water column range measurement previously by the author [53].

Simulation settings FLUKA uses a multi-group technique for neutron transport in the energy range where neutron cross section tables are used (typically for $E \leq 20 \text{ MeV}$). In the multi-group approach, 260 energy groups are used in the simulation of the elastic and inelastic interactions of neutrons [71]. The total energy spectra of secondary neutrons were obtained using FLUKA multichannel (260 fixed bins in the interval from 10^{-9} MeV to 20 MeV , log-equidistant above 20 MeV) detectors called USRTRACK scorers.

Four of these spherical USRTRACK detectors of 10 cm radius were placed as air spheres around the phantom isocenter in the reported ERBSS measurement positions. Because multi-scattering of secondary neutrons down to thermalisation is CPU-time consuming, simulated 3.5×10^9 primary protons were simulated for each of the four primary proton beam energies to acquire reasonable statistics in the fixed spectral neutron binning. A total of 600 statistically independent simulations were used to estimate the statistical uncertainty of the results in terms of the median of the standard error for each bin in the simulated neutron spectra. All simulations used FLUKA Version 2011.2c.3 with settings *HADROTHERapy*.

Secondly, the FLUKA user routine *fluscw.f* was used to filter during runtime the USRTRACK spectra, depending on the room element in which a scored secondary neutron had been generated. The neutron origin was accessed using the USDRAW section of the *mgdraw.f* user routine, which automatically is called at runtime after inelastic interactions. The region of neutron origin was saved in ISPUSR variables during the production reactions occurring, such as $X(p, xn)Y$, $X(n, xn)Y$ or $X(\gamma, xn)Y$. The information on the neutron origin was propagated through the simulation of each neutron trajectory and used for filtering when the neutron entered one of the four detector positions. The individually considered regions of neutron origin were:

- The 135° bending magnet
- The iron counterweight
- The PMMA phantom
- The two gantry cylinders
- The concrete floor of the maze
- The iron plate ranging into the gantry
- The outer concrete walls enclosing the shelter
- The gantry iron cone of reduced density.

Particle name	Baryon number	Electric charge [cgs]	Position			Direction cosine			E [MeV]
			x [cm]	y [cm]	z [cm]	p_x	p_y	p_z	
proton	1	1	0.1872	7.39E-002	16.9346	1.75E-003	-7.2E-004	0.99999	200.420
neutron	1	0	-0.2681	-1.3602	16.9346	9.983E-002	-0.28090	0.95453	93.152
e-	0	-1	0.5460	-0.4921	16.9346	0.4399383	5.4923E-002	0.89634	0.314
proton	1	1	6.40E-002	0.2621	16.9346	-5E-005	5.4E-004	0.99999	201.363
proton	1	1	-0.6152	0.4239	16.9346	6.4E-004	2.45E-003	0.99999	201.183
photon	0	0	-1.2805	6.5910	16.9346	-6.143E-002	0.79832	0.59079	0.716
deuteron	2	1	-3.6557	4.9493	16.9346	-0.26649	0.43285	0.86117	18.307
proton	1	1	-7.85E-002	-0.1097	16.9346	4.8E-004	1.67E-003	0.99999	201.500
proton	1	1	0.5471	0.6485	16.9346	1.44E-003	2.02E-003	0.99999	199.692

Table 4.1: Excerpt from the phase space file generated using the FLUKA *mgdraw.f* user routine. Phasespace is then read by GEANT4 to start the particle transport. The data show particles scored for the 200 MeV proton field at the z position of the nozzle exit.

Because the quality of the nuclear models in MC codes is energy dependent, the results for the four proton beam energies over the full neutron energy range were graphically analysed, in order to visually detect any possible systematics in the data.

For a quantitative evaluation, the neutron spectra subsequently were subsequently binned into four neutron energy intervals, similar to those of the ERBSS data [234]:

- Thermal energies ($1 \text{ meV} \leq E < 0.4 \text{ eV}$)
- Epithermal energies ($0.4 \text{ eV} \leq E < 100 \text{ keV}$)
- Fast energies ($100 \text{ keV} \leq E < 19.6 \text{ MeV}$)
- High energies ($E \geq 19.6 \text{ MeV}$)

The plots used for the graphical analysis are displayed in figure 4.3 - figure 4.16.

The results of the binning are presented in table 4.2 for relative / normalized fluences and in table 4.3 for the absolute fluences per Gray of treatment dose.

Crosscheck of FLUKA results with GEANT4 using in input the same FLUKA-generated phase space Although the FLUKA Monte Carlo code is known to provide accurately benchmarked results in the employed energy range, the GEANT4 general purpose Monte Carlo code was used to verify the FLUKA simulation results of the room model [5]. GEANT4 was also previously employed in the calculation of particle transport problems and the simulation of secondary neutron spectra [8, 45].

For the four energies 200 MeV, 140 MeV, 118 MeV and 75 MeV, particle phase space files were generated using the FLUKA user routine *mgdraw.f* in order to avoid a full remodeling of the nozzle and beam parameters in GEANT4. The phase space files were scored at the exit of the treatment nozzle downstream of all beam monitors and the vacuum window and contained information on a single particle level (table 4.1).

4 SIMULATION STUDIES OF SECONDARY RADIATION IN MODERN ACCELERATION FACILITIES

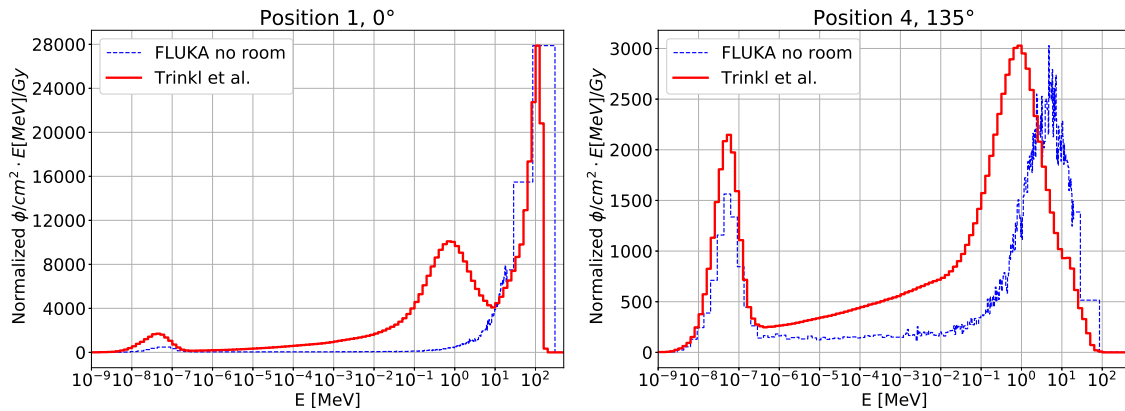


Figure 4.3: Bare phantom simulation without therapy room model (blue curve) and measurements by Trinkl et al. (red curve) in lethargy notation for forward 0° (pos.1, left panel) and 135° backscatter direction (pos. 4, right panel) [234].

GEANT4 was used with the same physics list as utilized for previously reported simulations of secondary neutron spectra (QGSP_BIC_HP with G4StandardEMPhysics_option3 and G4NeutronHPThermalScattering) [228, 234]. The same treatment room was set up in GEANT4 excluding the nozzle model as already taken into account through the phase space file.

Normalisation of the simulation results to absolute dose per treatment Gray for both FLUKA and GEANT4 results was obtained by using the established monitor unit to absolute dose relationship established for the nozzle model by Würfl et al. [249]. The normalized spectra were compared to the spectra from Trinkl et al., who normalized their spectra to the nominal planned Bragg peak dose as reported by the treatment planning system.

4.1.3 Results

In order to evaluate the necessity of a full treatment room model, the USRTRACK simulated neutron spectra per proton treatment Gray in preliminary simulations without any room components was evaluated first. Only the vacuum exit window, the beam monitor chambers, the air gap and the phantom were included and compared to the experimental results of Trinkl et al. [234].

It was found that also in the case of the considered beam scanning facility, oversimplifying the simulation model by omitting any room component causes mismatches over the whole energy range of the secondary neutrons. Exemplary, figure 4.3 shows the mismatches for the 0° and 135° positions of the 200 MeV proton field.

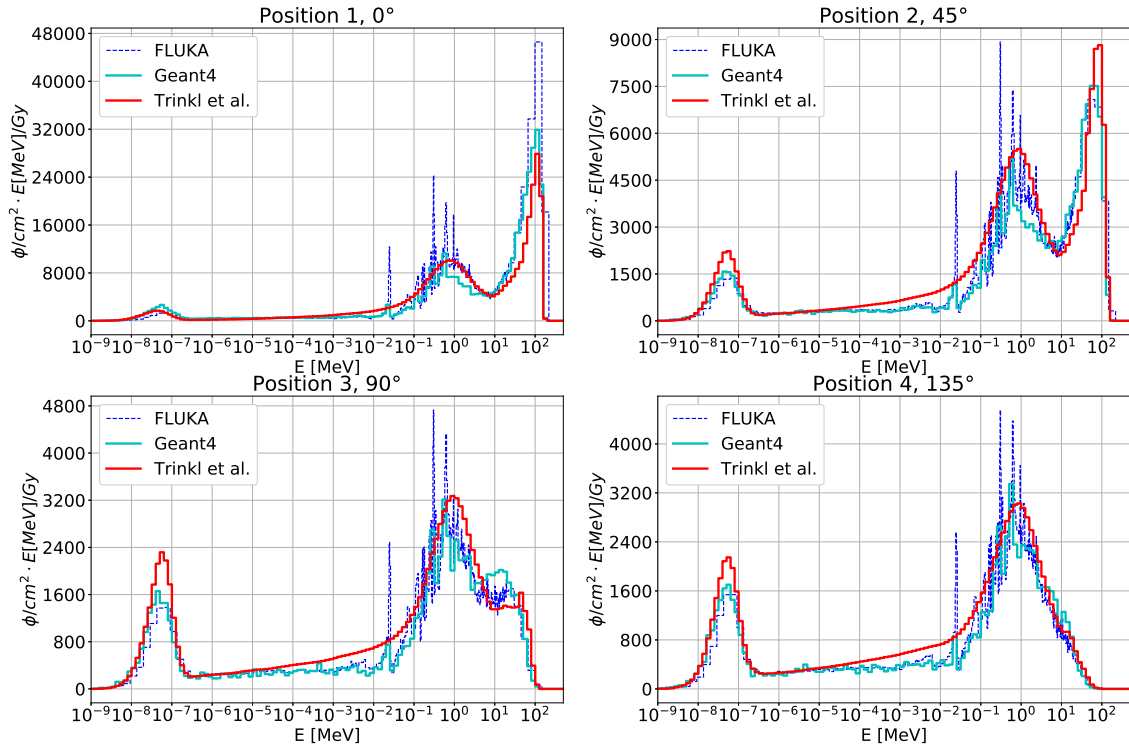


Figure 4.4: Measured and full-room simulated neutron spectra for the 200 MeV proton field.

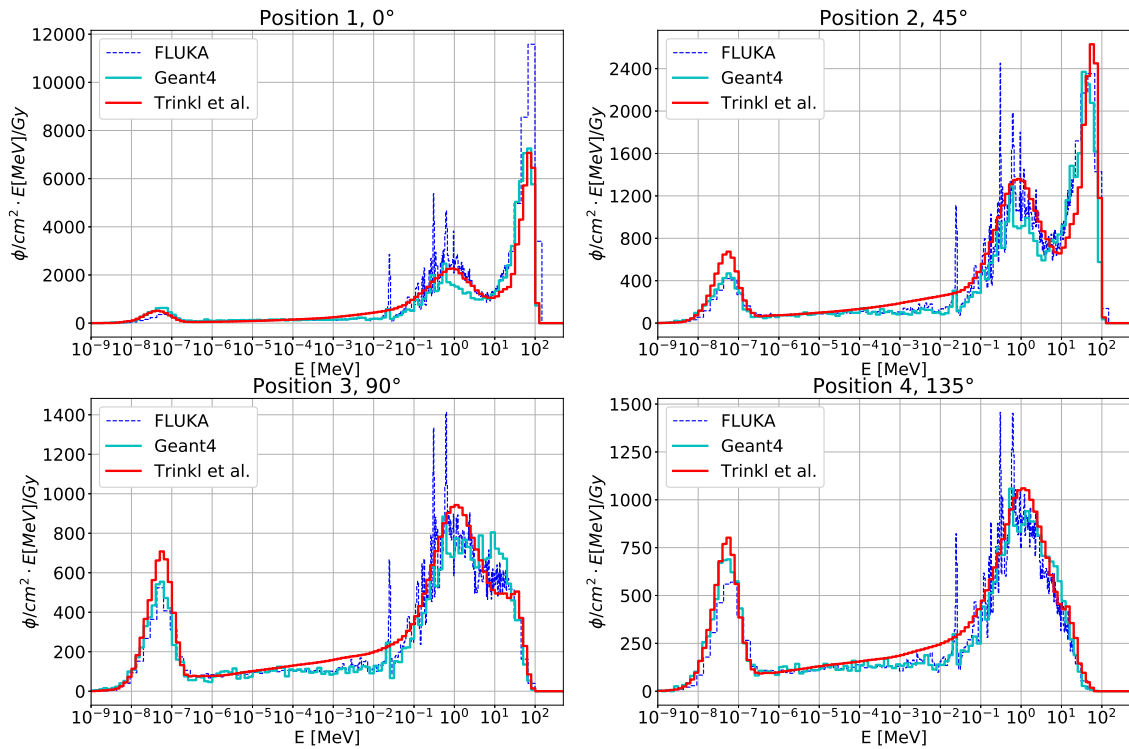


Figure 4.5: Measured and full-room simulated neutron spectra for the 140 MeV proton field.

4 SIMULATION STUDIES OF SECONDARY RADIATION IN MODERN ACCELERATION FACILITIES

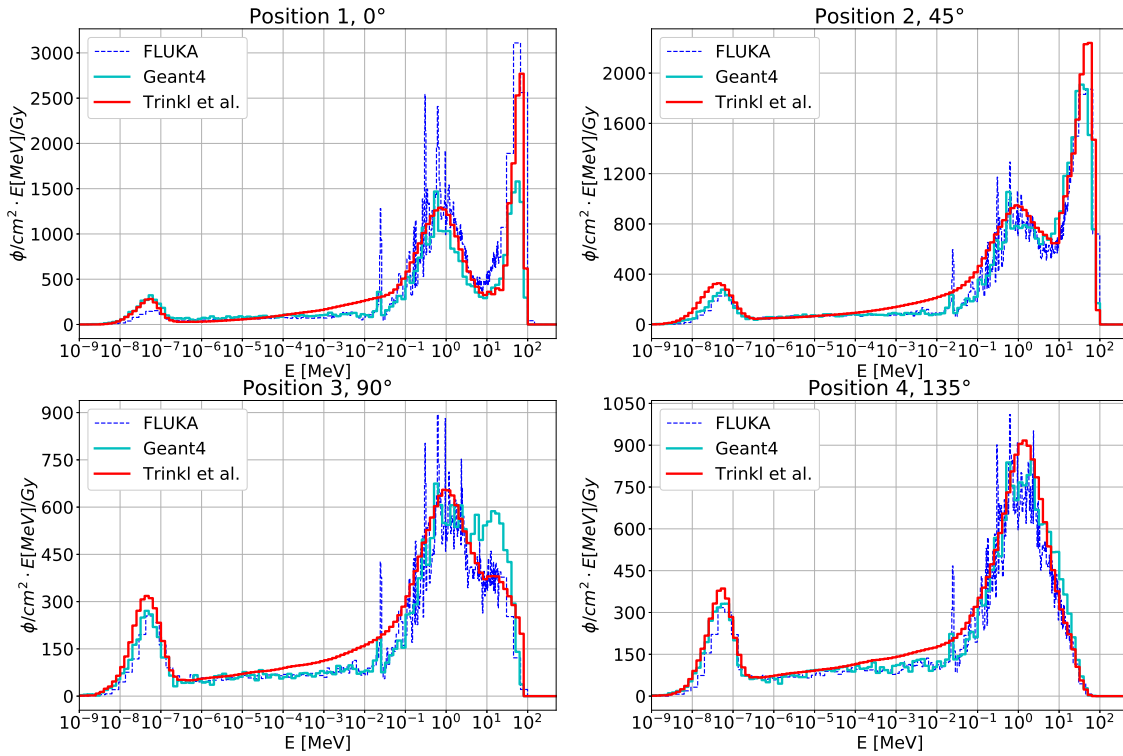


Figure 4.6: Measured and full-room simulated neutron spectra for the 118 MeV proton field using a PMMA range shifter of 5 cm thickness.

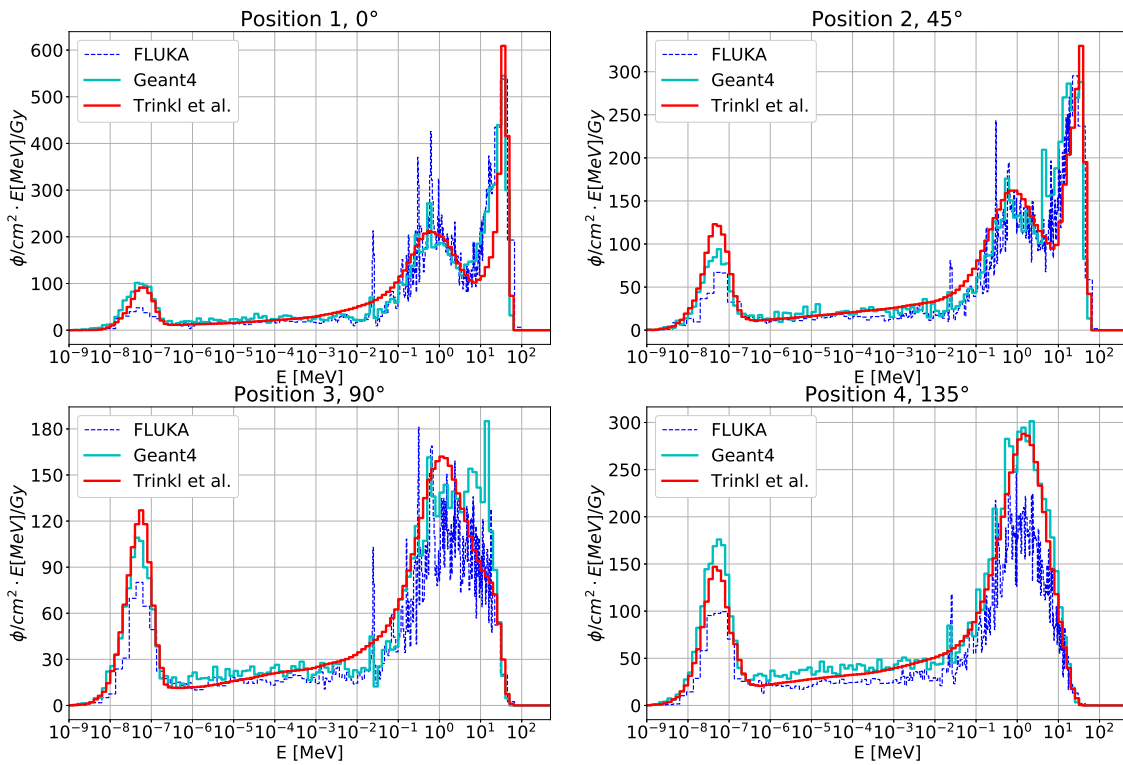


Figure 4.7: Measured and full-room simulated neutron spectra for the 75 MeV proton field.

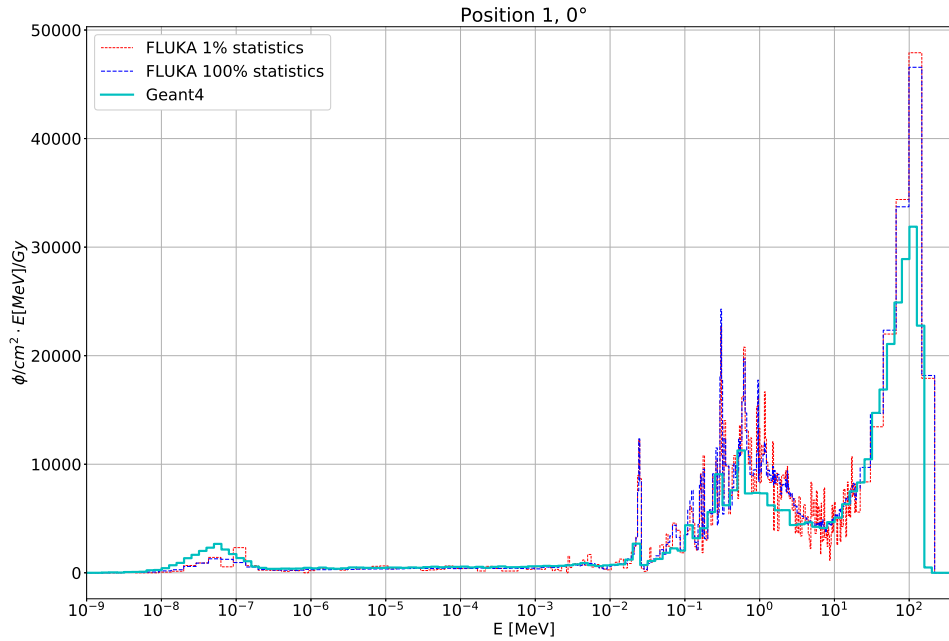


Figure 4.8: Comparison of full statistics versus 1 percent statistics FLUKA simulation for the 200 MeV simulation at position 1. GEANT4 data is shown additionally to compare the resonances.

Simulated full room model spectra compared to measurements As a second step, the neutron spectra of the full room model were analysed and compared these to the measured ERBSS spectra. The neutron spectra for the modelled proton beam therapy scanning nozzle and treatment room for azimuth angles of 0° , 45° , 90° and 135° relative to the beam axis at 2 m distance from isocenter are shown for the $11 \times 11 \text{ cm}^2$ fields at the initial beam energies of 200 MeV (figure 4.4), 140 MeV (figure 4.5), 75 MeV (figure 4.7), and 118 MeV with the PMMA range shifter of 5 cm thickness (figure 4.6). The fraction of neutrons from the nozzle in the four phase spaces was $< 0.6\%$ of all phase space particles. Nearly 100% of secondary neutrons hence originated from the treatment room and phantom.

The statistical uncertainty in terms of the standard error of each scoring bin was evaluated to be 3% for 200 MeV, 0° (best case) and 13% for 75 MeV, 135° (worst case).

In general, all simulation configurations present similar behavior of the neutron spectra inside the treatment room over the full energy range: a high-energy peak, elevated fluence in the fast neutron region, an approximately $1/E_n$ slope for the epithermal neutrons and a minor peak in the thermal neutron energy range. Depending on proton energy and measurement angle, the relative contributions of these features to the total spectrum differ.

The simulated FLUKA neutron spectra display fine resonances which are not present in the ERBSS data, because the ERBSS used response functions with only 130 log-equidistant energy bins and 18 measured count rates to unfold the spectrum in the full

4 SIMULATION STUDIES OF SECONDARY RADIATION IN MODERN ACCELERATION FACILITIES

energy range, which spanned approximately 11 orders of magnitude. That the peaks are coupled to actual material properties such as cross section resonances and not originating in insufficient statistics can be deduced from figure 4.8, which shows the most prominent peaks using only 1% of the total statistics and in parallel along with the GEANT4 data.

For FLUKA and GEANT4, the laterally integrated depth dose profiles in the PMMA phantom were scored. FLUKA and GEANT4 using the FLUKA phase space as input agreed in simulation of the 80% distal falloff range R_{80} of the primary proton beam for all four energies better than 1 mm .

Minor neutron spectra discrepancies between the measured ERBSS and the FLUKA and GEANT4 simulations were observed. FLUKA, compared to GEANT4 and the ERBSS data, tended to display higher fluence in the high-energy interval for 200 MeV, 0° (figure 4.4 top left) and 140 MeV, 0° (figure 4.5 top left), whereas FLUKA and ERBSS data agreed but were below the measurements for all four proton energies at the 90° off axis position (figure 4.4 - figure 4.7 bottom left). Larger discrepancies were present for the 118 MeV, 0° range shifter case for GEANT4 (figure 4.6 top left) and the 75 MeV, 135° FLUKA simulation (figure 4.7 bottom right).

Both codes showed reasonably good agreement with experimental data for the four energies and positions by adequately generating the fast neutron shoulder - often called evaporation peak - in the interval $10^{-1} \text{ MeV} \leq 19.6 \text{ MeV}$. For the whole epithermal interval, the simulations were in close agreement and reflected the spectrum in more detail than the approximately $1/E_n$ slope displayed by the ERBSS data.

Depending on the angular deflection of the detector position with respect to the beam axis, the relative contributions of the high-energy peak and evaporation peak systematically varied. For all four energies, the high-energy peak ($> 19.6 \text{ MeV}$) is more pronounced for smaller observation angles with respect to the beam axis. This finding agrees with the behaviour of the spectra reported by Hohmann et al. and Mares et al. [106, 146]. Table 4.2 displays quantitatively the neutron fraction per energy range. Approximately 50% of neutron fluence for nearly all angles and energies is in the fast neutron range between 10^{-1} MeV and 19.6 MeV . The absolute fluence values per treatment Gray are shown in table 4.3. It is evident that the total number of generated secondary neutrons scales with the initial energy of the proton beam. The extreme case is calculated by FLUKA as an increase by a factor of 121 for the 0° measurement position when comparing the integrated neutron fluence for the proton beam energies of 75 MeV and 200 MeV (table 4.3).

The data for the 118 MeV range shifter field are in line with the results from the measurements, showing that the absolute neutron fluence in the four detector positions is four to six times higher than the 75 MeV case having the same proton range.

The general systematic agreement between the FLUKA simulation model and the GEANT4 results compared to the reported measurements for all four energies at the four

Secondary neutrons in scanned proton therapy at RPTC

Proton Energy [MeV]	Position/ Angle	Data source	Fluence ϕ [%]				Total
			Thermal-n $10^{-9} < 4 \times 10^{-7}$ MeV	Epithermal-n $4 \times 10^{-7} \leq 10^{-1}$ MeV	Fast-n $10^{-1} \leq 19.6$ MeV	High-n > 19.6 MeV	
200 MeV	1 / 0°	Trinkl et al.	4.17	14.31	43.44	38.07	100
		GEANT4	5.56	10.11	36.35	47.99	100
		FLUKA	2.26	8.22	36.00	53.51	100
	2 / 45°	Trinkl et al.	9.46	18.43	44.82	27.28	100
		GEANT4	9.05	14.06	44.76	32.13	100
		FLUKA	7.20	15.64	46.19	30.97	100
	3 / 90°	Trinkl et al.	17.04	25.34	48.55	9.08	100
		GEANT4	16.18	20.67	54.23	8.91	100
		FLUKA	13.63	24.07	53.35	8.94	100
	4 / 135°	Trinkl et al.	18.61	30.20	49.14	2.05	100
		GEANT4	18.80	26.14	53.56	1.51	100
		FLUKA	15.92	29.16	53.29	1.62	100
140 MeV	1 / 0°	Trinkl et al.	5.09	15.39	42.14	37.39	100
		GEANT4	6.33	11.40	37.62	44.64	100
		FLUKA	2.73	9.25	38.35	49.67	100
	2 / 45°	Trinkl et al.	10.87	18.42	43.84	26.86	100
		GEANT4	9.79	14.62	46.65	28.94	100
		FLUKA	7.68	15.80	46.60	29.92	100
	3 / 90°	Trinkl et al.	18.06	25.1	49.03	7.82	100
		GEANT4	16.90	21.66	54.39	7.11	100
		FLUKA	14.89	23.99	54.02	7.04	100
	4 / 135°	Trinkl et al.	19.21	28.91	49.53	2.36	100
		GEANT4	20.88	25.66	52.32	1.14	100
		FLUKA	17.25	28.23	53.26	1.36	100
118 MeV + range shifter	1 / 0°	Trinkl et al.	5.66	20.6	47.08	26.66	100
		GEANT4	8.46	18.91	49.79	22.84	100
		FLUKA	3.05	13.36	48.06	35.53	100
	2 / 45°	Trinkl et al.	8.40	18.02	44.16	29.35	100
		GEANT4	6.99	14.23	50.20	28.58	100
		FLUKA	5.99	14.90	47.47	31.64	100
	3 / 90°	Trinkl et al.	13.77	26.83	50.41	8.97	100
		GEANT4	11.96	20.72	57.80	7.94	100
		FLUKA	11.77	24.08	56.38	7.77	100
	4 / 135°	Trinkl et al.	13.62	28.92	55.32	1.98	100
		GEANT4	12.38	27.67	58.39	1.97	100
		FLUKA	12.38	27.67	58.39	1.57	100
75 MeV	1 / 0°	Trinkl et al.	9.32	21.75	46.44	22.66	100
		GEANT4	11.19	18.81	49.33	20.36	100
		FLUKA	5.44	15.69	52.06	26.81	100
	2 / 45°	Trinkl et al.	15.76	20.73	44.9	18.41	100
		GEANT4	13.04	19.49	53.02	14.44	100
		FLUKA	10.33	18.01	51.68	19.92	100
	3 / 90°	Trinkl et al.	19.26	24.96	51.74	4.05	100
		GEANT4	18.01	26.72	55.11	3.17	100
		FLUKA	15.82	26.27	54.29	3.62	100
	4 / 135°	Trinkl et al.	17.22	26.99	55.28	0.63	100
		GEANT4	18.77	27.50	53.46	0.33	100
		FLUKA	16.16	28.59	54.69	0.56	100

Table 4.2: Normalized secondary neutron fluence ϕ by Trinkl et al., GEANT4 and FLUKA for the four proton energies at the four detector positions [234]. Data was normalized to the integral neutron fluence in order to compare the fractions.

4 SIMULATION STUDIES OF SECONDARY RADIATION IN MODERN ACCELERATION FACILITIES

Proton Energy [MeV]	Position/ Angle	Data source	Fluence ϕ [$1/cm^2$]				
			Thermal-n	Epithermal-n	Fast-n	High-n	Total
			$10^{-9} < 4 \times 10^{-7}$ MeV	$4 \times 10^{-7} \leq 10^{-1}$ MeV	$10^{-1} \leq 19.6$ MeV	> 19.6 MeV	
200 MeV	1 / 0°	Trinkl et al.	3491	11971	36327	31836	83625
		GEANT4	4821	8768	31530	41616	86736
		FLUKA	2460	8927	39110	581301	108629
	2 / 45°	Trinkl et al.	4088	7962	19359	11783	43192
		GEANT4	3164	4915	15648	11230	34959
		FLUKA	2688	5839	17244	11565	37338
	3 / 90°	Trinkl et al.	4114	6211	11697	1981	24004
		GEANT4	3207	4096	10746	1765	19815
		FLUKA	2743	4846	10740	1799	20129
	4 / 135°	Trinkl et al.	4073	6614	10763	450	21902
		GEANT4	3406	4737	9706	272	18122
		FLUKA	2917	5341	9763	297	18320
140 MeV	1 / 0°	Trinkl et al.	1007	3043	8335	7395	19779
		GEANT4	1223	2202	7265	8621	19312
		FLUKA	694	2351	9747	12627	25421
	2 / 45°	Trinkl et al.	1251	2119	5043	3090	11504
		GEANT4	930	1388	4431	2749	9499
		FLUKA	812	1671	4931	3166	10583
	3 / 90°	Trinkl et al.	1316	1829	3572	570	7286
		GEANT4	1069	1370	3440	445	6325
		FLUKA	948	1528	3441	453	6371
	4 / 135°	Trinkl et al.	1506	2266	3882	185	7839
		GEANT4	1446	1778	3625	78	6929
		FLUKA	1154	1889	3557	90	6691
118 MeV + range shifter	1 / 0°	Trinkl et al.	505	1839	4202	2380	8926
		GEANT4	614	1372	3615	1658	7260
		FLUKA	299	1310	4715	3485	9810
	2 / 45°	Trinkl et al.	774	1660	4067	2709	9210
		GEANT4	540	1098	3876	2206	7721
		FLUKA	456	1135	3618	2411	7621
	3 / 90°	Trinkl et al.	703	1370	2574	458	5106
		GEANT4	553	959	2674	440	4628
		FLUKA	489	1000	2343	322	4157
	4 / 135°	Trinkl et al.	778	1652	3160	113	5712
		GEANT4	715	1313	3061	102	5192
		FLUKA	586	1310	2766	74	4937
75 MeV	1 / 0°	Trinkl et al.	165	384	822	401	1772
		GEANT4	212	347	910	375	1845
		FLUKA	97	280	932	480	1790
	2 / 45°	Trinkl et al.	238	313	678	278	1507
		GEANT4	189	283	770	209	1453
		FLUKA	127	222	639	247	1236
	3 / 90°	Trinkl et al.	233	302	626	49	1210
		GEANT4	218	287	667	38	1211
		FLUKA	144	239	494	33	910
	4 / 135°	Trinkl et al.	303	475	973	11	1762
		GEANT4	367	538	1047	5	1959
		FLUKA	204	362	692	7	1266

Table 4.3: Absolute secondary neutron fluence ϕ [$1/cm^2$] by Trinkl et al., GEANT4 and FLUKA for the four proton energies at the four measurement positions [234].

measurement positions motivated the further study of the detailed room model.

Contribution of room components to neutron energy spectrum Simulated neutron spectra filtered according to the considered possible neutron sources are here presented for 200 MeV (figure 4.9, figure 4.10), 140 MeV (figure 4.11, figure 4.12), 118 MeV with range shifter (figure 4.13, figure 4.14) and 75 MeV (figure 4.15, figure 4.16).

The secondary neutron spectra, decomposed by the room elements of production, demonstrate for all proton energies a correlation between energy of the neutron and the room element, especially in the fast and high neutron energy intervals between 10^{-2} MeV and 10^2 MeV.

For the 200 MeV proton field, the high-energy peak at 0° relative to the beam axis (position 1 of figure 4.4) can exclusively be attributed to neutrons from the PMMA phantom (figure 4.9a). For all four positions, the high-energy region of 10 MeV to 10^2 MeV is governed by phantom-induced neutrons, although the total magnitude is reduced for larger beam angles. The same result holds for 140 MeV (figure 4.11, figure 4.12) and 75 MeV (figure 4.15, figure 4.16).

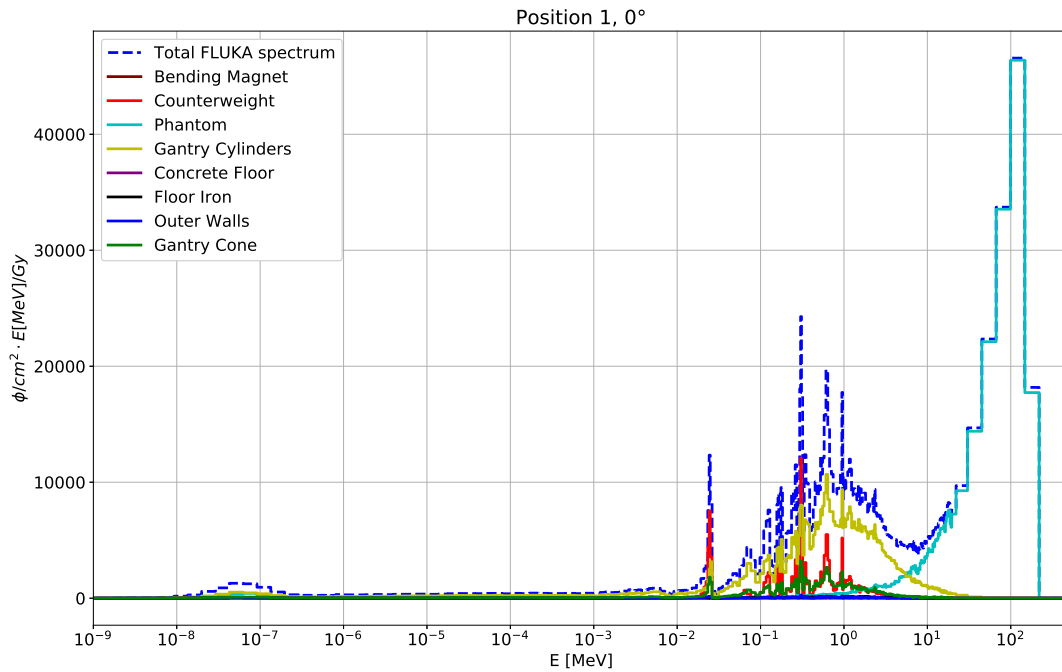
An exception is the 118 MeV field with range shifter. In the high-energy region and for all four measurement positions, the phantom contributes only up to $\approx 50\%$ (figure 4.13a, figure 4.13b). The remaining fraction, especially high for the measuring positions at 0° and 45° can be ascribed to neutrons which were generated in the range shifter - a behaviour which was expected.

In contrast, the origin of the neutrons in the fast neutron energy interval of 10^{-1} MeV to 10 MeV is more diverse. For 0° (figure 4.9a, figure 4.11a, figure 4.15a), the two consecutive gantry cylinders modelled as iron are the main source of $\approx 70\%$ contributing neutrons. The remaining fraction of $\approx 30\%$ is shared among counterweight and gantry cone. For the off-axis positions 45° , 90° and 135° , the gantry fraction reduces relative to all remaining room components, which equally contribute. Additionally, as the scoring positions are further off-axis relative to 0° , neutrons originating from the phantom dominate the fast neutron interval.

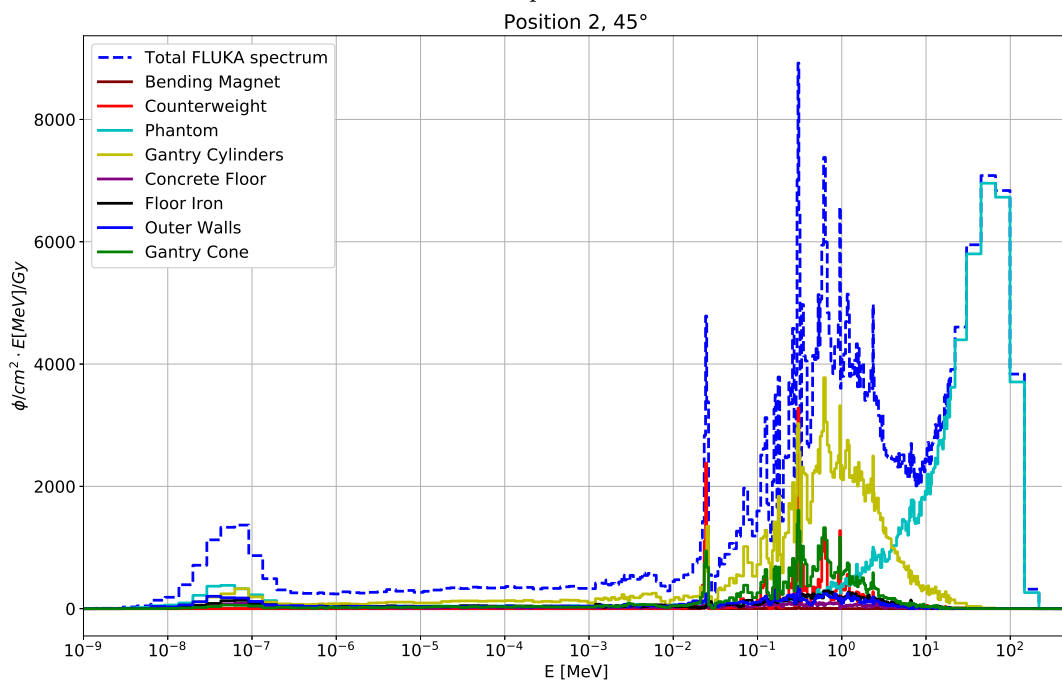
The neutrons in the thermal and epithermal neutron energy interval from 10^{-8} MeV to 10^{-1} MeV show no distinct room component as a main origin.

The contribution of the secondary neutrons originating within the concrete floor, the iron floor support plate, the bending magnet and the concrete walls individually is more than one order of magnitude lower than the total number generated across all four scorer positions.

4 SIMULATION STUDIES OF SECONDARY RADIATION IN MODERN ACCELERATION FACILITIES



(a) 0° position



(b) 45° position

Figure 4.9: Total neutron spectrum (dashed blue line) and room component spectra (solid lines) at 0° (top) and 45° (bottom) for the 200 MeV proton field.

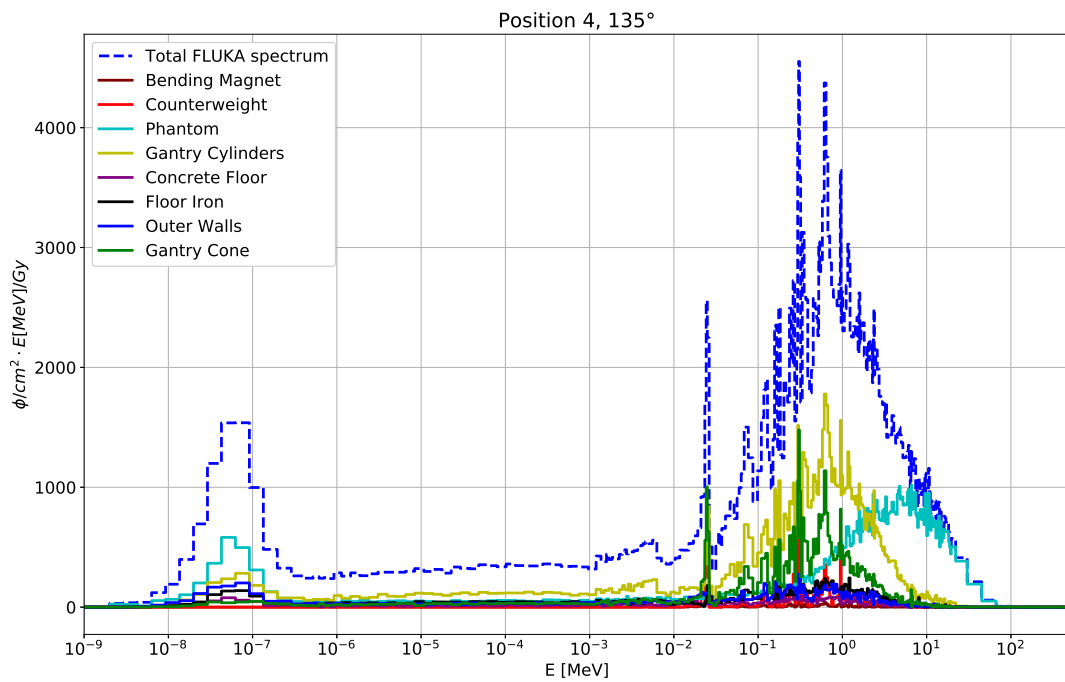
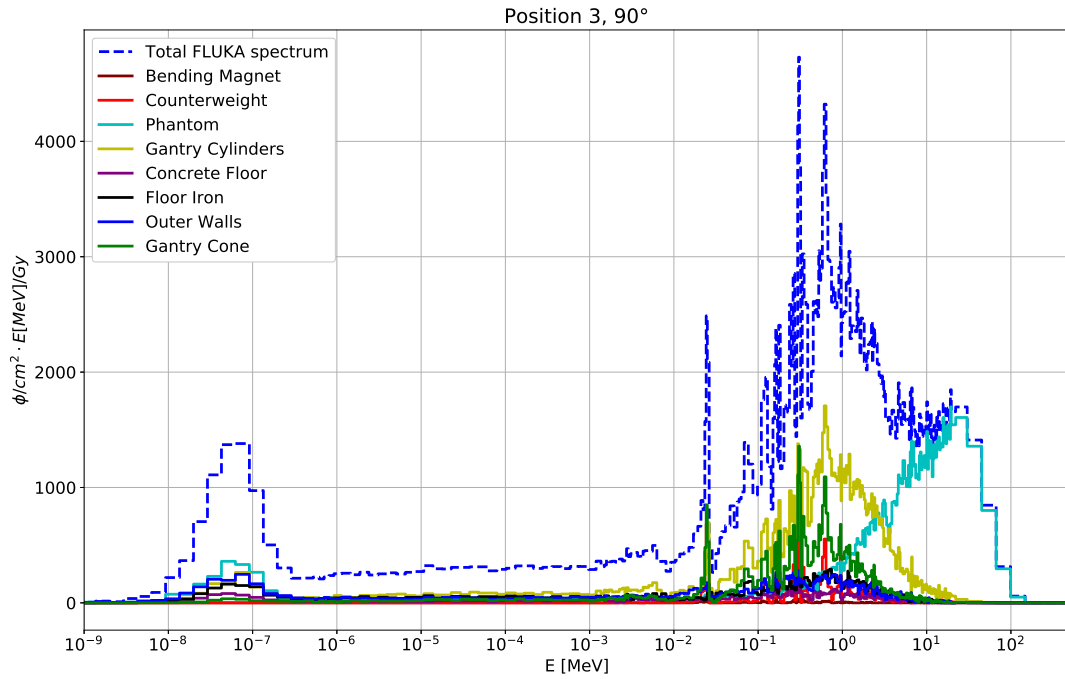
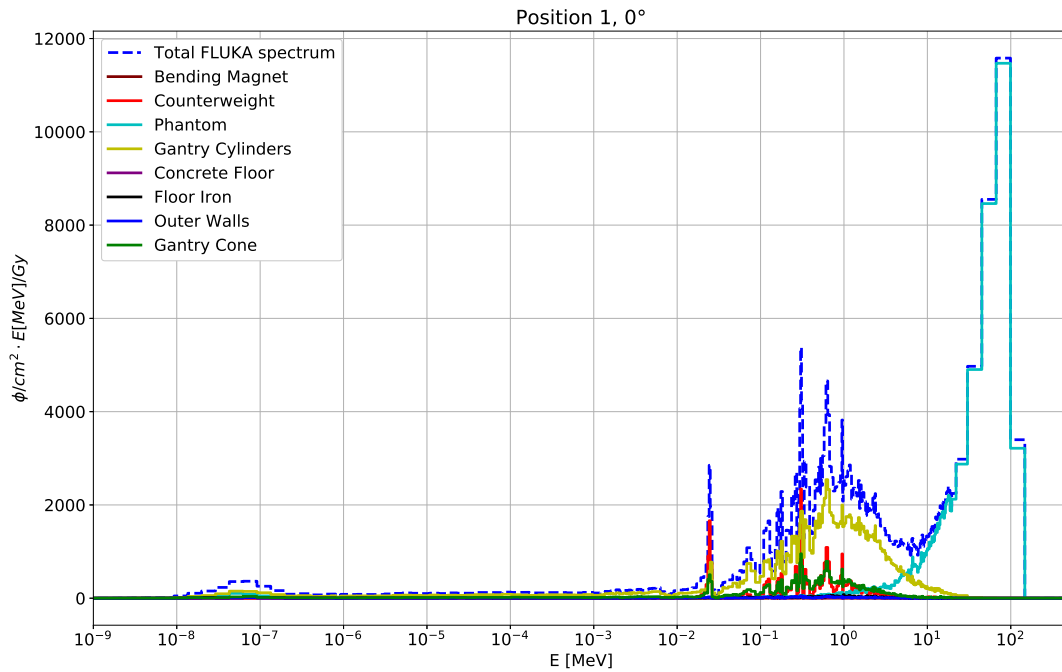
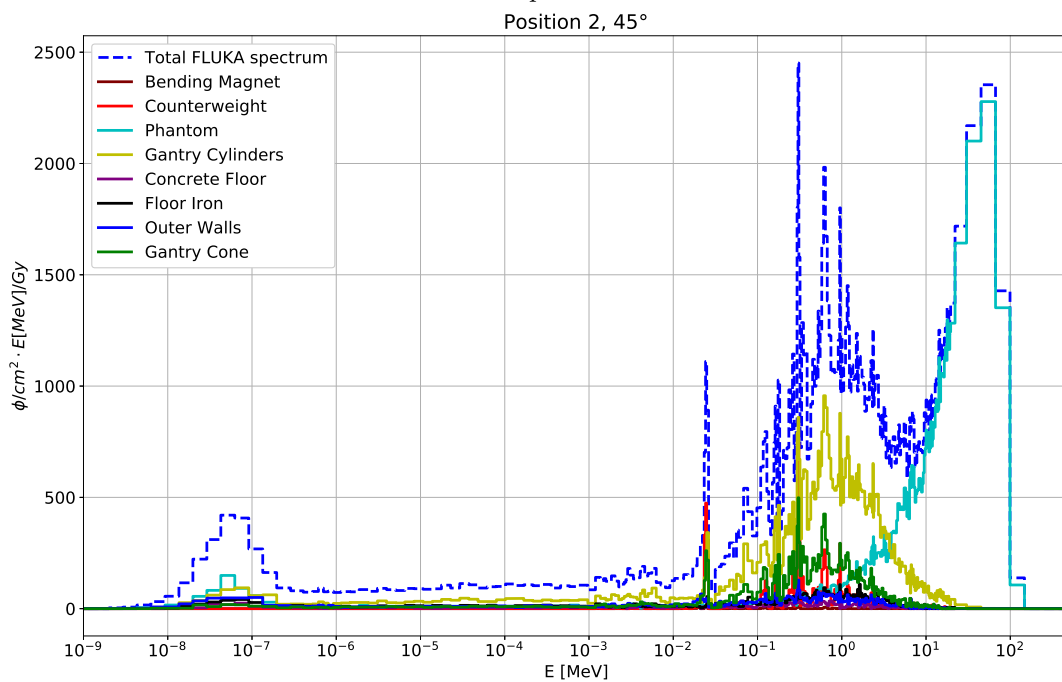


Figure 4.10: Total neutron spectrum (dashed blue line) and room component spectra (solid lines) at 90° (top) and 135° (bottom) for the 200 MeV proton field.

4 SIMULATION STUDIES OF SECONDARY RADIATION IN MODERN ACCELERATION FACILITIES

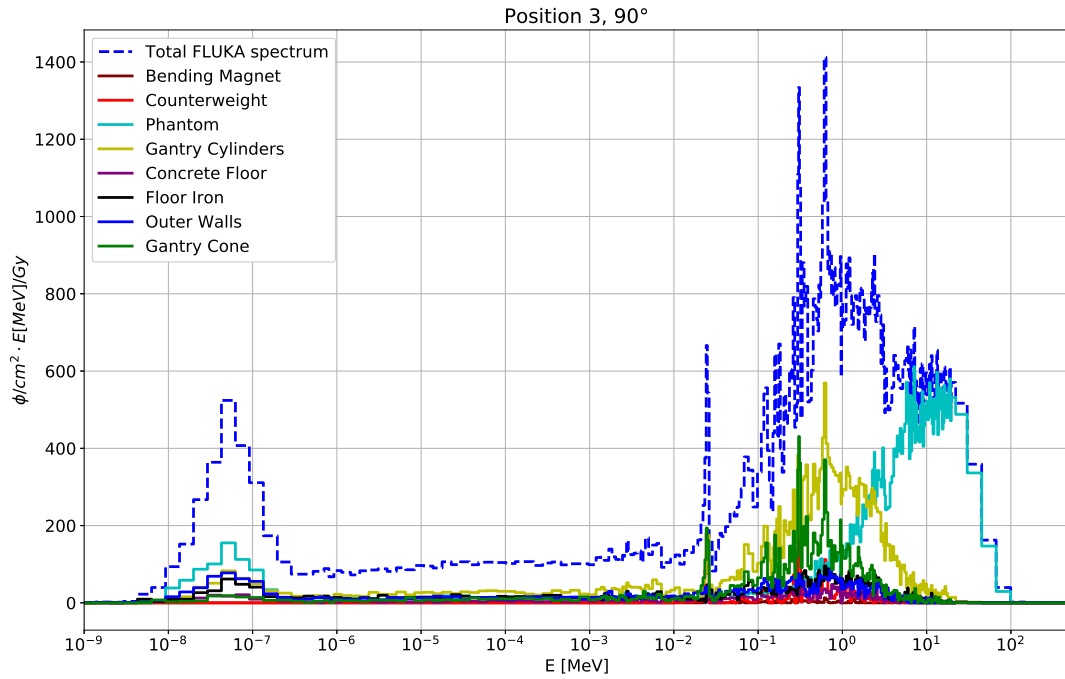


(a) 0° position

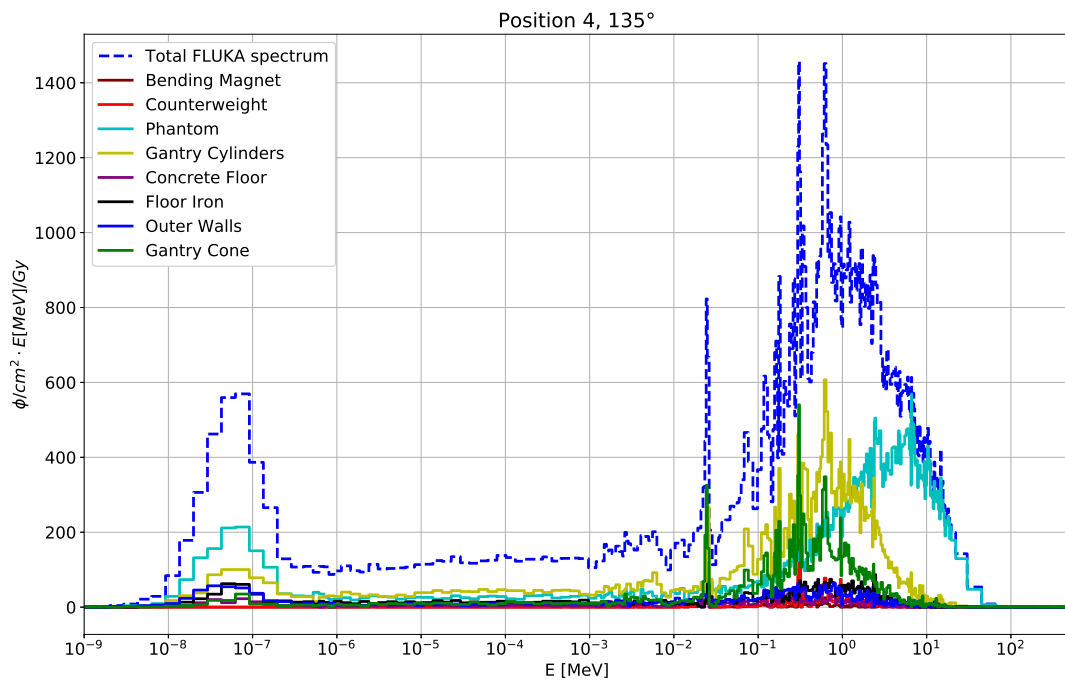


(b) 45° position

Figure 4.11: Total neutron spectrum (dashed blue line) and room component spectra (solid lines) at 0° (top) and 45° (bottom) for the 140 MeV proton field.



(a) 90° position



(b) 135° position

Figure 4.12: Total neutron spectrum (dashed blue line) and room component spectra (solid lines) at 90° (top) and 135° (bottom) for the 140 MeV proton field.

4 SIMULATION STUDIES OF SECONDARY RADIATION IN MODERN ACCELERATION FACILITIES

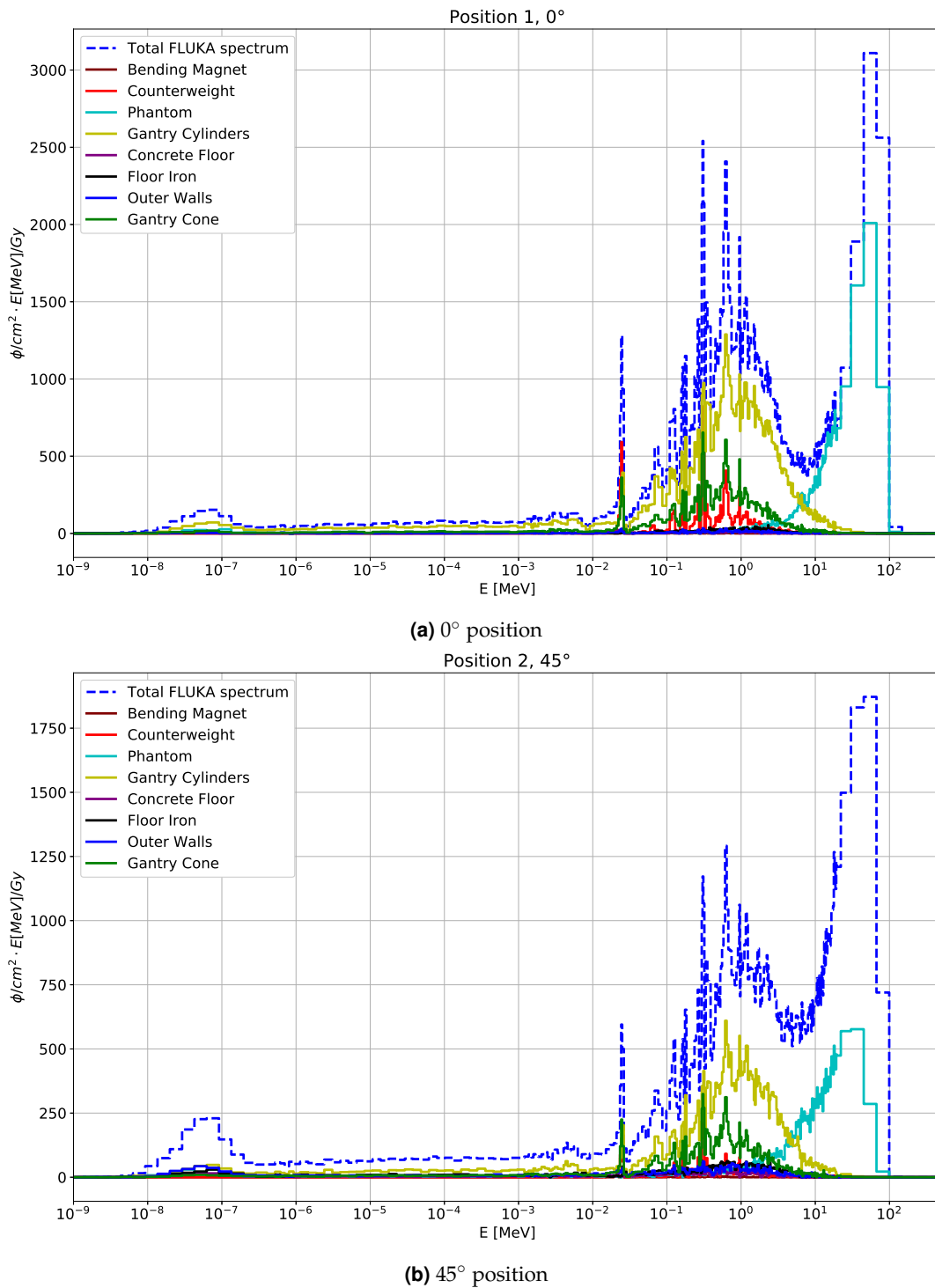


Figure 4.13: Total spectrum (dashed blue line) and room component spectra (solid lines) at 0° (top) and 45° (bottom) for the 118 MeV proton field using a PMMA range shifter of 5 cm thickness.

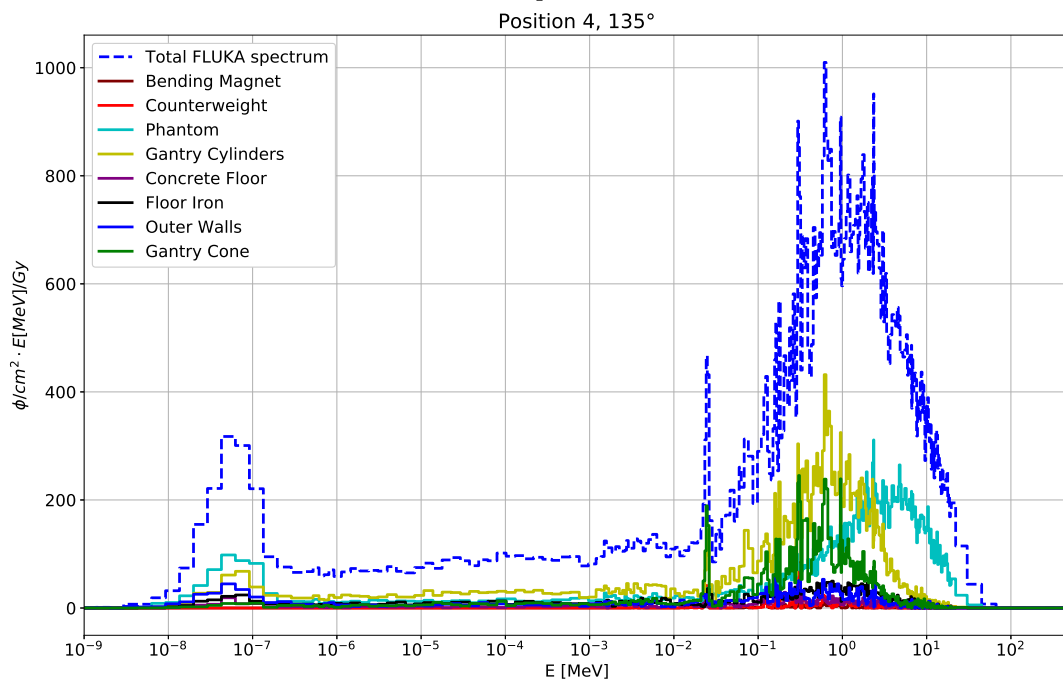
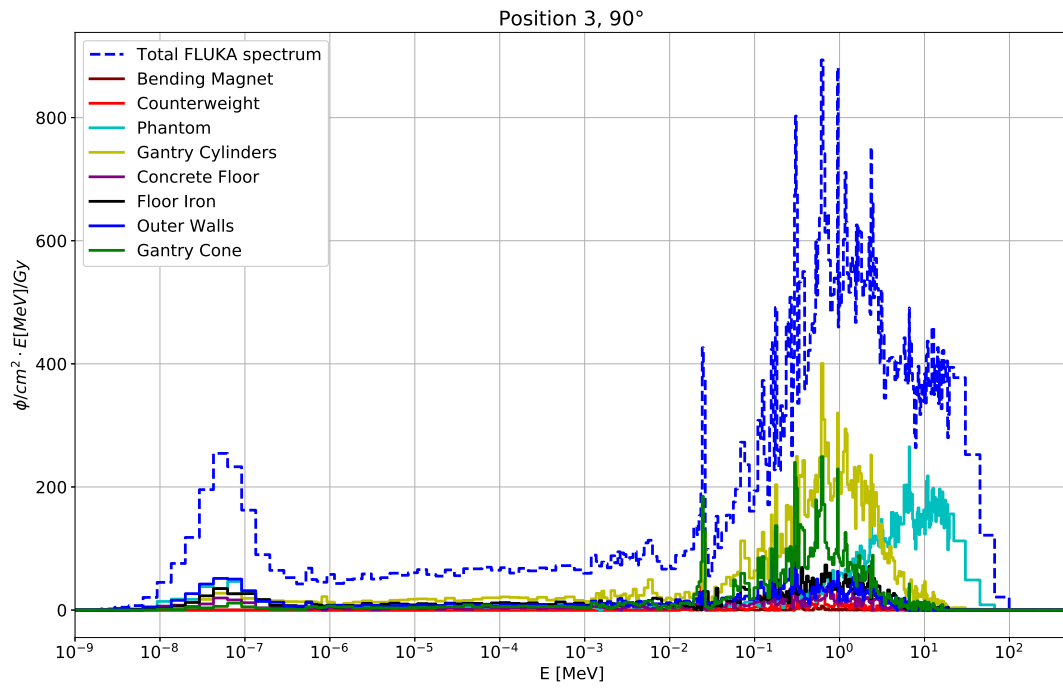
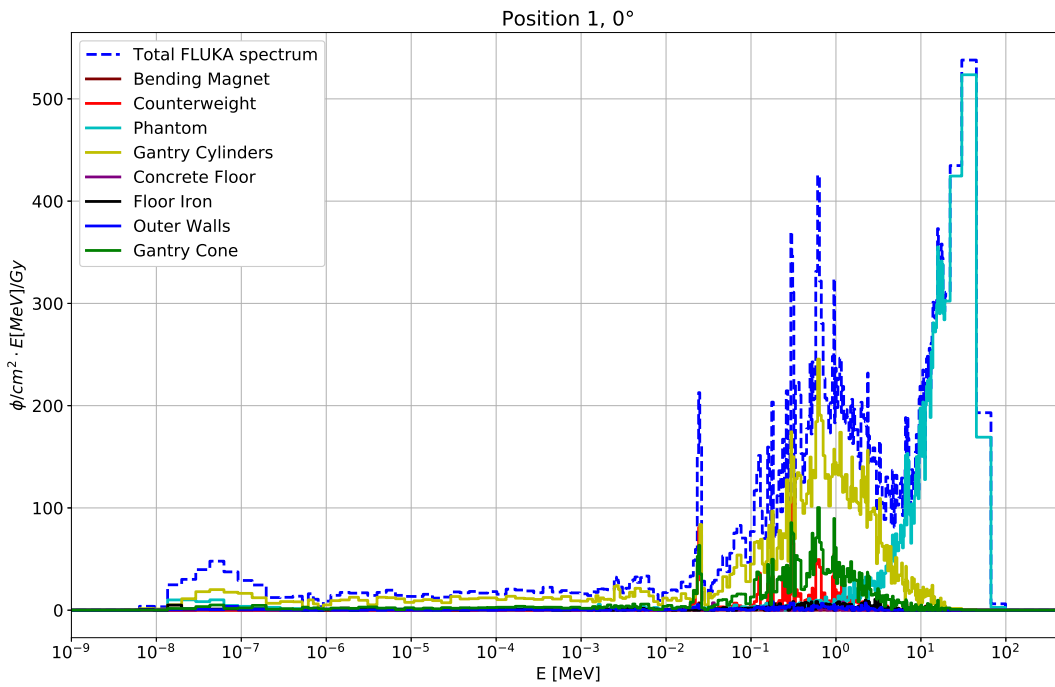
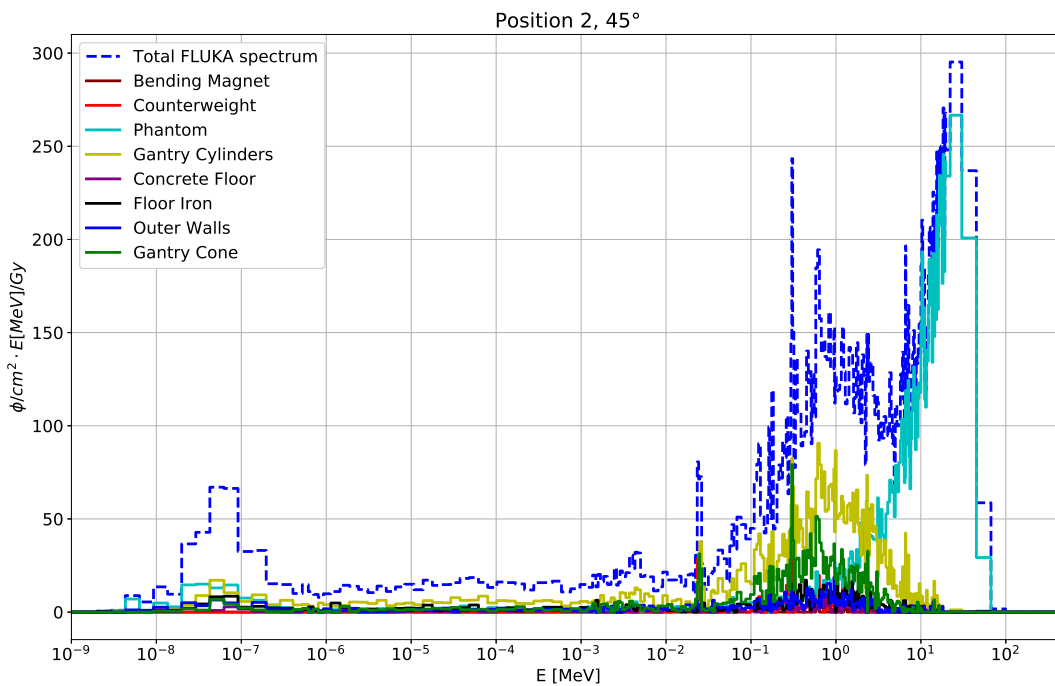


Figure 4.14: Total spectrum (dashed blue line) and room component spectra (solid lines) at 90° (top) and 135° (bottom) for the 118 MeV proton field using a PMMA range shifter of 5 cm thickness.

4 SIMULATION STUDIES OF SECONDARY RADIATION IN MODERN ACCELERATION FACILITIES

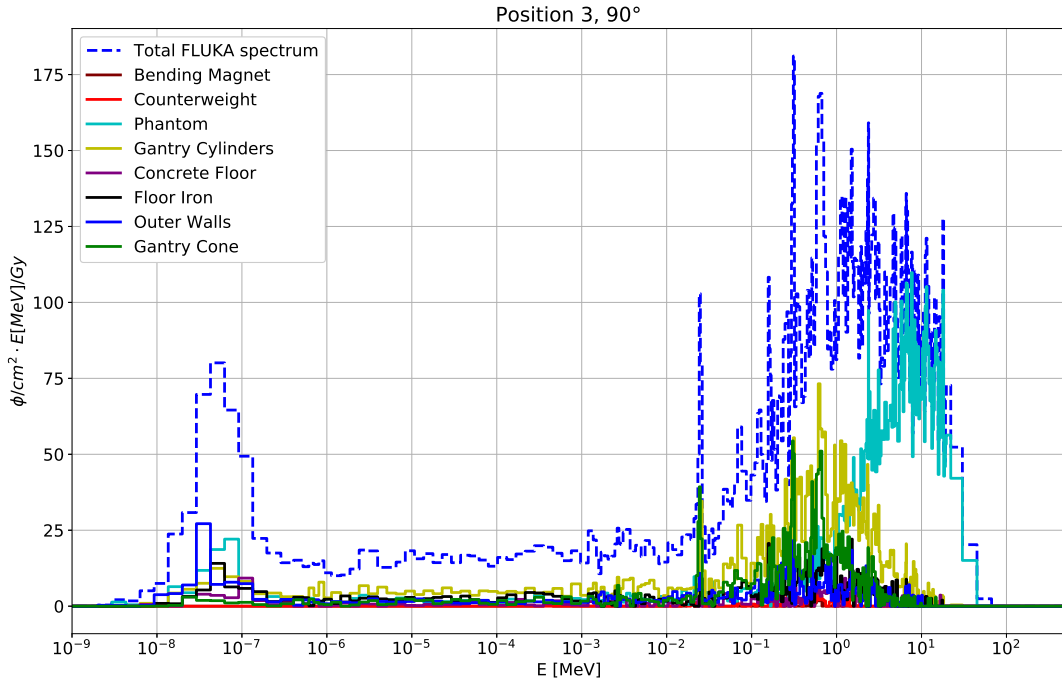


(a) 0° position

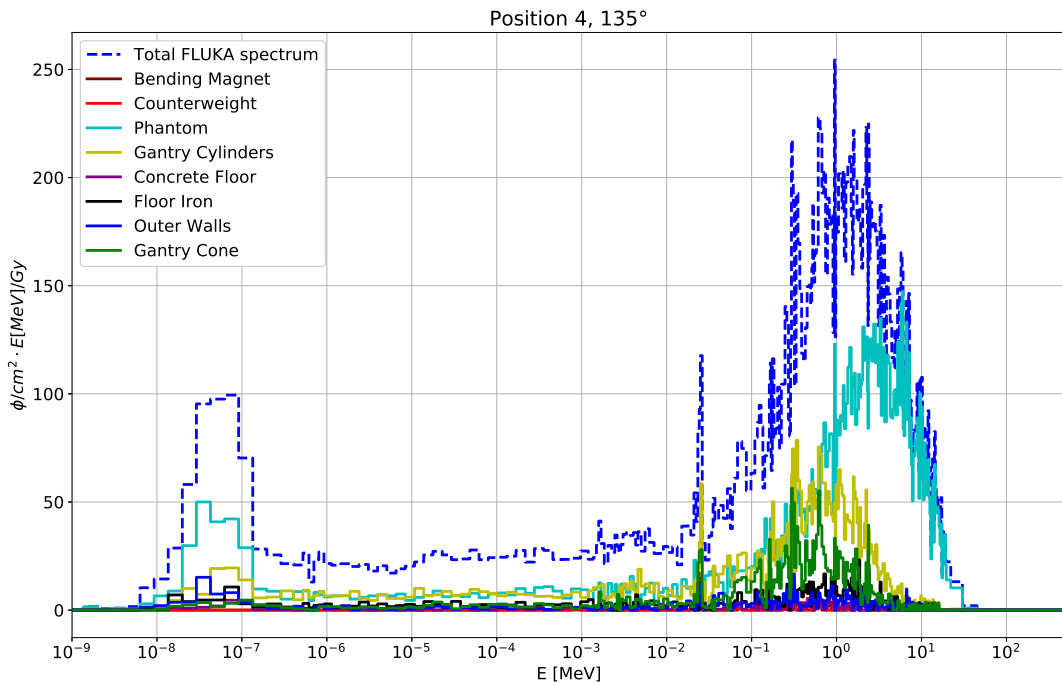


(b) 45° position

Figure 4.15: Total neutron spectrum (dashed blue line) and room component spectra (solid lines) at 0° (top) and 45° (bottom) for the 75 MeV proton field.



(a) 90° position



(b) 135° position

Figure 4.16: Total neutron spectrum (dashed blue line) and room component spectra (solid lines) at 90° (top) and 135° (bottom) for the 75 MeV proton field.

The statistical uncertainty of each component contributing to the total spectra, again evaluated in terms of the standard error of each scoring bin, was larger than for the total spectrum simulations. The best case due to larger neutron yield for the high energy and forward direction is for 200 MeV, 0°. The worst case 75 MeV, 135°, where the median of the standard errors of the bins for the spectrum of neutrons originated in the phantom is 20% and for the spectrum of the gantry cylinders 23%. Although even larger errors were found for the concrete walls or the iron floor, their absolute contribution anyway is negligible.

4.1.4 Discussion

Spectra of no room simulation versus full room simulation The measured ERBSS neutron spectra showed the evaporation peak around 1 MeV, i.e. at lower energies compared to the peak simulated spectra without room model, which indicates that the produced secondary neutrons scattered and lost energy inside the treatment room before they reached the detector. The agreement of the simulations to the measurements was improved when including the model of the relevant room components. It can be noted that for a scattering facility, Sayah et al. reported that the lack of treatment room contributions can lead to an underestimation of the simulated ambient dose equivalent $H^*(10)$ of up to 45% [196].

Comparison of all measured and simulated data for full room model Neutron spectra simulated using the room model implemented in this work, accounting for the main room components as listed in section 4.1.2 show a high energy / fast neutron peak, an evaporation peak and a thermal peak for all energies and detector positions. Depending on proton energy and measurement angle, the relative contributions of these components to the total spectrum differ.

For lateral and backward directions (90° and 135°) the high-energy peak merges with the evaporation peak. This behaviour was already experimentally reported for spot-scanning facilities [234, 66]. For all energies and forward angles, the high-energy peak amplitude exceeds the amplitudes of the evaporation and thermal peaks. Especially for the two forward directions (0° and 45°), the relative contributions of the high-energy interval can change dramatically, for example from 53.5% for 200 MeV, 0° to 1.6% for 200 MeV, 135°. The absolute fluence of thermal neutrons is similar within a factor of two for every initial proton beam energy across all four measurement positions. This was explained in the literature as isotropic scattering of the secondary neutrons from the walls [146].

The model enables reproduction of the reported ERBSS data for all four proton energies and for all four measurement positions. In particular, the fast neutron shoulder comes from the inclusion of a full room model as discussed. With the use of two different simulation codes, there is improved confidence in the reliability of the simulated room model. As a result, the origin of differences between simulation and measurement can more easily be attributed to differences in the implementation of nuclear models in FLUKA and

GEANT4. Since no severe systematic disagreement between the two simulation codes and measurements can be identified, the room model seems to be sufficiently detailed to reproduce the actual physical situation.

Identification of spectra as function of room model The results show that the neutrons contributing to the high-energy peak originate predominantly from the phantom itself while the neutrons generated in gantry cylinders and counterweight mainly contribute to the fast (evaporation) peak. A previous ERBSS measurement campaign, although without detailed modelling investigations, already presumed structures of high atomic number (high-Z) materials such as iron in forward direction, namely gantry and counterweight, to contribute to neutron production in this energy range [146].

The peaks in the evaporation region may be attributed to resonances in the total interaction cross section of iron. The detailed identification of their origin, coming hand in hand with the question for ways to reduce the evaporation neutron component for optimized facilities, will make a future study by its own. As a result, different therapy facility layouts and materials could be made. Investigations have been started to identify the origin using the following steps: a simple simulation was performed exchanging the iron of the bending magnet, the counterweight, the gantry cylinders and the low density iron gantry cone ($\rho = 2 \text{ g/cm}^3$) by titanium and low density titanium ($\rho = 2 \text{ g/cm}^3$). The result, exemplary shown for the 200 MeV proton field and the 0° position in figure 4.17a clearly shows that the substitution of iron changes the spectrum. The total spectrum remains similar in shape and magnitude. The position and magnitude of some of the sharp peaks in the spectra however change. The magnitude of neutrons in the evaporation energy range can be considered approximately to change by only some percent.

In the energy interval of evaporation neutrons, namely 10^{-2} MeV to 10 MeV, the total cross section (ENDF/B-VIII.0 dataset) for neutrons incident on iron $^{56}\text{Fe}(n,\text{total})$ may vary for example as an extreme case five orders of magnitude, between $\sigma_{tot}(24.5 \text{ keV}) = 0.024 \text{ barn}$ to $\sigma_{tot}(27.9 \text{ keV}) = 96.151 \text{ barn}$ within $\approx 3.4 \text{ keV}$ (figure 4.18a) [32]. This seems to correspond approximately to the first sharp peak present in all four simulated proton energies and positions, when approaching the evaporation region coming from the $1/E_n$ slope for the epithermal neutrons (figure 4.18b). Although for some peaks in the iron simulation spectrum a correlation can be identified to steep gradients in the iron cross sections, individual attribution seems difficult. The comparison to the simulation using titanium even strengthens this ambiguity.

The cross section dataset ENDF/B-VIII.0 was testwise rebinned to the 260 energy bins of the FLUKA multigroup transport binning (figure 4.18a). The evaporation region, magnified in figure 4.18b, gives the impression of a correlation between the spectrum resonances and the rebinned iron cross sections, but a similar correlation could be found when inspecting the results obtained with titanium.

4 SIMULATION STUDIES OF SECONDARY RADIATION IN MODERN ACCELERATION FACILITIES

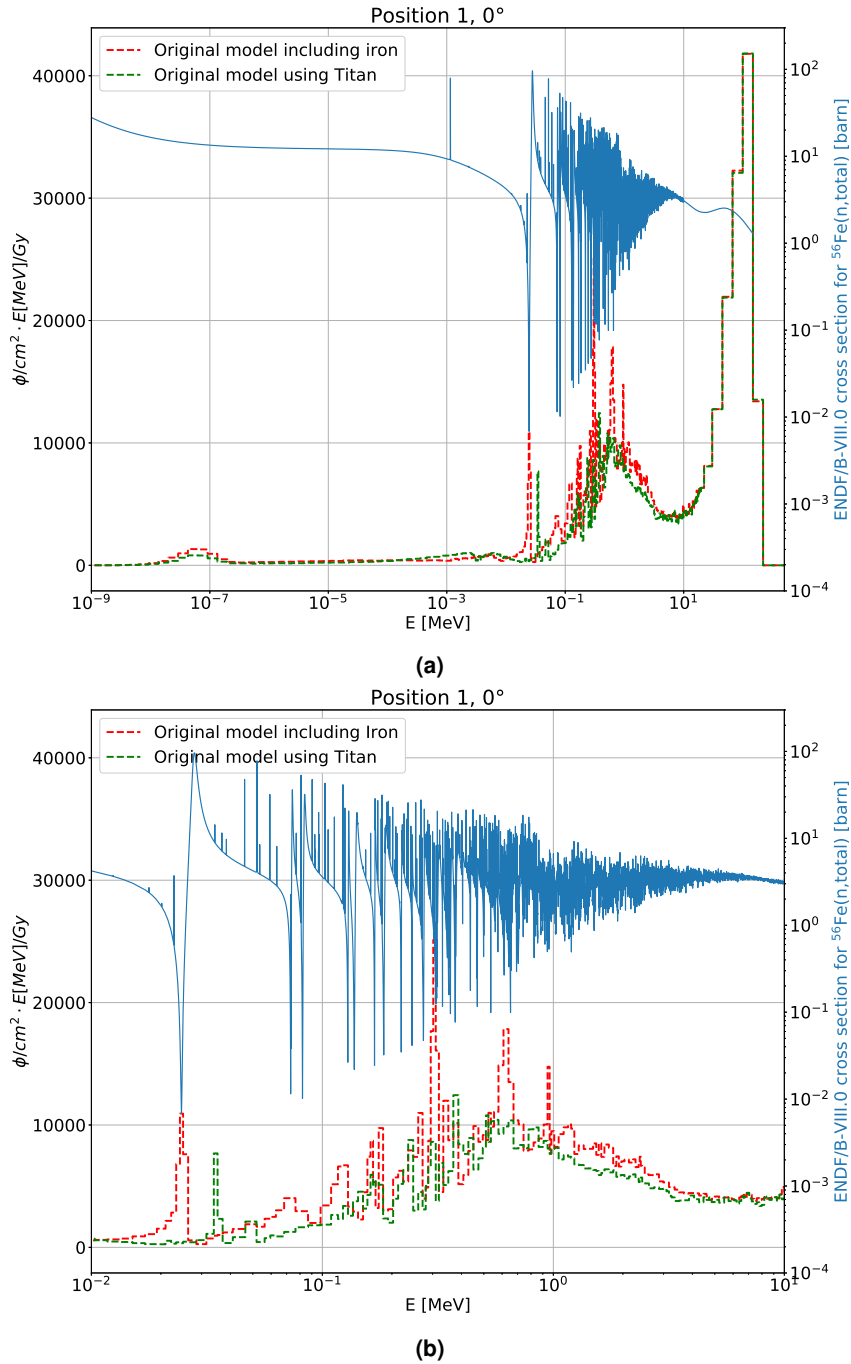
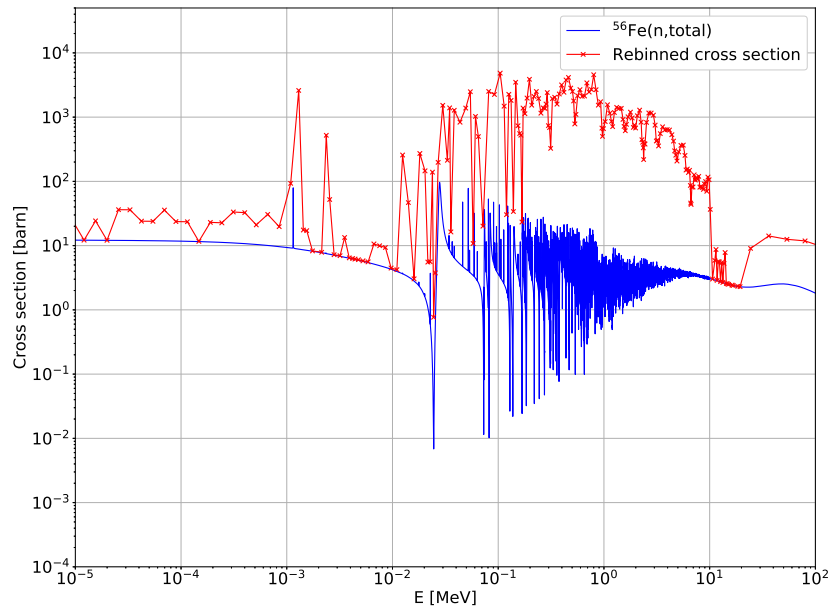
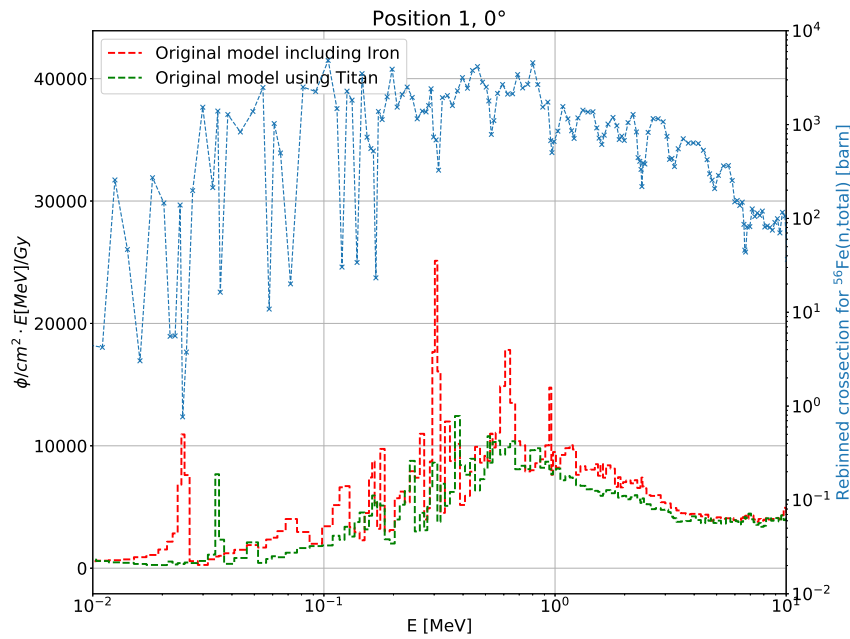


Figure 4.17: Investigation on the origin of the peaks observed in the FLUKA simulated neutron spectra using ENDF/B-VIII.0 neutron cross section data for $^{56}Fe(n, total)$ [32]. **(a)** Neutron spectra for 200 MeV protons delivered to the target, when considering the normal room model geometry and the one obtained by substituting iron by titanium, overlaid with the total cross section for neutrons in iron. **(b)** Magnification of the interval of evaporation neutron energies.

Although the nuclear structure of iron might be responsible for the peaks, a precise mapping of the energy of the peaks to the resonance peaks in cross sections is difficult. A so-



(a)



(b)

Figure 4.18: Rebinned cross section for $^{56}\text{Fe}(n,\text{total})$. (a) Original vs rebinned neutron cross section for $^{56}\text{Fe}(n,\text{total})$. (b) Magnification of the region of evaporation neutron energy.

lution could be the usage of angular resolved double differential cross sections instead of integrated cross sections (containing also elastic interactions) or cross sections of inelastic reactions with one or two neutrons only. But since the generation and propagation of secondary neutrons to the detector positions may be a multi-step process involving multiple scattering events, the certainly sharp peaks of secondary neutrons exiting iron structures may be broadened before reaching the detectors. Future isolated simulations of the room

4 SIMULATION STUDIES OF SECONDARY RADIATION IN MODERN ACCELERATION FACILITIES

components may help tackling this question.

Coming back to the general spectra descriptions, it can be noted that at all four measurement positions, the used initial beam energies of 200 MeV, 140 MeV, 118 MeV and 75 MeV show the same magnitude of thermal neutrons (table 4.3). As reported previously, these thermalized neutrons originate from high-energy neutrons, which were isotropically scattered multiple times inside the gantry room [146]. Hence, simulations lacking the treatment room failed to reproduce this spectral component (figure 4.3).

Because the neutrons in the energy range from 10^{-8} MeV to 10^{-1} MeV show no distinct room component as a main origin, the directionality of the initial emission appears to be lost. In contrast, nuclear reactions in the phantom of type $X(p, xn)Y$ directly generate the high-energy neutrons, which are emitted along the 0° beam axis and directly hit the detector at 0° (figure 4.9a). Such phantom-generated neutrons can interact in a next step via inelastic reactions of $Fe(n, xn)Fe$ with the structures of the counterweight (compared to the bending magnet located in backward direction) and the two gantry wheels, which are located in forward direction and all around the patient table, respectively (figure 4.9a and figure 4.9b). This finding corroborates the conjectures by Mares et al., who, based on ERBSS measurements, claimed that the fast neutron component originates from forward scattered neutrons interacting in the iron-rich counterweight [146]. Furthermore, at the 90° position, there are pronounced contributions in the fast neutron energy range from the bending magnet, while the contribution from the counterweight is less.

The position with 0° relative to the beam axis may also be governed by high-energy neutrons in the simulations, since the chemical composition of the PMMA phantom ($C_5H_8O_2$) exclusively is made of light elements. The disexcitation of such light nuclei ($A < 16$) in FLUKA is handled by a statistical fragmentation model of the hadron-nucleus compound (Fermi Break-up model), since the assumptions underlying the Weisskopf-Ewing model implemented in the FLUKA nuclear interaction event generator PEANUT do not hold anymore [71, 16]. The lack of evaporation neutrons from the PMMA phantom can therefore be expected, but it is expected to be small, since the emission probability for evaporation neutrons is low for light nuclei and rising with rising A [71].

Furthermore, at the 90° position, there are pronounced contributions in the fast neutron range from the bending magnet, while the contribution from the counterweight is less pronounced.

Although the contributions of the secondary neutrons generated within the concrete floor, the iron floor support, the bending magnet and the concrete walls individually are more than one order of magnitude lower than the total signal across all four scorer positions, the walls and massive components cannot be neglected in the model, because the neutrons, when generated in the gantry, are scattered multiple times in these components before reaching the scorer positions. In particular, the thermal peak at energies between 10^{-9} MeV and 4×10^{-7} MeV would be lost if omitting these components.

4.1.5 Conclusion

The present study has confirmed a strong dependence of the secondary neutron field on the angle of observation and incident proton beam energy as discussed in recent publications. The comparison of the simulated neutron spectra produced by geometrically well defined, monoenergetic proton fields with measured ERBSS neutron spectra around a homogeneous PMMA target have shown that a room model, although simplified, is needed to understand the origin of secondary neutrons in general and their energy dependence in particular. The results of this study, which was based on a systematic investigation of production of secondary neutrons from monoenergetic protons at defined geometries, may be generalized in that they can provide an estimation of neutron fields, even at spot-scanning facilities where detailed neutron measurements and simulations cannot be performed. Due to the unavoidable uncertainties from ERBSS measurement unfolding, as well as due to the heterogeneity of nuclear models, used cross sections and code discrepancies over 13 orders of magnitude of neutron energies between different Monte Carlo codes, a cross comparison of the used codes, FLUKA and GEANT4, has been useful.

Identification of the neutron origin has shown that iron-rich room components such as the gantry cylinders, the gantry cone and the counterweight contribute most to the evaporation energy interval in the room geometry. However, massive iron structures are needed for the stability in the whole beam gantry system, which in turn enables reaching the required sub-mm precision of the proton beam. The usage of MC simulations would be beneficial for the design of future PBS gantry rooms to investigate options for the reduction of secondary neutrons, also the concept of upright seated proton treatments may be feasible for certain indications without using heavy gantry structures [76]. Such simulations could influence the decisions on gantry construction material or structure, for example on the choice of massive gantry versus a bird-cage gantry-like structure.

Finally, the presented data can help in including the secondary neutron field in analytical treatment planning systems in order to predict the out-of-field neutron dose to organs far from the treatment field. This is already under investigation for scattering facilities, where a personalized estimate of organ specific neutron equivalent dose may eventually guide medical physicists to create treatment plans which feature reduced risk of late adverse effects [126, 127, 51].

4.2 Radiation protection studies for novel laser particle sources at the Centre for Advanced Laser Applications

4.2.1 Introduction

As introduced in section 3.3.5, the *Centre for Advanced Laser Applications* (CALA) is intended for laser-based acceleration of electron beams for brilliant X-ray generation (*Laser-driven Undulator X-ray Source* experiment (LUX), *Electron and Thomson Test Facility* experiment (ETTF), *Source for Powerful Energetic Compact Thomson Radiation Experiments* experiment (SPECTRE)) and laser-driven nanosecond bunches of protons and heavy ions (*Laser-driven Ion Acceleration* experiment (LION), *High Field* experiment (HF)) for the investigation of the laser-driven acceleration and application of high-energy protons and ions.

The ionizing radiation emerging from the experiments when using the up to 2.5 petawatt laser pulses with < 25 fs duration will be mixed particle species of high intensity, high maximum energy as well as broad in the energy spectrum and short pulsed. This poses new challenges on shielding and monitoring compared to conventional radiation protection:

- The mixed particle species nature of the bunches impedes the usage of conventional particle specific shielding concepts, since e.g. neutrons are well shielded using hydrogen rich materials such as plastics, whereas high material densities or Z are needed for electrons or photons (chapter 2).
- Conventional radiation protection mazes are designed such that the particles need to undergo at least two scatters to escape the room. Such designs, which avoid straight penetrations as straight paths, cannot be applied in CALA, since the optical laser pulses need to enter the experimental caves through straight penetration holes. Their diameter is large in order to lower the power density on the laser mirrors below their damage threshold. CALA uses holes of 40 cm diameter for the beamline.
- Electronic / online measurement of doses from high-energy particle bunches of ns duration is technically challenging. The performance of ionisation chambers such as the *RAM ION DIGILOG* portable ionisation chamber (Rotem Industries, Israel) is under evaluation, since such online measurements are favorable for experiments with 1 Hz repetition rates compared to offline detectors as TLDs or radiochromic films.

As part of the legal regulations, the areas in the CALA building have to be categorized in the four radiation protection categories, based on the predominant prompt *ambient dose equivalent rate* (simply called dose rate here) to be expected [33]:

Access classification	Color in scheme	Ambient dose equivalent limits for CALA [$\mu\text{Sv}/\text{h}$]
Unclassified Zone	■	< 0.5
locally tolerable		< 2
Supervised Zone	■	< 2.5
locally tolerable		< 7.5
Controlled Zone	not existing in CALA	-
Exclusion Zone	■	> 2.5

Table 4.4: Ambient dose equivalent rate limits for radiation protection areas in CALA. The color scheme refers to figure 3.12

- *unclassified* area
- *supervised* area
- *controlled* area
- *exclusion* area

The upper radiation dose rate limits for these zones were defined in agreement with the *Bavarian Agency for the Environment* (Bayerisches Landesamt für Umwelt LfU) as the Bavarian authority responsible for operation permissions for accelerators. The values are listed in table 4.4.

Personal electronic dosimeters, as required by law in *controlled* radiation protection areas have been reported to be unusable due to under response for bunches of ms duration [33, 26, 110, 27]. Controlled areas have therefore to be avoided by design of sufficient shielding in CALA.

In the CALA radiation protection scheme displayed in figure 3.12, the north and south corridors and the southern lab are the only *unclassified* zones. The radiation dose rate limit in an *unclassified* zone is $0.5 \mu\text{Sv}/\text{h}$, in order to ensure an accumulated dose of less than 1 mSv per year, assuming a 2000 h annual occupancy. A local maximum of about $2 \mu\text{Sv}/\text{h}$ is tolerable if monitored and/or not accessible.

All experimental caves, the air space above them and the experimental hall were categorized as *supervised* areas. The CALA design goal for *supervised* areas was a dose rate $< 2.5 \mu\text{Sv}/\text{h}$, assuming a 2000 h annual occupancy. Within a *supervised* zone, local dose rates were allowed to reach $7.5 \mu\text{Sv}/\text{h}$. The locations should be then made inaccessible or marked with warning signs. When the laser is in operation in a cave, then that particular cave is classified as an *exclusion* zone, while all the other caves remain *supervised* zones. There is no upper dose rate limit specified in excluded zones, as long as the dose rate limit in surrounding *supervised* and *unclassified* zones is not violated.

Since the laser can only be active and hence generate radiation in one cave at once, 2000 h per year is already a really conservative estimate. 2000 h per year would be equivalent to

4 SIMULATION STUDIES OF SECONDARY RADIATION IN MODERN ACCELERATION FACILITIES

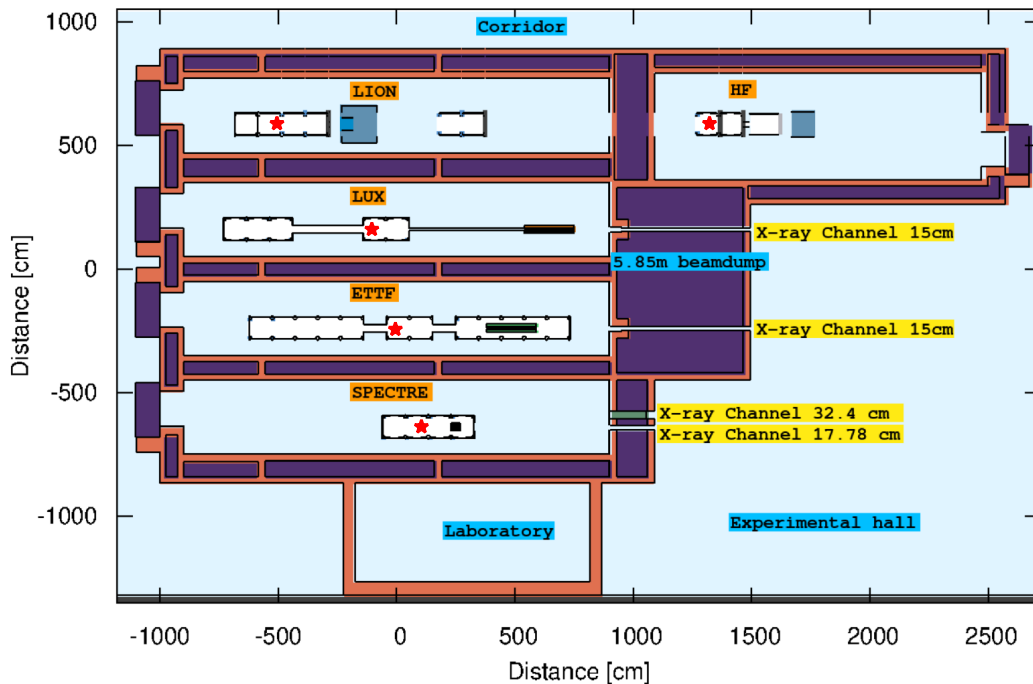


Figure 4.19: Layout of the CALA geometry model implemented in FLUKA. The 2D cross section was taken at the height in which the laser impinges onto the targets (called *bunch height*). These positions are indicated with a red star in each cave and the beams are propagated in general eastwards. The vacuum chambers (white areas) as well as the LION (gray-blue) and HF beam dumps (gray box) are also shown. The yellow labels indicate critical locations where the laser-generated primary radiation (e.g. X-rays) can leave the caves through cylindrical pipes and be used in the experimental hall.

a weekly occupancy of ≈ 38.5 h for a single cave.

Detailed dose rate estimations from Monte Carlo simulations can provide the insight necessary to categorize the local radiation exposure, especially since the envisioned particle source terms are still subject of active research and have not yet been reached experimentally.

Here the results of Monte Carlo simulations for the ETTF, LUX and SPECTRE caves of different source configurations in terms of prompt dose rates, with respect to the established dose limits, are reported. The modelling considerations and results of HF and LION are briefly discussed.

4.2.2 Material and Methods

The motivation and envisioned experiments are given in section 3.3.5. The geometrical description of the building, the surrounding areas and the caves along with their content for each of the five caves, relevant to this radiation protection investigation, is provided.

The FLUKA general purpose Monte Carlo code was used to model the five experimental caves of CALA. The model includes walls, doors, roof, vacuum chambers, spectrometer magnets and beam dumps, the experimental hall for X-ray experiments and unclassified areas such as transport floors. The vacuum pipes for the laser and other chamber content have not been included in the model. Figure 4.19 shows a horizontal cross sections of the detailed geometry model at the height level, where the laser pulses from the driving lasers (ATLAS or PFS-pro) are impinging on the target. .

CALA facility layout The five caves corresponding to the five CALA experiments are arranged around a central beamdump of 5.85 m thickness (figure 3.12). Due to the design of the CALA facility, the walls of the experimental caves, the roof and the floor as well as the central beam dump are the critical components shielding the exterior or the other experimental areas.

To the north side of the caves, a transportation corridor runs adjacent to the LION and HF cave. East of the central beamdump follows the *experimental hall* which will host X-ray cabins for X-ray experiments. South of the SPECTRE cave, another laboratory with is located, where possibly working personnel could be present during operation. The west side of all caves is the entrance corridor.

The walls, roof and cave doors consist of magnetite concrete (orange in figure 4.19) and magnetite aggregate of various water content (purple in figure 4.19) in a sandwich-like structure between either concrete or steel container walls. The inside is filled with at least 50 cm Magnetite, which contains around 1% of water. The ceiling of the caves is a 90 cm layer of magnetite aggregate containing around 2% water and was filled in to rectangular steel profile bars. The floor, which shields the groundwater from the radiation produced in the experimental caves, is made of 75 cm standard Portland cement of density $\rho = 2.30g/cm^3$. Such technically easy to realize sandwich-like construction was used for radiation protection buildings previously [74]. For CALA, the magnetite was compacted to a density of $\rho = 4t/m^3$, and allowed for thinner shielding walls at less cost. The used magnetite filling without cementitious interconnectionis sustainable, since it can be reused after the operation of CALA will have ended, in contrast to regular heavy concrete [74].

All caves (except of HF) are 18 m long, 3 m wide and 4.25 m high. The shorter HF cave is 13.81 m long, 4.3 m wide and 4.25 m high. A false floor is placed at 1 m above the concrete floor in all caves. Holes of 20 cm radius in the walls, allowing for the laser pulses from ATLAS or PFS-pro to enter the experimental caves (called laser penetration holes), are located 50 cm below the false floor. These holes are locations where dose can potentially leak outside of the experimental caves and are of particular interest for radiation protection.

Movable steel doors of 1 m thickness filled with magnetite aggregate seal the entrance to the caves during experiments.

4 SIMULATION STUDIES OF SECONDARY RADIATION IN MODERN ACCELERATION FACILITIES

	Particle type	Energy spectrum [MeV]	Spectral shape	Full divergence angle [mrad]	Charge / pulse [nC]	Shot frequency [Hz]
LION	^{12}C	10 - 400 /u	Box	180	0.016	1
	p^+	10 - 200	Box	180	0.16	1
	e^-	10 - 1000	e^{-x}	$10^3 / E[\text{MeV}]$	1.6	1
HF	^{197}Au	1 - 10 /u	Box	200	0.016	1
	^{12}C	10 - 200 /u	Box	200	0.016	1
	p^+	10 - 200	Box	200	0.16	1
	e^-	10 - 1000	e^{-x}	$10^3 / E[\text{MeV}]$	1.6	1
LUX	e^-	5000		2	1	1
	e^-	10 - 5000	Box	2	1	1
ETTF	e^-	5000		2	1	1
	e^-	10 - 5000	Box	2	1	1
SPECTRE	e^-	70		10	0.025	1000
	e^-	500		10	0.25	1
	e^-	10 - 500	Box	10	0.5	1

Table 4.5: Simulated particle source parameters of the five experiments in CALA: LION and HF [87, 4, 115, 61] as well as LUX and ETTF [50, 3, 240] are seeded by ATLAS-3000. SPECTRE can, in addition to ATLAS 300, be seeded by PFS-pro.

Due to the high power density of the laser pulses, the interaction between pulse and solid or gas target is performed in high vacuum ($\mathcal{O}(10^{-6}$ mbar)). Above the false floor, the caves contain hence vacuum chambers, which are depicted as white boxes in figure 4.19. The cubic chamber modules ($1.21 \times 0.98 \times 1 \text{ m}^3$) are made of 2.5 cm aluminium plates mounted on steel frames and are connected to the beamline vacuum pipe system. Each chamber weighs 1.2 tons.

Simulated sources As sources for the LUX, ETTF and SPECTRE simulations, electron bunches ($< 5 \text{ GeV}$) were simulated using spectra, divergences and bunch-charges based on expectations from latest published literature in ion and electron acceleration using high power lasers [195, 3]. As lower spectral cut-off, a value of 10 MeV was chosen. Photon-neutrons are present for electron energies above 8 MeV for out-of-field radiotherapy dose simulations. For laser-driven electron acceleration the generated particle beam is very directional, with a divergence of typically one mrad [49]. The angular pointing jitter is of a similar order and thus approximated using a fixed value (table 4.5). For the electron sources, kinetic energies of 2.7 GeV have been reported using 300 TW pulses in 2015 [3]. Optimistic upper boundaries were chosen for the simulations, since such upper boundaries account for the most challenging scenarios in terms of radiation protection and are hence a conservative estimate. These simulated optimistic upper boundaries have mostly not experimentally been achieved so far.

For proton acceleration, a 2013 experimental campaign at the TRIDENT laser at Los Alamos National Laboratory claims to have raised the 2011 published record of 67.5 MeV to 160 MeV [195, 1]. The results are under discussion. For the LION and HF simulations, it is thus mentioned for completeness that energies for protons up to < 200 MeV, ^{12}C ions of up to < 400 MeV/u and ^{197}Au ions of < 10 MeV/u were used in this work.

Characteristics of the sources used in the CALA radiation protection for all five caves are summarized in table 4.5.

Laser-driven Ion Acceleration (LION) cave layout The FLUKA geometry of the LION cave and HF cave, as well as their beamdumps, were initially modelled and optimized by Dr. George Dedes in a joint collaborative effort with the author.

Since the LION experiment produces high-energy proton and ions beams, intended to be also used inside the cave, the outside of the cave needed to be shielded from the electrons driving the acceleration, as well as neutrons. Electrons at the same energy are able to penetrate orders or magnitude deeper than protons (section 2.3). The details and results of the shielding optimisation of LION and HF are discussed as a part of the corresponding publication by the author [55].

On its south side the LION cave borders with the LUX cave and on the east side with the HF. On the north and west side it adjoins the north corridor and the entrance hall to the experimental areas, respectively.

Walls of 1.0 m-1.2 m thickness are employed in order to keep the dose rates outside the cave below the designated levels. The wall in forward direction towards east is 2 m thick and shields the HF cave during beam operation in LION. Three laser penetration holes are running through the north wall between the corridor and the LION cave (figure 3.12) and the south wall between the LION and the LUX cave (figure 4.20b).

The cave model contains a set of four vacuum chambers for the acceleration experiment and two for offline tests without ATLAS (figure 4.19). All vacuum chambers without magnets in all five caves are implemented as replicas of one master model using the FLUKA lattice command. The target foils are located 232 cm above the concrete floor (level of figure 4.19).

A dedicated, hybrid beam dump was designed using the FLUKA model for LION with the purpose of stopping the beam and containing as much as possible of the primary and secondary particles fluence and dose. The details of the optimisation by Dr. Dedes are found in the paper [54]. The size of the beam dump is $1.5\text{ m} \times 1.5\text{ m} \times 1.5\text{ m}$. It is made of heavy concrete, except for a cubic volume of $0.5\text{ m} \times 0.5\text{ m} \times 0.5\text{ m}$ filled with water. The water tank is placed in the middle of the beam dump on the vertical and horizontal dimension and starts at the front face of the beam dump.

High Field Physics (HF) cave layout Although not further studied here, the description of the HF cave is given to enable comparison to the LION and electron caves.

4 SIMULATION STUDIES OF SECONDARY RADIATION IN MODERN ACCELERATION FACILITIES

On its south side, the HF cave borders with the experimental hall for X-ray experiments outside the ETTF and LUX cave and the central beam dump. On the west side the LION cave is behind the 2 m thick wall. On the north and east side it adjoins the north corridor and the entrance hall to the experimental areas, respectively. The lower south-west edge of the HF cave was suspected to be potentially suffering from electron leakage through the 5.85 m beamdump from the LUX cave (figure 4.20a).

Two vacuum chambers are connected by a 25 cm long pipe ($r = 15.9$ cm) to a special chamber for the HF experiment ($0.85 \times 0.8 \times 1.25$ m³). Since the purpose of HF is similar to LION - protons and heavier ion acceleration - the HF beam dump is similar. The heavy concrete beam dump is $1 \text{ m} \times 1 \text{ m} \times 1 \text{ m}$ and stops the ion bunches and secondary particles, which are emitted 227 cm above the concrete floor.

The outside walls of HF are 1 m thick. Two laser penetration holes are running through the north (corridor - HF) wall.

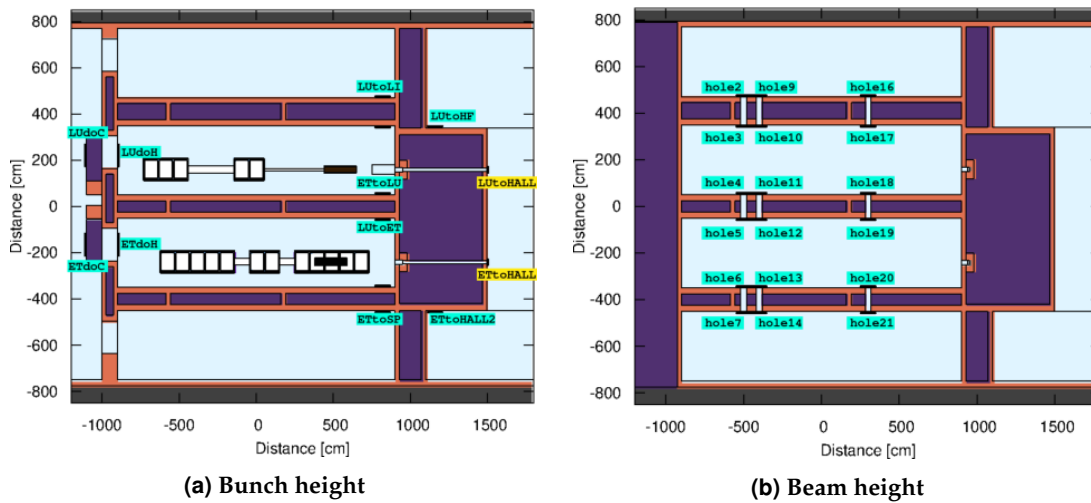


Figure 4.20: Illustration of the two height levels of USRTRACK scorers (turquoise / yellow) used for LUX and ETTF: The *bunch height* where the laser pulse strikes the target and the *beam height* where the laser pulse enters the caves through the laser penetration holes in the walls.

Laser-Undulator X-ray source (LUX) cave layout On its north side, LUX is separated from LION by a 1.2 m wall. On its south side it borders the ETTF cave via a 1 m wall and the east side of the cave terminates with the central 5.85 m thick beam dump (figure 4.19). Three laser penetration holes are running through the north and three through the south walls (figure 4.20b).

Two vacuum chambers for laser preparation are connected by a 3 m long pipe ($r = 35$ cm) to three chambers for the interaction of laser pulse and gas target. The interaction happens 220 cm above the concrete floor and the produced radiation propagates to the

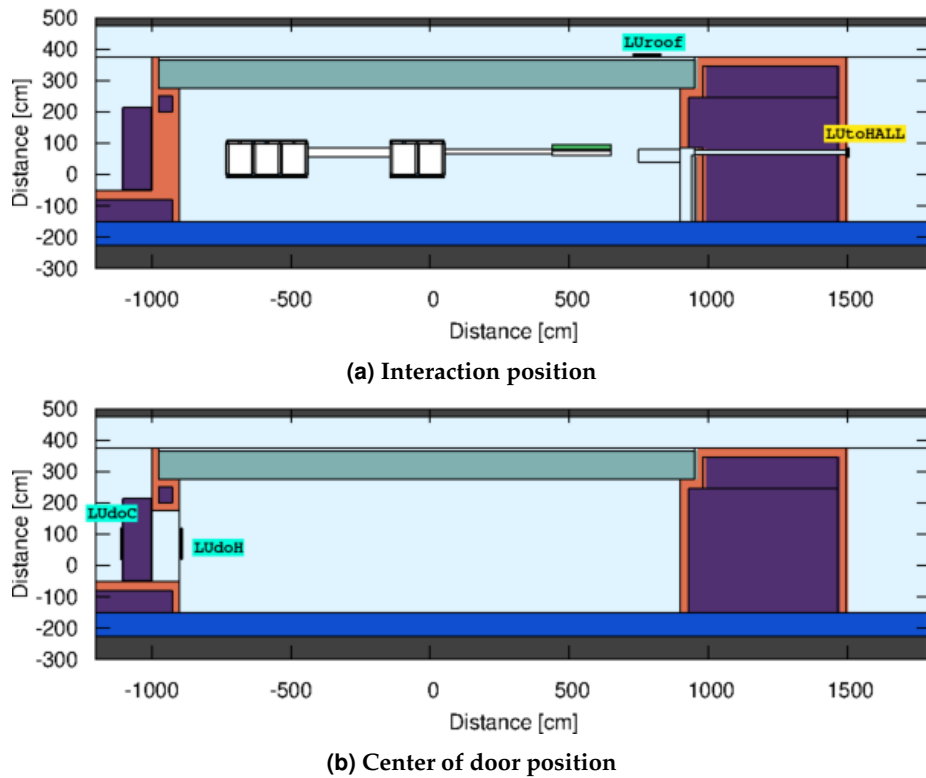


Figure 4.21: Additional to the bunch and beam height detectors depicted in figure 4.20, scorers are placed on the LUX roof, after the LUX X-ray channel in beam-dump and around the movable door.

east towards the 5.85 m beam dump (figure 4.20a). A 2.1 m long permanent magnet ($B = 0.85$ T) follows 4.87 m after the chamber (figure 4.21a). The magnet serves as diagnostic spectrometer for the electron energies and as a radiation protection device by bending the electrons down into the 5.85 m beam dump. The electron bunches will be emitted 220 cm above the concrete floor.

The generated X-rays pass the magnet travelling straight and may traverse the beam dump through a cylindrical 7.5 cm radius channel which is on axis with the laser propagation. The X-ray cabins in the experimental hall for LUX, ETTF and SPECTRE have not been included in the model.

Electron Thomson Test Facility (ETTF) cave layout On its north side, ETTF borders with LION and south with SPECTRE, both separated from ETTF by a 1 m thick wall. Like LUX, the east end of the cave is the 5.85 m beam dump with a $r = 7.5$ cm radius cylindrical channel for X-rays. Three laser penetration holes of the same dimensions as for LUX are running through the north and through the south walls (figure 4.20b).

Three sets of chambers (five and two and five chambers in each set) connected by pipes were implemented into the geometry model (figure 4.19). The interaction point of the laser pulse and the target is located 220 cm above the concrete floor and the electron

4 SIMULATION STUDIES OF SECONDARY RADIATION IN MODERN ACCELERATION FACILITIES

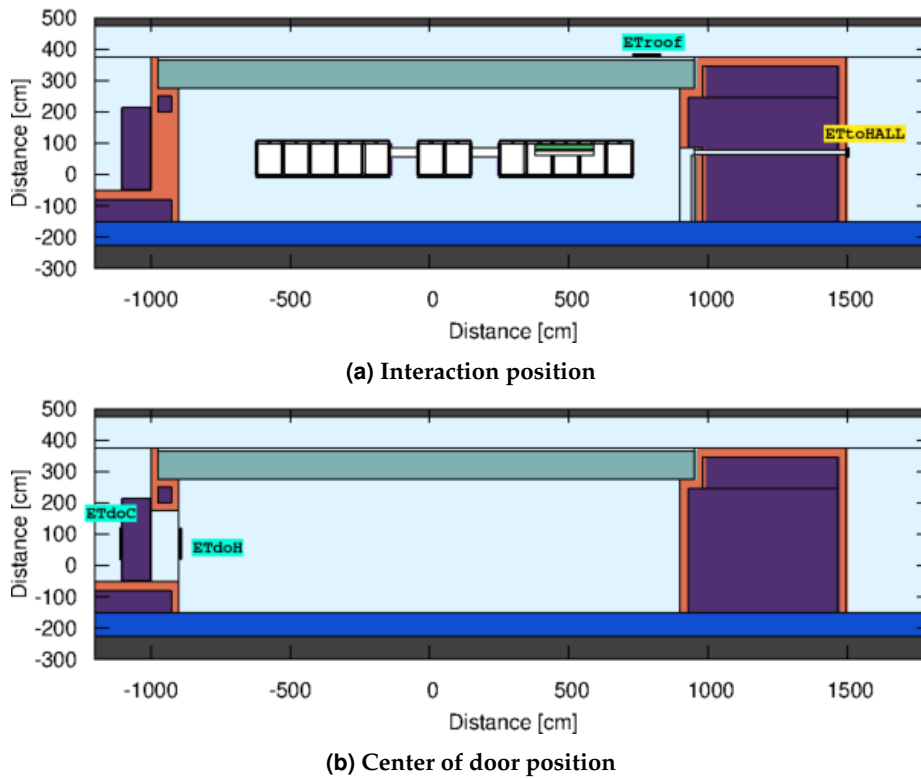


Figure 4.22: Additional to the bunch and beam height detectors depicted in figure 4.20, scorers are placed on the ETTF roof, after the ETTF X-ray channel in beam-dump and around the movable door.

bunches propagate eastwards. The last set of chambers hosts the same 2.1 m permanent magnet ($B = 0.85$ T) as in LUX. The chambers hosting the magnet are for LUX, ETTF and SPECTRE explicitly modelled and do not use the FLUKA lattice command. The magnet again is used for electron energy diagnostic and as a radiation protection device by bending the electrons down. The back-panel of the last ETTF chamber has a deepening of 10 cm width and 52 cm height, which leaves 3 mm of the 2.5 cm aluminium thickness and is aligned with the interaction height, in order to have a thinner material budget to interact with the broadband electron beam. This *extraction window* has been included respecting suggestions on the chamber stability with the mechanical engineering department and according to first FLUKA simulations.

For one special experiment only, the magnet will be removed, causing the 5 GeV beam to be directly aiming at the X-ray penetration hole in the central 5.85 m beam dump (compared to the situation in figure 4.22a). In order to keep the experimental hall dose within the legal dose rate limits, the channel will be shielded using lead bricks before and after the channel.

The choice how to practically shield in that case the outside of the cave was evaluated using the FLUKA simulations presented here. Different available so called *radiation protection bricks* made of graphite and lead in the industrial standard size of 5 cm \times 10 cm \times 15 cm were studied. An initial guess was to shield the inside side (*hot*

side) of the X-ray channel using graphite and the outside (*cold side*) side using lead. Compared to lead ($Z = 82$), the lower atomic number of graphite ($Z = 6$) should have been able to reduce the amount of bremsstrahlung photons after the brick and inside the X-ray pipe by scattering the electrons into the central 5.85 m beamdump. The argument is the cross section dependence on Z via $\sigma \propto Z^2$. The cold side of the beamdump is shielded using lead, in order to best absorb any showered photons and neutrons. The best shielding result and hence the final simulations for the authorities use 50 cm lead bricks on both the hot and cold side of the beamdump.

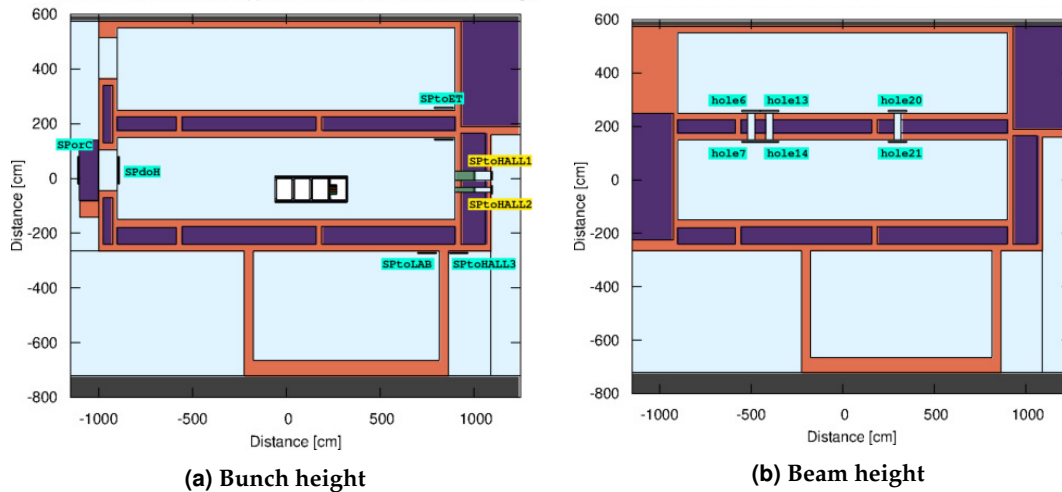


Figure 4.23: Two height levels of USRTRACK scorers (turquoise / yellow) used for SPECTRE, analog to figure 4.20. The two X-ray holes in the east wall are plugged with steel bars.

Source for Powerful Energetic Compact Thomson Radiation Experiments (SPECTRE) cave layout On its north side SPECTRE borders with ETTF and on the south with a laboratory, both separated from SPECTRE by 1 m thick walls. The north wall has three laser penetration holes (figure 4.23b). The east wall of 1.9 m thickness shields the experimental hall from radiation created in SPECTRE and has two cylindrical holes to allow for the extraction of the X-rays in future experiments (figure 4.24a). For most experiments, the two holes will be plugged with bars made of S235JR steel. Only the 70 MeV source, operated with up to 1 kHz, will be experimentally operated with the 17.78 cm channel open, in order to allow generated X-rays to enter the experimental hall.

A set of four chambers is installed and uses a 40 cm permanent magnet ($B = 0.85$ T) for electron energy diagnostic and radiation protection (figure 4.24a). All was properly modelled in FLUKA.

The particle bunches are emitted 219.5 cm above the concrete floor and propagate to the east towards the 5.85 m beam dump.

4 SIMULATION STUDIES OF SECONDARY RADIATION IN MODERN ACCELERATION FACILITIES

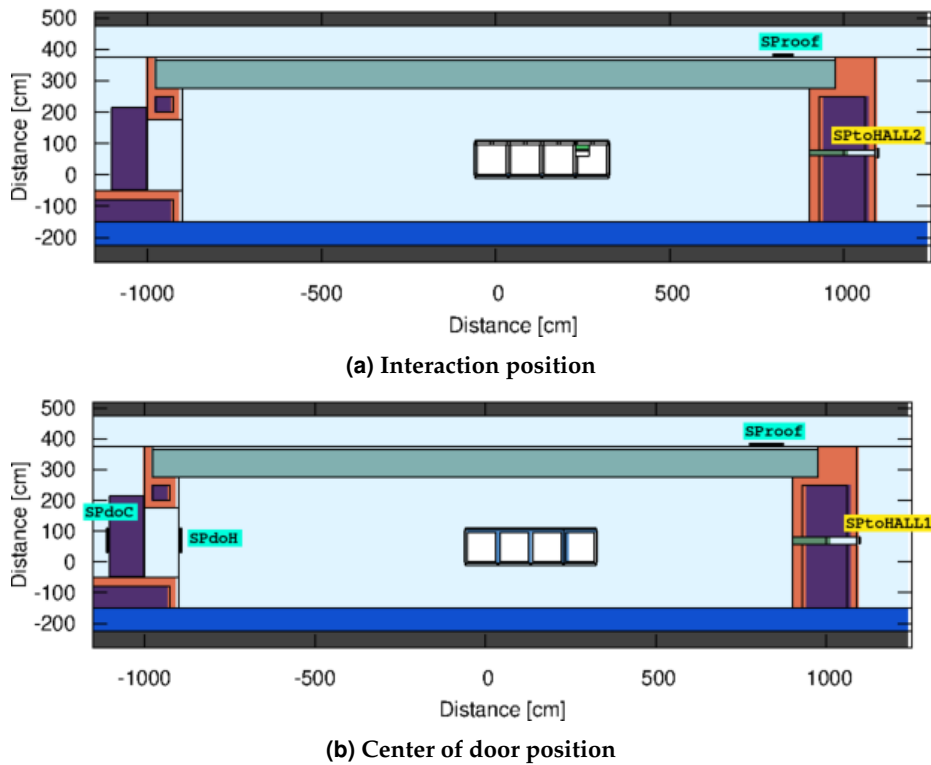


Figure 4.24: Additional to the bunch and beam height detectors depicted in figure 4.23, scorers are placed on the SPECTRE roof, after the plugged two SPECTRE X-ray channels in the east wall and around the movable door.

FLUKA Settings All radiation protection calculations for CALA were performed with the FLUKA Monte Carlo code version FLUKA2011.2x.2.

The FLUKA default settings *PRECISION* were chosen in the input files for all simulations. The low-energy transport cut-offs were chosen to transport all particles down to residual ranges, which are small compared to the geometry dimensions: neutrons were transported down to thermal energies, electrons down to 1.5 MeV, photons to 1 keV and all other particles down to 100 keV. The additional FLUKA option EMF was used to request a detailed transport of electrons, positrons and photons.

The simulations were performed using the 15 node high-performance computing cluster available at the *Department of Medical Physics* of the LMU, for which the author previously developed and tested the software and settings for FLUKA simulation and job scheduling [53]. Each node provided up to 16 parallel hyperthreads. For each simulation, $20 \cdot 10^6$ primary particles were simulated in using up to 200 parallel threads. The available computing resources allowed a set of simulations to be completed within two days. For statistical significance of the results, the total of $3 \cdot 10^9$ primary particles and approximately one year of computing time for a single CPU were hence used.

For the dosimetric evaluation of the results, the ambient dose equivalent $H^*(10)$ in units of pSv/primary particle was scored in a three dimensional cartesian mesh (USRBIN

Cave	e^- - energy [MeV]	Charge/bunch [nC]	Annual occ- upancy [h]	number of e^- per bunch	Factor $pSv/e^- \rightarrow \mu Sv/h$
LUX	5000	1	2000	6.24×10^{-9}	2.25×10^{-7}
	10 - 5000	1	2000	6.24×10^{-9}	2.25×10^{-7}
ETTF	5000	1	2000	6.24×10^{-9}	2.25×10^{-7}
	10 - 5000	1	2000	6.24×10^{-9}	2.25×10^{-7}
SPECTRE	70	0.025	2000	1.56×10^{-8}	5.62×10^{-8}
	500	0.25	2000	1.56×10^{-9}	5.62×10^{-6}
	10-500	0.5	2000	3.12×10^{-9}	1.12×10^{-7}

Table 4.6: Listing of electron source parameters used to convert FLUKA fluxes from $\phi / (\text{cm}^2 \cdot \text{primary})$ to ϕ / cm^2 and FLUKA dose rates from $pSv / \text{primary}$ to $\mu Sv / h$.

scorer) inside and outside the caves, using a voxel size of $10 \text{ cm} \times 10 \text{ cm} \times 10 \text{ cm}$. To allow for a detailed investigation of the geometrical distribution of different particle contributions to the total dose, also the dose from the primary source particles, electrons, neutrons, photons, muons and protons was individually scored.

At critical locations, where elevated doses were expected from the geometry (e.g. holes, short distance to the laser-target interaction), the dose equivalent was also scored in cylindrical air volumes of mostly 50 cm radius and 5 cm thickness (e.g. figure 4.20b for the laser pipe level below the false floor). The locations of these cylindrical USRTRACK scorers are indicated in figure 4.20 - figure 4.24, bearing the scorer name. In turquoise are indicated scorers with 50 cm radius and in yellow with radii of 15 cm to 32.4 cm, depending on the size of the hole preceding them (figure 4.20b and figure 4.23b).

Dose rate limits The radiation doses are required to be expressed as equivalent dose rates in units of micro-Sievert per hour ($\mu Sv/h$) in order to compete with the limits set by the authorities. The dose rates scored using FLUKA equivalent dose scorers in USRBIN and USRTRACK report the doses in pSv per simulated primary source particle. A conversion factor was thus established, using the conservative annual occupancy estimate of 2000 h for each cave (table 4.6).

4.2.3 Results

The quantitative evaluation of the USRTRACK scorers inside and outside the simulated caves and for the considered sources are collected in table 4.7, table 4.8 and table 4.10. Dose rates are presented separately for the contribution of neutrons, photons and electrons, together with the total value. Missing contributions to the dose rate included to a lower extend heavier ions or other charged particles, but in some cases a significant amount of dose rate generated by muon production.

4 SIMULATION STUDIES OF SECONDARY RADIATION IN MODERN ACCELERATION FACILITIES

The simulation results in general showed that, due to the locally high particle fluence ($\approx 10^{10}$ particles / cm^2) in a cave during operation, the dose rate can exceed 1.5 kSv/h (figure 4.25). A visual inspection of the 3D USRBIN scorers revealed that the peak dose rate occurred for each cave in the respective beam dump, since the radiation fields for all caves were strongly directional in forward direction. The scorers *LUdoH*, *ETdoH* and *SPdoH*, which are located inside the caves, give a feeling of the dose rate inside the caves in backward direction and are located in front of the sliding doors (figure 4.20a, figure 4.23a). Dose rates higher than $10 \mu\text{Sv/h}$ were present in large sections of each cave during operation of the laser in that specific cave (figure 4.26).

Depending on the cave in operation and the beam dump geometry there, different critical points were identified by graphical inspection of the USRBIN meshes. These critical points were in general located either behind open holes (vacuum pipes) or behind walls, but in positions where high fluences of particles were directed. The dose from particles escaping a cave and inside a specific cave during operation are quantified using the cylindrical USRTRACK scorers in tables 4.7 - 4.10. Dose rates above the dose rate limit are highlighted as red bold numbers in the tables.

All estimated dose rates listed in tables 4.7 - 4.10 entail statistical uncertainties. These uncertainties were strongly dependent on the absolute dose rate and on the particle fluence in the location under consideration. For calculated dose rates higher than $1 \mu\text{Sv/h}$, the statistical uncertainty ranged from 1% to 9%, with a mean value of 6%. For calculated dose rates between $0.1 \mu\text{Sv/h}$ and $1 \mu\text{Sv/h}$ the statistical uncertainty ranged from 1% to 40%, with a mean value of 15% and statistical uncertainties above 20% associated to dose rates below $0.5 \mu\text{Sv/h}$.

LUX The simulation results in table 4.7 summarize the dose rates at various positions outside the LUX cave for the two different electron spectra listed in table 4.5.

Since the primary source consists of highly penetrating electrons, the total dose rate is reported alongside with the individual contributions from neutrons, γ -rays and electrons.

For most scoring positions and for both the monoenergetic (5000 MeV) and the broad energy spectrum (10 – 5000 MeV), the neutron dose rate was found to be the highest contribution to the total dose rate. The calculated dose rates from the broad spectrum electron source were mostly lower than the corresponding ones from the monoenergetic 5 GeV electron beam and always lower than the $2.5 \mu\text{Sv/h}$ design limit.

For the 5 GeV monoenergetic electron source, at all positions, except for the critical location behind the channel of the central beam dump (*LUtoHALL*), the dose rate was kept below the $2.5 \mu\text{Sv/h}$ design limit. At that particular location, the dose rate calculated was $6.95 \mu\text{Sv/h}$, which is still below the $7.5 \mu\text{Sv/h}$ maximum local dose rate limit for the experimental hall.

The scorers *hole16* and *hole19*, which are closest to the beamdump eastwards, stay com-

	Dose rate limit [$\mu Sv/h$]	Detector position	Dose rate [$\mu Sv/h$]				
			n	γ	e^-	Total	
LUX	2.5	LUroof	7.64×10^{-1}	1.16×10^{-2}	4.27×10^{-3}	7.95×10^{-1}	
	2.5	LUtoLI	1.45×10^{-1}	3.43×10^{-3}	0.00	1.49×10^{-1}	
	2.5	LUtoET	8.51×10^{-1}	1.15×10^{-2}	8.43×10^{-3}	9.13×10^{-1}	
	2.5	LUdoC	1.36×10^{-1}	9.72×10^{-4}	0.00	1.37×10^{-1}	
	2.5	LUtoHF	1.69	2.60×10^{-2}	8.02×10^{-3}	1.82	
	2.5	LUtoHALL	7.49×10^{-1}	8.11×10^{-2}	6.08	6.94	
	5 GeV	2.5	hole2	7.35×10^{-2}	2.41×10^{-3}	0.00	7.59×10^{-2}
		2.5	hole5	7.45×10^{-2}	1.47×10^{-2}	2.79×10^{-3}	9.19×10^{-2}
		2.5	hole9	6.40×10^{-2}	4.94×10^{-3}	0.00	6.89×10^{-2}
		2.5	hole12	1.14×10^{-1}	1.15×10^{-2}	5.79×10^{-3}	1.31×10^{-1}
2.5		hole16	3.71×10^{-1}	4.55×10^{-2}	7.73×10^{-3}	4.25×10^{-1}	
2.5		hole19	7.86×10^{-1}	4.64×10^{-2}	5.71×10^{-3}	8.42×10^{-1}	
-		LUdoH	21.35	3.02	1.48	26.41	
LUX	2.5	LUroof	4.66×10^{-1}	5.60×10^{-3}	9.76×10^{-4}	4.72×10^{-1}	
	2.5	LUtoLI	4.20×10^{-2}	1.25×10^{-3}	1.83×10^{-2}	6.51×10^{-2}	
	2.5	LUtoET	3.88×10^{-1}	5.95×10^{-3}	3.08×10^{-15}	3.94×10^{-1}	
	2.5	LUdoC	7.04×10^{-2}	1.05×10^{-3}	3.36×10^{-6}	7.14×10^{-2}	
	2.5	LUtoHF	6.29×10^{-1}	1.18×10^{-2}	0.00	6.87×10^{-1}	
	2.5	LUtoHALL	5.52×10^{-2}	2.76×10^{-2}	2.31	2.40	
	Broad	2.5	hole2	8.84×10^{-2}	3.97×10^{-3}	5.46×10^{-4}	9.45×10^{-2}
		2.5	hole5	1.49×10^{-1}	2.92×10^{-3}	2.59×10^{-3}	1.54×10^{-1}
		2.5	hole9	2.36×10^{-2}	4.30×10^{-3}	6.82×10^{-4}	2.86×10^{-2}
		2.5	hole12	8.17×10^{-2}	6.32×10^{-3}	4.51×10^{-3}	9.25×10^{-2}
2.5		hole16	2.66×10^{-1}	1.72×10^{-2}	6.78×10^{-3}	2.90×10^{-1}	
2.5		hole19	3.05×10^{-1}	2.77×10^{-2}	8.63×10^{-3}	3.44×10^{-1}	
-		LUdoH	12.35	2.10	1.33	16.14	

Table 4.7: Dose rate calculations for LUX, at critical locations indicated in figure 4.20 and figure 4.21. The upper half of the table lists results for the 5 GeV monoenergetic electron source, while the lower half holds for the broad spectrum electron source.

parable between mono- and polyenergetic case and do not rise for the polyenergetic simulation.

ETTF The simulation results in table 4.8 summarize the dose rates at various positions outside the ETTF cave for three experiments: the broad spectrum electron source with the spectrometer magnet in place (10 – 5000 MeV) and a 5 GeV monoenergetic electron source with the spectrometer magnet and without the spectrometer magnet.

Since the primary electron source term is the same as in LUX and therefore consisting

4 SIMULATION STUDIES OF SECONDARY RADIATION IN MODERN ACCELERATION FACILITIES

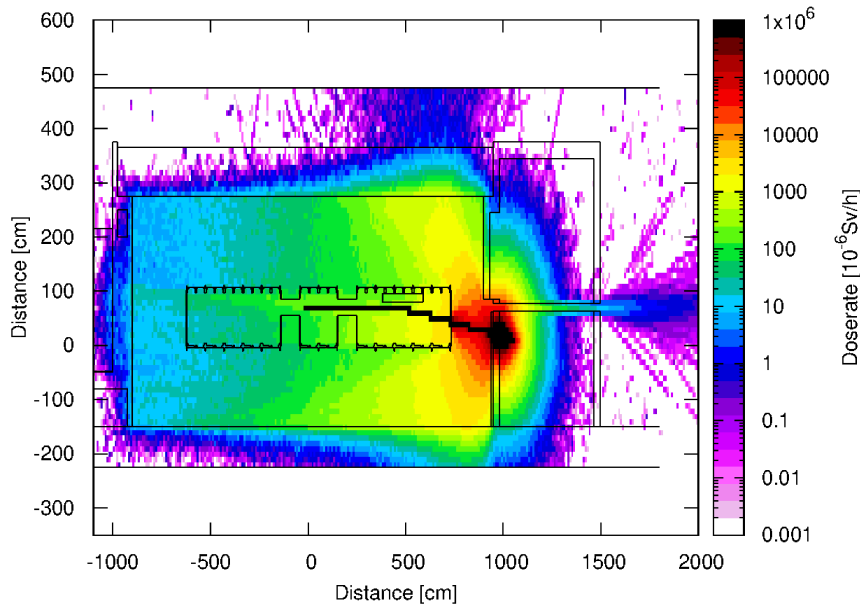


Figure 4.25: Case of locally highest dose rate in CALA. Inside ETTF, shown on a vertical plane, for a 5 GeV monoenergetic electron source and a spectrometer magnet, the local dose rate inside the beamdump exceeds 1.6 kSv/h.

of highly penetrating electrons, the total dose rate is again reported alongside with the individual contributions from neutrons, γ -rays and electrons.

For the broad spectrum source, the dose rates in all scoring locations remained below the $2.5 \mu\text{Sv/h}$ design limit. Out-of-cave doses from neutrons were in general found to be one order of magnitude higher than photon doses and two orders lower compared to electron dose rates. The lower energy electrons from the broad spectrum source were bent downwards at large angles after travelling in the spectrometer magnet and caused the highest total dose rate of $1.11 \mu\text{Sv/h}$ to occur behind the nearest laser penetration hole (*hole21*). The *hole21* scorer is located outside the ETTF cave inside the LUX cave.

Similar as for the LUX simulations, electrons were scattered through the 5.85 m central beam dump channel (*ETtoHALL1*) and induced a calculated dose rate of $1.04 \mu\text{Sv/h}$.

For the 5 GeV monoenergetic source scenario with the spectrometer magnet, the highest dose rate of $3.76 \mu\text{Sv/h}$ was calculated to occur behind the central beam dump hole (*ETtoHALL1*), as depicted in figure 4.25. That was above the design limit of $2.5 \mu\text{Sv/h}$, but less than the maximum allowed local dose rate value of $7.5 \mu\text{Sv/h}$.

The total dose rate of $3.76 \mu\text{Sv/h}$ is the result of high-energy electrons interacting with the vacuum chamber back-panel, as 92% of the total dose rate in *ETtoHALL1* is due to electrons ($3.46 \mu\text{Sv/h}$, compare to table 4.8 top). The effect of the thin 3 mm area in the back-panel of ETTF as explained in the ETTF cave layout section of section 4.2.2 is even clearer when comparing two extreme cases: the hypothetical removal (= 0 mm aluminium) compared to the 3 mm and the unchanged original massive back-panel of 2.5 cm. While the *no back-panel* situation does not cause any detectable electron component after the beam-

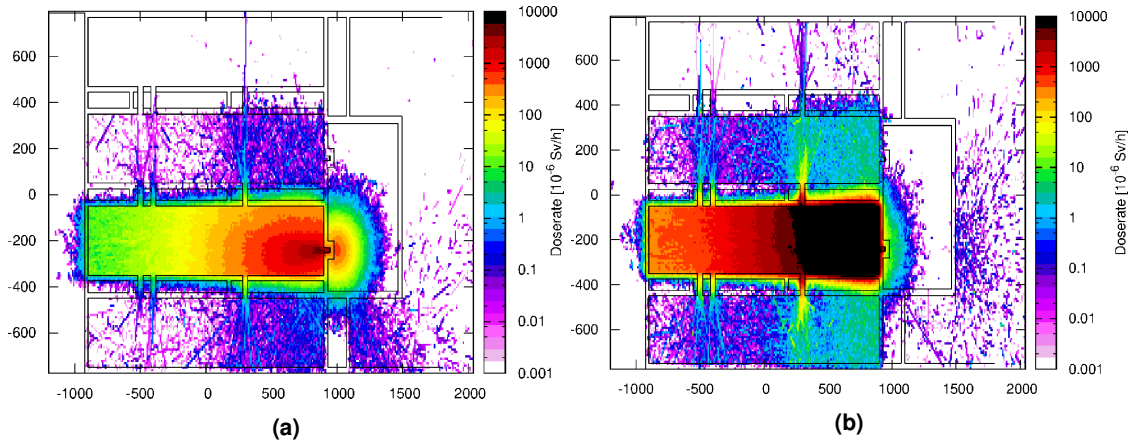


Figure 4.26: Dose rate distributions for the ETTF cave at the beamline level for 5 GeV monoenergetic electron source. **(a)** Normal setup with spectrometer magnet. **(b)** Setup without spectrometer magnet. In the latter 50 cm lead bricks were employed at both ends of the beam dump channel as shielding.

dump in *ETtoHALL1*, the result for the 2.5 cm situation changes (table 4.9). The dose rate limit-exceeding value of $48.14 \mu\text{Sv/h}$ is caused by showers generated in the 2.5 cm aluminum, of which 69.7% ($33.60 \mu\text{Sv/h}$) can be attributed to electrons. Adding the neutron and photon contribution, the missing fraction of 26.6% can be attributed to forward generated muons. The material in the beam path also causes the neutron component and hence the total dose rate to double towards the top (*ETroof*, *ETtoLU*) and sideways directions (*ETtoSP*, *ETtoLU*) when compared to the *no back-panel* situation. The 3 mm thinned region interacting with the primary electron beam was chosen as a compromise between technical feasibility and dose rate in *ETtoHALL1* (table 4.8 top).

For the 5 GeV monoenergetic source and the ETTF cave, the highest simulated dose rate inside the CALA facility of 1.6 kSv/h was encountered at $\approx 1 \text{ m}$ inside the central beam dump (figure 4.25). In this physically inaccessible location, the particle fluence locally was calculated to be up to 1.6×10^{10} particles / cm^2 .

The monoenergetic 5 GeV beam without the spectrometer magnet presented a challenging scenario for radiation protection. This is highlighted in figure 4.26, where the dose rate at beamline level is shown for the case with (left) and without (right) spectrometer magnet. The employed 50 cm lead bricks at both ends of the central beam dump channel were able to hinder direct electron penetration through the channel. The highest dose rates were $2.61 \mu\text{Sv/h}$ on the roof of the building (*ETroof*), $3.84 \mu\text{Sv/h}$ in the SPECTRE cave (*ETtoSP*), $5.33 \mu\text{Sv/h}$ and $6.83 \mu\text{Sv/h}$ in the two of the eastern laser penetration holes (*hole18* and *hole21*) to LUX and SPECTRE, respectively. Although the aforementioned dose rates exceeded the design limit of $2.5 \mu\text{Sv/h}$, they were below maximum local dose limit of $7.5 \mu\text{Sv/h}$.

Different sets of *radiation protection bricks* had been tested in order to shield the channel, which resulted in the solution to only use lead bricks on the hot and cold sides of the

4 SIMULATION STUDIES OF SECONDARY RADIATION IN MODERN ACCELERATION FACILITIES

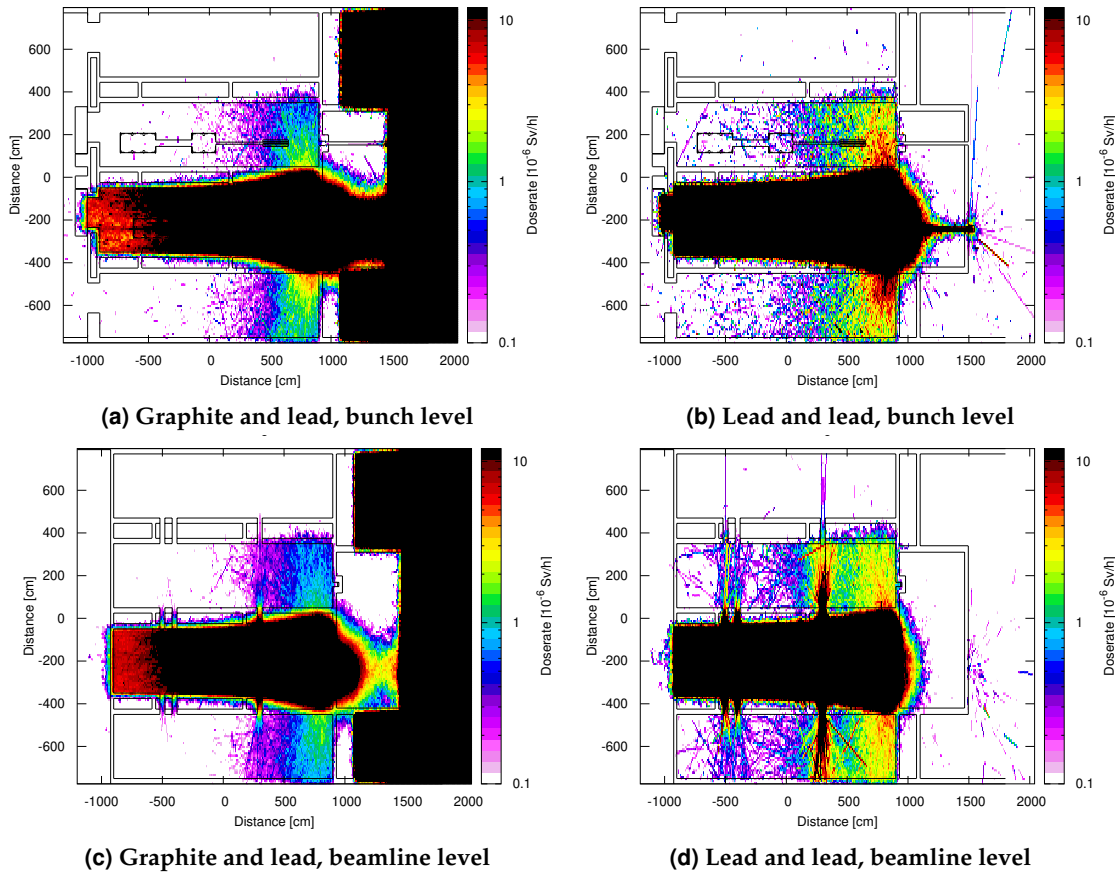


Figure 4.27: Shielding study for monoenergetic 5 GeV electrons in ETTF without using the spectrometer magnet. Colorbar is windowed to the acceptable dose rate boundaries.

beamdump (figure 4.27). The initial hybrid solution of 50 cm graphite inside the cave and 50 cm lead after the X-ray channel caused dose rates of $\approx 10^3 \mu\text{Sv/h}$ in the experimental hall, which is well above the limit (figure 4.27a). For the position *ETtoHALL1* inside the experimental hall, the dose rate of $1.05 \times 10^4 \mu\text{Sv/h}$ was reduced by five orders of magnitude using lead inside and outside ($4.11 \times 10^{-1} \mu\text{Sv/h}$, table 4.8). The fraction of neutron contribution for both cases is 96% or 90% respectively. The forward directed electrons motivating the initial preference of graphite instead of lead seem to be of less relevance compared to the high density of lead, which is needed to sufficiently shield the neutron component (figure 4.27b). It can be noted that, as typical for radiation protection problems, and especially for such a mixed field of particle types and energies, the shielding result is often a compromise. Going from 50 cm graphite inside the cave (figure 4.27a) to 50 cm lead heavily severely increases backscattering into the cave. The effect is especially visible for the windowed dose rate plots in the entrance door area ($-1000 \text{ m} < x < -500 \text{ m}$) (figure 4.27) and brings the laser penetration hole positions closer to the dose rate limit (figure 4.27b).

Radiation protection studies for novel laser particle sources at the Centre for Advanced Laser Applications

	Dose rate limit [$\mu Sv/h$]	Detector position	Dose rate [$\mu Sv/h$]			
			n	γ	e^-	Total
ETTF 5 GeV	2.5	ETroof	7.85×10^{-1}	1.28×10^{-2}	3.87×10^{-2}	8.37×10^{-1}
	2.5	ETtoLU	2.46×10^{-1}	4.91×10^{-3}	3.45×10^{-3}	2.63×10^{-1}
	2.5	ETtoSP	7.58×10^{-1}	1.49×10^{-2}	3.21×10^{-3}	7.83×10^{-1}
	2.5	ETdoC	5.35×10^{-2}	5.03×10^{-4}	0.00	5.40×10^{-2}
	2.5	ETtoHALL1	1.10×10^{-1}	7.51×10^{-2}	3.46	3.76
	2.5	ETtoHALL2	6.34×10^{-1}	1.09×10^{-2}	1.29×10^{-2}	6.67×10^{-1}
	2.5	hole4	3.83×10^{-2}	5.30×10^{-3}	5.66×10^{-3}	5.34×10^{-2}
	2.5	hole7	4.83×10^{-2}	4.48×10^{-3}	0.00	5.28×10^{-2}
	2.5	hole11	4.88×10^{-2}	5.78×10^{-3}	0.00	5.46×10^{-2}
	2.5	hole14	1.04×10^{-1}	4.87×10^{-3}	0.00	1.09×10^{-1}
	2.5	hole18	8.02×10^{-1}	5.09×10^{-2}	6.50×10^{-3}	8.66×10^{-1}
	2.5	hole21	5.34×10^{-1}	5.42×10^{-2}	8.47×10^{-3}	6.29×10^{-1}
	-	ETdoH	7.04	7.67×10^{-1}	4.83×10^{-1}	8.44
ETTF 5 GeV no Magnet	2.5	ETroof	2.50	8.47×10^{-2}	6.32×10^{-3}	2.61
	2.5	ETtoLU	2.07	4.80×10^{-2}	6.10×10^{-2}	2.20
	2.5	ETtoSP	3.50	8.69×10^{-2}	3.17×10^{-2}	3.84
	2.5	ETdoC	3.96×10^{-3}	8.92×10^{-5}	0.00	4.05×10^{-3}
	2.5	ETtoHALL1	3.95×10^{-1}	5.50×10^{-4}	0.00	4.11×10^{-1}
	2.5	ETtoHALL2	1.69×10^{-2}	1.29×10^{-4}	0.00	1.87×10^{-2}
	2.5	hole4	2.63×10^{-1}	3.84×10^{-2}	1.24×10^{-18}	3.02×10^{-1}
	2.5	hole7	4.39×10^{-1}	3.49×10^{-2}	8.98×10^{-2}	5.64×10^{-1}
	2.5	hole11	2.57×10^{-1}	3.34×10^{-2}	1.19×10^{-3}	2.91×10^{-1}
	2.5	hole14	3.62×10^{-1}	4.21×10^{-2}	1.71×10^{-2}	4.22×10^{-1}
	2.5	hole18	4.77	3.42×10^{-1}	2.12×10^{-1}	5.33
	2.5	hole21	5.86	3.93×10^{-1}	5.43×10^{-1}	6.83
	-	ETdoH	66.64	4.23	1.10	72.14
ETTF Broad	2.5	ETroof	6.86×10^{-1}	9.94×10^{-3}	8.19×10^{-4}	7.00×10^{-1}
	2.5	ETtoLU	2.20×10^{-1}	3.80×10^{-3}	2.86×10^{-3}	2.28×10^{-1}
	2.5	ETtoSP	4.63×10^{-1}	1.03×10^{-2}	2.02×10^{-3}	4.86×10^{-1}
	2.5	ETdoC	2.92×10^{-2}	3.16×10^{-4}	0.00	2.95×10^{-2}
	2.5	ETtoHALL1	3.52×10^{-2}	5.01×10^{-2}	8.84×10^{-1}	1.04
	2.5	ETtoHALL2	2.27×10^{-1}	3.81×10^{-3}	2.83×10^{-3}	2.35×10^{-1}
	2.5	hole4	4.51×10^{-2}	4.40×10^{-3}	4.68×10^{-3}	6.38×10^{-2}
	2.5	hole7	3.92×10^{-2}	8.15×10^{-3}	7.16×10^{-4}	4.80×10^{-2}
	2.5	hole11	6.41×10^{-2}	8.23×10^{-3}	1.04×10^{-3}	7.34×10^{-2}
	2.5	hole14	4.93×10^{-2}	5.30×10^{-3}	7.62×10^{-4}	5.53×10^{-2}
	2.5	hole18	7.01×10^{-1}	8.60×10^{-2}	2.35×10^{-2}	8.19×10^{-1}
	2.5	hole21	9.86×10^{-1}	7.78×10^{-2}	3.98×10^{-2}	1.11
	-	ETdoH	7.95	2.30	5.11×10^{-1}	10.94

Table 4.8: Dose rate calculations for ETTF, at critical locations indicated in figure 4.20 and figure 4.22. The upper third of the table lists results for the 5 GeV monoenergetic electron source, the middle third refers to the same source without magnet but lead shielding, while the lower third lists the results for the broad spectrum electron source.

4 SIMULATION STUDIES OF SECONDARY RADIATION IN MODERN ACCELERATION FACILITIES

	Detector position	Dose rate [$\mu Sv/h$]			
		n	γ	e^-	Total
no back panel	ETroof	7.08×10^{-1}	1.17×10^{-2}	1.06×10^{-2}	7.36×10^{-1}
	ETtoLU	2.46×10^{-1}	3.77×10^{-3}	4.03×10^{-4}	2.59×10^{-1}
	ETtoSP	8.22×10^{-1}	1.40×10^{-2}	1.70×10^{-3}	8.38×10^{-1}
	ETdoC	3.38×10^{-2}	1.06×10^{-3}	0.00	4.10×10^{-2}
	ETtoHALL1	8.93×10^{-1}	3.72×10^{-3}	0.00	8.96×10^{-1}
	ETtoHALL2	6.42×10^{-1}	9.42×10^{-3}	1.46×10^{-3}	6.59×10^{-1}
	ETdoH	7.65	8.06×10^{-1}	5.11×10^{-1}	8.91
2.5 cm back panel	ETroof	1.27	1.86×10^{-2}	4.83×10^{-3}	1.30
	ETtoLU	7.01×10^{-1}	1.31×10^{-2}	5.38×10^{-3}	7.26×10^{-1}
	ETtoSP	1.47	3.25×10^{-2}	6.57×10^{-3}	1.53
	ETdoC	5.80×10^{-2}	1.04×10^{-3}	0.00	5.91×10^{-2}
	ETtoHALL1	8.63×10^{-1}	9.46×10^{-1}	33.60	48.14
	ETtoHALL2	7.84×10^{-1}	1.13×10^{-2}	7.26×10^{-4}	8.11×10^{-1}
	ETdoH	8.80	8.84×10^{-1}	7.49×10^{-1}	10.68

Table 4.9: Simulation of 5 GeV electrons in ETTF with the spectrometer magnet, comparing a hypothetical vacuum chamber without chamber back-panel to the massive original 2.5 cm back-panel case.

SPECTRE For the SPECTRE cave three very different source types were simulated (table 4.5): a 500 MeV electron source at a repetition rate of 1 Hz. A broad spectrum electron source with energies up to 500 MeV, also generated with 1 Hz repetition frequency. Finally, 70 MeV monoenergetic electrons with 1 kHz repetition frequency.

Table 4.10 summarizes the dose rates outside the cave in all scoring locations for the three source configurations.

The calculated dose rates for the *supervised areas* were approximately two orders of magnitude below the respective limit of $2.5 \mu\text{Sv/h}$. The sole exception to this was in the critical location *hole20* behind one of the laser penetration holes leading to ETTF, for the 70 MeV monoenergetic electrons with 1 kHz repetition frequency and the open 17.78 cm channel. There the dose rate was quantified to exceed the $2.5 \mu\text{Sv/h}$ design limit ($3.62 \mu\text{Sv/h}$), but still below the maximum allowed local dose rate of $7.5 \mu\text{Sv/h}$.

The *SPtoLAB* position, located in an *unclassified area* with the $0.5 \mu\text{Sv/h}$ dose rate limit for *unclassified areas*, is safely below $10^{-2} \mu\text{Sv/h}$.

The neutron component dominated again the out-of-cave doses for all USRTRACK scorers by one to two orders of magnitude. Electron doses outside the cave are negligible due to the short ranges in the MeV energy regime of secondary electron showers in the shielding walls.

The scorer position *hole20* is the most critical position in SPECTRE, since the highest (but still safe) dose rates outside the SPECTRE cave were detected there: *hole20* displays $1.79 \times 10^{-1} \mu\text{Sv/h}$ for the monoenergetic 500 MeV beam. For the broadband case, the additional lower energies case raise the dose rate in *hole20* to $8.33 \times 10^{-1} \mu\text{Sv/h}$. Due to the high repetition frequency of 1 kHz, which enters the dose rate calculation linearly, the dose rate in *hole20* is for the 70 MeV simulation locally even above the $2.5 \mu\text{Sv/h}$ design limit ($3.62 \mu\text{Sv/h}$). For the 70 MeV and 10 – 500 MeV simulations the neutrons-induced dose rate, as well as the γ and electrons dose rate each contribute equally $\approx 1/3$ to the total dose rate.

4 SIMULATION STUDIES OF SECONDARY RADIATION IN MODERN ACCELERATION FACILITIES

	Dose rate limit [$\mu\text{Sv}/h$]	Detector position	Dose rate [$\mu\text{Sv}/h$]			
			n	γ	e^-	Total
SPECTRE 70 MeV	2.5	SProof	5.07×10^{-3}	2.33×10^{-3}	0.00	7.40×10^{-3}
	2.5	SPtoET	6.92×10^{-4}	8.54×10^{-4}	0.00	1.55×10^{-3}
	2.5	SPdoC	0.00	1.47×10^{-4}	0.00	1.47×10^{-4}
	2.5	SPtoHALL1	0.00	0.00	0.00	0.00
	2.5	SPtoHALL2	0.00	0.00	0.00	0.00
	2.5	SPtoHALL3	0.00	0.00	0.00	0.00
	0.5	SPtoLAB	0.00	0.00	0.00	0.00
	2.5	hole6	2.03×10^{-2}	9.05×10^{-3}	0.00	2.94×10^{-2}
	2.5	hole13	1.54×10^{-2}	1.05×10^{-2}	0.00	2.59×10^{-2}
	2.5	hole20	1.30	1.39	9.25×10^{-1}	3.62
-	SPdoH	5.95	14.50	2.97	23.61	
SPECTRE 500 MeV	2.5	SProof	4.82×10^{-2}	8.19×10^{-4}	1.15×10^{-4}	4.91×10^{-2}
	2.5	SPtoET	6.29×10^{-2}	1.34×10^{-3}	6.55×10^{-4}	6.67×10^{-2}
	2.5	SPdoC	5.89×10^{-3}	9.22×10^{-5}	0.00	5.98×10^{-3}
	2.5	SPtoHALL1	5.15×10^{-2}	1.42×10^{-3}	1.90×10^{-3}	5.48×10^{-2}
	2.5	SPtoHALL2	5.09×10^{-2}	6.96×10^{-4}	0.00	5.16×10^{-2}
	2.5	SPtoHALL3	1.63×10^{-2}	2.02×10^{-4}	0.00	1.65×10^{-2}
	0.5	SPtoLAB	3.20×10^{-2}	6.03×10^{-4}	1.79×10^{-4}	3.28×10^{-2}
	2.5	hole6	1.53×10^{-2}	1.54×10^{-3}	4.12×10^{-4}	1.73×10^{-2}
	2.5	hole13	1.62×10^{-2}	1.91×10^{-3}	5.66×10^{-4}	1.87×10^{-2}
	2.5	hole20	1.43×10^{-1}	2.05×10^{-2}	1.06×10^{-2}	1.79×10^{-1}
-	SPdoH	3.46	1.28	1.90×10^{-1}	5.00	
SPECTRE 10 - 500 MeV	2.5	SProof	3.21×10^{-2}	5.85×10^{-4}	0.00	3.27×10^{-2}
	2.5	SPtoET	3.05×10^{-2}	6.61×10^{-4}	0.00	3.12×10^{-2}
	2.5	SPdoC	1.69×10^{-3}	9.00×10^{-5}	0.00	1.78×10^{-3}
	2.5	SPtoHALL1	1.47×10^{-2}	9.63×10^{-4}	0.00	1.56×10^{-2}
	2.5	SPtoHALL2	1.43×10^{-2}	1.07×10^{-3}	0.00	1.54×10^{-2}
	2.5	SPtoHALL3	6.87×10^{-3}	8.69×10^{-5}	2.74×10^{-4}	7.23×10^{-3}
	0.5	SPtoLAB	1.29×10^{-2}	2.52×10^{-4}	0.00	1.34×10^{-2}
	2.5	hole6	9.22×10^{-3}	1.71×10^{-3}	7.53×10^{-4}	1.17×10^{-2}
	2.5	hole13	1.62×10^{-2}	2.16×10^{-3}	3.05×10^{-3}	2.14×10^{-2}
	2.5	hole20	2.01×10^{-1}	1.51×10^{-1}	3.77×10^{-1}	8.33×10^{-1}
-	SPdoH	3.11	2.38	8.20×10^{-1}	6.38	

Table 4.10: Dose rate calculations for SPECTRE at critical locations indicated in figure 4.23 and figure 4.24. The upper third of the table lists results for the 70 MeV monoenergetic electron source at 1 kHz, the middle third for the 500 MeV monoenergetic electron source at 1 Hz, while the lower third represents the broad spectrum electron source at 1 Hz.

4.2.4 Discussion

General discussion As presented in the results in section 4.2.3 and summarized in table 4.7, table 4.8 and table 4.10, adequate beam dumps, magnets, passive shielding using sufficient cave walls, steel bars to temporarily plug X-ray holes, lead bricks and laser pulse repetition limits allow to achieve the desired result that the the average dose rates in- and outside the experimental caves stay below design specifications ($< 0.5 \mu\text{Sv/h}$ for unclassified areas, $< 2.5 \mu\text{Sv/h}$ for supervised areas, $< 7.5 \mu\text{Sv/h}$ locally). *Controlled areas* requiring personal electronic dosimeters can be avoided in CALA. For most configurations, the shielding components cause a five orders of magnitude difference in dose rate between proximal and distal scorers around the shielding.

The areas of highest doses inside each cave were directly correlated to the location of the respective beam dump. For the LUX, ETTF and SPECTRE caves, the beam was terminated in the central 5.85 m beam dump, at the eastern end of each cave. This meant that the dose was higher in the eastern part of these caves and in the experimental hall behind the beamdump. LION and HF in contrast use individual beam dumps located at the center of these caves [54]. As such, the highest dose rates outside these caves occurred behind the walls in the direct vicinity of the beam dumps in the cave middle [54]. Common to all caves, as expected, was the trend for elevated dose rates to occur behind the laser penetration holes that are located closest to the beam dump. These locations directly behind the holes, however, are below the false floor, hence not readily accessible to the working personnel.

Secondary neutrons were in the majority of the cases the dominant contribution to dose rates calculated outside a cave in operation. A different situation was observed when beams were hitting the central beam dump and the X-ray extraction channels were open in the east walls of LUX and ETTF. In these cases, high-energy electrons scattered in the chamber backwall were the main component of the calculated out-of-cave high dose rate. Thicker walls significantly increase the angular distribution of the electron beam, allowing a larger part of it to go through the beam dump channels.

The high-energy electrons produced in ETTF and SPECTRE yield a non-negligible fluence of muons (up to about $1000 \mu / \text{cm}^2$), which is approximately two orders of magnitude lower than the maximum encountered neutron fluence. These muons are predominantly produced at shallow locations inside the central beam dump. An evaluation of their energy spectrum shows a broad distribution with energies reaching up to a several GeV. According to a FLUKA simulation, such high-energy muons can have a maximum range in water of $\approx 2 - 3 \text{ m}$, which means that they cannot penetrate the central 5.85 m thick concrete beam dump (of $\rho = 4 \text{ t/m}^3$). Their contribution to the dose rate outside the caves is therefore negligible.

Such muon production is logical and observed at conventional electron accelerator facilities, since the muon mass of $\approx 106 \text{ MeV}/c^2$ is within the scope of non-clinical research accelerators. Especially the CALA electron acceleration experiments aiming at a kinetic

4 SIMULATION STUDIES OF SECONDARY RADIATION IN MODERN ACCELERATION FACILITIES

energy of the electrons of up to 5 GeV may even consider muon monitoring for peripheral evaluation of the acceleration performance.

Specific locations of concern The maximum quantified dose rate outside a cave in operation was $6.94 \mu\text{Sv/h}$ and was estimated for a monoenergetic 5 GeV electron source behind the central beam dump for the LUX cave (*LUtoHALL* position). That location, similar for ETTF, is one of the most critical points of the CALA design. Despite the massive central beam dump, two channels through it are required in order to allow for the transport of X-ray beams from the experimental caves LUX and ETTF to the experimental hall to the east. Behind these two channels dose rates were expected to be high.

The almost 3-fold excess of the $2.5 \mu\text{Sv/h}$ design limit for supervised areas was mainly attributed to high-energy electrons escaping through one of the central beam dump channels. The dose was below the locally allowed dose rate of $7.5 \mu\text{Sv/h}$, which means that this particular location has to be made temporarily inaccessible during experiments in the LUX cave.

In the case of the most demanding configuration in ETTF, that of a monoenergetic 5 GeV electron source without a spectrometer magnet, a similar dose rate ($6.83 \mu\text{Sv/h}$) was calculated to leak through one of the laser penetration holes towards SPECTRE (*hole21*). Due to the lack of magnetic downward deflection, almost the entire electron beam hit a small area of the central beam dump (the lead brick blocking the X-ray channel) and created a high backscatter radiation field around this small section of the eastern region of the ETTF cave. The creation of secondary neutrons there was the primary dose rate component leaking through the two laser penetration holes most proximal to the beam dump (*hole18*, *hole21*) and through the roof there (*ETroof*). As in the previous case, this dose rate was still safely below the maximum locally allowed rate of $7.5 \mu\text{Sv/h}$.

Safety of working in neighbouring caves and areas during operation of the laser in a cave One of the main goals of the CALA radiation protection design was to allow caves and experimental areas neighbouring a cave, in which the laser is in operation, to remain accessible. This goal was in general achieved according to the presented simulations, with a few exceptions at a handful of locations (dose rates exceeding $2.5 \mu\text{Sv/h}$): first, in the experimental hall (*LUtoHALL1*, *ETtoHALL1*), when LUX or ETTF (only for 5 GeV monoenergetic) were in operation, due to the electron leakage through the central beam dump channels. Then in SPECTRE and LUX when ETTF was in operation with 5 GeV monoenergetic electrons without spectrometer magnet due to neutron dose. Finally, in ETTF (*hole20*) when SPECTRE was in operation with 70 MeV at the high repetition rate of 1 kHz, again due to neutrons.

How conservative are the results? In this study the dose rate from each individual cave being in operation was calculated, without assuming cumulative effects due to op-

4 SIMULATION STUDIES OF SECONDARY RADIATION IN MODERN ACCELERATION FACILITIES

Environment. The measurements, accompanied by measurements using portable ionisation chamber, which are able to work in vicinity of pulsed sources, will prove the safety of workers and confirm the results of this thorough simulation study.

Finally, in the unlikely case that the laser and targetry would enable reaching higher energies/fluences (e.g. come close to the worst case scenario for shielding) in the far future of CALA, decreasing the shot frequency for some particular experiments/sources would allow to remain within the radiation protection limits.

4.3 Study of secondary neutrons at the Centre for Advanced Laser Applications

4.3.1 Introduction

As lasers systems may potentially serve as biomedical accelerators in future, knowledge of unwanted radiation such as secondary neutrons is desirable. To this end, a combination of the knowledge on FLUKA simulations of secondary neutrons and the resulting spectra at RPTC (section 4.1) together with the radiation protection model generated for the LION experiment in CALA (section 4.2) was started.

These investigations were especially motivated to serve as benchmark of results obtained with another simulation code and are continued in future, using the FLUKA model, the neutron spectra and dose rate results as benchmark. The studies regarding the generated secondary neutron spectra along with neutron and photon doses and possibly measurements are performed using GEANT4 in a PhD Thesis at the Helmholtz Zentrum München, Department for Radiation Medicine. The LION cave model developed in this work in FLUKA was transferred to GEANT4 and extended by the vacuum chamber content interacting with the diverging bunches, namely the quadrupole lenses and laser light screens, which led to the publication: *GEANT4 Monte Carlo Simulation Study of the Secondary Radiation Fields at the Laser-driven Ion Source LION* [231].

4.3.2 Material and Methods

The radiation protection model of LION@CALA as shown in figure 4.29 was extended by placement of 8 USRTRACK neutron spectrum scorers in the cave at the bunch level with the same energy range and binning as for the RPTC simulations in section 4.1.2.

In the cases of laser-proton or laser-ion acceleration experiments LION and HF, the simulated sources were mixed radiation fields of electrons and protons or ions [54]. To simplify the simulations while allowing for detailed interpretation of the results, each initial component of a mixed radiation field was simulated separately and their contributions was summed up to yield the total dose.

The spectrum of secondary neutrons inside and outside the LION cave for a proton energy spectrum of a box-like shape was simulated, similar to the radiation protection studies done for 10 – 200 MeV, but using a range of 10 – 75 MeV, as this is in the scope of energies to be reached in the year 2021 and may therewith soon enable first biomedical experiments at LION. The beam divergence was 180 mrad.

4 SIMULATION STUDIES OF SECONDARY RADIATION IN MODERN ACCELERATION FACILITIES

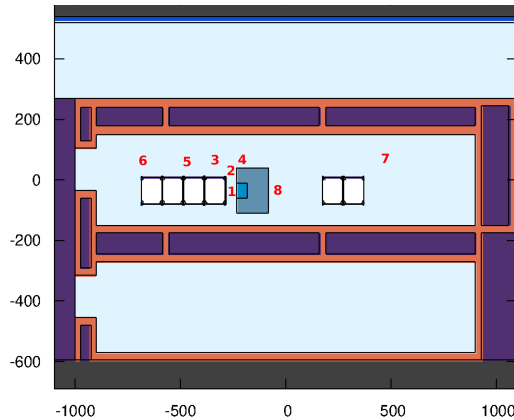


Figure 4.29: LION model of CALA used for the simulation of secondary neutrons. Scorer positions are indicated using numbers.

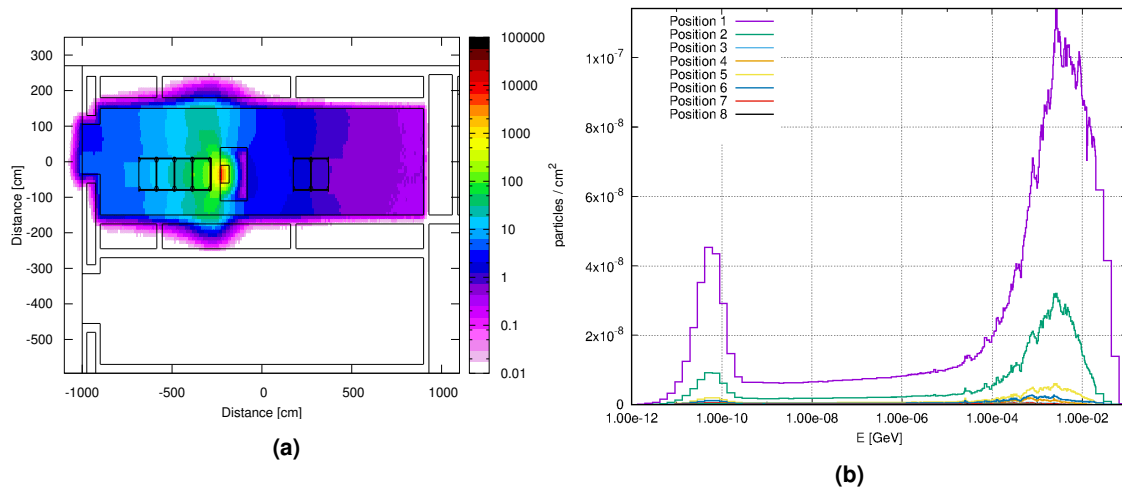


Figure 4.30: First results of secondary neutron simulation using the LION radiation protection model. (a) Energy integrated fluence of secondary neutrons at bunch level. (b) FLUKA simulated secondary neutron spectra in the LION cave at locations indicated in figure 4.29 (Arbitrary units).

4.3.3 Results and Discussion

As it could be expected from the fluence simulations performed for RPTC (table 4.3) and in the fluence simulations for the dose rate simulations in section 4.2, the field of secondary neutrons has a strong forward directional dependence (figure 4.30a). The high-energy peak at position 1 in 0° forward direction outrages the position 2 at 45° by a factor of 3 (figure 4.30b).

In general, all positions in the polyenergetic LION simulation, similar to the monoenergetic RPTC simulations, present the same neutron spectra characteristics over the full energy range: a high-energy peak, elevated fluence in the fast neutron region, an approximately $1/E_n$ slope for the epithermal neutrons and a minor peak in the thermal neutron energy range (figure 4.30b). The further off-axis the measurement is performed, as for

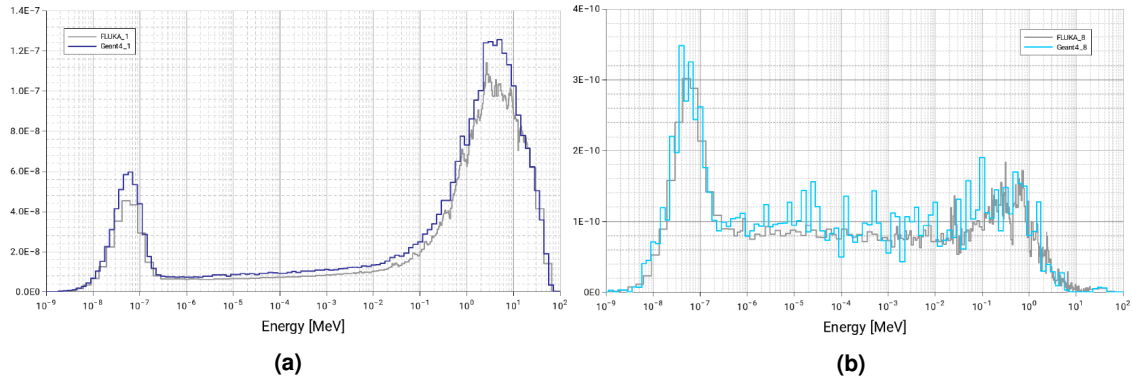


Figure 4.31: Comparison of neutron spectra in lethargy representation for FLUKA and GEANT4 simulated 10 – 75 MeV box-like proton energy spectra, exemplarily shown for (a) position 1, 0° and (b) position 8, 0° behind beamdump. The GEANT4 data is courtesy of M. Tisi.

RPTC the more are the thermal energy neutrons of importance. Position 8 behind the beamdump shows the high-energy neutron to be about three orders of magnitude lower than for position 1.

The FLUKA simulated spectra calculated in this work were used as a Monte Carlo model benchmark to spectra simulated by GEANT4 (figure 4.31). Future detailed evaluation of all positions will try to better understand where differences come from and help to reach congruence to the future measurements. Simulations of energy integrated fluence for 10 – 75 MeV initial proton energy spectrum serve as preliminary benchmark comparison of the FLUKA and GEANT4 models. The data, partially presented here, is included in the manuscript in preparation and reflects a general relative overestimation of GEANT4 to FLUKA fluence densities for all eight scorer positions of up to 21% [231].

4.3.4 Conclusion and Outlook

At CALA, the features of the secondary neutron spectra in the LION cave are dependent on proton energy and measurement angle, and the relative contributions of these features to the total spectrum differ. This behaviour was expected from the RPTC simulations.

First measurements of secondary neutron spectra are expected for 2021. The comparison to the simulation results will be a next milestone for the simulation benchmarks. The simulations, normalized to absolute dose, will help to answer the question whether the ERBSS as used at RPTC are sensitive enough for single bunch detection. Otherwise, it can be estimated how much proton bunch charge is needed for a reliable single shot detection of neutron spectra.

Future investigations will try to systematically link different spectra of laser-accelerated proton bunches to simulated / measured neutron spectrum using simulations. As ultimate goal, such investigations may lead to non-invasive proton bunch diagnostic by online secondary neutron spectrometry.

Chapter 5

Investigation of pixel detectors for applications at laser-driven particle beams

The author has published the work presented in section 5.1.4 as a journal paper in *Radiation Protection Dosimetry* and presented the results orally at the *NEUDOS-13* conference and as a poster at the *DGMP 2017*.

- Paper: **F Englbrecht** et al.: An online, radiation hard proton energy-resolving scintillator stack for Laser-driven proton bunches, *Radiation Protection Dosimetry*, pp. 1–5, 2018
- Oral Presentation: **F Englbrecht** et al.: An Online, Radiation Hard Proton Energy-Resolving Scintillator Stack for Laser-Driven Proton Bunches, *Neutron and Ion Dosimetry Symposium, NEUDOS-13, Krakow, Poland*
- Poster: **F Englbrecht** et al.: An online, radiation hard proton energy-resolving scintillator stack for Laser-driven proton bunches, *Annual conference of the German Society for Medical Physics, DGMP 2017, Dresden, Germany*

The author has published the work presented in section 5.1.5 as a paper in the journal *Current Directions in Biomedical Engineering* and presented the results orally at the *Workshop on Low-Energy Ion-Beam Diagnostics*.

- Paper: **F Englbrecht** et al.: Characterization of online high dynamic range imaging for laser-driven ion beam diagnostics using visible light, *Current Directions in Biomedical Engineering* 3(2), pp. 343–346 2017
- Oral Presentation: **F Englbrecht** et al.: Pixel detectors for laser-driven proton and carbon ion acceleration at CALA, *Workshop on Low-Energy Ion-Beam Diagnostics, Centre for Clinical Application of Particles (CCAP), Imperial College London 2019, London, UK*

The work presented in section 5.2 has been published as a masters thesis at LMU, supervised by the author.

- Master thesis: M. Sng: Characterization of the CM49 CMOS detector for laser-driven ion acceleration, 2019
-

5.1 RadEye CMOS sensor

Pioneering work for the selection, implementation and testing of pixel detectors for the detection of laser-driven ions has been done by Reinhardt et al. [193, 194]. In particular, for the RadEye sensor, they performed an absolute particle number calibration for detection of protons with the sensor, test-wise operated it in vacuum, built EMP and a shielding housings along with vacuum compatible cables, feedthrough-flanges and control PCs [47].

Building upon these achievements, this work realized further steps to use the RadEye as a sensitive, low-dark current, low-background triggerable, automated and EMP-insensitive main diagnostic tool for laser-driven ion experiments at the LION beamline LEX and CALA (figure 5.2b). Features of the control software were developed, tested and employed in multiple experiments, as illustrated in the following sections after a short introduction to the detector sensors and their characteristics.

5.1.1 RadEye CMOS sensor characteristics

The employed RadEye CMOS detector system has been proven suitable for direct insertion into the beam path of laser-accelerated protons, offering up to approximately $5\text{ cm} \times 10\text{ cm}$ sensitive area, radiation hardness up to 6×10^{10} protons / cm^2 , sensitivity to both optical photons, X-rays and charged particles and live image display [193]. It showed linear behaviour to proton irradiation over six orders of magnitude, from 10^6 protons / cm^2 / ns down to single proton sensitivity [194]. No charge sharing effects between neighbour pixels as known from e.g. the Timepix sensor was observed [140].

The sensor modules were sold (section 5.2) commercially as industrial X-ray detectors, reading out the visible scintillation light from $5\text{ cm} \times 10\text{ cm}$ large X-ray plastic scintillators [180]. For all experiments, the plastic scintillator had been removed and engineering grade quality sensors, allowing for pixel and line defects and an increased dark current, were used.

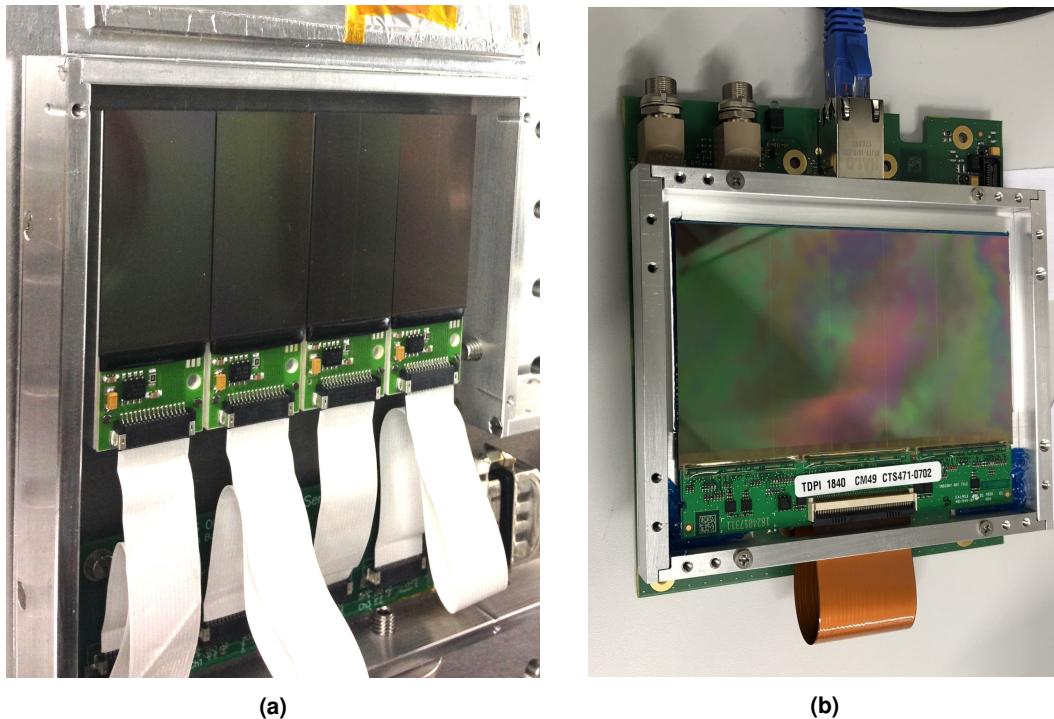


Figure 5.1: Sensor heads of the two used CMOS pixel detector systems. **(a)** Four RadEye sensors are combined using a DVI-multiplexer board for a detection area of approximately $5 \times 10 \text{ cm}^2$ in LION. **(b)** Potential successor CM49 sensor for $6.4 \times 11.4 \text{ cm}^2$ detection area.

A single sensor module has an active area of 1024×512 pixels (≈ 0.5 Megapixels) of $48 \mu\text{m}$ pixel size. The sensor is 1.8 mm thick, from which 1.1 mm are a ceramic substrate and 0.7 mm the silicon wafer. The wafer is a two-dimensional array of photodiodes with a nominal active thickness of $2 \mu\text{m}$ below an approximately $2 \mu\text{m}$ passivation layer SiO_2 and a capacitance of 15 pF for the fill factor of 80% [193, 181].

5.1.2 RadEye as detector system for laser-ion acceleration experiments

Up to four single sensor modules can be combined using a DVI-multiplexer board, which interconnects the four sensor by 10-lane flat-ribbon cables to yield an active area of $5 \text{ cm} \times 10 \text{ cm}$ (figure 5.1a). The presented work used the remote RadEye configuration of the detector system, which separates the sensor modules (figure 5.2a) from the control electronics inside the *Remote RadEye box* (RRB) by a several meter long DVI cable. The four sensors were placed in a previously developed light tight aluminium housing of 5 mm thickness [138]. The DVI cable connected the housing to the RRB, placed in air, and detached most electronics from the harsh vacuum and radiation environment.

Sensor signals were digitized by several *analog-digital converter units* (ADCs) in the remote control electronics box as 14-bit, but quantized as 12-bit. The converted images were hence scaled to a maximum pixel count of 4096 *Analog-Digital-Units* (ADUs).

Radiation hard CMOS sensors can be mounted directly in the beam path for radiation

5 INVESTIGATION OF PIXEL DETECTORS FOR APPLICATIONS AT LASER-DRIVEN PARTICLE BEAMS

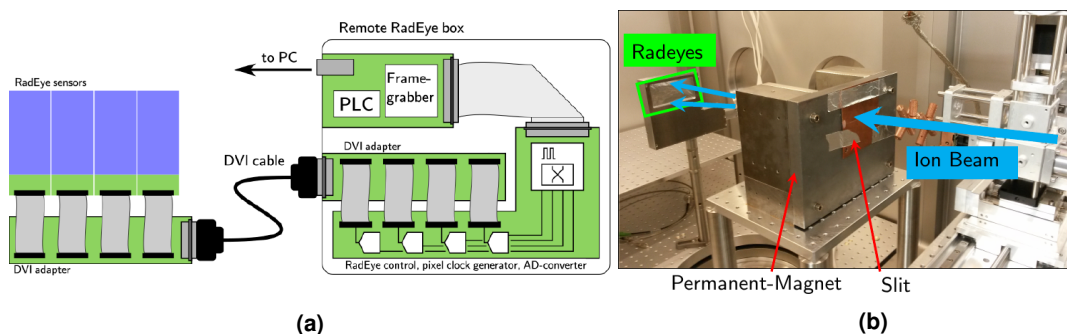


Figure 5.2: Remote RadEye system used at laser-ion acceleration experiments. **(a)** Schematic representation of the remote RadEye configuration [47]. **(b)** Remote RadEye configuration used in the LION experiment as part of the proton Wide-angle spectrometer [138].

beam profile measurements. Also, the RadEye has been used at LION as position sensitive pixel detector in a magnetic dipole spectrometer used for particle type discrimination and the detection of the magnetic deflection, which can provide an indirect energy measurement (figure 5.2b). Lindner et al. built such *Wide Angle Spectrometer (WASP)* by using electron scintillators for the combined detection of proton and electron bunches at laser-ion experiments and implemented it at the LION beamline in LEX and CALA, together with the author (figure 5.2b, chapter 6, chapter 7).

5.1.3 RadEye control software

Programmable logic controller (PLC) The remote RadEye configuration uses a *Pleora iPort PT1000* as frame grabber inside the RRB with a *GigE-Vision* Ethernet interface for sensor readout control. The PT1000 uses a PLC, low-voltage electronics hardware with *real-time* timing properties and is faster than high-level computer electronics and software. It controls three pulse generators (PG1, PG2, PG3) to generate the relevant control, clear and readout commands using pulse sequences for the connected RadEye sensors [175].

The PLC is controlled using string-commands, which are written to the controller using custom made C++ software with a graphical interface using the QT-framework (figure 5.3). The software runs on a Windows computer equipped with the *Coyote-driver* used to configure the GigE Ethernet interface and the *Pleora iPort Vision SDK*, which provides the libraries used to control the GigE network interface. The core of the C++ software (*CamOuflage.exe*), which exists since 2014, was widely extended with new features within this work [47].

New developed features In order to use the RadEye-sensors as a sensitive, low-dark current, low-background triggerable, automated and EMP-insensitive main diagnostic tool for laser-driven ion experiments at the LION beamline LEX and CALA (figure 5.2b),

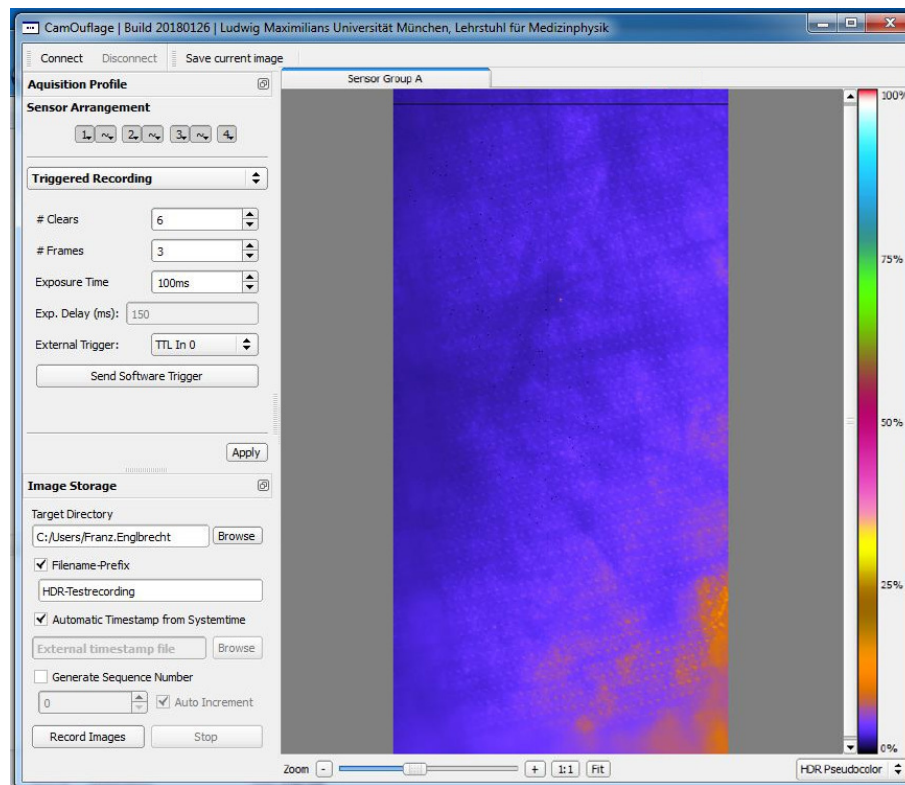


Figure 5.3: User interface of HDR-RadEye control software.

as well as for further development of new detector systems using the RadEye-sensors (figure 5.4), several software features were developed, tested and employed in multiple experiments. In the framework of the thesis, the software was extended to enable well timed multi-clearing, *High dynamic range* (HDR) recording, automatic and server based time stamping for multi-diagnostic correlation and was tailored to the experimental timing at LEX and CALA.

The time of arrival at the detector of a laser-generated particle bunch is known in a time interval of several ms with respect to the laser trigger and even to a few ns with respect to the arrival of the laser pulse at the target. The image acquisition for the sensor sold as commercial device was previously performed using the *free running* acquisition mode, a freely running video-camera-like mode constantly taking images, in a rolling shutter manner. In setting, a typically few ns short particle bunch and its signal generation inside the CMOS would then be usually split over two consecutive frames. An important feature of the customized system was hence the exact timing control over the acquisition. For the spectrometry of the LION experiment at the LEX laboratory, the PLC string commands were tailored to the ATLAS-300 laser timing. For each external TTL trigger pulse from from the laser system, the RRB then started the readout for each shot after the same time interval, which is approx. 150 ms after arrival of the charged bunch on the remote RadEye head. As part of a system-integration approach, multiple independent diagnostics of the LION experiment were cross-correlated over several experimental campaigns to form an automated 0.5 Hz *Integrated Laser-Driven Ion Accelerator System*, able to auto-

matically perform up to 1683 individual shots [115, 79, 78]. The scans of the experimental parameter spaces such as laser pulse contrast, laser pulse delay, target thickness and material, laser focal position and focus size, laser pulse energy and laser intensity on target became possible due the deployment of a central timestap-server instance. The functionality to reliably include the external timestamp, e.g. 20190521_223005_05_04, generated by the issue of the TTL trigger pulse, was integrated to the automatic saving functionality of the software in order to correlate the mentioned experimental parameters with the generated charged particle spectra and the signal from other photodiodes and cameras like for the amount of back scattered laser light.

The generated heat of electrical components inside vacuum chambers cannot be spread via convection or diffusion as easily as at atmospheric pressure via convection or diffusion, since the air pressure inside the chamber is up to seven orders of magnitude lower. It was observed previously that the level of dark current of the sensor is dependent on its temperature [85]. When operated in vacuum in LEX, the RadEye background signal without the impact of any bunch of ionizing radiation quickly accumulated to a level comparable to the bunch impact signal, especially when operated in free running acquisition mode. A minimal background signal of < 100 ADUs was achieved by integrating six detector-clearing signals from the Coyote-driver within the 130 ms of the readout delay from the TTL trigger signal and enabled quantitative comparison of the particle numbers between various experimental days. The quantitatively reliable spectra were used for quantitative proton radiography in chapter 7, as ground truth for the development of other diagnostics such as I-BEAT or several time-of-flight detectors [93, 251]. A background subtraction with an intrinsic particle number calibration, without the need of cumbersome magnetic field measurements for the use as magnetic dipole spectrometer (section 6.1), less alignment sensitivity and less coarse assumptions on the bunch energy loss in the active layer is under development by Hartmann et al., using quantitative image quality [96].

In order to allow for a simple software deployment without the need for cumbersome backward-compatible GigE driver installations in modern Microsoft Windows versions and to avoid dependencies on a specific version of the available Visual C++ as well as upgrade-compatibility problems with the iPort-Vision SDK and QT, the amount of dependencies on external *dynamic-link libraries* (DLL) was reduced. To this end, efforts were taken to recompile the detector control software statically, which includes the driver- and QT libraries in a portable 20 MB executable.

The portable Camouflage GUI including the new features developed in this thesis work is in use at the laser-driven particle acceleration facilities of *Helmholtz-Zentrum Dresden-Rossendorf* (Germany), at the *Extreme Light Infrastructure* (ELI, Romania), *Laboratoire pour l'Utilisation des Lasers Intenses / Appolon* (LULI, France) and *Berkeley Lab Laser Accelerator* (BELLA, USA).

To expand the portfolio of diagnostic instruments, an attempt to build and experimentally characterize a compact and online scintillator stack, read out by the RadEye detector



(a)



(b)

Figure 5.4: Scintillator stack for proton energy determination at laser-ion experiments. **(a)** Aluminium housing with the scintillator layers moulded in place. Proton bunches (magenta arrow) can enter through a hole. Scintillation light is induced in nine detection layers (red arrows) and digitized by a RadEye sensor (green box). **(b)** Two RadEye sensors, mounted perpendicular for future two-sided readout of the scintillators.

was undertaken [57].

5.1.4 RadEye as position sensitive scintillator stack detector

Similar to an RCF stack (section 3.4.3), the determination of the kinetic energy distribution of a proton bunch can be done by the evaluation of the amount of scintillation light from the different scintillation layers stopping the bunch. The prototype stack presented in this work was designed for the diagnostics of polyenergetic proton bunches of up to 20 MeV. Such bunches were expected from the 300 TW laser system in LEX from the LION experiment.

5 INVESTIGATION OF PIXEL DETECTORS FOR APPLICATIONS AT LASER-DRIVEN PARTICLE BEAMS

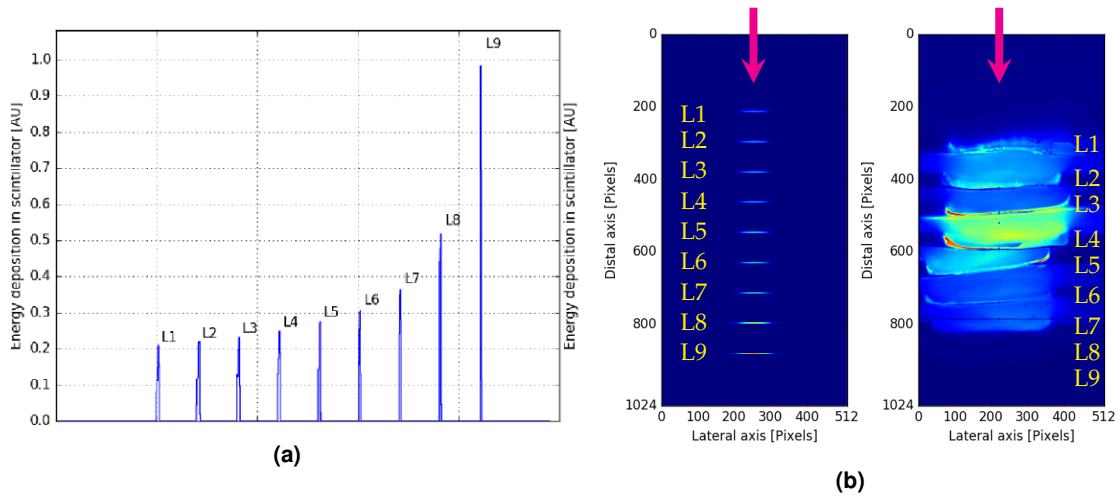


Figure 5.5: Signals in stack induced by a monoenergetic bunch. **(a)** Simulated energy deposition in scintillator layers [57]. The two dimensional signal (figure 5.5b) was reduced to 1D to yield a depth-dose curve. **(b)** Comparison of expected 2D distribution of proton-bunch-induced (magenta) energy deposition in the RadEye based on MC simulation (left) and corresponding scintillation light measurement at the MLL tandem accelerator (right) [57].

Stack layout The prototype device consisted of a stack of nine layers of *Polydimethylsiloxane* (PDMS) scintillators on Teflon support structures. The thickness of the PDMS and *Polytetrafluorethylen* (PTFE / Teflon) layers was designed to be $150\ \mu\text{m}$ each. PDMS was chosen as scintillation material, as it is liquid during manufacturing, non-toxic, radiation hard up to 10 kGy and has been shown to have a high light output [166, 165]. The PDMS layers were mounted perpendicularly to a single RadEye, which light-sensitive, can detect the radiation-induced scintillation light edge-on (figure 5.4a). The Teflon layer served as support structure in the manufacturing process, since the scintillator was molded warm and liquid onto the frame and onto the CMOS to enable optical coupling to the detector. The direct interconnection of scintillator and the $2\ \mu\text{m}$ SiO_2 layer on top of the $2\ \mu\text{m}$ active Si layer of the RadEye made optical glue superfluous and reduces potential light losses. To avoid optical cross-talk of adjacent layers, each PDMS layer was covered with a $8\ \mu\text{m}$ thin Mylar foil coated with a thin aluminium layer.

The scintillating layers offered a direct and online measure for the range of the impinging particle bunches and hence their kinetic energy, when reducing the two-dimensional RadEye signal to a laterally integrated depth-dose curve (figure 5.5b). An example, simulating the energy deposition using FLUKA and neglecting scintillator effects such as quenching for high LET protons, is given by the layers L1 - L9 in figure 5.5a. Figure 5.5a was generated from the simulated two-dimensional data in figure 5.5b. The result is showing the familiar Bragg peak-like signal as expected for the simulated monoenergetic 17 MeV proton beam. A simple estimation of the proton beam high energy cut-off can possibly be done by counting the number of penetrated layers, i.e. layers showing scintillation signal and using a prior calculated look-up table quantifying the energy needed to penetrate each layer (figure 5.5a). Given that the light yield in PDMS is supposed to

scale linearly with the energy deposition of each particle in the bunch, a broadband spectrum could be reconstructed as described by Englbrecht et al., similarly as for the offline RCF stacks (section 3.4.3) [165, 57]. Such simple evaluation is enabled by the optically separated layers and difficult for monolithic scintillators.

The RadEye sensor in general is sensitive to optical photons, protons, electrons and X-rays and had to be therefore shielded from ambient light, laser light, EMP and the multi-species spray from the LION acceleration process. To this end, the stack was placed in a light tight aluminium housing with a 4 mm entrance hole shielded by a 15 μm aluminium foil (figure 5.4a). Additionally, radiation-induced damages of the RadEye sensor were reduced by the housing and the sensor mounting parallel to the beam axis.

The performance of the developed prototype was evaluated in experiments performed in controlled conditions using a 22 MeV proton beam at the MLL tandem accelerator. In these first tests, several shortcomings of this prototype scintillator stack have been identified: non-uniform coupling of the layers to the CMOS sensor, bright halo-areas in-between the scintillation layers, non-homogeneous thickness of the layers (figure 5.5b) and severe discrepancies between idealized FLUKA simulations and the measured number of scintillating layers [57, 158]. Accurate and precise proton energy spectrometry using a-priori MC simulations was hence not possible within the time of the project. The usage of calibration measurements of the 22 MeV proton beam, degraded by various numbers of plastic layers, allowed to roughly calibrate the layer numbers against proton beam energy. Simple polyenergetic metallic filters were also roughly reconstructed [57].

After proving reliably operating in a vacuum chamber at the tandem accelerator, the prototype stack was tested at the LION experiment in LEX. Device failures and distorted images stopped to occur after the vacuum side of the RRE cable (DVI-cable) inside the vacuum chamber had been jacketed in a copper fabric tube. Background noise due to electrons and X-rays stopped after the front face was covered with 5 mm lead. Data of the exponentially decaying proton spectrum at the LION experiment, in order to test the stack and the reconstruction using calibration data, could not be measured, as the proton energies did not exceed 7 MeV at that time. The reasons are discussed in section 7.2.1.

The destructive dismount of the stack after all experiments were performed, the disagreement of MC simulation and measured ranges was found mainly to originate from observed differences (between 297 μm – 366 μm) in the real and the nominal thickness (150 μm) of PTFE and PDMS (83 μm – 231 μm \neq 150 μm) [158].

Further developments and improvements in the design could potentially result in a reliable spectral diagnostic device for laser-accelerated ion bunches. Especially the manufacturing process should be improved to avoid manual fabrication steps, leading to differences in the layer thickness.

The limited spatial resolution could be enhanced by the use of a second RadEye along the long edge to read out the perpendicular edge of the PDMS layers. The two-sided read-out could allow to judge not only the energy spectrum of the bunch, but also the beam pointing and divergence (figure 5.4b). Two *RadEyes* could in future also be connected

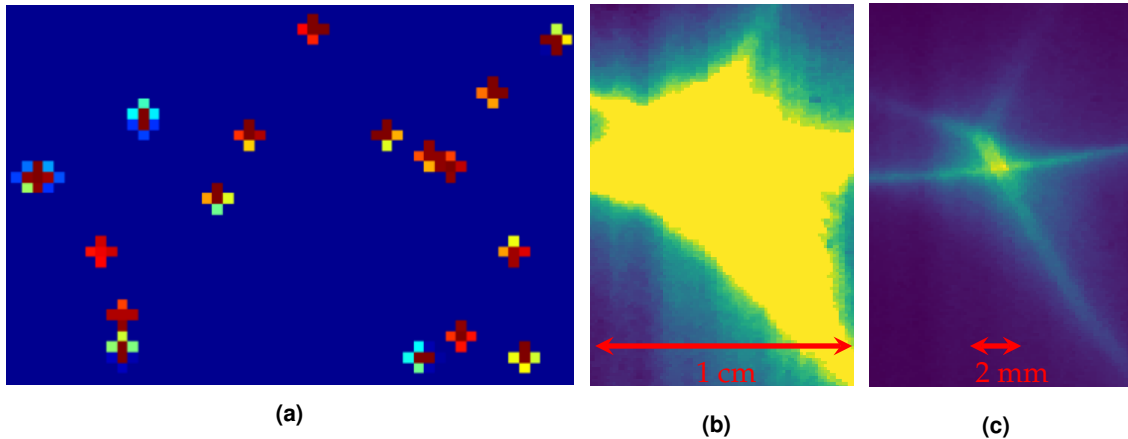


Figure 5.6: Experimental results motivating HDR-readout development. (a) RadEye signal from single gold ions [61]. (b) QP focus of 12 MeV protons from LION@LEX measured using the 2nd IP scan. (c) 6th IP scan.

on the short edge to build a 10 cm long scintillator stack using thicker layers, according to a simple MC estimation. For the spectrometry up to 100 MeV protons as expected for LION@CALA, 33×1 mm PDMS and 33×0.5 mm PTFE layers would be needed and easier to manufacture due to larger material thickness [57].

5.1.5 Dynamic range extension for RadEye

The usually undesired *Image-lag* phenomenon was investigated to be beneficially exploited, in order to compute 2D-images with a higher dynamic range than the 12-bit range of a single frame. Using visible light pulses from a laser diode and analytical simulations for single-slit diffraction, RadEye-specific calibration factors to stack multiple consecutive readouts were successfully derived. They can be used to quantitatively reconstruct spatial information about the optical diffraction beam in saturated areas and hence extend the dynamic range of the detector compared to a single frame.

Several limitations in the dynamic range of the RadEye during proton acceleration experiments and an experimental observation using ^{79}Au ions motivated the development of high-dynamic range (HDR) imaging.

^{79}Au ions were accelerated by the MLL accelerator to 7 MeV/u and directly impinged onto the RadEye sensor in vacuum. Individual ions saturated the impact pixel due to high energy deposition. The created star-like pattern of the individual ions can be attributed to an overflow of the potential well, which traps the created charge in the pixel, since the cluster-sums are of the same order of magnitude. The consecutive frames in free-running mode showed *after glowing* in the hit pixels (figure 5.6a).

When used as position detector for laser-driven proton bunches in the LION@LEX and LION@CALA experiments, the dynamic range of the RadEye sensors hindered the quan-

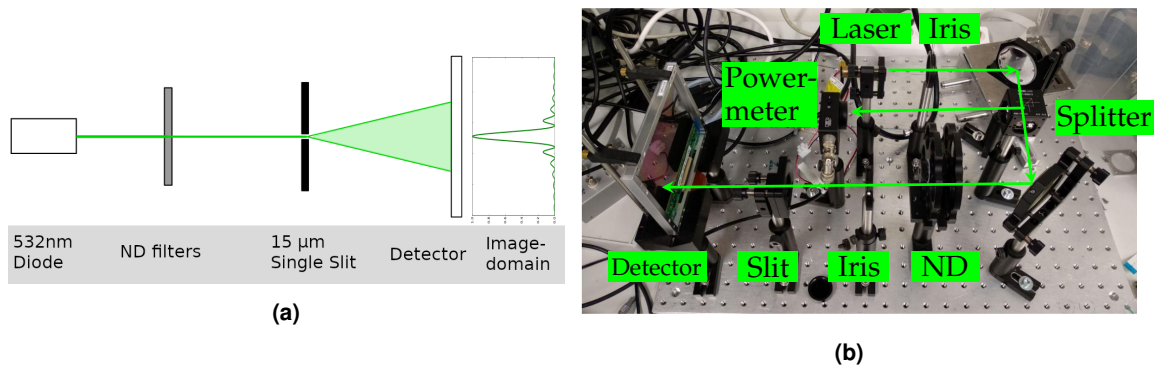


Figure 5.7: Optical characterisation of pixel detectors. (a) Schematic setup (adapted from [52]). (b) Experimental setup using laser diode, pixel detector and parallel power meter monitoring.

titative measurement of the bunch spectrum over the full kinetic energy range. The exponential bunch spectrum always saturated the detector in the low energy region (figure 7.3b) [52].

The refocusing of the initially divergent proton bunches from the LION experiment is crucial in order to have sufficient particle numbers for possible applications. The measurement of the proton focus achieved by the PMQs relies on the usage of IPs, as the number of focused protons is so high that the large dynamic range of IPs has to be used (section 3.4.3). Each scan of the IP requires time, as the dynamic range of available digital flatbed scanners has to be used multiple times in order to calculate HDR images (figure 5.6b, figure 5.6c). The final goal would be a focus quantification for PMQs at repetition rates around 1 Hz rather than the $\approx 1/3600$ Hz for IPs.

Image lag in CMOS detectors The so called *Image lag* phenomenon is known from classical photography as the existence of signal through multiple readouts of an illuminated semiconductor pixel sensor. Technically, each CMOS pixel acts as a capacitor storing the generated charge and has integrated read-out and amplification electronics. The fraction of pixel area used for available for charge collection and not used by the electronics is called fill factor and today typically around 80% for CMOS pixels. A typical pixel layout is the so called *three transistor (3T)* layout. Each pixel contains a photodiode and three transistors for reset, buffering and multiplexing. In contrast to CCD sensors with an amorphous sensor surface, the charge in a 3T pixel is hence physically confined inside the photodiode. The transistor for reset usually is only able to partially restore the voltage of the capacitance and thereby reset the pixel count [75, 117]. Furthermore, crystal defects and impurities in the active layer of the photodiode can be trapping free charge carriers. These traps release the photo-induced charge through thermal disexcitation with a characteristic time constant, similar to the simulated disexcitation of IPs (section 3.4.3).

As described, the RadEye system is controlled by self-written C++ software, which writes the configuration strings to the PLC (section 5.1.1). In order to record consecutive frames

5 INVESTIGATION OF PIXEL DETECTORS FOR APPLICATIONS AT LASER-DRIVEN PARTICLE BEAMS

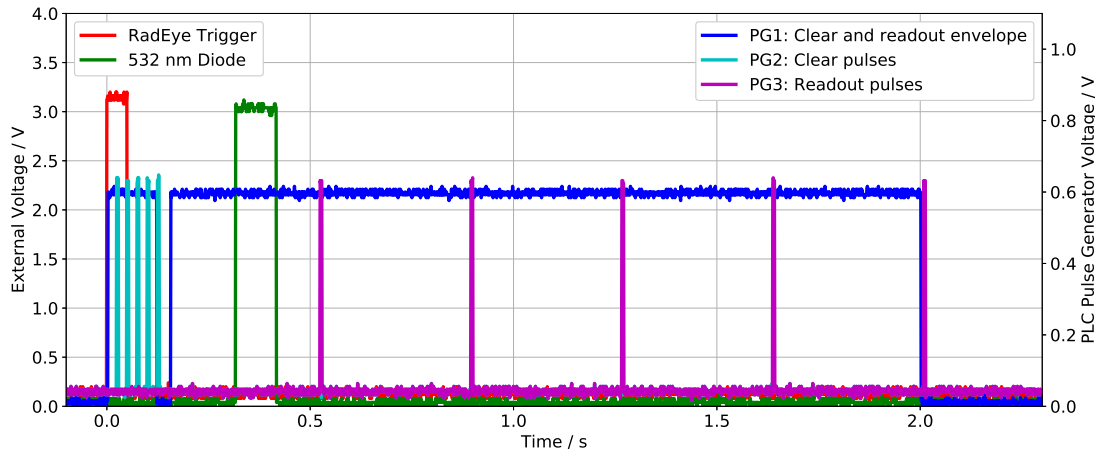


Figure 5.8: Timeline of PLC pulse generator signals used for HDR-Readout of five frames (PG3) after laser illumination (green) of the cleared sensor (PG2), triggered by a time-controlled external TTL trigger (red).

with controlled clearing, readout and frame-spacing times after receiving an external TTL trigger, the timing capabilities developed in section 5.1.3 were extended and made available in the graphical user interface [178].

Optical setup The scheme of the setup for controlled measurements of saturation is displayed in figure 5.7b. A 532 nm, 1 mW green laser diode was used to illuminate a single slit of $15 \mu\text{m}$ width. The light intensity was varied by insertion of different *neutral density filters* (ND-filters) into the beam path, in order to explore the 2D-ADU distribution in second readouts as function of incident light. The ND filter reduced the beam power logarithmically for all wavelengths. The single slit diffraction pattern directly shined onto a single RadEye sensor module of $5 \text{ cm} \times 2.5 \text{ cm}$ active area, mounted at 11.5 cm distance from the diode.

The exact timing for all experiments is shown in figure 5.8. A two-channel *function generator* (FG) DG1032 (Rigol Technologies EU) was used to generate the external TTL trigger signal (red) for the RadEye ($t=0$). The *delay generator* (DG) DG535 (Stanford research systems) was used to self-trigger the second channel of the FG to generate a 250 ms *diode on* pulse, ending 50 ms before the first readout. The *diode on* pulse controlled a dedicated 230 V-powered transistor, acting as operational-amplifier delivering sufficient power to the 532 nm, 1 mW diode. The light output was constantly monitored by a power meter (ThorLabs PM100USB with S120C sensor head) using a 50:50 beam splitter (figure 5.7b). The light output seemed to be randomly varying but the absolute ADUs by the light on the RadEye could be normalized using the power meter reading [10].

The PLC logic was set up to issue five clearing pulses of 25 ms length (PG2) and five readout pulses of 5 ms length (PG3) while PG1 is high, in order to have the 250 ms illumination by the diode to strike the sensor in low dark current condition (figure 5.8).

	ND filter setting	Transmission (of ND filter) [%]	Ratio $O^{th}Max/1^{st}Max$	Deviation of ratio to ground truth
Ground truth (eq. 5.1)	0.0	100.00	20.3	0%
Measured first frames (unsaturated)	2.7	0.20	22.6	11%
	2.5	0.32	21.5	6%
Measured first frames (saturated) stacked with second frames using regression calibration	2.4	0.40	20.3	0%
	2.2	0.63	23.1	14%
	2.0	1.00	17.7	16%
	1.8	1.59	8.2	60%
	1.3	5.01	2.7	87%

Table 5.1: Characteristics of used ND filters and simulated and measured ratios between O^{th} and 1^{st} order maximum for equation 5.1. Column 4 lists the deviation of the measured ratios to the analytical ratios [52].

The readout period was fixed to 370 ms for all frames, since this is the minimal frame duration of the RadEye. Shorter frame duration and hence shorter time between illumination and the consecutive readouts may enable a readout of the induced signal in future measurements, before the signal decays or before electronic noise is accumulated.

Measured one-dimensional lineouts were generated from the two-dimensional images perpendicular to the slit direction. Images were acquired and evaluated for a set of ND filters, causing various levels of saturation in the central maximum (0^{th} order) of the measured intensity distribution (ND 1.8 and ND 2.4 shown in figure 5.10):

Evaluation Mathematically, the one-dimensional intensity pattern of single slit diffraction using the Fraunhofer approximation in the far field can be approximated using equation 5.1 [98].

$$(5.1) \quad I(x) = I_0 \cdot \text{sinc}^2\left(\frac{D \cdot x}{d \cdot \lambda}\right)$$

Using analytical Python calculations of the expected intensity distribution $I(x)$ with the wavelength $\lambda = 532$ nm, the slit width $b = 15$ μm and the slit-to-screen distance D from the setup (figure 5.7b), one-dimensional lineouts in the observation plane using equation 5.1 were generated as ground truth.

Consecutive multiple readouts of the RadEye sensor showed that a distinct signal remained in the second readout frame after illumination with the 250 ms flash from the laser diode. The magnitude of the signal (ADUs) was about one order of magnitude lower than the ADUs in the first readout (figure 5.9a and figure 5.9c). In areas of satura-

5 INVESTIGATION OF PIXEL DETECTORS FOR APPLICATIONS AT LASER-DRIVEN PARTICLE BEAMS

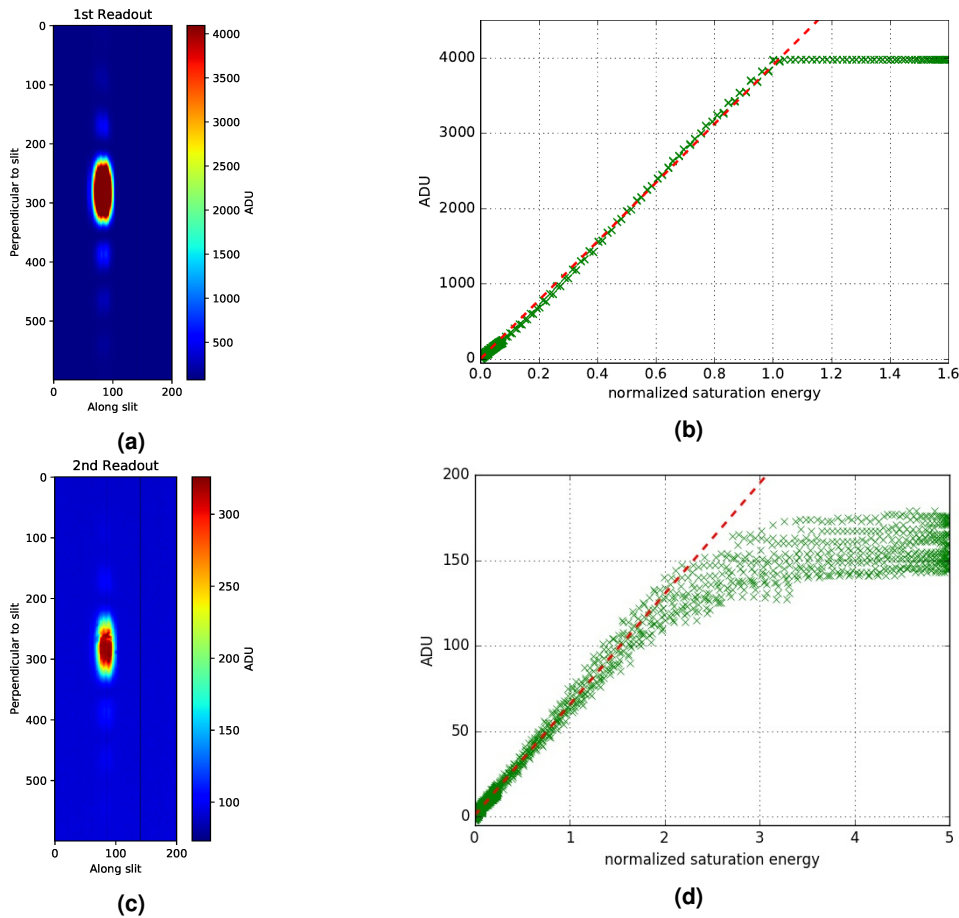


Figure 5.9: Test of RadEye linearity and image lag using visible light. (a) First frame and (c) second frame after single pulse illumination using ND 2.4. The diffraction pattern saturates part of the first frame. The second readout reveals an ADU pattern of up to 350 ADU in the previously saturated area. (b) ADUs in the first and (d) second frame plotted against the normalized saturation energy (energy content of the laser pulse) derived from equation 5.1. The dashed red line is a linear fit through all values below one time saturation energy.

tion in the first frame, the second frame displayed non-saturated shapes following equation 5.1, which indicated the presence of quantitatively usable information not present in the first frame. Only the first two readouts were included in the evaluation (figure 5.9), since the consecutive frames 3, 4 and 5 only showed signal at the noise level.

HDR Stacking results As the ADU values in the second frames of the optical experiments generally were for all ND filters smaller than the ADU values in the first frames (figure 5.9), a suitable calibration factor per ND filter was derived in order to stack the second onto the first frame and extend the dynamic range (figure 5.10). To this end, linear regression between the non-saturated pixels in the first frame and the spatially corresponding pixels in the second frame was performed for each pixel (figure 5.9b, figure 5.9d).

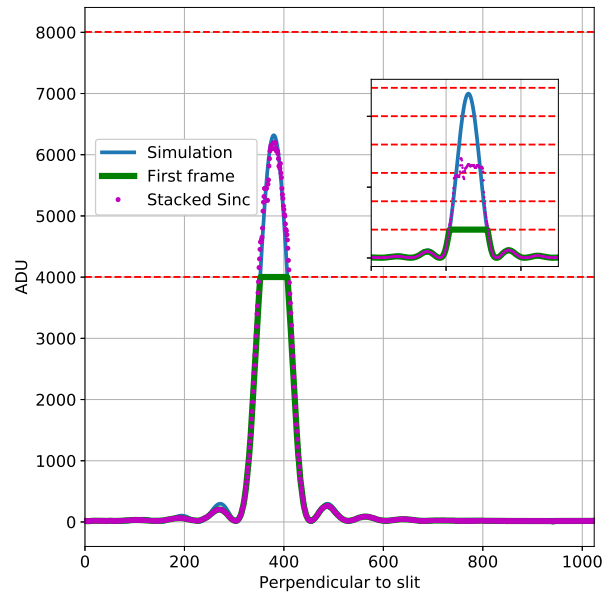


Figure 5.10: Range extension of the saturated first and signal from second readout for ND 2.4. Dashed red lines mark multiples of the saturation level (4096 ADU). The inlay panel proves that the trustworthiness of the stacking method breaks down for stronger over-illumination (ND 1.8).

The response of the RadEye was found linear up to the saturation level in the first frame (figure 5.9b) and up to $2 \times$ the saturation level in the second frame (figure 5.9d). However, the variance around the linear mean is clearly larger for the second frame. The regression to obtain the calibration factor between the first and second frame signal was hence linear between ADUs in first and second frames. The regression was extrapolated into the saturated area above $2 \times$ saturation level (figure 5.9d). This enabled to double the dynamic range of the sensor by single global calibration value for the ADUs in the second frame (figure 5.10).

To stack extended dynamic range images, the saturated part of the first frame, typically the O^{th} order maximum of the diffraction pattern (figure 5.9a) was automatically masked and replaced. Replacement was done with the ADUs from the second frame (figure 5.9c) using the calibration factor (figure 5.9). As both frames came from the same short laser diode pulse, no spatial jitter occurred and the slope of the transition between both frames was guaranteed.

The stacking was repeated for the different ND filters. The 1^{st} order maximum was unsaturated for all ND-settings. The O^{th} order maximum of the diffraction pattern, i.e. the shape of equation 5.1, was retrieved using the scaled second frame. The ratio of the O^{th} order maximum (the central and possibly saturated but reconstructed maximum) and the unsaturated 1^{st} order maximum was calculated (column 4 in table 5.1). By comparison of the measured unsaturated, the reconstructed and the analytical ratios, the level of reliable dynamic range extension was derived (column 3 in table 5.1).

For ND 2.2 and 2.4 (slight saturation depicted in figure 5.10) the 0^{th} order maximum is found to lie in-between one and two times the saturation level. The stacked images for ND 2.2 and 2.4 are, judging from the uncertainty of the measured ADU from the unsaturated ND 2.5 and 2.7, in agreement with the ADU level predicted by equation 5.1. ND 2.5 and 2.7 were used to have also the 0^{th} order maximum unsaturated, in order to validate agreement of analytical ground truth and measured $I(x)$. ND values of 2.0 or smaller resulted in a simulated 0^{th} order maximum with more than two times saturation level and therefore exceed the dynamic range extension enabled by this work (inlay of figure 5.10).

The deviations of the observed ratio between simulation and ND 2.5 and ND 2.7 (column 4 in table 5.1) might be attributed to a slight dependence of the *quantum efficiency* (QE) on the signal level of the RadEye sensor. For 532 nm, the QE is reported to rise from 32% for a signal level of 500 ADU to 37% for 1500 ADUs (saturation of 4096 ADUs) [181].

The conservative evaluation revealed a range extension of one bit, which means that the dynamic range was successfully doubled. Although such range extension was successful for visible light, the results can not directly be translated for the case of higher LET-radiation.

Further experiments and results for the dynamic range extension with the RadEye sensor using conventionally accelerated proton bunches at the MLL tandem accelerator, as well as using laser-accelerated proton bunches at the LION experiment at CALA, can be found in the appendix. There, first results for the derivation of a calibration factor for higher-LET radiation (protons) is shown (section A.1).

5.2 CM49 CMOS sensor

Although the RadEye system proved to be radiation hard and durable in the harsh laser-ion acceleration environment, the accumulated radiation damage, wrong mechanical and electrostatic handling, together with the engineering grade quality, lead to the inevitable replacement of approximately 20 RadEye sensors during 5 years of operation in the LION experiment. As the sensors can hence be seen as a consumable, the discontinuation of the RadEye product family in 2019 by the manufacturer demanded for research in an successor sensor.

5.2.1 CM49 CMOS sensor characteristics

For the SIRMIO-project, CM49 and other position-sensitive CMOS detectors were tested for pre-treatment proton imaging for position verification and treatment planning [169, 208, 205, 207, 206, 204, 203].

	4 × RadEye sensor	CM49
Sensor Type	CMOS	CMOS
Pixel size [μm^2]	48 × 48	49.5 × 49.5
Active area [cm^2]	4.92 × 9.84	6.4 × 11.4
Resolution [pixels]	1024 × 2048	1300 × 2304
Network interface	GigE	GigE
Commercial detector for	X-rays (using scintillator)	X-rays (using scintillator)
Manufacturer	Rad-icon (now Teledyne DALSA)	Teledyne DALSA
Active thickness [μm]	2	$\approx 2 - 10$
Fill factor	> 80%	79%
Readout [Hz]	2.5	20
Fluence tested [p^+ / cm^2]	6×10^{10}	tbd
Flux tested [$p^+ / \text{cm}^2 / \text{ns}$]	10^5	tbd
Sensitivity	single proton	single proton

Table 5.2: Technical specifications of the used commercial CMOS detector systems RadEye [193, 194, 178, 179, 180, 181, 85] and CM49 [225, 226].

A possible candidate, based on the similarity to the RadEye sensor was the CM49 sensor (table 5.2). It is included in the Shad-o-Box HS 3K HS detector system (Teledyne DALSA, Canada) for scintillator based X-ray detection in dental medicine [225, 226]. It offers similar pixel size, a comparably large sensor area, a similar pixel fill factor and it is also based on the CMOS technology with updated pixel design. The active thickness was expected to be similar but was not known initially.

Inside the Shad-o-Box, the CM49 sensor is connected to the frame grabber and control electronics on the Xineos-PCB with a 11 cm long, rigid SB3KHS flat ribbon cable with 80-lanes (figure 5.1b). The sensor is placed below a light tight X-ray plastic scintillator, which was removed permanently. The same procedure was done for the RadEye initially. In contrast to the old RadEye section 5.1.2, the ADCs digitizing the pixel signals are on the sensor PCB, rather than inside a remote control electronics box together with the frame grabber as for the remote RadEye system.

The 4.92 cm × 9.84 cm active silicon surface is free standing without any ceramic substrate, possibly allowing to build a two-dimensional pixelated range telescope in order to deduce the particle kinetic energy using multiple free-standing CM49 sensors. Initially, the sensor was glued to an aluminium housing, as visible in figure 5.11b.

As described in the following sections, the CM49 was tested and characterized for the desired features listed in section 3.4.2. First results regarding the charge sharing between pixels, the temperature stability in vacuum and the HDR capability using visible light and protons can be found in section A.2 of the appendix.

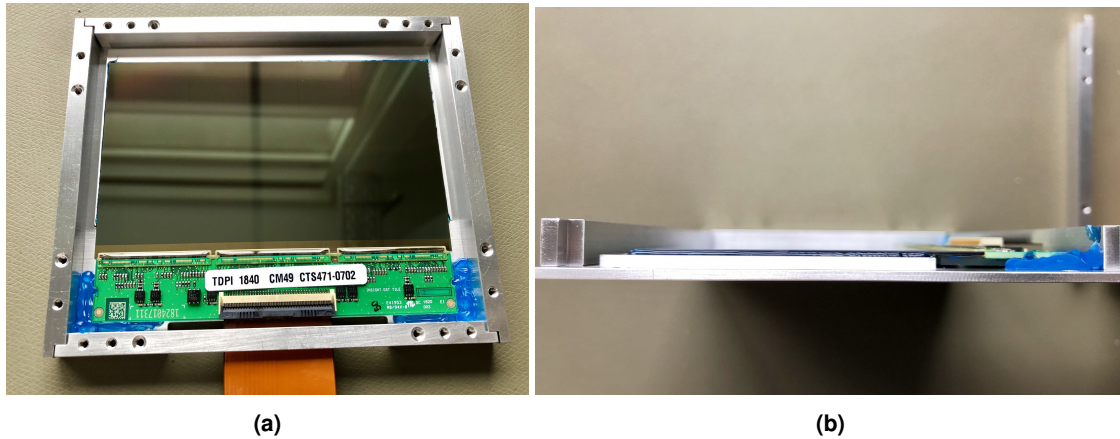


Figure 5.11: Uncovered CM49 sensor surface. (a) Front view. A PCB with the ADC units (b) Side view. The $6.4 \times 11.4 \text{ cm}^2$ sensitive surface was glued by the manufacturer using blue glue to a bulky aluminium housing. The glue was removed by multiple cycles of air-removal and venting in a vacuum chamber.

5.2.2 CM49 as photon sensitive position detector

As first test of the photon sensitivity and physical robustness, a sheet of white paper, printed with black ink, was directly brought in contact with the sensitive area. Using the framegrabber driver, a C-program was developed and employed to reproducibly illuminate the sensor upon external TTL-trigger for 1 s. Figure 5.12 clearly shows the LMU seal, printed with black ink on white paper, with fine detail. The detector was found to be sensitive to light, acquiring low-dark current, triggerable and robust.

5.2.3 Initial investigations of the CM49 as position sensitive proton detector for conventional and laser protons

Remote RadEye-like configuration The presence of the ADCs on the sensor PCB makes the CM49 sensor more likely to fail in a laser-driven ion accelerator application, since thereby the ADCs are placed in the beam path of the primary electron and proton radiation, as well as the shower of secondary particles and the EMP.

The Xineos-PCB with further control electronics was successfully spatially separated from the CM49 sensor by more than the initial 11 cm of the SB3KHS cable. The creation of a more flexible setup with longer cables was initially thought to be hindered by the digital signal timing. The clock timing of the Xineos-PCB, which can not be changed using software, is tailored to the 11 cm cable length. However, the detector system was still fully operational after the addition of a 25.4 cm cable (Samtec EQCD-040-10-TBR-STR-1), as visible in figure 5.13a.

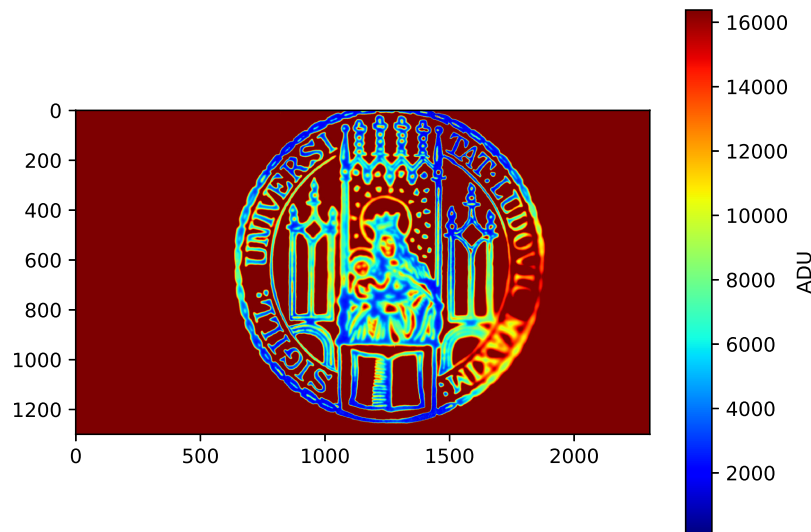


Figure 5.12: Test of visible light sensitivity using an LMU seal printed with black ink on paper, directly laid onto the sensitive area (figure 5.11a).

Vacuum compatibility The CM49 sensor, the Xineos-PCB and the Samtec extension cable were successfully operated in a small vacuum chamber pumped down to vacuum. After the first ≈ 165 h long pump down to a pressure of 6×10^{-7} mbar, the outgassed electronics were still fully functional. The blue glue fixing the sensor to the aluminium housing (figure A.5) had dried due to pump down. The then outgassed components were altogether successfully operated inside the pumped down chamber using two 8-pin LEMO feedthroughs (4+2-pin for readout trigger and power supply, 8-pin for Ethernet data connection) in 10 Hz continuous readout mode. After 30 minutes of readout in vacuum, the on-board temperature sensor of the PCB displayed the final maximum temperature of $\approx 65^\circ$. The dark-current level was well below 1%.

As TTL trigger pulses, 20 ms long square pulses of 6 V at a frequency of 10 Hz proved reliable.

Sensitivity to alpha particles The CM49 sensor proved to be sensitive to ionizing particles. A mixed nuclide α -source was placed in the evacuated vacuum chamber directly on the CM49. The α -source, consisting of ^{239}Pu , ^{241}Am and ^{244}Cm with dominant α -lines at 5.16 MeV, 5.49 MeV, 5.80 MeV, resulted in single-pixel responses with no sign of charge sharing or blooming.

However, the activity was too low in order to experimentally determine the active thickness of the CM49 sensor, as the thickness could not be provided by the manufacturer. The value of $\approx 10 \mu\text{m}$, as stated by the manufacturer is subject to ongoing discussion because in-house experiments $3 \mu\text{m}$ [214, 204]. Based on FLUKA calculations, the collimated α -source was scanned in distance around 26.5 mm of air away from the sensor surface, in order to place the Bragg peaks of the α -particles in the $\approx 10 \mu\text{m}$ active thickness under

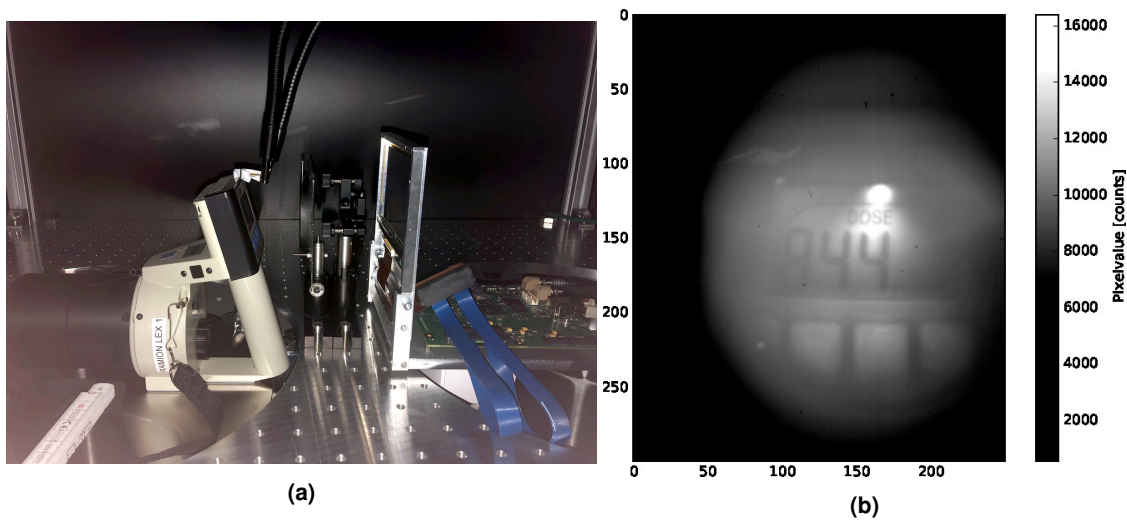


Figure 5.13: EMP viability test of the CM49 outside the LION chamber. **(a)** RAM ION Meter ionization chamber and CM49 detector above interaction target on top of LION chamber. **(b)** Image of RAM ION using CM49. Accumulated dose reads $84.4 \mu\text{Sv}$.

the assumed $2 \mu\text{m}$ passivation layer of SiO_2 as deduced from the RadEye [193, 184, 194].

The determination of the active thickness of the active layer thickness will in future give a crucial calibration factor in order to extract quantitative particle numbers from the pixel counts, namely convert ADUs to particle numbers. This factor is essential for the measurement of quantitative charged particle beams impinging on the detector in laser-ion acceleration experiments, as well as for the usage of the detector in the SIRMIO project [169, 208, 205, 207, 206, 204, 203].

Operation at LION@CALA close to the laser-plasma interaction In order to test the EMP viability, the CM49 and the Xineos-PCB were as a first experiment mounted on top of the LION experimental chamber in CALA. The distance of the CM49 system to the laser-plasma interaction target, i.e. the source of the intense EMP, was $\approx 1.5 \text{ m}$ of vacuum and shielded by the $\approx 3 \text{ cm}$ of steel roof (figure 5.13a). A RAM ION Meter ionisation chamber (*Rotem Industries, Israel*) was imaged by a lens onto the CM49. The sensor was still fully operational after the accumulation of 60 shots on 50 nm and 200 nm thick plastic foil targets. The $84.4 \mu\text{Sv}$ of dose measured by the IC served as a proof that the laser pulses hit the target (figure 5.13b).

As a second step, the CM49 with Xineos-PCB was then placed inside the LION chamber at $\approx 1.5 \text{ m}$ distance in forward direction. The angle relative to the beam axis was $> 35^\circ$, such that no radiation originating from the target could strike the sensor (figure 5.14). Shots on 50 nm plastic foil targets left the detector fully functional.

Future experiments may test the performance for acceleration beamtimes using metal foils, which will increase the strength of the EMP.

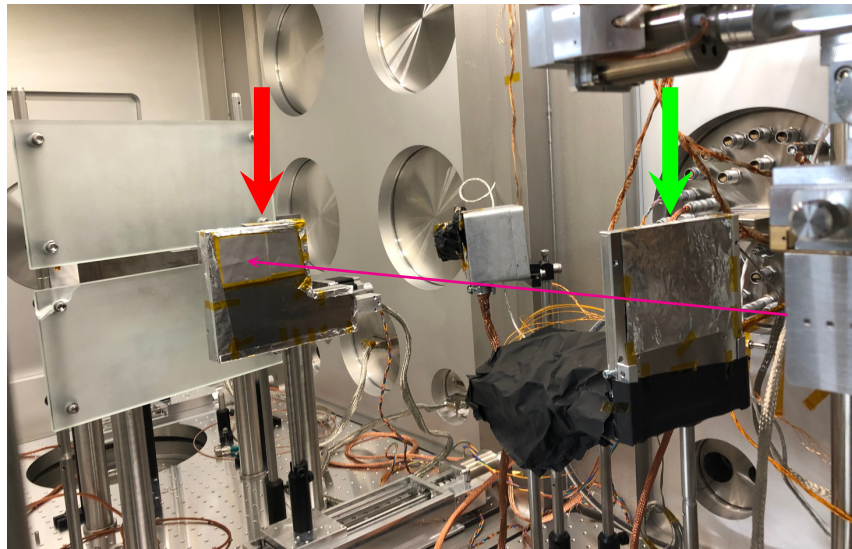


Figure 5.14: EMP viability test of the CM49 detector inside the LION chamber. The proton bunches (beam direction along magenta coloured arrow) impinge under 0° onto the four RadEye sensors (red arrow). The CM49 was placed of-axis (green arrow) to avoid direct proton hits for this first EMP test.

Further experiments and results for the dynamic range extension with the CM49 sensor using the single-slit experiment described in section 5.1.5, as well as using conventionally accelerated proton bunches at the MLL tandem accelerator, can be found in the appendix (section A.2).

Chapter 6

Detector application 1: Development of MC based reconstruction of secondary electrons in Laser-ion acceleration

Results acquired by the author from the work presented in section 6.1 have been published as a journal paper in *Review of Scientific Instruments*.

- Paper: F H Lindner, J Bin, **F Englbrecht** et al.: A novel approach to electron data background treatment in a new online wide-angle spectrometer for laser-accelerated ion and electron bunches, *Review of Scientific Instruments* 89: 013301, 2018

The author has presented the work in section 6.2 orally at the *DGMP 2016* conference and as a poster at the *AAPM 2016* conference.

- Oral Presentation: **F Englbrecht** et al.: Messung und Monte Carlo Simulation von Elektronen Phasenräumen mittels eines magnetischen Elektronen Spektrometers mit großem Akzeptanzwinkel, *Annual conference of the German Society for Medical Physics, DGMP 2016, Würzburg, Germany*
- Poster: **F Englbrecht** et al.: SU-F-T-217: Measurement and Monte Carlo Simulation of Electron Phase Spaces Using a Wide Angle Magnetic Electron Spectrometer, *Annual Meeting of the American Association of Physicists in medicine, AAPM 2016, Washington DC, USA*

Part of the work presented in section 6.4 and section 6.5 has been published as a master thesis at LMU, supervised by the author. The author has presented the results as a poster at the *ALPA 2015* conference.

6 DETECTOR APPLICATION 1: DEVELOPMENT OF MC BASED RECONSTRUCTION OF SECONDARY ELECTRONS IN LASER-ION ACCELERATION

- **F Englbrecht** et al.: Angular-energy Distribution Reconstruction of Electrons Emitted from Laser Irradiated Foils, *Application of Laser-driven Particle Acceleration, ALPA 2015, Venice, Italy*
 - Master thesis: A. Wislsperger: Monte Carlo Based Phase Space Reconstruction for Electrons in Laser Driven Ion Acceleration, 2017
-

Particle detector technology for laser-accelerated ion bunches is facing the transition from offline, low repetition rate diagnostics towards online, up to few Hz repetition rate detector systems (section 3.4) [61, 250]. The characterisation of typical ion bunch parameters (such as energy spectrum, absolute particle number and spatial bunch divergence) with high shot numbers is the key ingredient allowing experimental exploration of the optimal parameters for the acceleration (e.g. laser energy density on target, laser pulse temporal contrast, target material and spatial shape) in order to develop a stable particle source for applications.

Both the experiments LION@LEX and the LION@CALA relied on a combined electron proton *wide angle spectrometer* (WASP) as main electron and ion diagnostics. As described in section 3.3, the hot electrons exiting the target surface generate the accelerating field gradient between the target backside and the electrons and could thus be correlated to the ion bunch characteristics. Using RadEye sensors (section 5.1), the WASP allows the simultaneous online detection of spectrum and divergence of protons and electrons originating in the same laser shot. Their correlation may give insight into the acceleration mechanism (in LEX: mostly TNSA [215]) as predicted by simulations and experiments and may help to narrow down the experimental parameter space to an optimum [155, 209, 222, 61].

The demand for quantitative reconstruction of the electron energy and spatial distribution from the laser-target interaction, together with the demand for a model able to describe the explicit correlation of electron and proton spectrum motivated the presented studies, which aimed at characterizing the influence of the WASP onto the finally reconstructed spectrum of electrons and protons. Another motivation is that by measuring the electron distribution only and being able to predict the proton distribution, the protons could directly be used for experiments. Experiments today therefore either try to be less demanding on the shot-to-shot stability or are deducing the spectrum of protons from invasive, so beam manipulating or degrading measurements of the proton bunches (or of at least some fraction, as necessary for the proton-radiographies in section 7.2.1).

For the experiments in LEX and CALA, the electron and ion spectra were deduced from the two-dimensional particle fluence distribution on the corresponding two $5\text{ cm} \times 10\text{ cm}$ detector maps of the WASP (section 6.1). Physically *meaningful* approximate spectra are

gained by manually excluding areas of the detector using prior experience and knowledge on the WASP limitations. Such areas are regions where particles from the laser-target interaction (source position) are not supposed to be found, i.e. in too low or too high kinetic energy areas on the detector or in shades of the front-plate (figure 6.1). The manually selected *safe-to-evaluate-region* is usually then analysed by analytical tracking codes, which use the experimentally measured three dimensional magnetic vector field inside the WASP to assign to each detector pixel a fixed *energy-angle* coordinate. In this way, the real origin, for example scattered radiation or secondary particles from electromagnetic showers is not properly considered and scattered or secondary radiation is assigned a wrong *energy-angle* coordinate as it would have originated from the laser-target interaction. Moreover, any influence of the detection system *point-spread function* (PSF), namely the energy resolution of the WASP as an imaging system, is ignored. Additionally, the magnetic field measurement is challenging and prone to uncertainties. To overcome these limitations, forward Monte Carlo simulations may be used to disentangle the influence of the source and of the WASP on the reconstructed spectra.

In order to experimentally characterize the WASP (described in section 6.1), a well defined electron source was needed. To this end, a medical electron linac (*Siemens ONCOR*) was characterized using MC simulations of dosimetrically measured depth-dose distributions (DDD) and lateral field profiles (section 6.2). The forward simulations of the linac were done starting from *phasespaces* (PS) from the *International Atomic Energy Agency* (IAEA) database describing the considered accelerator model (section 6.2.1) [35]. The simulations of relevant dosimetric data were used to ensure concordance of the phasespaces with the used accelerator (section 6.2.2). After this validation, an experimental campaign using the WASP was then performed. Scintillators were tested for their visible light yield to allow for the best electron detection. The spatial distribution of large electron fields was recorded and the experiment was simulated using the phasespaces and a MC model of the WASP (section 6.2.3).

As second step, the system matrix method (section 6.3), which had previously been developed for the MC based reconstruction of electrons in magnetic spectrometers, had been used to generate a system matrix for the WASP at the ONCOR accelerator (section 6.4).

6.1 Combined electron proton spectrometer

The permanent-magnetic WASP had been built and equipped with RadEye sensors previously for low-power laser experiments (> 25 MeV proton energy). Here, a brief system overview is given, based on detailed and published descriptions [61, 138]:

Two neodymium permanent magnets ($10\text{ cm} \times 10\text{ cm}$, red in figure 6.1a) are mounted using an iron yoke. The magnetic field strength in the center is $|\vec{B}| \approx 150\text{ mT}$. The field-region inside the magnets and the front plate is $10\text{ cm} \times 10\text{ cm} \times 10.5\text{ cm}$ large. Bunches of particles enter the field-region through a thin slit in the front plate. By removing one

6 DETECTOR APPLICATION 1: DEVELOPMENT OF MC BASED RECONSTRUCTION OF SECONDARY ELECTRONS IN LASER-ION ACCELERATION

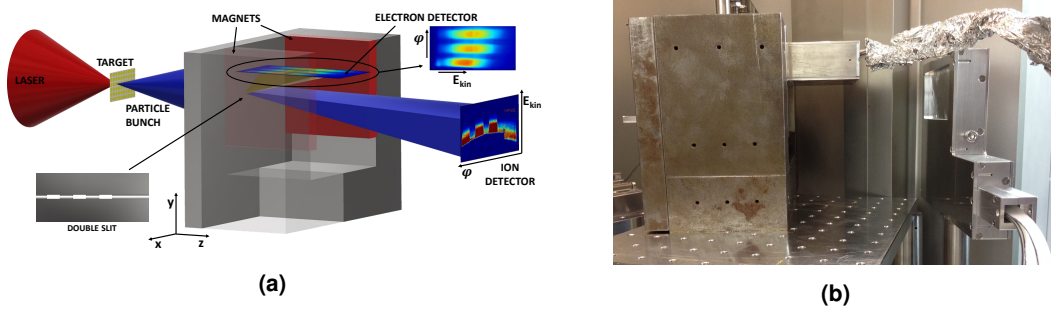


Figure 6.1: Simultaneous detection of electrons and protons at LEX. **(a)** Scheme depicting the WASP using a special slit, not used in the presented characterisation but in the LEX experiments: two 2 cm thick steel blocks are overlapping the left side of the cone-shaped bunch with a tooth-like array (light gray) for special ion-energy resolution [61]. **(b)** Setup of combined WASP in the LION@LEX vacuum chamber.

spatial dimension from the beam, the electron kinetic energy through magnetic deflection can be resolved. The height of the entrance slit is chosen experimentally as $200 \mu\text{m}$, balancing the energy resolution of the WASP and the signal-to-noise ratio. According to MC simulations using the FLUKA code, the CSDA range of a 25 MeV electron beam in tungsten of density $\rho = 19.3 \text{ g/cm}^3$ is 0.56 cm. The slit material is hence not transparent to electron energies accessible to the used linac ($< 25 \text{ MeV}$, figure 6.2). The entrance slit is 5 cm wide in order to allow for the lateral profile of the cone-beam-shaped beam profile induced by the laser to be measured.

For the electron detection, four RadEye sensors (chapter 5) are combined to yield a detection area of $5 \text{ cm} \times 10 \text{ cm}$. The four sensors are placed inside a compact aluminium housing ($10 \text{ cm} \times 3.5 \text{ cm} \times 16.5 \text{ cm}$), which, in laser-driven applications, is shielding them from visible light, the intense laser pulse and EMP. Electrons are deflected upwards and enter the housing after a drift in the field-region of 2.3 cm through a $10 \text{ cm} \times 5 \text{ cm}$ entrance opening. The opening is covered by $15 \mu\text{m}$ aluminium foil as laser light shield at 7 mm before the sensors, which corresponds to a total y -drift of 1 cm above the slit (figure 6.1a). The positioning of the sensors and the drift allow for the detection of up to 25 MeV electrons.

For proton detection, a second unit with four RadEye sensors can be mounted upright at $\approx 50 \text{ cm}$ behind the magnet yoke (figure 6.1b).

In the combined configuration for proton and electron detection, the WASP has been used in several thousand automated shots at LION@LEX and LION@CALA [79].

Although the $|\vec{B}|$ -field was precisely measured and analytical electron-trajectories were in sufficient agreement with the measured electron spectra, an experimental characterisation of the response function to monoenergetic electron beams was desirable, in order to discriminate between true signal and background contribution.

6.2 MC model of electron linac Siemens ONCOR

Similar to the GEANT4 simulations based on phasespaces generated with the FLUKA code in section 4.1, the usage of an accelerator phasespace (PS) allows to simulate the radiation fields generated by the accelerator, while representing the technology of the accelerator as a *black box* without the need to explicitly model the components of the linac head like target, yokes and jaws (figure 3.2b).

For the characterisation experiments of the WASP and the electron-reconstructions, the Siemens ONCOR linear accelerator at the university hospital Großhadern of Ludwig-Maximilians Universität München therefore was chosen, since the *International Atomic Energy Agency* (IAEA) provides phasespaces for ONCOR accelerators in their database of PS files for linear accelerators [35].

From the IAEA database, the binary PS files were downloaded for electron treatment fields without electron applicator, exhibiting a nominal size of $40\text{ cm} \times 40\text{ cm}$ and nominal beam energies of 6, 9, 12, 15, 18 and 21 MeV. The PS files are based on a full MC model of the accelerator treatment head, which had been tuned to dosimetric measurements in GEANT4 simulations by Faddegon et al. [63, 62, 64]. The PS files provide information such as energy, position and momentum vector on a single particle basis for all particles needed to simulate the treatment field as planned by the TPS. All PS files measure 380 GB in size and provide the single particle information for in total 450×10^6 particles across the six treatment field energies.

6.2.1 Phasespace analysis

The phasespace files were analysed using Python scripts running on the LS-Parodi HPC cluster. For each of the field energies, the types of particles, the energy spectrum of the electrons, the distribution of momentum vectors and the spatial field shape at $z = 19\text{ cm}$, the plane where the phasespace had been scored, were analysed.

Electrons make up the major fraction of particles, namely 88% (6 MeV), 82% (9 MeV), 77% (12 MeV), 59% (15 MeV), 54% (18 MeV) and 55% (21 MeV). The rest are photons give a minor yet non-negligible contribution to the depth-dose distribution, but are of lesser importance for the spectrometer simulations. The electrons in the six phasespaces are not monoenergetic, but present a Gaussian distribution with the mean value μ being within $\pm 0.5\text{ MeV}$ around the nominal energy, together with a small low-energy tail as shown in figure 6.2. The σ of the Gaussian distributions are below 0.9 MeV.

According to the PS analysis, at $z = 19\text{ cm}$, the field shape for all six energies differs from the nominal field size at isocenter $z = 100\text{ cm}$, which was specified as a flat $40\text{ cm} \times 40\text{ cm}$ square shape. The shape is more circular with $r = 15\text{ cm}$, but is more smooth and flat due to scattering at the measurement position $z = 95\text{ cm}$.

6 DETECTOR APPLICATION 1: DEVELOPMENT OF MC BASED RECONSTRUCTION OF SECONDARY ELECTRONS IN LASER-ION ACCELERATION

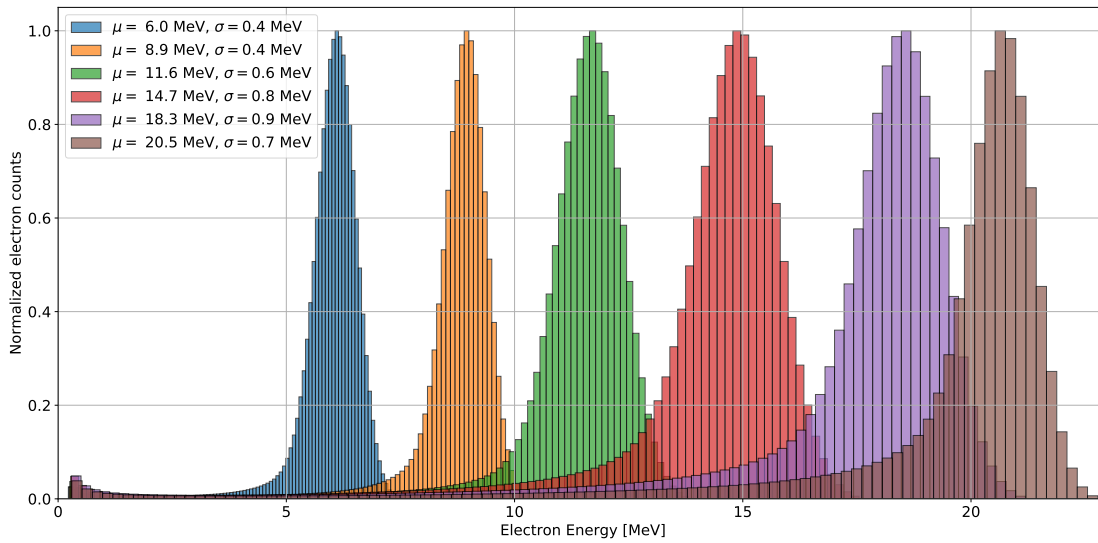


Figure 6.2: Spectra of electron energies extracted from the available IAEA phasespaces.

6.2.2 Measured dosimetric data as benchmark for phasespace beam model

Measured dosimetric depth-dose and lateral profiles At the time of this work, the ON-COR accelerator had been extensively used for photon treatments (X-ray target in) and electron treatments (X-ray target out) of patients. Although being the oldest linac machine in the radiation oncology department in Großhadern, it was still in use for scattered whole body palliative electron irradiation and hence maintained and dosimetrically characterized at the time of the WASP experiments.

The medical physics group of the radiation oncology department had measured central axis depth-dose profiles (DDD) and lateral profiles for the six treatment field energies using $40\text{ cm} \times 40\text{ cm}$ fields. The surface of an *IBA Blue* water phantom was placed at a *Source Surface Distance* (SSD) of 95 cm. The DDD and lateral profiles were measured using a small pin point ionisation chamber (PTW *Semiflex Chamber* 0.125 cm^3), scanned in 3D by motorized stages with an accuracy of $\pm 0.1\text{ mm}$.

FLUKA simulation of measured dosimetric depth-dose and lateral profiles The corresponding depth-dose distributions and lateral profiles were extracted from FLUKA Monte Carlo simulations using in input the six different phasespaces for the nominal field energies of 6, 9, 12, 15, 18 and 21 MeV.

To this end, the described measurement geometry was recreated in FLUKA. The water in the water phantom was modelled with a water density $\rho = 0.99777\text{ g/cm}^3$ as expected for water at a temperature of 20°C [174]. The correct inclusion of the water density at the corresponding 20°C room temperature had been crucial for simulations of clinical proton beams [53]. To model the particle source, the FLUKA user routine *source.f* was used for random sampling of 20×10^6 particles from the phasespace files. A total of

144 statistically independent simulations were run for each field energy and the results merged. In order to avoid the copying of the large phasespace files for each simulation run, symbolic file system links in the FLUKA run-directory, pointing to the central storage of the files, were created using the SLURM bash scripts.

The central axis depth-dose distribution as measured in the experiment with the water tank was extracted from a 3D USRBIN scoring of the dose deposition in a grid of 0.1 mm resolution [229]. The lateral profiles were also extracted from the same data, sampling the profiles from a 2D plane in the depth corresponding to the measurement depth below the water surface, namely $z = 96.4$ cm (6, 18 and 21 MeV), $z = 97.1$ cm (9 MeV) and $z = 97.7$ cm (12 and 15 MeV).

Nominal energy	$R_{80}(\text{Meas.})$ [mm]	$R_{80}(\text{Sim.})$ [mm]	$\ \Delta(R_{80}(\text{Meas.}) - R_{80}(\text{Sim.}))\ $ [mm]
6 MeV	20.6	20.2	0.4
9 MeV	30.8	30.6	0.2
12 MeV	41.2	40.6	0.6
15 MeV	50.9	51.5	0.6
18 MeV	63.1	63.3	0.2
21 MeV	72.4	70.0	2.4

Table 6.1: Measured and phasespace simulated R_{80} of the $40 \text{ cm} \times 40 \text{ cm}$ electron fields.

Validation of the simulated dosimetric data against measurements Using the 80% distal fall-off range R_{80} along the z-direction and the lateral profiles for the x- and y-direction, the agreement between the measurements and the simulations starting from the IAEA phasespace files was evaluated (figure 6.3, figure 6.4).

The range agreement of the R_{80} is displayed in table 6.1 and deemed satisfactory. All six simulations reproduce accurately the measured dose build-up region within the first few cm after the water surface, until the secondary electron equilibrium is reached. Except for 21 MeV, the range difference is less than 1 mm, which is the dosimetric criterion for a sufficient agreement between *treatment planning system* (TPS) and an accelerator commissioned for patient treatment. According to the medical physics department of the hospital, the 21 MeV beam energy is not used clinically and the field delivered by the accelerator is thus not commissioned. The large R_{80} difference in this case of 2.4 mm hence seemed plausible (figure 6.3f).

The agreement of the measured and simulated lateral distributions in x- and y-direction in terms of normalized mean square error is within a few percent and the profiles were seen as sufficiently flat along the central part corresponding to the 5 cm WASP entrance slit along all six field energies (figure 6.4). The phasespace hence seemed to sufficiently

6 DETECTOR APPLICATION 1: DEVELOPMENT OF MC BASED RECONSTRUCTION OF SECONDARY ELECTRONS IN LASER-ION ACCELERATION

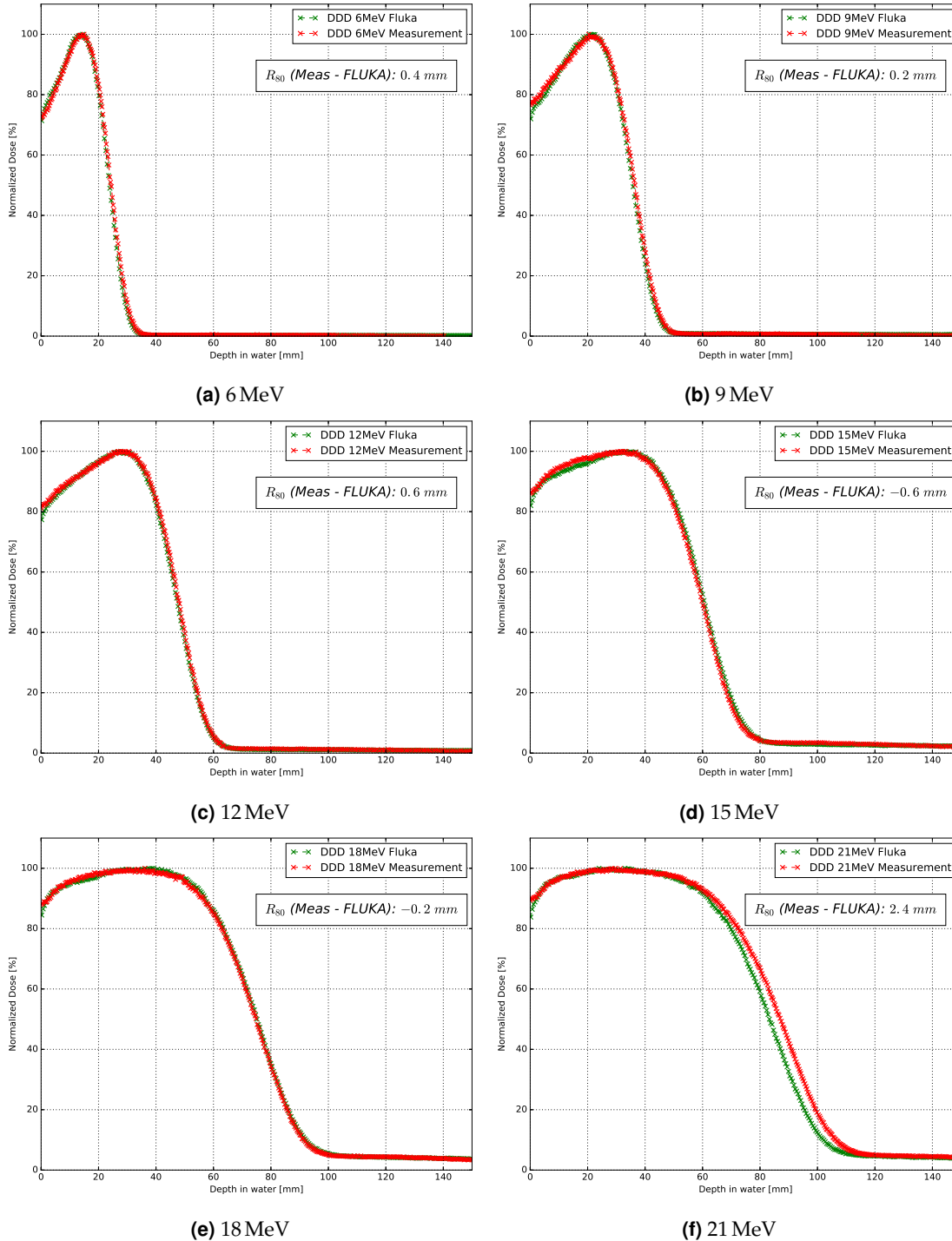


Figure 6.3: Measured (red) and FLUKA simulated (green) central axis depth-dose-profiles in water: 40 cm × 40 cm open fields were measured and forward simulated using the IAEA Phasespaces. Range discrepancies are below 1 mm for all energies except 21 MeV.

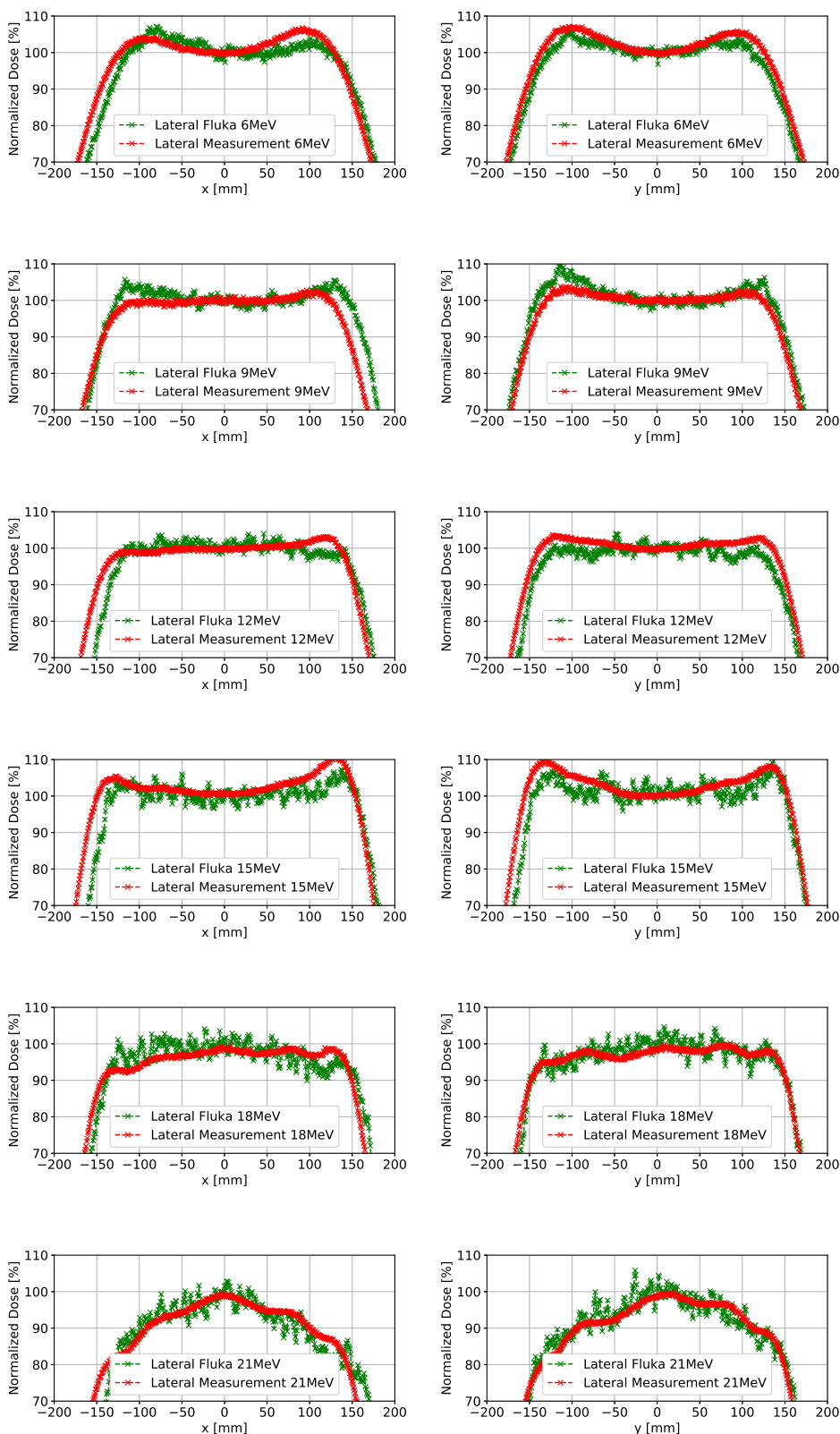


Figure 6.4: Measured (red) and FLUKA simulated (green) dose profiles in x- and y-direction in water: 40 cm × 40 cm fields without electron applicator were measured and forward simulated in the water phantom.

well represent the actual accelerator and to be of sufficient agreement in terms of the dosimetric data to be further used in the MC model of the spectrometer response, especially for the commissioned beam energies below 20 MeV.

6.2.3 WASP measurements of electron spectra and corresponding simulations using magnetic field measurements and phasespace

Measurement of electron spectra In order to measure the electron spectra corresponding to the six electron fields from the ONCOR linac, the magnetic spectrometer described in section 6.1 was placed on the patient table, perpendicular to the beam exit window. The accelerator gantry angle was set to 270° (figure 6.5a). The iron frontplate of the spectrometer was aligned using the patient positioning lasers to be at $z = 95$ cm SSD and centered in x - and y -direction. A dose of 100 *Monitor Units* (MU) was delivered to the spectrometer and measured by the RadEye detectors, which integrated the signal at a rate of one frame per second. A dose-rate of 300 MU / min, corresponding to 3 Gy/min was found as a good compromise between noise in each frame and signal level above background. The average across the 20 frames was calculated and *beam-off* frames, taken before and after the irradiation, subtracted from the average for background reduction.

CMOS sensors are usually sensitive to all kinds of radiation and measure the deposited energy in each pixel in terms of the current of electron-hole pairs generated in the silicon layer. According to a FLUKA simulation, the energy deposition in the $2 \mu\text{m}$ thick silicon layer of the RadEye is 1000-times lower for electrons compared with protons and heavier ions, which makes direct electron detection difficult. Since the RadEye can detect scintillation light, the detection efficiency for electrons can be increased by placing electron scintillators directly on top of the sensor.

The RadEyes were irradiated in four configurations: the bare detectors covered with $15 \mu\text{m}$ aluminium foil for light tightness or using $15 \mu\text{m}$ aluminium together with available scintillators: The *MS intensifying screen*, the *Lanex fine* and the *Min R* were tested to determine which scintillator has the largest light-yield.

Forward simulation of the WASP experiment in FLUKA The experimental setup was rebuilt in FLUKA. The model included the geometry of the magnetic spectrometer and the patient table (figure 6.5b). The spectrometer was modelled as an iron yoke with an iron frontplate and the magnets as neodymium plates. The RadEye housing is included as aluminium box housing the four detectors, modelled as $2 \mu\text{m}$ SiO_2 with a $2 \mu\text{m}$ *Si* layer beneath and covered with $500 \mu\text{m}$ PMMA plastic to represent the position of one of the three used scintillators. The central part of the magnetic field inside the iron yokes ($7.2 \text{ cm} \times 5.0 \text{ cm} \times 13.2 \text{ cm}$) had previously been measured using a Hall-probe mounted on a system of three dimensional stages and was provided to FLUKA as a 3D map of \vec{B} values via the FLUKA user routines *usrini.f* and *magfld.f* [138]. Spacing of the field points

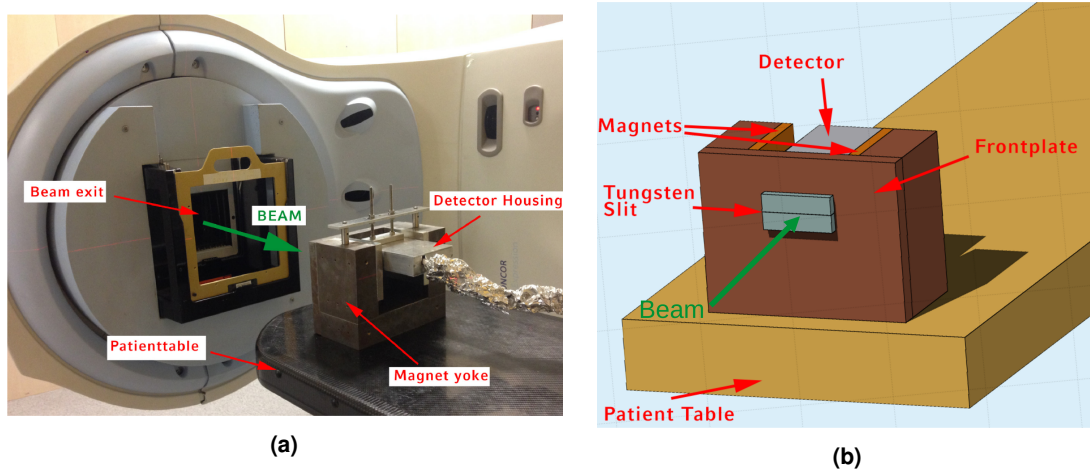


Figure 6.5: Setup for spectrometer characterisation. (a) Back view of the spectrometer mounted on the patient table and aligned to ONCOR linac using the room laser system. (b) Corresponding front view in FLUKA simulations.

was 2 mm. As source, random sampling of all types of particles from the IAEA phasespaces was again used. The frontplate was placed at 95 cm distance from the phasespace origin.

Scoring of energy deposition and particle fluence was done in analogy to the RadEye resolution along 2048×1024 pixels using USRBIN scorers. An additional manual implementation of the scoring in *mgdraw.f* later allowed to generate the data needed for the system matrix used for reconstruction (section 6.3). Energy deposition in depth was scored using one single bin along the $500 \mu\text{m}$ PMMA thickness and inside the $2 \mu\text{m}$ silicon layer.

Results In the experimental acquisition, *MS Intensifying screen* showed the highest light yield compared to the other scintillators and was used as scintillator for all measurements. The *Lanex fine*, *Min R* and the RadEyes without scintillator showed only half of the ADUs for all six treatment field energies.

Figure 6.6 shows the expected behaviour for the measurements and the corresponding simulations: for higher beam energies, the electrons are deflected less towards the detector-plane and hit the scintillators at higher x-pixel-numbers. The signal is bent into a *banana-like* shape along the slit dimension (y-pixels), since the magnetic field is minimal in the middle ($\approx 150 \text{ mT}$) and higher towards the neodymium magnets [138]. In order to have reasonable statistics in each bin, the USRBIN results had to be rebinned to $1/4$ of the RadEye resolution. Both datasets show a considerable *halo-like* signal for smaller x-pixel-numbers (0-500 for the measurement data), which is higher for higher beam energies and can be even higher than the signal peak (figure 6.7f). This gives the impression of the presence of low-energy electrons, which were not expected from the phasespace spectra

6 DETECTOR APPLICATION 1: DEVELOPMENT OF MC BASED RECONSTRUCTION OF SECONDARY ELECTRONS IN LASER-ION ACCELERATION

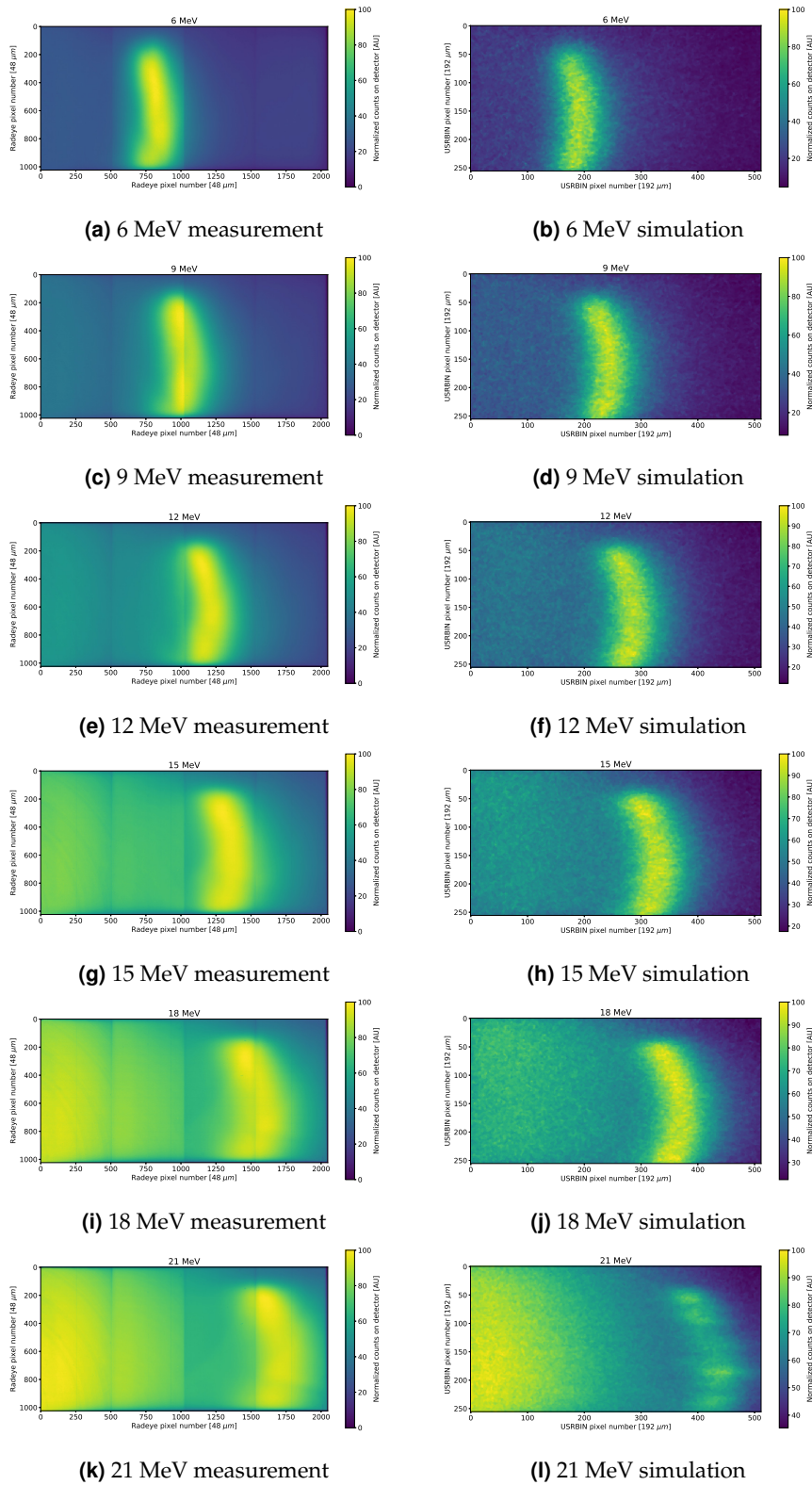


Figure 6.6: X-Z-detector maps of the signal measured/simulated in the $5\text{ cm} \times 10\text{ cm}$ detector area, which is normalized to the maximum signal.

Left: Measured scintillation light using RadEye detectors (full resolution).

Right: FLUKA simulation of the energy deposition in the $500\ \mu\text{m}$ scintillation layer (1/4 resolution).

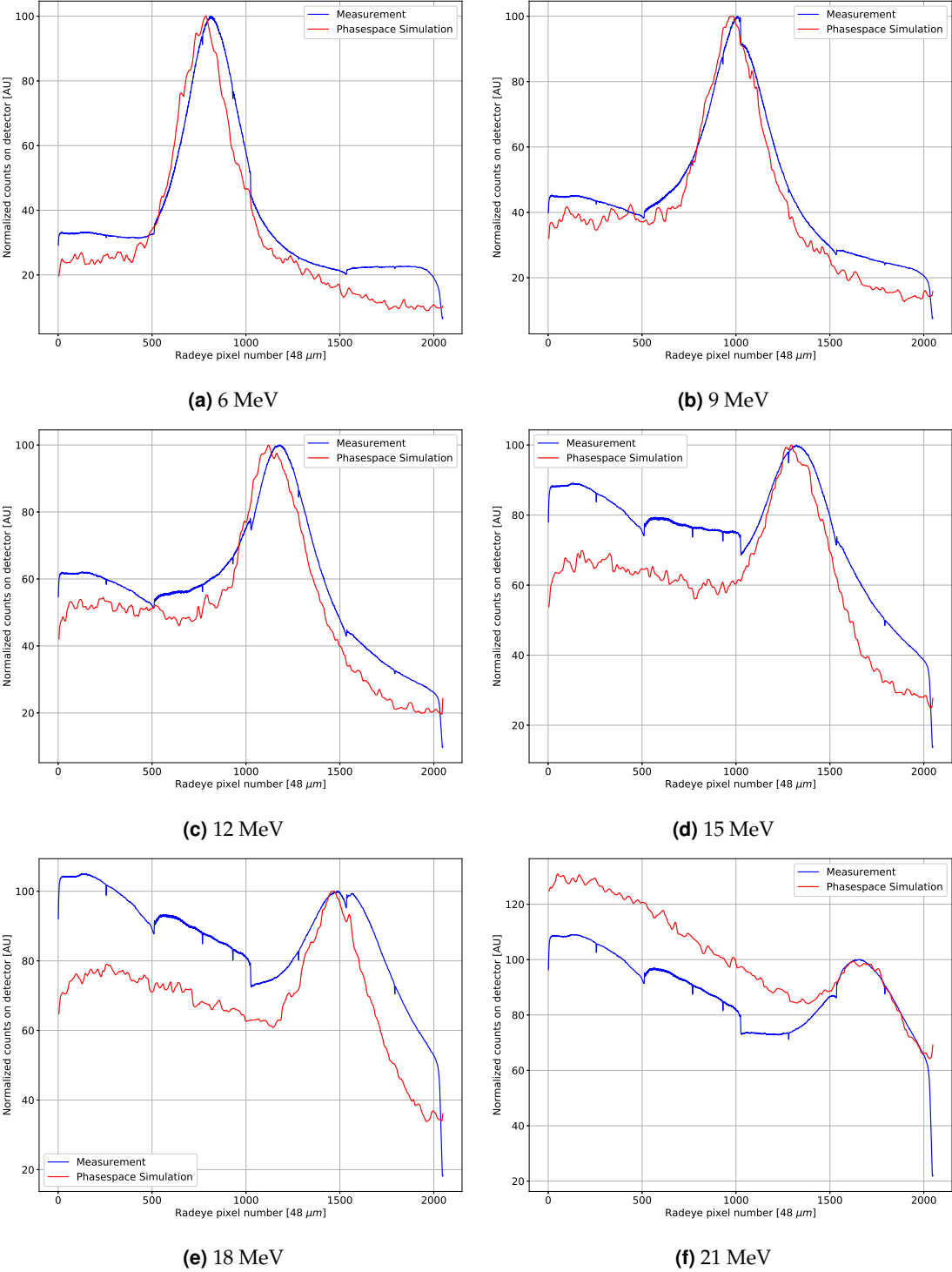


Figure 6.7: Lineouts along z-dimension through the 2D distributions in figure 6.6 for the middle of the slit position (half height in figure 6.6).

6 DETECTOR APPLICATION 1: DEVELOPMENT OF MC BASED RECONSTRUCTION OF SECONDARY ELECTRONS IN LASER-ION ACCELERATION

at the source position (figure 6.2), but may be generated by scattered electrons from the interaction with the spectrometer or bremsstrahlung X-rays with the front-plate.

Since all used sensors were of engineering grade quality, which allows for pixel-defects and up to 10% dark-current, the detector-background level and quantitative radiation response differed. Even after the removal of the detector-background by subtraction of frames without beam-on, the borders between two adjacent sensors are visible in figure 6.6k.

Figure 6.7 displays the plots corresponding to the central lineouts through the 2D plots in figure 6.6. Using the normalisation to the peaks, the agreement of forward phasespace simulation and measurement in terms of the signal shape, the x- and y-position is encouraging. For 6, 9 and 12 MeV, the relative differences along the whole lineouts are below 10%. For 15, 18 and the uncommissioned 21 MeV, the simulations either underestimate or overestimate (21 MeV) the count values in the low-energy-electron region of small pixel numbers at maximum by $\approx 20\%$. Also the forward simulations starting from the PS generate the *halo-like* signal, which hence seems to be a physical signal component and would be misinterpreted as low-energy electrons from the interaction at the source position if any measurement data would be evaluated using the simple analytical tracking algorithms mentioned in section 6.1.

Outlook The scattering and showering of primary source electrons caused by the spectrometer front plate and general design are possibly sources of unwanted signal. The discrepancies in the magnitude of the *halo* between measurement and simulations for 15, 18 and 21 MeV may be caused by several effects: generation of electromagnetic showers from bremsstrahlung in the front plate for higher energies leading to additional scintillation light, together with the idealized modelling of the scintillator and detector as simple *energy deposition* in the PMMA and silicon layer, as well as the lack of any modelling of the scintillation process and detector response itself. Especially scattered low-energy X-rays photons might generate a significant amount of scintillation photons, for which the RadEye sensor has a high quantum efficiency [181].

First steps in this direction were taken by preliminary investigations, separately simulating the primary phasespace particles and the secondary particles from scattering in the WASP as well as performing the simulation of the whole setup in vacuum and using a *black-hole-like* absorbing material for the slit and front plate. Their evaluation might help to identify the origin of the *halo*-signal and help to design WASP spectrometers with reduced impact on the signal of interest, caused by the source electrons.

However, due to the fair agreement of the forward simulation (figure 6.6) and the RadEye measured data (figure 6.7), along with the good agreement of the measurement and phasespace-based simulation of the dosimetric data in water (figure 6.3, figure 6.4), the FLUKA model of the spectrometer was used in further investigations. It was considered promising enough to be used for a first attempt of spectral reconstruction as addressed in the next section.

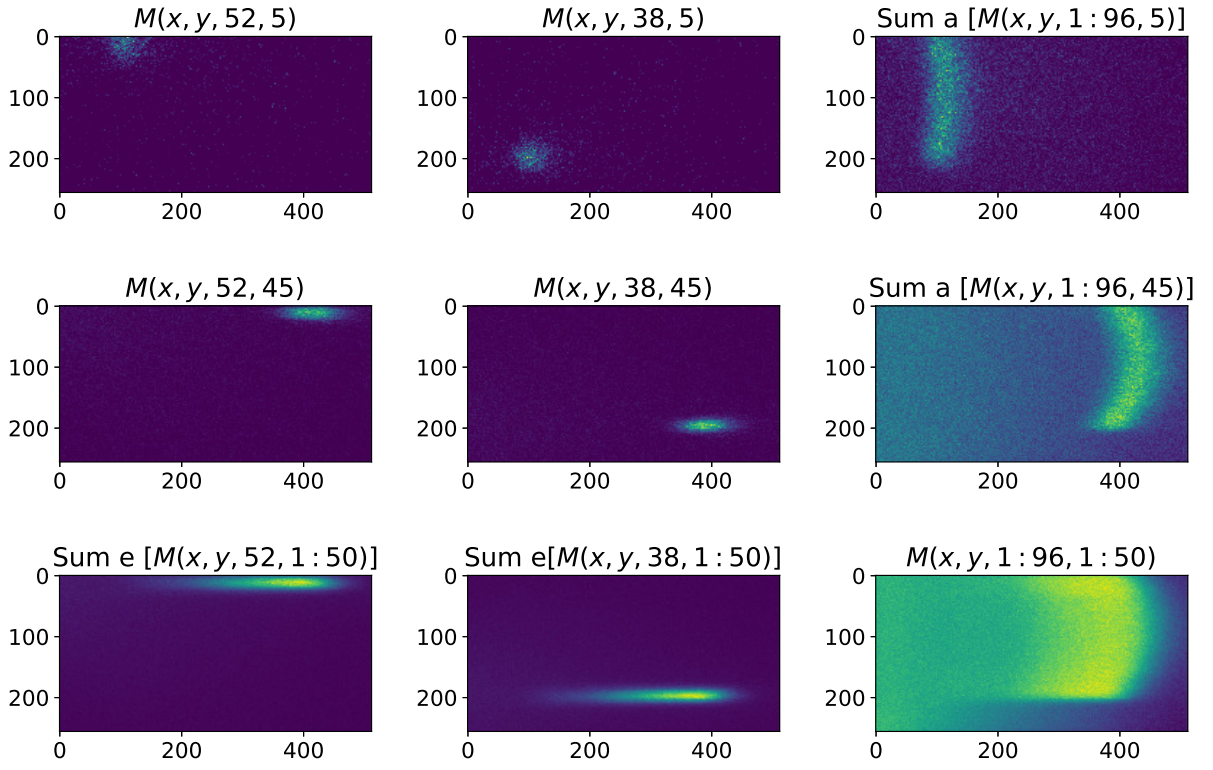


Figure 6.8: The system matrix consists of 4800 beamlets formed by energy-angle combinations (four examples shown). Energy and angle integrated slices are shown for visualisation.

6.3 Modelling the spectrometer as linear system

In order to reconstruct any input electron spectrum and using Monte-Carlo-generated prior knowledge on the secondary radiation and scattering caused by the spectrometer, the formation of the two-dimensional detector image was tried to be decomposed into the linear superposition of individual small *beamlet simulations* of certain energy-angle combinations (figure 6.8).

The formation of the detector signal was formulated as a linear superposition, that can be solved by a linear system of equations. To do so, the two-dimensional *detector signal* in the x and y bins has to be interpreted as a matrix $D(x, y)$ and vectorized into a one-dimensional column vector \vec{d} with elements d_j , where j is the index of the column vector and $j \in [1, \dots, x \cdot y]$. The detector signal is formed by the application of the *system response matrix* $M(x, y, e, a)$, which has all influences of the *imaging system* to the vectorized *input spectrum* \vec{s} . The originally two dimensional *input spectrum* $S(e, a)$, composed of e *energy bins* and a *spatial bins* (thereafter referred to as *angle bins*) was therefore vectorized into the column vector \vec{s} , with elements s_i , where i is the index of the column vector and $i \in [1, \dots, e \cdot a]$. The image formation can then be written as matrix equation:

6 DETECTOR APPLICATION 1: DEVELOPMENT OF MC BASED RECONSTRUCTION OF SECONDARY ELECTRONS IN LASER-ION ACCELERATION

$$(6.1) \quad \vec{d} = \mathbf{M} \cdot \vec{s}$$

The unknown original *two dimensional input spectrum* $S(e, a)$ can be retrieved by inverting this matrix equation to get the elements s_i of \vec{s} , if the elements $M_{i,j}$ of the system matrix \mathbf{M} are known for all combinations of i and j (figure 6.8).

$$(6.2) \quad M_{i,j} \cdot s_i = d_j$$

In general, overdetermined ($m \geq n$) matrix equations of type $\mathbf{A} \cdot \vec{x} = \vec{b}$ can be inverted using the QR decomposition for the matrix \mathbf{A} of dimension $m \times n$:

$$(6.3) \quad A_{m,n} \cdot x_m = b_n$$

When finding the QR factorisation for \mathbf{A} as $\mathbf{A} = \mathbf{Q}\mathbf{R}$, the solution to the linear problem can be found:

$$(6.4) \quad \vec{x} = \mathbf{R}_1^{-1} \left(\mathbf{Q}_1^T \cdot \vec{b} \right)$$

In equation 6.4, \mathbf{Q}_1 is a matrix of dimension $m \times n$, containing the first n columns of the full orthonormal basis \mathbf{Q} and \mathbf{R}_1 is a square (dimension $m \times m$) right triangular matrix. The \mathbf{R}_1^{-1} can be found by Gaussian elimination or using the numerical approximation to backward substitution to calculate x without explicitly inverting \mathbf{R}_1 .

The QR decomposition for $\mathbf{M}(x, y, e, a)$ was implemented in Matlab and results for $\mathbf{S}(n, m)$ were reconstructed for the six measurements of $\mathbf{D}(x, y)$, which served as test dataset.

Data for the system matrix $\mathbf{M}(x, y, e, a)$ in the lower-resolution simulation example (256×512 detector pixels) were generated using FLUKA and stored in a four dimensional matrix of dimension (256, 512, 96, 50). The matrix consists of 4800 building blocks, so called *beamlets*, to be weighted and summed for the final detector signal. The matrix was simulated to have $e = 50$ monoenergetic energy slices, chosen between 0.5 MeV and 25 MeV at 500 keV bin spacing, and, for the finally used system matrix, $a = 96$ angles between $\pm 15^\circ$. At the chosen source-frontplate distance, the angle resolution corresponds to 2.5 mm intervals along the 5 cm slit. Each n, m combination was simulated using 10^8 primary electrons. The source for the matrix simulations, in order to represent the ONCOR, was modelled as a *cone-beam-like* point source at 90 cm distance from the slit and irradiated the whole spectrometer front plate along the x dimension along the $a = 96$ angles. The height of the frontplate along x was 16 cm, the width along the slit dimension y was 24 cm.

The modelling as a cone-beam-geometry was supported by further python evaluations of the phasespace-files in the x-y plane (not plotted here) and the analysis of the dosimetric simulations in water: although the fields are nominally 40 cm \times 40 cm treatment fields at isocenter, which raises the expectation of a square field, neither the field shapes at the position of phasespace scoring ($z = 90$ cm) nor transversal dose distributions inside the water tank at the three aforementioned depths $z = 96.4$ cm, $z = 97.1$ cm and $z = 97.7$ cm (SSD 95 cm) are square (figure 6.4). The doses are not flat but higher in the center and are not squared but rather of circular shape with radii between 10 cm - 15 cm (compare the trend at 5 cm water depth in figure 6.4). Additionally the concept of SSD is idealizing the true accelerator as a virtual point source at an average distance, since technically the z-positions of the source in x- and y-directions are not identical.

6.4 Reconstruction of ONCOR measurements and simulations

The generated system matrix was used to reconstruct the measured energy-angle spectra and the detector maps simulated using the FLUKA phasespaces (figure 6.9).

The reconstructed spectra for measurement and simulation show the same features: as desired, the algorithm superimposed the beamlets to generate the two-dimensional spectrum. Thereby, the formerly curved (figure 6.6) iso-energy lines are straight lines in the energy-angle space. Also the contribution of scattered electrons and background signal is removed for both the phasespace simulation and measurements, since the high-energy FLUKA beamlets of the system matrix include it.

The 2D-reconstruction results, representing the electron spectra at the source position, were analysed along the energy-dimension using a central lineout for each reconstructed treatment field (figure 6.10). The lineouts, sliced at the central 0° position, were evaluated both in terms of general shape and quantitatively after a Gaussian fit via the mean value μ and standard deviation σ and compared to the electron spectra known from the phasespace, evaluated using the same fit routine. The results are challenging to interpret.

The reconstructed spectra for measurement (figure 6.10 left) and simulation (figure 6.10 right) show the same trend: the reconstructed distributions have a σ , which is 2-4 times too large compared to the ground truth from the phasespace spectrum (0.9 MeV-1.5 MeV difference). At the same time, all reconstructed spectra are free of the unphysical scattered electrons that would be reconstructed as source electrons using the simple conventional tracking approach (figure 6.7d, figure 6.7e). The FLUKA based reconstruction beamlets successfully represent the background signal generated for high beam energies.

The reconstructed mean energies μ are, apart from the 18 MeV case, within the 500 keV energy interval size, which is an intrinsic resolution limit to the reconstruction algorithm.

6 DETECTOR APPLICATION 1: DEVELOPMENT OF MC BASED RECONSTRUCTION OF SECONDARY ELECTRONS IN LASER-ION ACCELERATION

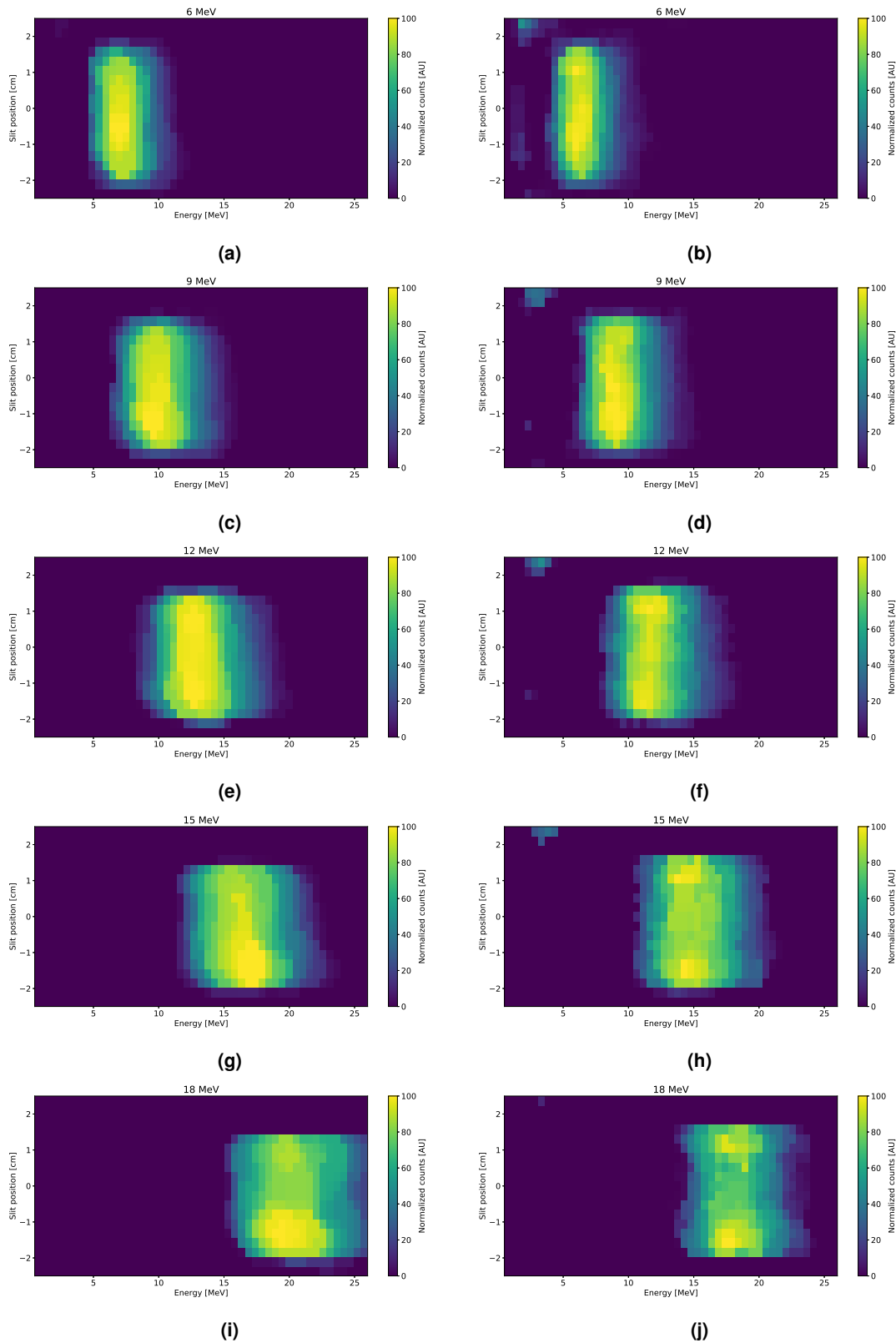


Figure 6.9: 2D-spectrum reconstructions of the $5\text{ cm} \times 10\text{ cm}$ signals using the system matrix method.

Left: ONCOR measurements reconstructed in the e - a space

Right: Phasespace simulations reconstructed in the e - a space

Reconstruction of ONCOR measurements and simulations

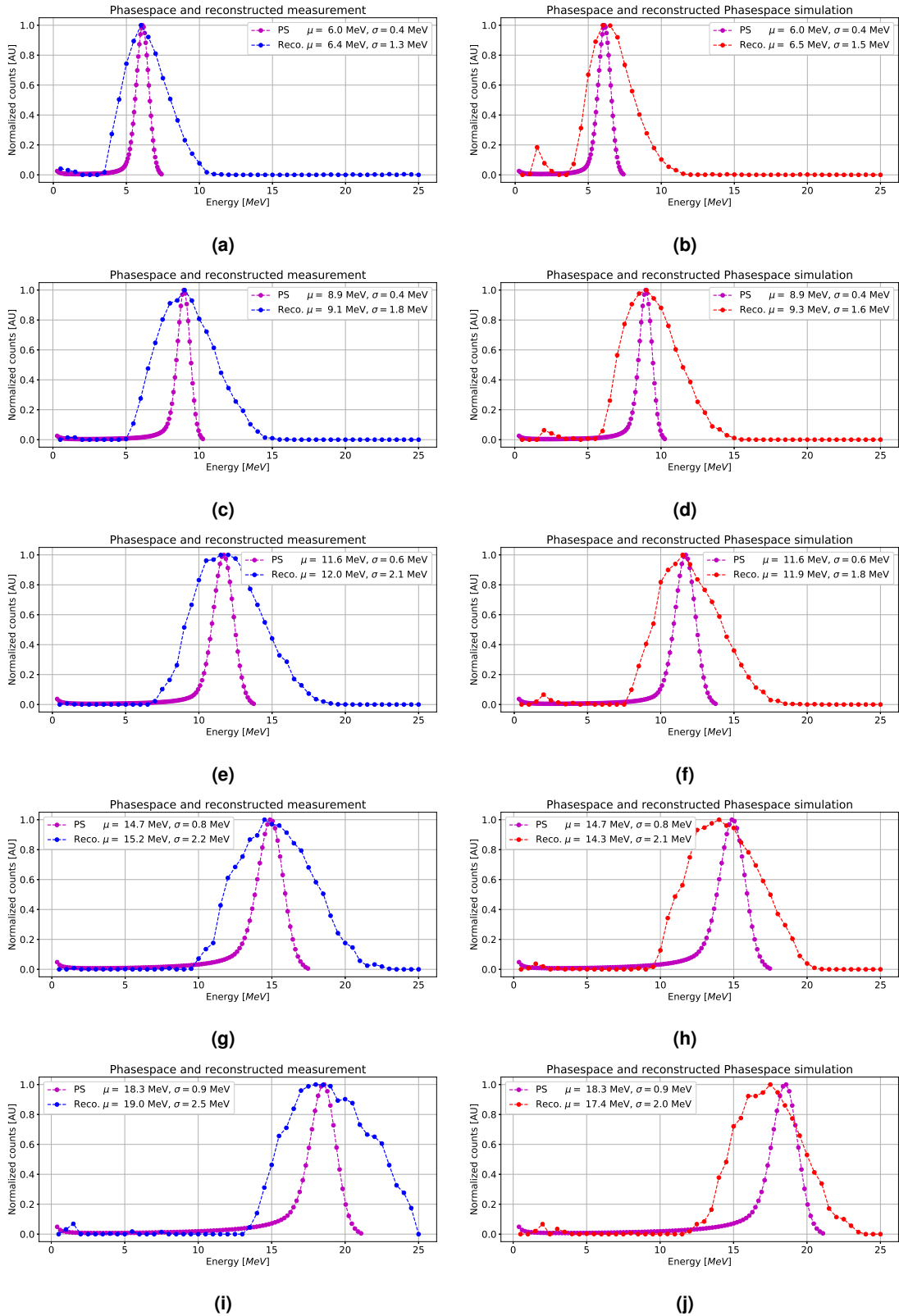


Figure 6.10: Lineouts of spectrum reconstructions for measurements and PS-simulations for $a = 0^\circ$.

Left: Reconstructed measurement (blue) and the **phasespace spectrum** (magenta).

Right: Reconstructed phasespace simulation (red) and the **phasespace spectrum** (magenta).

6 DETECTOR APPLICATION 1: DEVELOPMENT OF MC BASED RECONSTRUCTION OF SECONDARY ELECTRONS IN LASER-ION ACCELERATION

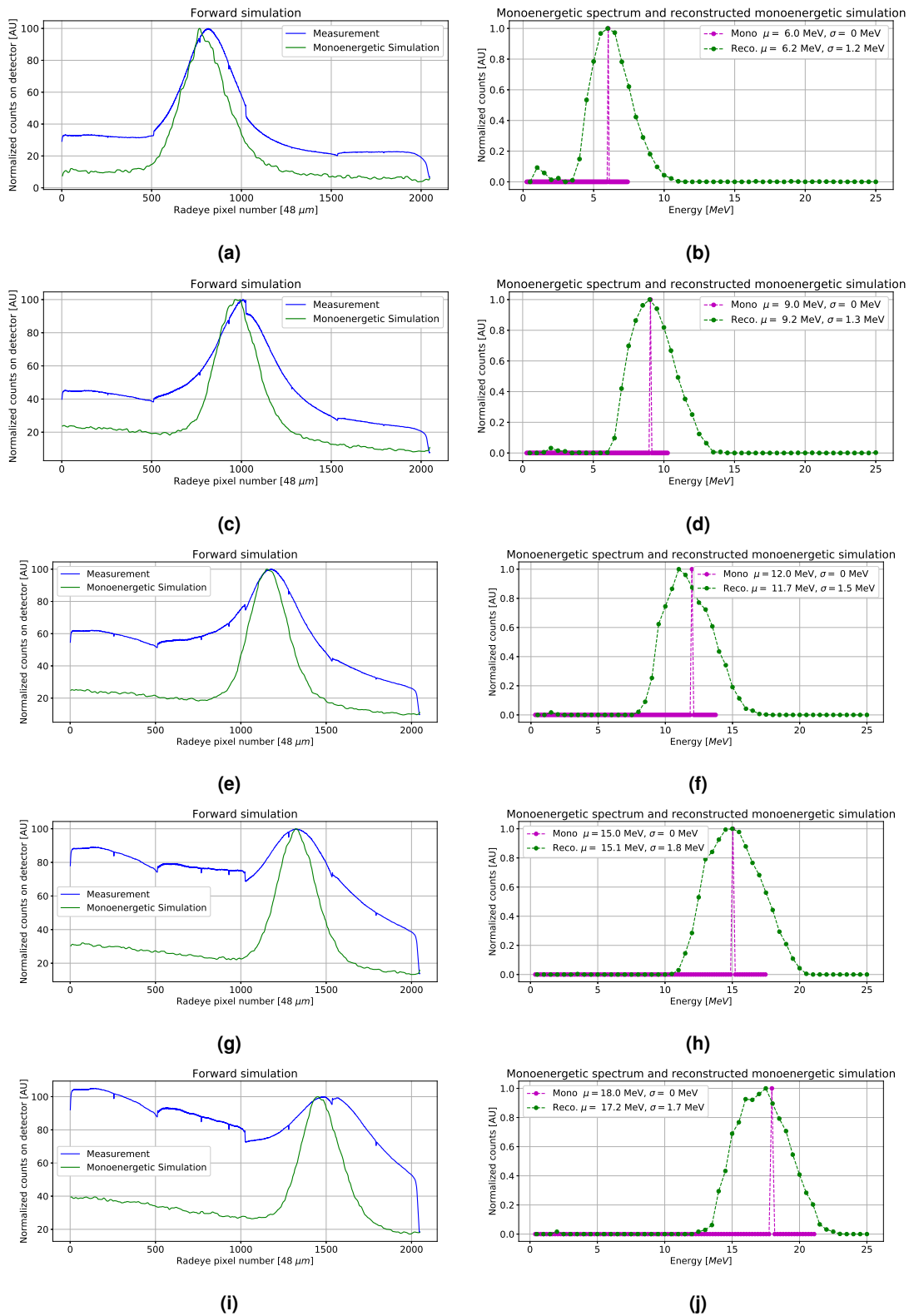


Figure 6.11: Lineouts of monoenergetic simulation detector maps and corresponding spectrum reconstructions for $a = 0^\circ$.

Left: Simulated detector signal (green) and the measured signal (blue).

Right: Reconstructed monoenergetic simulation using a cone-beam-geometry for the system matrix (green) and the monoenergetic input spectrum (magenta).

6.5 Limitations of system matrix reconstruction and WASP

The cause of the large σ for all reconstructed fields was found using purely monoenergetic electron simulations of the nominal electron field energies 6, 9, 12, 15 and 18 MeV. The forward simulated 2D-detector signals were compared again to the experimentally measured 2D-detector signals from the treatment fields (lineouts in the left column in figure 6.11). Also the monoenergetic simulations were reconstructed using the system matrix (figure 6.11 right column). The monoenergetic simulations may be seen as the PSF of the spectrometer in the energy resolution dimension.

The lineouts for the monoenergetic simulations (green in the left column of figure 6.11), do not reproduce the background signal level, especially for the higher field energies, similar to figure 6.7. High-energy photon showers from phasespace / measurement may play a relevant role in generating the background signal for x-pixel numbers of 0-500 for 6 and 9 MeV and 0-1000 for 12, 15 and 18 MeV. The lineouts of the monoenergetic simulations expand for all energies over a FWHM of ≈ 300 pixels, which is only 20% (6 MeV, figure 6.11a) to 100% (18 MeV, figure 6.11i) smaller than the peak from the ONCOR fields. The monoenergetic simulations, although spaced by 3 MeV initial beam energy (6, 9, 12, 15 and 18 MeV), overlap by 50% on the detectors (e.g. figure 6.10a and figure 6.10c, figure 6.10g and figure 6.10i). The overlap is even worse for the 500 keV wide beamlets in the system matrix and can explain the broad reconstructed spectra (figure 6.8).

An additional idealisation which can be questioned is the modelling of the system matrix as a point source with a cone beam shape.

It can be concluded, that the Monte-Carlo-based reconstruction using the linear-system model does not allow be used for the electron reconstruction of the presented WASP, which is in use in LEX and CALA using a slit height of 200 μm and energy range of up to 25 MeV electrons.

Besides optimizing the WASP in order to reduce the background from scattered radiation and induced secondary showers, the reconstruction could benefit from a more realistic MC simulation of the detector signal and scintillation.

Chapter 7

Detector application 2: Concepts for laser-driven proton radiography

The work presented in section 7.2.1 has been presented orally at the DGMP 2015 conference.

- **Oral: F Engbrecht et al.:** Monte Carlo studies for the development of laser-driven proton radiography, *Annual conference of the German Society for Medical Physics, DGMP 2015, Marburg, Germany*

The recent developments of novel laser-based particle sources towards higher particle numbers, particle energies, stability and higher repetition rates as enabled by adequate radiation protection (chapter 4) and measurement instrumentation (chapter 5, chapter 6), allows for novel experiments of possibly biomedical relevance. The distinct beam properties (section 3.3.2) allow novel applications to exploit these distinct features, but at the same time hinder the direct transfer of established experimental concepts from conventional electron-, photon-, proton- or light ion-beam accelerator facilities to laser-based sources (section 3.2). The *FLASH* effect (section 2.5.4) could further raise the demand for laser-driven ion imaging for pre-clinical research.

The following chapter gives conceptual thoughts on for quantitative imaging using laser-particle sources (section 7.1). These general thoughts were guiding experiments carried out at two different laser systems (section 7.2). Section 7.2.1 describes an imaging experiment at the LION beamline in the LEX facility. Section 7.2.2 reports on a beamtime at the TPW laser system.

7.1 Introduction

Experiments in applied fields of research like radiation biology or radiotherapy have tried to preserve established concepts. Tailoring of the source properties of laser-driven proton bunches was common, neglecting the potential of the distinct bunch-features (section 3.3.2) in order to recreate the conventional RF-based monoenergetic, spatially stable, energy tunable and continuous beam in a top-down approach.

Detectors with counting rates needed for laser-generated proton bunches are not available, as the conventional beam delivered in a second now impinges within a few nanoseconds (table 3.1). As concepts without single-particle tracking at conventional accelerators are as well desirable, new proton imaging concepts are under research.

7.1.1 Previous proton radiography with laser-driven protons

Proton radiography with lasers has been employed to investigate ultrafast processes in materials, to probe the evolution of electric fields at ns time scales or as diagnostic of dense plasmas. Typically, deflection or streaking imaging was performed. The traversed thicknesses of material were μm up to mm thin, due to the keV to few MeV proton energies [25, 187]. For transmission imaging, the imaging contrast was relying on the created shadow in single CR-39 or RCF film, not providing any quantitative measure of the object thickness.

7.1.2 Proton radiography with a broad energy spectrum

Simulation studies using energy-upscaled proton spectra from bunch parameters expected for LION@LEX and a considerably simple setup using temporal bunch-integration to perform transmission radiography were performed previously by Würfl, Englbrecht et al. [248]. They used FLUKA simulations using detector characteristics of a hypothetically possible $2 \times 2 \text{ cm}^2$ pixelated time-of-flight (that is bunch energy spectrum resolving) transmission detector of only $20 \mu\text{m}$ thickness, together with the Timepix or the RadEye detector for spatially-resolved detection after the object [248].

In simulation, quantitative radiographic imaging of mm thick objects was possible, however MCS did lower the spatial resolution, making a short object to 2D-detector desirable. But the broad energy spectrum, especially due to the exponential decay towards higher energies, caused a high dose inside the object. Most low energetic particles were stopped in the object.

Proton radiography concepts using combined single proton beam energies have been introduced in section 3.2.4. Würfl and Englbrecht performed experiments using the RadEye detector at the MLL proton accelerator to generate energy-modulated proton beams by placing 3D printed plastic phantoms in vacuum [250, 57]. The broad energy spectrum of laser-accelerated proton bunches can intrinsically present multiple energies, which is

desirable for contact radiographies. A broad bunch will automatically present the desired energy for maximum contrast (see experiments in section 7.2.2) and not only using a single energy for a limited depth range, as stated by Koehler et al. [124, 125]. They also used lead scattering foils in order to have a sufficiently large homogeneous proton field to irradiate macroscopic objects [125]. The divergent nature of laser-originating proton bunches could automatically solve that problem.

7.1.3 Concepts for radiography at LEX

Due to the availability of low-energy proton bunches, low-energy imaging applications were tested using FLUKA, exploring the potential to transfer them to the LION experiment at LEX (section 7.2.1) [56].

Transmission radiography with WASP In order to have not only a shadow contrast but an energy resolution after the object, a proton residual energy system after the imaging object is desirable. In such a way even a single energy would be sufficient, as done for clinical proton radiography (section 3.2.4). The existing WASP, described in section 6.1, uses the RadEye detector as a fluence detector (section 5.1.2) to provide the kinetic energy of the whole bunch and compatible with laser-proton acceleration experiments. It was hence the detection system of choice.

The WASP was simulated in FLUKA with an energy-upscaled proton spectrum (< 14 MeV) as expected for LION@LEX. If the object of interest is mounted upstream of the WASP-slit (figure 6.5b), a 1D lineout through the object along the slit with energy resolution is generated on the RadEye detector system. Such 1D transmission radiography would have the energy-loss imprinted onto the spectrum of the bunch leaving the object and would rely on a sufficiently high bunch energy. By scanning the object perpendicular to the slit direction in up-down direction (y-direction), acquiring multiple 1D lineouts in a step-and-shot approach using multiple laser-shots, a 2D mapping of the object would be possible.

Due to the MCS in the object the signal on the detector after the large driftspace of typically 75 cm does not allow for any reconstruction. As stated multiple times, a short distance to the position-resolving detectors is always needed, especially without any tracking capabilities for individual protons.

This transmission-radiography concept would not benefit from the laser-generated bunches, as a single incoming proton energy would be sufficient. Additionally one would need to monitor the bunch-spectrum due to the shot-to-shot fluctuations, for example by only using half of the slit for the object and leaving the other half free for the undisturbed bunch.

Stopping radiography with WASP A different approach was modelled in FLUKA and proposed for an experiment using the LION@LEX proton source in transmission imaging

7 DETECTOR APPLICATION 2: CONCEPTS FOR LASER-DRIVEN PROTON RADIOGRAPHY

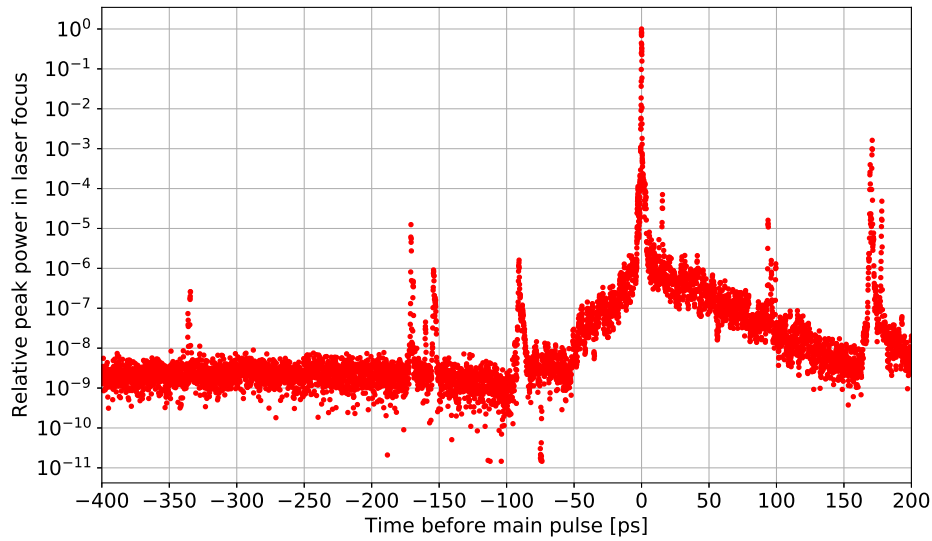


Figure 7.1: Measured contrast curve of the ATLAS-300 laser used for the LION@LEX experiment displaying various pre-pulses. Measurement was performed using a *Sequoia HD* (Amplitude Systemes, Pessac, France).

approach [56]. Instead of scanning the object of interest in front of the slit, the object can be scanned in front of the detector.

In a step-and-shoot manner, each position of the object will be covered with multiple proton energies. Each shot represents a monoenergetic contact radiography of the object, providing the binary information if the kinetic energy from the broad bunch spectrum, which is deflected to the same position in space for each shot by the magnet, was sufficient to penetrate the sample thickness at this position. By scanning the object for example upwards in +y direction towards the higher proton bunch energies, the object will at a certain step be traversed by the protons. In a reconstruction and knowing the magnet field strength and drift space distance, water equivalent thickness or the density for a known thickness can be obtained for the whole phantom.

As the information is based on the proton just being able to exit the object, the choice of biologically relevant samples was difficult and hindered due to the available proton energies (following section).

7.2 Experiments

7.2.1 Experiments with protons at LEX

Experiments for proton radiographies with non-binary contrast of thin biological samples were planned and have been realized in a single beamtime at the LEX photonics laboratory at the end of 2016. Although the quality of the obtained data should have

been improved and the concept revisited in consecutive beamtimes, the preliminary results are listed here for completeness, as the LION experiment and the ATLAS-300 laser were dismantled and transferred to CALA after 1.5 years of operation. Hence no further experiments were possible.

Evolution of the LEX proton source A general introduction regarding the laser pulse properties expected from the used ATLAS-300 laser system along with the experimental layout, can be found in section 3.3.4. Despite the considerable number of successful applications of the generated proton bunches, summarized in section 3.3.4, the proton bunch energies of 20 MeV as comparable to the MLL accelerator could not be reached. A great number of improvements in instrumentation of the laser system, the targets and the various detector systems (chapter 5, chapter 6) have been implemented during the 1.5 years in order to increase the total particle numbers, to allow for bunch refocussing of the divergent beam and a high-energy cut-off increase [79, 95, 215, 61, 219, 191, 93, 44].

The laser energy on target in LEX was below the idealistic 7.5 J but, indirectly judging from mirror leakage, 2.2 J. The corresponding laser power on target was thus not 300 TW but 70 TW [92].

In order to achieve higher proton kinetic energies and to optimize the TNSA process, the LION@LEX experiment during the 1.5 years of operation tried to find target materials and lower thickness compatible with the laser pulse shape of the ATLAS-300 laser system. Generally speaking, the laser contrast is a crucial factor for the target choice and the achievable proton spectra, as low contrast values, corresponding to high pre-pulses preceding the main laser pulse, can destroy the target before the accelerating plasma-dynamics inside the target has emerged (figure 3.9, section 3.3, section 3.3.1). The laser-contrast measurement of ATLAS-300, depicted in figure 7.1, displayed several pre-pulses at a few hundred ps and amplitudes of up to 10^{-5} before the main pulse arrival, which had to be identified and removed using fast *Pockels cells* [92]. With the implementation of integrated double plasma-mirror targets, proton energies of about 11 MeV, corresponding to a doubling of the proton energy, were achieved [215]. At the cost of more-difficult to manufacture targets and lower shot numbers, the plasma-mirror principle of pre-pulse elimination as introduced in section 3.3.1 was applied using dedicated inline plasma-mirror targets and enabled a contrast improvement by factor of 100. This finally allowed to reduce the target thicknesses from 600 nm to 20 nm [215]. Practically, the usual target holders were able to host 99 targets, of which typically only 33 were shot, since neighboring targets often were destroyed. The same effect reduced the available shots for the double-plasma mirror case from 18 to 6. The automated target positioning system allows to accommodate up to 18 of these holders.

A high-energy proton cut-off energy of 11 MeV has been achieved in a dedicated beamtime using ^{79}Au foil targets, however only 7 MeV protons had been accelerated on a regular basis before the double-plasma mirror implementation [79]. 7 MeV correspond to a proton range of 600 μm in water, which limited the choice of usable imaging objects and

7 DETECTOR APPLICATION 2: CONCEPTS FOR LASER-DRIVEN PROTON RADIOGRAPHY

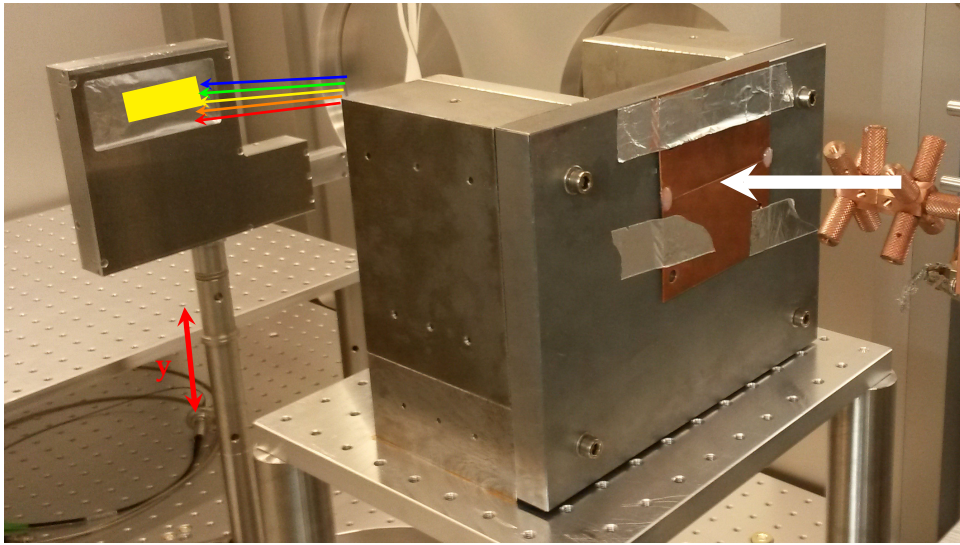


Figure 7.2: Experimental setup for the scanning 1D radiography. The bunch enters the WASP through a thin slit, making 2D cone beam into a 1D fan beam. The energy dispersion in the magnetic field deflects the different proton beam energies onto different y positions on the RadEye detector.

the achievable contrast between the different structures and tissues, for which an even higher energy resolution is then needed (figure 7.3b).

Scanning 1D radiography Figure 7.2 depicts the experimental setup used in LEX to test the 1D scanning radiography concept as described in section 7.1.3. The polyenergetic bunch (white arrow) entered the field region of the combined electron proton spectrometer (section 6.1) through a $250\ \mu\text{m}$ wide copper slit of sufficient thickness to stop the proton bunch.

Three radiography objects were mounted in contact with the four *RadEye* sensors of the spectrometer setup, below the $15\ \mu\text{m}$ aluminium foil used for light tightness. The three objects are shown in figure 7.3a: a $\approx 100\ \mu\text{m}$ thin hand-cut slice of salami, made vacuum compatible by wrapping in two $50\ \mu\text{m}$ layers of Kapton tape, a 3D printed step phantom, as well as a target holder used for the LION experiment as proton source, a structure of $99 \times 500\ \mu\text{m}$ wide holes drilled in a $250\ \mu\text{m}$ metal sheet. The phantom with twenty steps of up to $48\ \mu\text{m}$ thickness and 5 mm width were chosen to stop protons of $\approx 10\ \text{MeV}$. It was printed using the high-resolution *Projet* technique, which uses $16\ \mu\text{m}$ thin layers of an acryl photopolymer. The 3D printed twenty steps are aligned like a spiral staircase in two rows with ten steps each. A part of the detectors was left without samples, in order to have an undisturbed spectrum for spectrum measurement and particle number reconstruction.

This concept of proton imaging with a step phantom was and is now employed as pro-

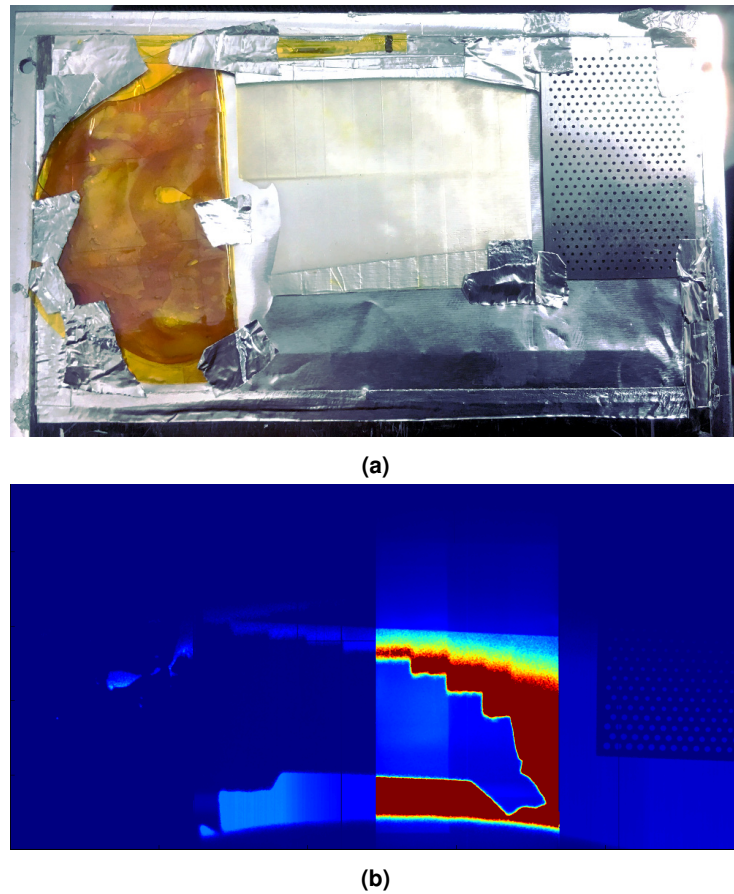


Figure 7.3: Quantitative proton radiography experiment using *RadEye* spectrometer. (a) Phantoms used for Imaging in LEX: salami wrapped in $50\ \mu\text{m}$ Kapton, 3D printed plastic staircase step phantom, target holder used in laser-ion acceleration experiments as hole pattern. (b) Radiography image acquired using *RadEye* detectors.

ton energy diagnostic for the LION experiment in LEX and CALA. After precisely milling steps from an aluminium block, the step phantom was mounted upstream of the light-tight *RadEye* housing and allows an online-deduction of the proton high-energy cut-off for each shot simply by counting the number of cut-off lines [133]. No cumbersome measurement of the \vec{B} field is needed for the used spectrometer, as well as no analytical tracking is needed if the spectrometer-detector distance is changed due to experimental demand. Reinhardt et al. used a fixed energy deposition value in the $2\ \mu\text{m}$ active layer for the particle number calibration, based on data for 20 MeV protons [193]. Lindner et al. started to correct for the energy dependence of the stopping power (equation 2.6). The particle numbers for 1 MeV protons should drop by $\times 8.67$ according to a *pstar* estimation [19]. Using the aluminium step phantom, an automatic self-calibration of the energy dependency of the particle number calibration is addressed systematically and in preparation by Hartmann et al. [96].

A yellow rectangle indicates the position of the imaging objects in figure 7.2. The higher proton energies (blue arrow) penetrate the upper part of the objects, while due to the magnetic deflection the lower energies (green arrow, yellow arrow, etc.) penetrate the

7 DETECTOR APPLICATION 2: CONCEPTS FOR LASER-DRIVEN PROTON RADIOGRAPHY

lower parts of the samples. In order to make sure that every height (y-direction) position of the phantoms was covered with multiple proton energies for good energy loss resolution, the object was moved in a step-and-shoot manner. The detector was scanned in y-direction over 17 consecutive steps of 0.5 mm covering 8 cm.

115 consecutive shots on 600 nm foil targets were acquired, together with their corresponding electron spectra. After the 71.7 cm of driftspace behind the magnet yoke, the broad proton spectrum between 1 MeV, being the kinetic energy needed to penetrate the 15 μm aluminium foil, and the high-energy cut off of 7 MeV, covered 3 cm on the y-dimension of the detector.

Figure 7.3b shows the results of a single laser-shot for one y-position. The different signal levels are caused by previous irradiation of the RadEye sensors and can be corrected in the evaluation, as the RadEye sensors behave linear even after radiation damages [193]. Each of the three phantoms shows an image contrast.

The signal in the region of the salami clearly shows boundaries where the protons were not energetic enough to penetrate the sample, as well as signal in areas which could either be a hole or passing protons. The holes of the target holder are clearly visible. Remarkable is the tendency of the hole boundaries to appear washed out in the lower energy region (bottom) compared to the higher energy region (top).

The step phantom clearly shows 11 distinct thickness steps. Additionally visible is the reduced deflection of higher-energy protons, where the interval 2-3 MeV covers 4 mm, while 3-7 MeV cover 10 mm.

As data quality and shot numbers should be improved, a reconstruction of the images of the phantoms using the 17 consecutive steps was not performed.

Some remarks for further experiments: This concept combines multiple stopping radiographies. The broad spectrum of the bunch also irradiates the interior part of the phantom, similar to the protons in passive proton beam therapy, which stop proximal to the tumour site and deposit dose without any therapeutic benefit (figure 3.3). This causes high dose in the phantom and may be a problem for animal samples, especially from the broad spectrum with exponential shape (figure 3.11a).

As samples for these low proton energies have to be brought into vacuum due to the limited proton energies achieved, they need to be made vacuum-compatible. Imaging of biological samples should be conducted in air with the proton beam passing an additional vacuum window before reaching the imaging setup. This may then again degrade the image quality due to MCS.

As the particles producing the needed contrast are the ones just able to pass through the sample, they are of low kinetic energy and will have large scattering angles onto the detector.

Based on these thoughts, such low-energy laser-driven proton source may be best suited for contract radiographies of non-biological but technical samples of low thickness.

7.2.2 Experiments at the TPW Laser

Acceleration experiments using high-power lasers typically create a multi-species spray of particles. Single-shot experiments using e.g. imaging with protons and X-rays can be performed by adequate choices of the laser target. While the energy loss of protons is probing the electron density or RSP of an object (section 2.2), the intensity reduction of a photon beam is a measure for the attenuation coefficient / mass density of an object (section 2.1.2). The single-shot nature, together with a smart detector alignment, allows for direct co-registration of the two images and may provide complementary information due to the different physical nature of the interaction mechanisms, possibly reducing the 3.5% calibration uncertainty for proton treatment planning (section 3.2.4). The long term perspective of such multimodal source of high-energy protons and X-rays could be a sort of single-shot laser-driven image guided proton radiation therapy. The X-ray (or even the high energy proton) component could be used for position verification imaging and adaptive treatment planning and the lower energy proton bunches for tumour irradiation.

Imaging experiments at the TPW laser system (section 3.3.6) have been performed during a three weeks beamtime with a total of 69 laser shots. Shots were performed on generic *atomic force microscopy* (AFM) needles made of tungsten (Bruker TT-ECM10), as well as Formvar plastic foils, gold and tungsten metal foils for comparison. The spatial confinement of the plasma dynamics to spheres or needles have been reported to lead to source parameters different to foil targets [104]. The reduced source size for X-rays allows for imaging using in-line X-ray phase contrast of higher resolution than absorption based imaging [148]. The results of the experiments measuring the source sizes for the protons and X-rays from the needle target, the corresponding FLUKA MC simulations done by the author and imaging results were published by Ostermayr, Kreuzer, Englbrecht et al. [160]. A general description of the laser system properties and the shot repetition rate at TPW are introduced in section 3.3.6. A brief introduction into the published results and another multimodal imaging experiment with non-binary contrast of a fish sample is presented here.

X-ray spectrum and proton spectrum and source sizes characterisation The generation of X-rays using needle targets was qualitatively proven in LEX before the TPW beamtime using *RadEye* sensors and the MinR scintillator for improved X-ray sensitivity (section 6.1). Due to the higher laser pulse energy and high level of EMP at TPW, only offline diagnostics like CR-39 for protons and IPs for X-ray detection were used (section 3.4). The X-ray spectrum at TPW was reconstructed to be peaked at 6 keV and of bremsstrahlung-like shape. Aluminium filters of up to $14 \times 30 \mu\text{m}$ were therefore placed on an IP [243, 160].

The proton spectrum emitted towards the sides of the needles at TPW was measured to be peaked around 12 MeV with 20% FWHM energy spread using a WASP placed at 83°

7 DETECTOR APPLICATION 2: CONCEPTS FOR LASER-DRIVEN PROTON RADIOGRAPHY

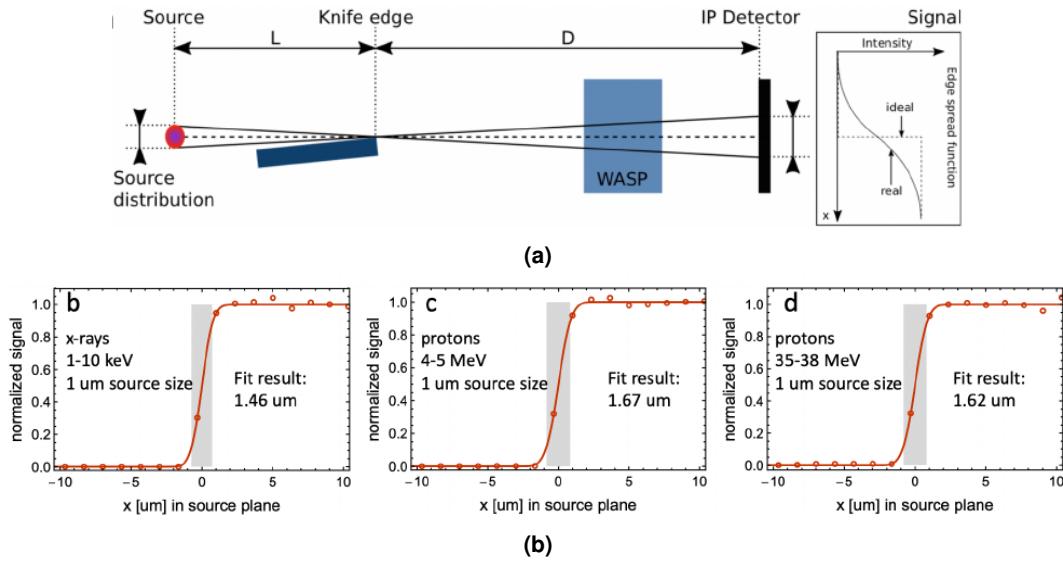


Figure 7.4: FLUKA setup to demonstrate the feasibility of the source size measurements. (a) The projection of the shadow of the spherical source distribution onto the IP is magnified by the factor $M = D/L$. The figure displays the planned experimental WASP position for proton energy measurement. (b) Fits of error-function to simulated data for X-rays and protons are close to the simulated $1 \mu\text{m}$ source size. Figures reproduced from [161].

relative to the laser propagation direction (figure 1C in [160]). The 0° forward spectrum showed energies above 20 MeV with a FWHM of 100% (figure 1C in [160]), similar to the spectra typically observed for laser-proton acceleration from foil targets. The probability to hit the few $10 \mu\text{m}$ wide target area of the needle tip with the laser focus of approximately the same size was low due to the laser pointing stability. The consequence were strong shot-to-shot fluctuations in the proton energy and particle number [159]. For direct comparison of the source sizes, $5 \mu\text{m}$ tungsten foils were used. The highest proton energies were achieved with 190 nm thin Formvar plastic foils, showing up to 65 MeV protons in the Thompson parabola spectrometer at 0° .

Due to the needle geometry, the source size perpendicular to the needle direction was measured using the shadow a sharp silicon blade to be $2.8 \mu\text{m}$ for X-rays and $\approx 5 \mu\text{m}$ for protons, while along the needle values of $6 - 10 \mu\text{m}$ were measured for X-rays and $12 \mu\text{m}$ for protons [160].

An extensive amount of FLUKA simulations had previously been carried out by the author in order to show the feasibility of the sharp silicon blade source-size measurement technique and is summarized in figure 7.4. The data was published by T. Ostermayr in his PhD thesis, the supplementary material of the aforementioned paper and substantially contributed to the positive evaluation of the beam-time application [159, 160, 161]. The simulations modelled the experiment to measure the effective source size for protons and X-rays via the image blur of sharp, tilted silicon knife edges of a few cm thickness (figure 7.4a). It could be shown that the used silicon wafer edge is non-transparent to protons up to 38 MeV and X-rays between $1 - 10 \text{ keV}$, as well as that the IP resolution of $25 \mu\text{m}$ is sufficient to resolve the source modelled as an exploding $1 \mu\text{m}$ sphere. A

geometrical magnification of $M = 20\times$ was assumed (figure 7.4b).

Phase-contrast imaging using X-rays Ostermayr et al. published the radiographic imaging of an insect using the AFM needle [160]. The imaging setup used the combination of several distinct features to the experiment, which are beneficial for imaging.

The 25 mm long insect was placed in vacuum a few cm behind the needle (distance L) in figure 7.4a) at 103° . An IP followed at $D = 0.75$ m behind. The large 103° angle, together with a WASP magnet between insect and IP, reduced the impact of neutrons, laser light and electrons to the IP. The estimated X-ray source size in the few μm -range results a magnification of the projection between $17.5\times$ and $27\times$. The image shows edge enhancements of the insect via phase-contrast of sub $10\ \mu\text{m}$ structures. The magnification was enabled by the combination of the small source size, together with the sufficiently high flux and the 360° emission angle (fig. 3 in [160]). A contact radiography with protons on CR-39 was recorded by increasing the source-insect distance to $L = 25$ cm and inserting the CR-39 directly behind. The X-ray image on the IP did not show phase-contrast features (magnification $M = 2.56\times$) but resolved features of $100\ \mu\text{m}$ width, while the MCS of the protons blurred features smaller than 0.5 mm on the CR-39.

Energy resolved proton image with X-ray radiography The single CR-39 concept for contact radiography was extended at TPW. For a quantitative, i.e. using proton energy loss resolution, combined laser-driven proton and X-ray single-shot radiography, a *Paracheirodon innesi* fish and the used detectors were placed in an KF40 tube. The aluminium tube had a $50\ \mu\text{m}$ Kapton entrance window, covered by $15\ \mu\text{m}$ of Mylar foil and was vented to air in order to preserve the anatomical fish structure. The fish was placed on top of a varying number (6-12) of CR-39 nuclear track detectors ($2.5\ \text{cm} \times 2.5\ \text{cm}$, each $1.5\ \text{mm}$ thick), which were placed on a $2\ \text{cm} \times 2\ \text{cm}$ Fuji BAS-TR imaging plate (figure 7.5b). The number of CR-39 was varied depending on the expected proton energies and performance of the last shots, in order to stop the full proton beam while optimizing the material usage. Four shots on an AFM needle, a DLC, a Formvar and a gold foil were tested as sources. While metal foils and needles are known to provide an increased X-ray yield, the hydrogen contamination layer on the DLC and Formvar foils allowed for higher proton energies [160].

Directly after each shot, the IPs were scanned with their nominal $25\ \mu\text{m}$ resolution, although the true resolution in the detector plane was found to be slightly worse than $\approx 50\ \mu\text{m}$ (figure 7.5a) [160]. Back in Germany, the CR-39 detectors were etched in six-molar NaOH solution for 60 minutes at 80°C , enlarging the single-proton tracks into macroscopically visible pits (figure 7.5c).

Figure 7.5 summarizes results from the second imaging approach, performed by the author. Figure 7.5a shows an example of the Fish mounted to 12 pieces of CR-39 with the IP below (Shot 22). Figure 7.5b displays an acquired X-ray radiography of the fish using a $100\ \text{nm}$ Formvar foil target (Shot 16). The laser pulse parameters were measured

7 DETECTOR APPLICATION 2: CONCEPTS FOR LASER-DRIVEN PROTON RADIOGRAPHY

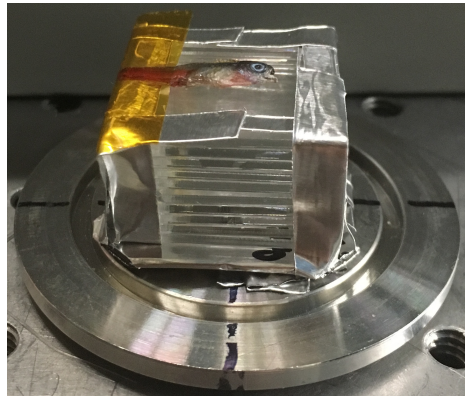
to be 99 J in 144 fs, resulting in 688 TW power, which was focused to a peak intensity of 1.5×10^{21} W/cm². The X-ray image, which is blurred by the direct impact of electrons, allows to identify the fish eye, the mouth and the swim bladder. However is the soft-tissue contrast low and does not allow to deduce the internal organ structure. The reason is the kV X-rays, low and does not allow to deduce the internal organ structure.

Although the image quality of the X-ray image should be improved by the usage of the tungsten needles, leading to a higher photon flux, a single-shot bimodal X-ray and proton energy resolving radiography of a biological sample with soft tissue and bones in air was successfully acquired. The high photon flux from the non-metal foil is anyway notable.

Figure 7.5c and figure 7.5d show photographs of the front sides of the first and second CR-39 behind the fish for the same shot. A few protons were visible even on the third and fourth CR-39 using a 10× magnification microscope, so having penetrated the 4.5 mm CR-39 in this shot (not shown). The results could also be seen as five contact radiographies with the corresponding X-ray image (section 3.2.4). The great density/thickness resolution of the protons is clearly visible, displaying the internal fish organ structure. Especially the open mouth with its different thicknesses is visible in the whitening of the first CR-39 (figure 7.5c), but also in the second one (figure 7.5d).

Re-etching and automated scanning with the microscope could have been performed in order to improve the proton image quality on the third and fourth CR-39, but an inaccurate reconstruction of the RSP using the five depth positions with visible proton pits, although feasible, was beyond the scope of this proof of concept.

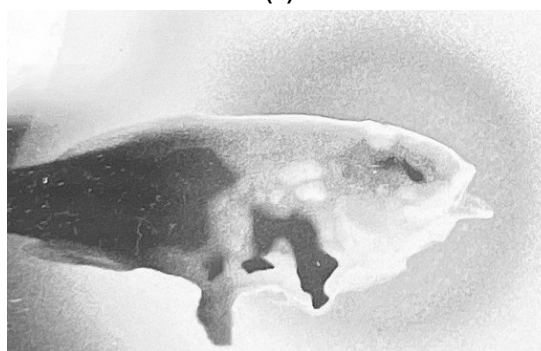
Due to the limited number of available laser shots and CR-39 detectors, as well as the limited proton energies achieved by the AFM needles shots during the beamtime, the results of only one successful shot on Formvar are shown here. The image quality of proton and X-ray images could not be optimized for proton energy and photon yield. A more stable source, as well as higher shot frequencies are desirable and should be realized for improved images with higher X-ray flux and more proton energy.



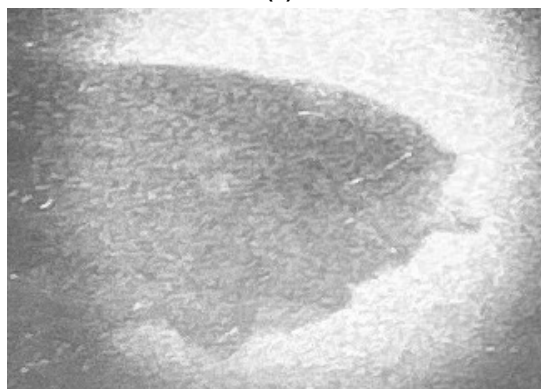
(a)



(b)



(c)



(d)

Figure 7.5: Multimodal imaging experiment at TPW with non-binary contrast. (a) Dead fish mounted on multiple proton detectors (CR-39) and an image plate (IP) (Shot 22). (b) X-ray radiography. (c) Proton radiography on front side of first CR-39. (d) Proton radiography on front side of second CR-39.

Chapter 8

Summary and Outlook

This chapter is intended to summarize the achievements and point towards future directions of the topics.

Overall, this thesis has contributed to a deeper understanding of the distinct features of laser-driven particle bunches and has presented efforts taken for generation, application and their detection.

Secondary radiation and radiation protection Chapter 4 discussed the angular dependence of proton-induced secondary neutrons at RPTC, as well as the distribution of secondary electrons, neutrons, pions, X-ray and γ photons generated by primary proton, electron, carbon and gold ion beams at CALA.

The secondary neutron fields at RPTC presented a strong dependence of the on the angle of observation and incident proton beam energy. A simplified treatment room model was needed to understand the origin of secondary neutrons in general and their energy dependence. The results of the study may be generalized in that they can provide an estimation of the secondary neutron fields. Identification of the neutron origin has shown that iron-rich room components contribute most to the evaporation energy interval in the room geometry. The simulations will influence the future decisions on gantry construction materials or structures, for example on the choice of massive gantry versus a bird-cage gantry-like structure. The presented data will have to be included in analytical treatment planning systems in order to predict the out-of-field neutron dose to organs far from the treatment field in order to guide medical physicists to create treatment plans which feature reduced risk of late adverse effects.

The results of the extensive Monte Carlo simulations of the CALA facility demonstrate the effectiveness of adequate beam dumps, magnets, passive shielding using sufficient cave walls, steel bars to temporarily plug X-ray holes and lead bricks. Additionally can laser pulse repetition limits allow the average dose rates in- and outside the experimental caves to stay below design specifications ($< 0.5 \mu\text{Sv/h}$ for unclassified areas,

(< 2.5 $\mu\text{Sv/h}$ for supervised areas, < 7.5 $\mu\text{Sv/h}$ locally). Caves and experimental areas neighbouring a cave, in which the laser is in operation can remain accessible. *Controlled areas* requiring personal electronic dosimeters can be avoided. For most configurations, the shielding components cause a five orders of magnitude difference in dose rate between proximal and distal scorers around the shielding wall. Elevated dose rates occurred behind the laser penetration holes that are located closest to the beam dump. These locations, however, are below the false floor inaccessible to the personnel.

At CALA, the features of the secondary neutron spectra in the LION cave are dependent on proton energy and measurement angle, and the relative contributions of these features to the total spectrum differ as expected from the RPTC simulations. Future investigations should try to systematically link different spectra of laser-accelerated proton bunches to the secondary neutron spectrum. A usage as non-invasive proton bunch diagnostic by online secondary neutron spectrometry would be desirable.

Radiation detection systems Chapter 5 described the RadEye CMOS pixel detector and the software and hardware developments undertaken for the implementation as a sensitive, low-dark current, low-background, triggerable, automated and EMP-insensitive main diagnostic at the LION experiment. The wave and particle nature of optical photons was used to characterize the RadEye and the CM49 CMOS pixel detector in order to increase their dynamic range using the image-lag phenomenon for protons.

As a possible replacement candidate for the RadEye the CM49 sensor was investigated. The tests undertaken to use the CM49 at the LION@CALA experiment, namely vacuum compatibility, alpha-particle sensitivity and operation in vicinity of the intense EMP were presented.

Chapter 6 discussed the signal characterisation of the LION WASP at the Siemens ONCOR electron linear accelerator by means of electron field measurements and phasespace simulations.

The used IAEA phasespaces of the Siemens ONCOR linac were successfully used to simulate the R_{80} in water and the lateral field shapes for 6, 9, 12, 15 and 18 MeV. Further were the phasespaces used to perform forward-simulations of the measurements using four RadEye sensors and the WASP at the University hospital Grosshadern. The lineouts of the measured and simulated spectrometer signals showed differences only in the regions, where mostly scattered particles should contribute to the signal. The scattering and showering of primary source electrons caused by the spectrometer front plate and general design are possibly sources of unwanted signal.

In order to use the electron distribution as a surrogate diagnostic for the proton bunch, the reconstruction should be optimized. Besides optimizing the WASP in order to reduce the background from scattered radiation and induced secondary showers, the reconstruction could benefit from a more realistic MC simulation of the detector signal and scintillation. The idealized modelling of the scintillator and detector as simple *energy deposition* in the PMMA and silicon layer, as well as the lack of any modelling of the scintillation process

and detector response itself and the modelling of the system matrix as a point source with a cone beam shape should be questioned in future.

Application of the distinct features for imaging Chapter 7 showed preliminary radiography using laser-driven proton and x-ray sources.

As samples at the LION@LEX experiment had to be brought into vacuum due to the limited proton energies achieved, they needed to be vacuum-compatible. Imaging of biological samples or a biologically motivated application should in future be conducted in air with the proton beam passing an additional vacuum window before reaching the object and experimental setup. This may then again degrade the image quality due to MCS. Low-energy laser-driven proton contact radiographies may be best suited for non-biological but technical samples of a few hundred μm thickness.

The μm small source size for X-rays and protons from tungsten needle targets achieved at the TPW laser system allowed for imaging using in-line X-ray phase contrast of higher resolution than absorption based imaging. A single-shot, combined X-ray and proton radiography of a fish was acquired. Such multimodal source of high-energy protons and X-rays could allow for applications combining single-shot therapy and imaging.

The CALA facility with the petawatt-class laser system ATLAS-3000 will allow to push the maximum energy and particle numbers of the proton bunches available at the LION experiment closer towards 100 MeV enabling biomedical applications like a mouse experiment.

The experimental efforts should concentrate to achieve higher shot repetition rates with reproducible and reliable bunches parameters. Additionally surrogate diagnostics and reliable detector systems be investigated in order to optimize the parameter space of the sources. Such way, the full potential of the unique features of laser-driven particle sources will certainly provide valuable contributions to radiobiology and radiotherapy and other applications.

Appendix A

Further RadEye and CM49 characterisation and HDR experiments

A.1 RadEye HDR proton detection at MLL and LION

RadEye HDR proton detection at MLL In order to probe the existence of image-lag in the RadEye sensor under proton beam irradiation, a sensor was set up at the MLL tandem accelerator and irradiated with proton bunches. For a controlled readout and bunch timing, as well as a reproducible bunch charge, the aforementioned two-channel function generator DG1032 and the delay generator DG535 were set up to produce proton bunches of duration between $5\ \mu\text{s}$ to 2 ms. The timing of bunch arrival was varied within the frame duration of 370 ms, in order to probe the dependence of the signal level in the second frame as function of the delay between saturation and readout. In order to have a geometrically defined beam spot, the sensor was set up in a dedicated vacuum chamber behind the two-lens permanent magnetic quadrupole system of the LION experiment [219].

Due to technical problems with the proton beam steering system, the amount of measured frames was too low for a reliable quantitative evaluation. The position fluctuation of the beam at the beam exit translated to a fluctuating spot intensity due to the spatially fixed aperture of the quadrupole system. Additionally, the general accelerator shutdown of the MLL tandem accelerator in 2017 prohibited a repetition of the measurement campaign.

Data from consecutive readouts usually showed signal in second frames, even before the bunch duration was long enough to saturate the first frame. Due to technical problems of the beam steering system, the magnitude of ADUs in the first and second frames varied from bunch to bunch between 0 ADU and saturation of the first frame. For bunches not

A FURTHER RADEYE AND CM49 CHARACTERISATION AND HDR EXPERIMENTS

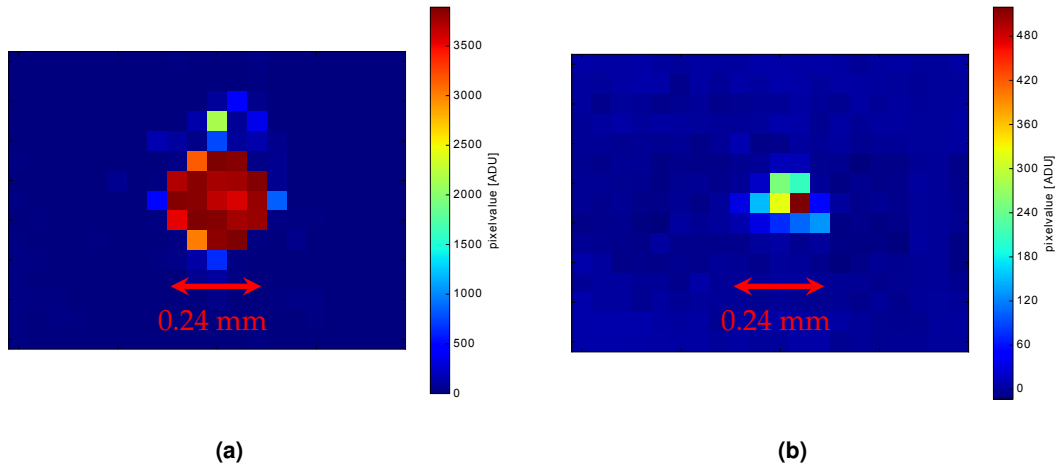


Figure A.1: HDR Readout of quadrupole focus using RadEye at MLL Tandem accelerator. (a) Saturated first frame ($\text{ADU}(1^{\text{st}}\text{frame}) > 4096$). (b) Second frame showing signal.

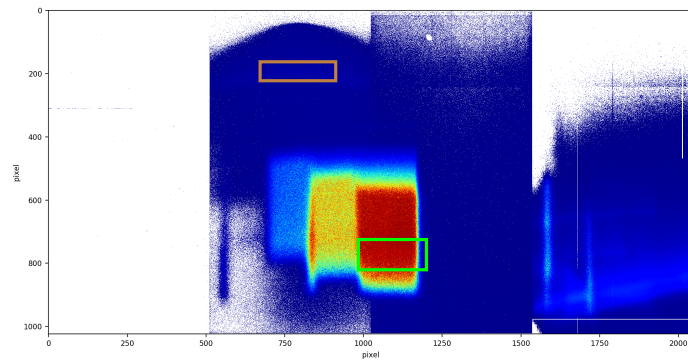
saturation of the first frame, the clustersum for all pixels with signal from the first (mostly saturated in figure A.1a) and the corresponding second frame (figure A.1b) was calculated.

The acquired usable data for $\text{ADU}(1^{\text{st}}\text{frame}) < 1500$ indicates a scaling factor for frame-stacking of ≈ 2 for all explored bunch duration lengths below saturation (equation A.1) [10]. This high value compared to the calibration factor for 532 nm light (figure 5.9) together with the finding of signal in non-saturated frames may originate from the shorter bunch length and the higher LET of the 20 MeV proton bunches and motivated to test the image lag for the few ns short proton bunches from laser-ion acceleration (see next section).

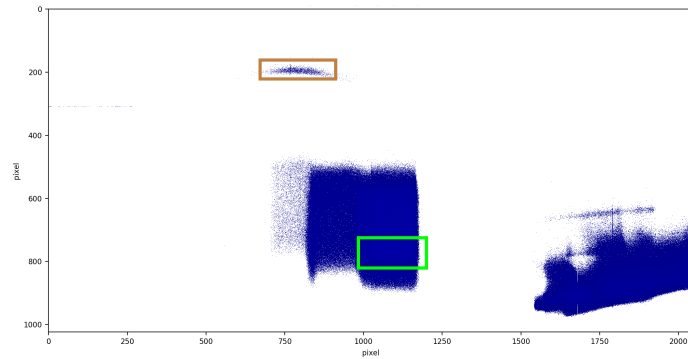
$$(A.1) \quad \text{ADU}(2^{\text{nd}}\text{frame}) \approx 1/2 \times \text{ADU}(1^{\text{st}}\text{frame})$$

Unfortunately, the varying bunch intensity from the tandem accelerator hindered to take enough frames with a bunch duration nearly saturating the first frame and then double the bunch duration in order to obtain a proton calibration factor. Due to the lack of such scaling factor to scale the net-ADU of the second frame figure A.1b to the true values, no frame stacking to extend the dynamic range of the saturated first frame figure A.1a was possible.

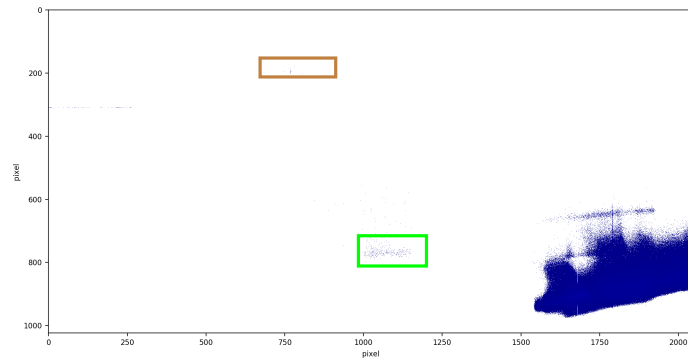
RadEye HDR proton detection for LION@CALA Although no quantitative calibration factor for protons was successful obtained from the proton measurements at the MLL accelerator due to low statistics, the image-lag for the RadEye sensor for ns short proton bunches accelerated by the 300 TW ATLAS laser was explored in a beamtime at the LION experiment in CALA in August 2019.



(a)



(b)



(c)

Figure A.2: HDR Readout of the proton spectrometer of the LION experiment at CALA. (a) First Frame. (b) Second Frame. (c) Third Frame. The multiple consecutive readouts after the impact of the few ns short proton bunch clearly show image-lag signal in irradiated areas.

Judging from the evaluation of the wide-angle spectrometer with a $10\ \mu\text{m}$ slit (section 6.1), the maximum cut-off energy of the broadband proton spectrum was $\approx 8\text{ MeV}$ (figure A.2a).

Figure A.2 presents three consecutive readouts of a proton bunch with kinetic energy up to 8 MeV but using a 1 mm slit and has rectangles indicating detector areas with signal in the first, second and third readout with a brown and green frame. Figure A.2a shows

A FURTHER RADEYE AND CM49 CHARACTERISATION AND HDR EXPERIMENTS

proton-induced signal, both saturated and non-saturated, together with the typical *beam-on* background consisting of forward directed radiation from the laser-plasma interaction.

The brown rectangle in figure A.2a indicates the region, where low-energy (≈ 36 MeV) ^{12}C -ions are deflected onto. Although unsaturated, the second readout in figure A.2b shows image-lag signal, which is not present in figure A.2c. figure A.2c also shows image-lag signal for the saturated area of proton impact in a green rectangle.

The existence of the lagged signal compared to 532 nm diode light could again be related to the high-LET nature of the ^{12}C -ions and protons, in addition to the ns short bunch duration as well as the known charge carrier trapping in crystal defects (section 5.1.5). The marked regions had in general showed an increased dark current due to pre-irradiation .

A.2 Initial CM49 proton characterisation and HDR photon and proton detection

CM49 HDR detection of light from a laser diode The experimental setup and evaluation scripts used for the HDR characterisation of the RadEye sensor as described in section 5.1.5 were reused for the CM49 sensor.

The CM49 sensor showed a linear response to the 532 nm photons in a single slit experiment. The single pixel values were plotted against the relative energy deposited there, based on the mathematical expectation from equation 5.1 (figure A.3a). The sensor showed a linear ideal response up to $\approx 85\%$ signal level (figure A.3).

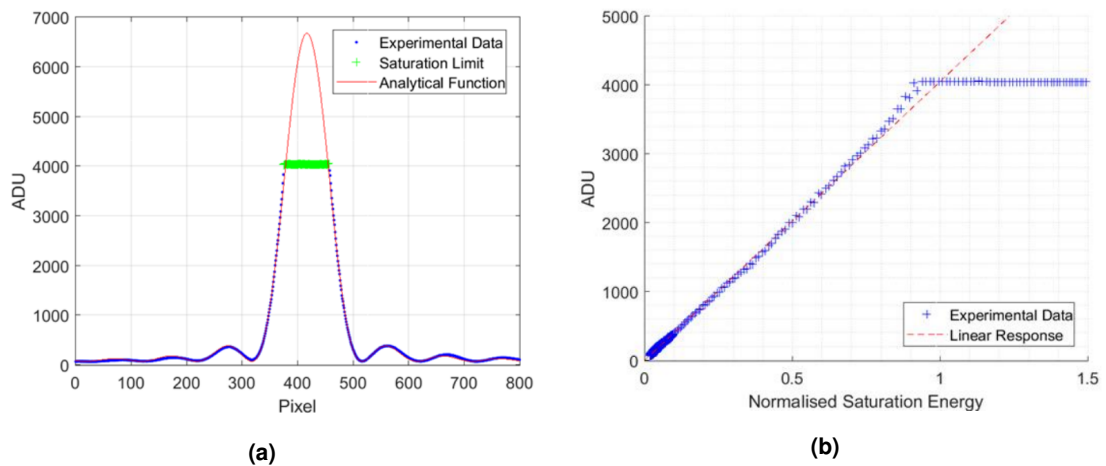


Figure A.3: Test of linearity and HDR using visible light. **(a)** Sinc curve fitted to unsaturated data. **(b)** CM49 responds to visible light linear over a range of $\approx 85\%$. Plots courtesy of M. Sng [214].

No signal due to image-lag was found using the 532 nm diode. This is in contrast to the RadEye sensor (figure 5.9). Although the diffraction pattern saturated the part of the first frame as expected for the Sinc-shaped light distribution (figure A.3a), the second readout never showed signal above background (figure A.4). The HDR experiments were performed at 10 Hz readout frequency, in contrast to the RadEye experiments with 370 ms readout period (≈ 2.7 Hz). The finding of non-existing image lag is in accordance with the results obtained by the manufacturer, who states 0.1% image lag for 9 Hz operation [227].

CM49 proton characterisation at MLL Proton beams at the MLL Tandem accelerator were used to assess the single-proton response, to test the existence of charge sharing between pixels, to probe the active thickness and the radiation hardness of the CM49 sensor and were carried as described for the RadEye in the PhD thesis of Sabine Reinhard [184]. Additionally, high-dynamic range imaging with protons was tested in analogy to

A FURTHER RADEYE AND CM49 CHARACTERISATION AND HDR EXPERIMENTS

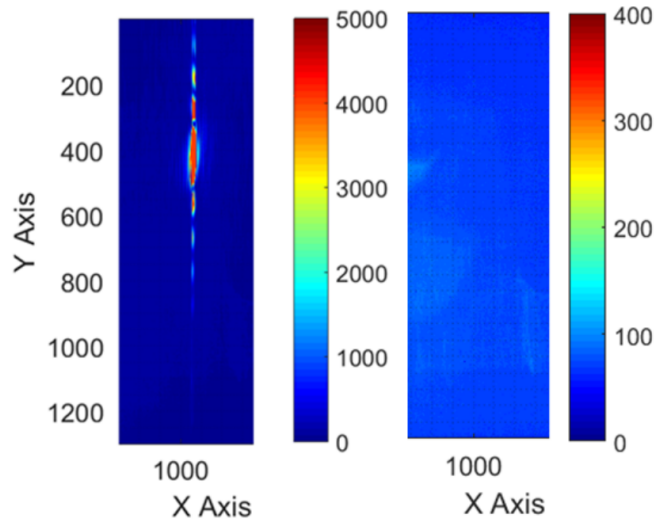


Figure A.4: Test of image-lag in the CM49 sensor using 532 nm pulses [214]. First and second frame after single pulse illumination at 10 Hz. No signal in the second frame indicates the absence of image-lag.

section A.1. Although the data quality seemed to be good, the evaluation proved to be demanding. The non-conclusive, but detailed evaluations of the measured data can be found in the Master thesis of M. Sng [214].

Protons with kinetic energy of 22 MeV and 10 MeV were provided by the accelerator and degraded in energy 6 cm upstream the CM49 sensor using up to $32 \times 200 \mu\text{m}$ thin plastic slabs. The slabs had been characterized for their energy degradation and the introduced energy spread previously [250].

At very low beam currents, areas of single and multiple proton hits were visible on the sensor (figure A.5a). A first evaluation of the histogram of pixel counts shows that the majority of hits, i.e. single 22 MeV protons, correspond to a reading of 180 ADU (figure A.5b). A double proton peak may be identified at 200 ADU. Fitting a Landau distribution for the energy deposition in such thin sensitive layer, together with proper background subtraction, which seems to be however difficult using the obtained data, will allow to assign a single proton response of $X \text{ ADU}(E)$ and to identify a linear double proton response by $2 \times \text{ADU}(E)$ [134]. A calibration of $\text{ADU} \rightarrow \text{energy deposition}$ (and hence particle number) can then be made and should be in future established for the CM49 sensor, which was however beyond the purpose of this work. Such procedure was successfully done by Reinhard et al. for the RadEye sensor [193].

Using the ADU values from single α -particle impacts (obtained in the experiments from section 5.2.3) together with the ADU values obtained by the 32 different degraded energies, the active layer thickness can be calculated. A first evaluation shows that the ADUs scale logarithmically with the proton beam energy, as expected from the Bethe-Bloch equation (equation 2.6).

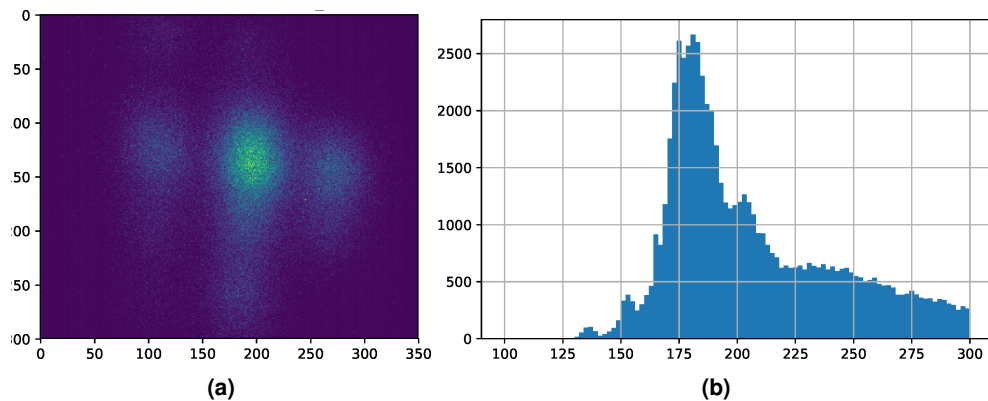


Figure A.5: Single proton sensitivity of CM49. **(a)** Highly degraded proton beam from tandem accelerator on the CM49. **(b)** Histogram of pixel counts.

CM49 HDR proton detection at MLL In analogy to the proton HDR setup for the Rad-Eye sensor in section A.1, the CM49 sensor was irradiated with protons at the MLL tandem accelerator.

As expected from the non-existing image-lag for the 532 nm diode, no signal in second frames was measurable. It was hence impossible to use the image-lag to further extend the dynamic range of the CM49 sensor.

List of abbreviations

ADC	Analog-to-Digital Converter
ADU	Analog-to-Digital Unit
ATLAS	Advanced Titanium Sapphire Laser
CALA	Centre For Advanced Laser Applications
CCD	Charge-Coupled Device
CERN	Conseil Européen pour la Recherche Nucléaire
CMOS	Complementary Metal-Oxide-Semiconductor
CR39	Columbia Resin 39
CPA	Chirped Pulse Amplification
CSDA	Continuous Slowing Down Approximation
CsI	Caesium iodide
CT	Computed Tomography
DDD	Depth Dose Distribution
DECT	Dual Energy Computed Tomography
EMP	Electromagnetic Pulse
ERBSS	Extended Range Bonner Sphere Spectrometer
ETTF	Electron Thomson Test Facility
FC	Faraday Cup
FLAIR	FLUKA Advanced Interface
FLUKA	Fluktuierende Kaskade
GEANT4	Geometry And Tracking 4
GSI	GSI Helmholtzzentrum für Schwerionenforschung
HDR	High Dynamic Range
HF	High Field
HMGU	Helmholtz Zentrum München für Gesundheit und Umwelt
HU	Hounsfield Unit
IAEA	International Atomic Energy Agency

I-BEAT	Ion-Bunch Energy Acoustic Tracing
IBT	Ion Beam Therapy
ICRU	International Commission on Radiation Units and Measurements
ICRP	International Commission on Radiological Protection
IP	Image Plate
LET	Linear Energy Transfer
LEX	Laboratory For Extreme Photonics
LION	Laser Driven Ion Acceleration
LIBT	Laser Ion Beam Therapy
LINAC	Linear Accelerator
LUX	Laser-Undulator X-ray Source
MC	Monte Carlo
MCS	Multiple Coulomb Scattering
MLL	Maier-Leibnitz-Laboratorium
MSIC	Multi Strip Ionization Chamber
ND	Neutral Density
PET	Positron Emission Tomography
PFS-pro	Petawatt Field Synthesizer-pro
PG	Pulse generator
PMMA	Polymethyl Methacrylate
PS	Phasespace
PDMS	Polydimethylsiloxan
PSI	Paul Scherrer Institute
PT	Proton Therapy
PTFE	Polytetrafluorethylen / Teflon
QE	Quantum Efficiency
QP	Quadrupole
RBE	Relative Biological Effectiveness
RCF	Radiochromic Film
RF	Radiofrequency

RPA	Radiation Pressure Acceleration
RPTC	Rinecker Proton Therapy Center
SECT	Single Energy Computed Tomography
SIRMIO	Small Animal Proton Irradiator For Research In Molecular Image-Guided Radiation-Oncology
SPECTRE	Source For Powerful Energetic Compact Thomson Radiation Experiments
SOBP	Spread Out Bragg Peak
SSD	Source Surface Distance
TNSA	Target Normal Sheath Acceleration
TOF	Time Of Flight
TPW	Texas Petawatt Laser
TPS	Treatment Planning System
TTL	Transistor Transistor Logic
USRTRACK	User Defined Tracking
USRBIN	User Defined Binning
WASP	Wide Angle Spectrometer
WET	Water Equivalent Thickness

List of scientific contributions

Co-supervised thesis

Bachelor

- **Benedikt Kopp:** Implementation of a Spot Scanning Coordinate System in a Monte Carlo Simulation for Quality Assurance at a Proton Treatment Facility. *LMU Munich*
- **Felix Balling:** Test of dynamic range extension of the RadEye sensor using a laser diode. *LMU Munich*

Master

- **Alexander Wislperger:** Monte Carlo Based Phase Space Reconstruction for Electrons in Laser Driven Ion Acceleration. *LMU Munich*
- **Francesco Olivari:** Investigating two prototype detector systems for spectrometry of polyenergetic proton bunches. *University of Padua, Italy*
- **Matthew Sng:** Characterization of the CM49 CMOS detector for laser-driven ion acceleration. *LMU Munich*

Publications

2022

- J Hartmann, **F Englbrecht** et al.: Quantitative spectrometry of protons using CMOS detectors from >10000 shots at the Centre for advanced Laser applications, *tba, In preparation*
- N Kurichiyani, M Pinto, T F Rösch, S Kundel, M Würll, **F Englbrecht**, J Schreiber, K Parodi: Design of an adaptable permanent-magnet lattice for refocusing of degraded proton beams for small animal irradiation, *tba, In preparation*

- N Kurichyanil, J Bortfeld, **F Englbrecht**, Z Huang, K Parodi: Reproducible kinematic alignment and precision field measurements of an adaptable permanent-magnet lattice for refocusing of degraded proton beams for small animal irradiation, *tba*, *In preparation*
- Z Huang, J Bortfeld, **F Englbrecht**, N Kurichyanil, M Pinto, K Parodi: Performance of an adaptable permanent-magnet lattice for refocusing of degraded proton beams for small animal irradiation, *tba*, *In preparation*

2021

- **F Englbrecht**, S Trinkl, V Mares, J Wilkens, M Wielunski, K Parodi, W Rühm, M Hillbrand: A Comprehensive Monte-Carlo Study of Out-Of-Field Secondary Neutron Spectra in a Scanned-Beam Proton Therapy Treatment Room, *Journal of Medical Physics* 31, 2:215-228
- M Tisi, V Mares, J Schreiber **F Englbrecht**, W Rühm: Geant4 Monte Carlo Simulation Study of the Secondary Radiation Fields at the Laser-driven Ion Source LION, *Nature Scientific Reports* 11, 24418

2020

- S Meyer, J Bortfeld, P Lämmer, **F Englbrecht**, M Pinto, K Schnürle, M Würzl, K Parodi: Optimization and Performance Study of a Proton CT System for Pre-Clinical Small Animal Imaging, *Physics in Medicine and Biology* 65, 155008
- M Würzl, C Gianoli, **F Englbrecht**, J Schreiber, K Parodi: A Monte Carlo feasibility study on quantitative laser-driven proton radiography, *Zeitschrift für medizinische Physik* 32, 1:109-119
- T F Rösch, D Haffa, J Bin, S Brunner, **F Englbrecht**, A Friedl, Y Gao, J Hartmann, P Hilz, C Kreuzer, F H Lindner, T M Ostermayr, R Polanek, M Speicher, Z Szabó, E R Szabó, D Taray, T Tóké, M Würzl, K Parodi, K Hideghéty, J Schreiber: A feasibility study of Zebrafish embryo irradiation with laser accelerated protons, *Review of Scientific Instruments* 91, 063303
- **F Englbrecht**, F H Lindner, J Hartmann, A Döpp, H F Wirth, S Karsch, J Schreiber, K Parodi, G Dedes: Radiation protection modeling for 2.5 Petawatt-laser production of ultrashort x-ray, proton and ion bunches: Monte Carlo model of the Munich CALA facility, *Journal Of Radiological Protection* 40, 1048–1073
- T M Ostermayr, C Kreuzer, **F S Englbrecht**, J Gebhard, J Hartmann, D Haffa, P Hilz, K Parodi, J Wenz, M E Donovan, G Dyer, E Gaul, J Gordon, M Martinez, E Mccary, M Spinks, G Tiwari, B M Hegelich, J Schreiber: Laser-driven x-ray and proton micro-source and application to simultaneous single-shot bi-modal radiographic imaging, *Nature Communications* 11, 6174

2019

- M Hillbrand, G Landry, S Ebert, G Dedes, E Pappas, G Kalaitzakis, C Kurz, M Würfl, **F Englbrecht**, O Dietrich, D Makris, E Pappas, K Parodi: Gel dosimetry for three dimensional proton range measurements in anthropomorphic geometries, *Zeitschrift für Medizinische Physik* 29, 162-172
- D Haffa, R Yang, J Bin, S Lehrack, F-E Brack, Hao Ding, **F Englbrecht**, Y Gao, J Gebhard, M Gilljohann, J Götzfried, J Hartmann, S Herr, P Hilz, S D Kraft, C Kreuzer, F Kroll, F H Lindner, J Metzkes-Ng, T M Ostermayr, E Ridente, T F Rösch, G Schilling, H-P Schlenvoigt, M Speicher, D Taray, M Würfl, K Zeil, U Schramm, S Karsch, K Parodi, Paul R Bolton, Walter Assmann, J Schreiber: I-BEAT: New ultrasonic method for single bunch measurement of ion energy distribution, *Nature Scientific Reports* 9, 6714
- J Lascaud, R Kalunga, S Lehrack, HP Wieser, **F Englbrecht**, M Würfl, W Assmann, A S Savoia, K Parodi: Applicability of Capacitive Micromachined Ultrasonic Transducers for the detection of proton-induced thermoacoustic waves, *IEEE International Ultrasonics Symposium*, 143-146

2018

- **F Englbrecht**, M Würfl, F Olivari, A Ficorella, C Kreuzer, F H Lindner, M D Palma, L Pancheri, G-F Betta, J Schreiber, A Quaranta, K Parodi: An online, radiation hard proton energy-resolving scintillator stack for Laser-driven proton bunches, *Radiation Protection Dosimetry*, 1-5
- F H Lindner, J Bin, **F Englbrecht**, D Haffa, P R Bolton, Y Gao, J Hartmann, P Hilz, C Kreuzer, T M Ostermayr, T F Rösch, M Speicher, K Parodi, P G Thirolf, J Schreiber: A novel approach to electron data background treatment in a new online wide-angle spectrometer for laser-accelerated ion and electron bunches, *Review of Scientific Instruments* 89, 013301
- M Würfl, **F Englbrecht**, S Lehrack, C Gianoli, F H Lindner, T F Rösch, D Haffa, F Olivari, M Petasecca, M Lerch, A Pogosso, L T Tran, W Assmann, J Schreiber, A B Rosenfeld, K Parodi: Time-of-Flight Spectrometry of Ultra-Short, Polyenergetic Proton Bunches, *Review of Scientific Instruments* 89, 123302

2017

- **F Englbrecht**, F Balling, T F Rösch, M Würfl, F H Lindner, K Parodi, J Schreiber: Characterization of online high dynamic range imaging for laser-driven ion beam diagnostics using visible light, *Current Directions in Biomedical Engineering* 3(2), 343-346

- F H Lindner, D Haffa, J Bin, **F Englbrecht**, Y Gao, J Gebhard, J Hartmann, P Hinz, C Kreuzer, S Lehrack, T M Ostermayr, T F Rösch, M Speicher, M Würzl, K Parodi, J Schreiber, P G Thirolf: Towards swift ion bunch acceleration by high-power laser pulses at the Centre for Advanced Laser Applications, *Nuclear Instruments and Methods in Physics Research Section B: Beam Interactions with Materials and Atoms* 402, 354-357
- S Trinkl, V Mares, **F Englbrecht**, J Wilkens, M Wielunski, K Parodi, W Rühm, M Hillbrand: Systematic Out-of-Field Secondary Neutron Spectrometry and Dosimetry in Pencil Beam Scanning Proton Therapy, *Medical Physics* 44, 1912–1920
- T F Rösch, P Hinz, J Bin, **F Englbrecht**, Y Gao, D Haffa, J Hartmann, S Herr, F H Lindner, M Speicher, M Würzl, K Parodi, J Schreiber: Considerations on employing a PMQ-doublet for narrow and broad proton energy distributions, *Current Directions in Biomedical Engineering* 3(2), 339-342

2016

- Y Gao, J Bin, D Haffa, C Kreuzer, J Hartmann, M Speicher, F H Lindner, T M Ostermayr, P Hinz, T F Rösch, S Lehrack, **F Englbrecht**, S Seufferling, M Gilljohann, H Ding, W Ma, K Parodi, J Schreiber: An automated, 1 Hz nano-target positioning system for intense laser plasma experiments, *High Power Laser Science and Engineering* 5
- M Würzl, **F Englbrecht**, K Parodi, M Hillbrand: Impact of a scanned proton beam's low-dose envelope on the accuracy of clinical dose delivery at a ProBeam based facility: a comparison of measurements with TPS and MC calculations, *Physics in Medicine and Biology* 61, 958–973

Conference Contributions

2022

- **tba: C. Steinbrecht et al:** Entwicklung eines FPGA basierten Strahlsteuerungs- und Überwachungssystems für die SIRMIO Plattform, *Annual conference of the German Society for Medical Physics, DGMP 2022, Aachen, Germany*
- **tba: J Bortfeld et al:** Entwicklung und Charakterisierung eines präklinischen Micromegas pCT-Systems, *Annual conference of the German Society for Medical Physics, DGMP 2022, Aachen, Germany*
- **Oral: K Schnürle et al:** Integration mode proton imaging with pixelated large-area CMOS sensor, *23rd International Workshop on Radiation Imaging Detectors, IWORID 2022, Riva del Garda, Italy*

- **Oral: K Schnürle et al:** CMOS Integration Mode Proton Imaging for a Small Animal Irradiator, *5th conference on small animal precision image-guided radiotherapy, SMART 2022, Munich, Germany*
- **Oral: J Bortfeld et al:** Development of a Small Animal Proton Computed Tomography System using High Precision Single Particle Tracking, *5th conference on small animal precision image-guided radiotherapy, SMART 2022, Munich, Germany*

2021

- **Oral: M Würfl et al:** On the Feasibility of Quantitative Laser-Driven Proton Radiography, *'Applying Laser-Driven Particle Acceleration: Medical and Nonmedical Uses of Distinctive Energetic Particle and Photon Sources II', ALPA 2021, Prague, Czech Republic*
- **Oral: T Ostermayr et al:** Multimodal emission from laser-plasma accelerators and possible applications, *Conference on Laser Acceleration of Electrons, Protons, and Ions, SPIE 2021, Prague, Czech Republic*
- **Oral: K Schnürle et al:** Development of integration mode proton imaging with a single CMOS detector for a small animal irradiation platform, *3rd European Congress of Medical Physics, ECMP 2021, Torino, Italy*
- **Oral: K Schnürle et al:** Integration mode proton imaging with a single CMOS detector for a small animal irradiation platform, *Annual conference of the German Society for Medical Physics, DGMP 2021, Wien, Austria*
- **Oral: K Schnürle et al:** Small Animal CMOS Integration Mode Proton Imaging at Different Treatment Facilities 7th Annual Loma Linda Workshop on Particle Imaging and Radiation Treatment Planning 2021, Loma Linda, USA

2020

- **Oral: K Schnürle et al:** Development of integration-mode proton imaging for a small animal irradiation platform with a CMOS detector at synchro-cyclotron based proton therapy facilities, *5th conference on small animal precision image-guided radiotherapy, SMART 2020, Munich, Germany*
- **Oral: J Bortfeld et al:** Development of a small animal proton radiography system using high precision single particle tracking, *5th conference on small animal precision image-guided radiotherapy, SMART 2020, Munich, Germany*
- **Oral: J Schreiber et al:** Laser-driven ion source development at the Centre for Advanced Laser Applications, *5th conference on small animal precision image-guided radiotherapy, SMART 2020, Munich, Germany*

- **Oral: K Schnürle et al:** Development of integration-mode proton imaging with a single CMOS detector for a small animal irradiation platform, *3rd European Congress of Medical Physics, ECMP 2020, Torino, Italy*
- **Oral: K Schnürle et al:** Entwicklung von Protonenbildgebung mit einem einzelnen integrierenden CMOS-Detektor für eine Kleintierbestrahlungsanlage, *Annual conference of the German Society for Medical Physics, DGMP 2020, Leipzig, Germany*
- **Oral: K Schnürle et al:** Development of integration-mode proton imaging with a single CMOS detector for a small animal irradiation platform, *Applied Nuclear Physics conference, ANPC 2020, Prague, Czech Republic*

2019

- **Oral: J Bortfeld et al:** Development of a Time Projection Chamber for ion transmission imaging, *Vienna Conference on Instrumentation, VCI 2019, Vienna, Austria*
- **Poster: S Kundel et al:** Beamline optimization studies for small animal irradiation at clinical proton therapy facilities, *Particle Therapy Co-Operative Group, PTCOG 58 2019, Manchester, UK*
- **Oral: S Meyer et al:** Optimization and Performance Evaluation of a Proton Computed Tomography System for Small Animal Imaging, *Particle Therapy Co-Operative Group, PTCOG 58 2019, Manchester, UK*
- **Oral: F Englbrecht et al:** Pixel detectors for laser-driven proton and carbon ion acceleration at CALA, *Workshop on Low-Energy Ion-Beam Diagnostics, Imperial College London 2019, London, UK*
- **Oral: J Boertfeld et al:** Development of novel ultra-thin Micromegas and a Time Projection Chamber for animal ion transmission tomography, *Micro Pattern Gaseous Detectors, MPGD 19 2019, La Rochelle, France*
- **Poster: N Kurichyanil et al:** Design of an adaptable permanent-magnet lattice for refocusing of degraded proton beams for small animal irradiation, *Annual Meeting of the American Association of Physicists in medicine, AAPM 2019, San Antonio, USA*
- **Poster: S Kundel et al:** Optimierung einer neuartigen Strahlführung für Kleintierbestrahlungen an einem klinischen Protonen-Therapiezentrum, *Annual conference of the German Society for Medical Physics, DGMP 2019, Stuttgart, Germany*
- **Oral: M Würfl et al:** Machbarkeitsstudie zur Entwicklung von laser-beschleunigter Protonenradiographie, *Annual conference of the German Society for Medical Physics, DGMP 2019, Stuttgart, Germany*
- **Oral: S Meyer et al:** Optimierung und Performance Evaluierung eines Protonen Computertomographie Systems für präklinische Bildgebung, *Annual conference of the German Society for Medical Physics, DGMP 2019, Stuttgart, Germany*

- **Poster: T Rösch et al:** Eine Machbarkeitsstudie zur Bestrahlung von Zebrafischembryonen mit Laser-beschleunigten Protonen, *Annual conference of the German Society for Medical Physics, DGMP 2019, Stuttgart, Germany*
- **Oral: K Schnürle et al:** Monte-Carlo Studie zur Protonenradiographie für die Positionsverifikation für Kleintierbestrahlungen an einem klinischen Protonen-Therapiezentrum, *Annual conference of the German Society for Medical Physics, DGMP 2019, Stuttgart, Germany*
- **Oral: F Englbrecht et al:** Erzeugung ultrakurzer Röntgen-, Protonen- und Ionenstrahlen mittels Petawatt-Laser: Monte-Carlo Simulationen für den baulichen Strahlenschutz, *Jahrestagung Fachverband für Strahlenschutz 2019, Würzburg, Germany*
- **Oral: J Lascaud et al:** Applicability of Capacitive Micromachined Ultrasonic Transducers for the detection of proton-induced thermoacoustic waves, *IEEE Ultrasonics, Ferroelectrics, and Frequency Control Society, IEEE IUS 2019, Glasgow, Scotland, UK*
- **Poster: T Rösch et al:** A feasibility study of zebrafish embryo irradiation with laser accelerated protons, *Laser-driven Particle Accelerator Workshop, LPAW 2019, Split, Croatia*
- **Poster: J Bortfeld et al:** Novel Micro-pattern Gaseous Detectors for a Small Animal Proton Irradiation Platform, *Nuclear Science Symposium and Medical Imaging Conference, IEEE NSS MIC 2019, Manchester, UK*
- **Oral: P Cirrone et al:** Monte Carlo Methods in Particle Therapy, *International Conference on the Use of Computers in Radiation Therapy and the International Conference on Monte Carlo Techniques for Medical Applications, ICCR MCMA 2019, Montreal, Canada*
- **Oral: J Bortfeld et al:** Ultra-Thin Gaseous Detectors for Small Animal Proton Transmission Imaging, *International Workshop on Detection Systems and Techniques in Nuclear and Particle Physics, DeSyT 2019, Messina, Italy*

2018

- **Oral: F Englbrecht et al:** Monte-Carlo simulations for radio protection shielding design of 3 petawatt laser based production of ultrashort X-ray, proton and ion bunches for biomedical applications, *Annual conference of the German Society for Medical Physics, DGMP 2018, Nürnberg, Germany*
- **Poster: M Würfl et al:** Silicon detectors in medical applications and for characterization of laser-driven ion sources, *13th Trento Workshop on Advanced Silicon Radiation Detectors 2018, Munich, Germany*
- **Poster: M Würfl et al:** Feasibility study for small-animal proton radiography using passive energy variation and a single planar detector, *Annual conference of the German Society for Medical Physics, DGMP 2018, Nuremberg, Germany*

2017

- **Oral: F Englbrecht et al:** An online, radiation hard proton energy-resolving scintillator stack for laser-driven proton bunches, *Neutron and Ion Dosimetry Symposium, NEUDOS-13, Krakow, Poland*
- **Oral: M Würfl et al:** Development of TOP-Spectrometry for laser-accelerated protons using a novel silicon detector, *Neutron and Ion Dosimetry Symposium, NEUDOS-13, Krakow, Poland*
- **Oral: G Landry et al:** Patient specific 3D gel dosimetry for proton therapy, *Neutron and Ion Dosimetry Symposium, NEUDOS-13, Krakow, Poland*
- **Oral: F Englbrecht et al:** Laser Driven Proton Radiography Using A High Repetition Rate Laser System, *Conference on Lasers and Electro-Optics, CLEO/Europe 2017, Munich, Germany*
- **Poster: T Rösch et al:** Laser-driven ION (LION) Acceleration at the Centre for Advanced Laser Applications (CALA), *Conference on Lasers and Electro-Optics, CLEO/Europe 2017, Munich, Germany*
- **Oral: M Würfl et al:** Development of TOF-Spectrometry of Laser-Accelerated Proton Pulses using Silicon Microdosimeters, *Conference on Lasers and Electro-Optics, CLEO/Europe 2017, Munich, Germany*
- **Oral: T Ostermayr et al:** Laser interactions with micro-targets for imaging applications, *Conference on Lasers and Electro-Optics, CLEO/Europe 2017, Munich, Germany*
- **Poster: F Englbrecht et al:** An online, radiation hard proton energy-resolving scintillator stack for Laser-driven proton bunches, *Annual conference of the German Society for Medical Physics, DGMP 2017, Dresden, Germany*
- **Poster: M Würfl et al:** A new method for position-sensitive spectrometry of laser-accelerated proton pulses using the Timepix detector, *Annual conference of the German Society for Medical Physics, DGMP 2017, Dresden, Germany*
- **Poster: T Rösch et al:** Considerations on employing a PMQ-doublet for narrow and broad proton energy distributions , *Annual conference of the German Society for Medical Physics, DGMP 2017, Dresden, Germany*
- **Oral: M Hillbrand et al:** A 3D polymer gel dosimeter coupled to a patientspecific anthropomorphic phantom for pencil beam scanned proton therapy, *Annual meeting of the european society for radiotherapy oncology, ESTRO 36 2017, Vienna, Austria*
- **Poster: M Würfl et al:** Development of two prototype spectrometers for laser-accelerated proton bunches, *International Symposium on Microdosimetry, MICROS 2017, Venice, Italy*

2016

- **Poster: F Englbrecht et al:** SU-F-T-217: Measurement and Monte-Carlo Simulation of Electron Phase Spaces Using a Wide Angle Magnetic Electron Spectrometer, *Annual Meeting of the American Association of Physicists in medicine, AAPM 2016, Washington DC, USA*
- **Poster: F Englbrecht et al:** SU-F-T-84: A Comprehensive Monte-Carlo Study of Out-Of-Field Secondary Neutron Spectra in a Scanned-Beam Proton Therapy Treatment Room, *Annual Meeting of the American Association of Physicists in medicine, AAPM 2016, Washington DC, USA*
- **Oral: F Englbrecht et al:** Monte-Carlo Studie der Energiespektren sekundärer Neutronen außerhalb des Bestrahlungsfeldes in einem mit der Scanning Technik und Gantry ausgestatteten Protonentherapie Behandlungsraum, *Annual conference of the German Society for Medical Physics, DGMP 2016, Würzburg, Germany*
- **Oral: F Englbrecht et al:** Messung und Monte-Carlo Simulation von Elektronen Phasenräumen mittels eines magnetischen Elektronen Spektrometers mit großem Akzeptanzwinkel, *Annual conference of the German Society for Medical Physics, DGMP 2016, Würzburg, Germany*
- **Oral: F Englbrecht et al:** Messung und Monte-Carlo Simulation von Elektronenphasenräumen mittels eines magnetischen Elektronen-Spektrometers für Laser-Plasma-Experimente, *DGMP/DPG Webinar, German society for Medical Physics DGMP*
- **Oral: G Dedes et al:** MEDical and multidisciplinary applications of laser-driven ion beams at ELI-Beamlines, *3rd ELIMED Workshop 2016: Laser driven proton imaging: Focus on imaging for proton therapy, Catania, Italy*

2015

- **Oral: F Englbrecht et al:** Monte-Carlo studies for the development of laser-driven proton radiography, *Annual conference of the German Society for Medical Physics, DGMP 2015, Marburg, Germany*
- **Poster: F Englbrecht et al:** Angular-energy Distribution Reconstruction of Electrons Emitted from Laser Irradiated Foils, *Application of Laser-driven Particle Acceleration, ALPA 2015, Venice, Italy*
- **Poster: M Würfl et al:** Dose output dependence on field size and spot spacing in scanned proton therapy – a comparison of measurements with TPS and MC calculations, *Annual conference of the German Society for Medical Physics, DGMP 2015, Marburg, Germany*

- **Poster: G Dedes et al:** Angular-energy distribution reconstruction of electrons emitted from laser irradiated foils, *Annual conference of the German Society for Medical Physics, DGMP 2015, Marburg, Germany*
- **Poster: M Würfl et al:** Monte-Carlo studies for the development of laser-driven proton radiography, *Application of Laser-driven Particle Acceleration, ALPA 2015, Venice, Italy*
- **Poster: M Würfl et al:** Dose output dependence on field size and spot spacing in scanned proton therapy: A comparison of measurements with TPS and MC calculations, *55th annual conference of the Particle Therapy Co-operative Group, PTCOG 2015, Prague, Czech Republic*

2013

- **Poster: F Englbrecht et al:** Monte-Carlo modeling to support quality assurance at a clinical proton therapy facility, *Annual conference of the German Society for Medical Physics, DGMP 2013, Cologne, Germany*

Bibliography

- [1] B. M. Hegelich, D. Jung, B. J. Albright, M. Cheung, B. Dromey, D. C. Gautier, C. Hamilton, S. Letzring, R. Munchhausen, S. Palaniyappan, R. Shah, H.-C. Wu, L. Yin¹, J. C. Fernández. 160 MeV laser accelerated protons from CH₂ nanotargets for proton cancer therapy. *arXiv:1310.8650 v1 physics.plasm-ph*, 2013. (Cited on page 93.)
- [2] 14th Fluka Course, Dresden, Germany. FLUKA Beginner’s Course lecture notes. In *An Introduction to FLUKA: a Multipurpose Interaction and Transport MC code*, 2013. (Cited on pages 34 and 35.)
- [3] A. J. Gonsalves, K. Nakamura, J. Daniels, H. S. Mao, C. Benedetti, C. B. Schroeder, Cs. Toth, J. van Tilborg, D. E. Mittelberger, S. S. Bulanov, J.-L. Vay, C. G. R. Geddes, E. Esarey, W. P. Leemans. Generation and pointing stabilization of multi-GeV electron beams from a laser plasma accelerator driven in a pre-formed plasma waveguide. *Physics of Plasmas*, 22:056703–8, 2015. (Cited on pages 43 and 92.)
- [4] A. Macchi, M. Borghesi, M. Passoni. Ion acceleration by superintense laser-plasma interaction. *Review of modern physics*, 85:751–793, 2013. (Cited on pages 35, 38, 40, 41, 43, 50, and 92.)
- [5] Agostinelli S. et al. Geant4—a simulation toolkit. *Nuclear Instruments and Methods in Physics Research Section A: Accelerators, Spectrometers, Detectors and Associated Equipment*, 2003. (Cited on pages 34, 61, and 65.)
- [6] Allen A M; Pawlicki T; Dong L et al. An evidence based review of proton beam therapy: The report of ASTRO’s emerging technology committee. *Radiotherapy and Oncology*, 2012. (Cited on page 59.)
- [7] M. Arjomandy B; Sahoo N; Cox J; Lee A; Gillin. Comparison of surface doses from spot scanning and passively scattered proton therapy beams. *Physics in Medicine and Biology*, 2009. (Cited on page 60.)
- [8] S. Avery, C. Ainsley, R. Maughan, and J. McDonough. Analytical shielding calculations for a proton therapy facility. *Radiation Protection Dosimetry*, 131(2):167–179, 05 2008. (Cited on page 65.)
- [9] F. Ballarini, G. Battistoni, F. Cerutti, A. Empl, A. Fassò, A. Ferrari, E. Gadioli, M. Garzelli, A. Ottolenghi, L. Pinsky, et al. Nuclear models in fluka: Present capabilities, open problems, and future improvements. In *AIP Conference Proceedings*, volume 769, page 1197, 2005. (Cited on page 35.)
- [10] F. Balling. Test of dynamic range extension of the RadEye sensor using a laser diode . *LMU Munich Bachelor Thesis*, 2017. (Cited on pages 128 and 180.)
- [11] M. Baradaran-Ghahfarokhi, F. Reynoso, A. Darafsheh, et al. A Monte Carlo-based analytic model of neutron dose equivalent for a mevion gantry-mounted passively scattered proton system for craniospinal irradiation. *Med. Phys.*, 47(9):4509–4521, 2020. (Cited on page 60.)
- [12] M. Baradaran-Ghahfarokhi, F. Reynoso, A. Darafsheh, et al. A Monte Carlo based analytic model of the in-room neutron ambient dose equivalent for a Mevion gantry-mounted passively scattered proton system. *J. Radiol. Prot.*, 40:980–996, 2020. (Cited on page 60.)
- [13] W. Barkas and D. Evans. *Nuclear Research Emulsions: Techniques and theory*. Pure and applied physics. Academic Press, 1963. (Cited on page 9.)
- [14] B. Barnes, K. Kraywinkel, E. Nowossadeck, I. Schönfeld, A. Starker, A. Wienecke, and U. Wolf. Bericht zum Krebsgeschehen in Deutschland 2016, 2016. (Cited on page 1.)
- [15] V. A. Bashkirov, R. W. Schulte, R. F. Hurley, R. P. Johnson, H. F.-W. Sadrozinski, A. Zatserklyaniy, T. Plautz, and V. Giacometti. Novel scintillation detector design and performance for proton radiography and computed tomography. *Medical Physics*, 43(2):664–674, 2016. (Cited on page 32.)

- [16] G. Battistoni, F. Cerutti, A. Fassó, A. Ferrari, S. Muraro, J. Ranft, S. Roesler, and P. R. Sala. The FLUKA code: description and benchmarking. *AIP Conference Proceedings*, 896(1):31–49, 2007. (Cited on pages 61 and 86.)
- [17] J. Bauer, F. Sommerer, A. Mairani, D. Unholtz, R. Farook, J. Handrack, K. Frey, T. Marcelos, T. Tessonier, S. Ecker, B. Ackermann, M. Ellerbrock, J. Debus, and K. Parodi. Integration and evaluation of automated Monte Carlo simulations in the clinical practice of scanned proton and carbon ion beam therapy. *Physics in Medicine and Biology*, 59(16):4635–4659, jul 2014. (Cited on page 32.)
- [18] Benton, E R; Islam M R; Collums T L; Zheng Y; Monson J. Off-axis dose equivalent due to secondary neutrons from uniform scanning proton beams during proton radiotherapy. *Physics in Medicine and Biology*, 2013. (Cited on page 60.)
- [19] M. Berger, J. Coursey, and M. Zucker. ESTAR, PSTAR, and ASTAR: Computer Programs for Calculating Stopping-Power and Range Tables for Electrons, Protons, and Helium Ions (version 1.21), 1999-01-01 1999. (Cited on page 168.)
- [20] H. Bethe. Zur Theorie des Durchgangs schneller Korpuskularstrahlen durch Materie. *Annalen der Physik*, 397(3):325–400, 1930. (Cited on page 9.)
- [21] J. Bin, K. Allinger, W. Assmann, G. Dollinger, G. A. Drexler, A. A. Friedl, D. Habs, P. Hilz, R. Hoerlein, N. Humble, S. Karsch, K. Khrennikov, D. Kiefer, F. Krausz, W. Ma, D. Michalski, M. Molls, S. Raith, S. Reinhardt, B. Röper, T. E. Schmid, T. Tajima, J. Wenz, O. Zlobinskaya, J. Schreiber, and J. J. Wilkens. A laser-driven nanosecond proton source for radiobiological studies. *Applied Physics Letters*, 101(24):243701, 2012. (Cited on page 21.)
- [22] J. Bin, L. Obst-Huebl, J.-H. Mao, K. Nakamura, L. D. Geulig, H. Chang, Q. Ji, L. He, J. De Chant, Z. Kober, A. J. Gonsalves, S. Bulanov, S. E. Celniker, C. B. Schroeder, C. G. R. Geddes, E. Esarey, B. A. Simmons, T. Schenkel, E. A. Blakely, S. Steinke, and A. M. Snijders. A new platform for ultra-high dose rate radiobiological research using the BELLA PW laser proton beamline. *Scientific Reports*, 12(1):1484, 2022. (Cited on page 21.)
- [23] F. Bloch. Zur Bremsung rasch bewegter Teilchen beim Durchgang durch Materie. *Annalen der Physik*, 408(3):285–320, 1933. (Cited on page 9.)
- [24] H.-J. Borchert, M. Mayr, R. A. Schneider, M. R. Arnold, D. E. Geismar, M. Wilms, L. Wisser, and M. Herbst. Proton therapy with spot scanning: the Rinecker Proton Therapy Center in Munich. Part 2: Technical & physical aspects. *Nowotwory Journal of Oncology*, 58(2):62e–70e, 2008. (Cited on pages 30, 59, 61, and 62.)
- [25] M. Borghesi, A. Schiavi, D. H. Campbell, M. G. Haines, O. Willi, A. J. MacKinnon, L. A. Gizzi, M. Galimberti, R. J. Clarke, and H. Ruhl. Proton imaging: a diagnostic for inertial confinement fusion/fast ignitor studies. *Plasma Physics and Controlled Fusion*, 43(12A):A267–A276, nov 2001. (Cited on page 162.)
- [26] D. G. M. A. Borne F. Radiation protection for an ultra-high intensity laser. *Radiation Protection Dosimetry*, 102:61–70, 2002. (Cited on page 89.)
- [27] I. A. Borowski M. Considerations concerning the use of counting active personal dosimeters in pulsed fields of ionising radiation. *Radiation Protection Dosimetry*, 139:483–493, 2010. (Cited on page 89.)
- [28] J. Bortfeldt, M. Bender, O. Biebel, H. Danger, B. Flierl, R. Hertenberger, P. Loesel, S. Moll, K. Parodi, I. Rinaldi, A. Ruschke, and A. Zibell. High-Rate Capable Floating Strip Micromegas. *Nuclear and Particle Physics Proceedings*, 273-275:1173–1179, 2016. 37th International Conference on High Energy Physics (ICHEP). (Cited on page 54.)
- [29] J. Bortfeldt, O. Biebel, B. Flierl, R. Hertenberger, F. Klitzner, P. Lösel, L. Magallanes, R. Müller, K. Parodi, T. Schlueter, B. Voss, and A. Zibell. Low material budget floating strip Micromegas for ion transmission radiography. *Nuclear Instruments & Methods in Physics Research Section A-Accelerators Spectrometers Detectors and Associated Equipment*, page 210–214, 2017. (Cited on pages 32 and 54.)
- [30] W. Bragg and R. Kleeman. LXXIV. On the ionization curves of radium. *The London, Edinburgh, and Dublin Philosophical Magazine and Journal of Science*, 8(48):726–738, 1904. (Cited on page 10.)

- [31] H. Brenner D J; Elliston C D; Hall E J; Paganetti. Reduction of the secondary neutron dose in passively scattered proton radiotherapy, using an optimized pre-collimator/collimator. *Physics in Medicine and Biology*, 2009. (Cited on page 60.)
- [32] D. Brown, M. Chadwick, R. Capote, A. Kahler, A. Trkov, M. Herman, A. Sonzogni, Y. Danon, A. Carlson, M. Dunn, D. Smith, G. Hale, G. Arbanas, R. Arcilla, C. Bates, B. Beck, B. Becker, F. Brown, R. Casperson, J. Conlin, D. Cullen, M.-A. Descalle, R. Firestone, T. Gaines, K. Guber, A. Hawari, J. Holmes, T. Johnson, T. Kawano, B. Kiedrowski, A. Koning, S. Kopecky, L. Leal, J. Lestone, C. Lubitz, J. Márquez Damián, C. Mattoon, E. McCutchan, S. Mughabghab, P. Navratil, D. Neudecker, G. Nobre, G. Noguere, M. Paris, M. Pigni, A. Plompen, B. Pritychenko, V. Pronyaev, D. Roubtsov, D. Rochman, P. Romano, P. Schillebeeckx, S. Simakov, M. Sin, I. Sirakov, B. Sleaford, V. Sobes, E. Soukhovitskii, I. Stetcu, P. Talou, I. Thompson, S. van der Marck, L. Welsch-Sherrill, D. Wiarda, M. White, J. Wormald, R. Wright, M. Zerkle, G. Žerovnik, and Y. Zhu. ENDF/B-VIII.0: The 8th Major Release of the Nuclear Reaction Data Library with CIELO-project Cross Sections, New Standards and Thermal Scattering Data. *Nuclear Data Sheets*, 148:1–142, 2018. Special Issue on Nuclear Reaction Data. (Cited on pages 13, 83, and 84.)
- [33] Bundesministerium für Umwelt, Naturschutz und nukleare Sicherheit. Verordnung zum Schutz vor der schädlichen Wirkung ionisierender Strahlung (Strahlenschutzverordnung - StrlSchV) . *Bundesgesetzblatt BGBL.*, 41:2034, 2018. (Cited on pages 19, 88, and 89.)
- [34] T. Böhlen, F. Cerutti, M. Chin, A. Fassó, A. Ferrari, P. Ortega, A. Mairani, P. Sala, G. Smirnov, and V. Vlachoudis. The FLUKA Code: Developments and Challenges for High Energy and Medical Applications. *Nuclear Data Sheets*, 120(0):211–214, 2014. (Cited on page 34.)
- [35] R. Capote, R. Jeraj, C.-M. Ma, D. W. Rogers, F. Sanchez-Doblado, J. Sempau, J. Seuntjens, and J. V. Siebers. Phase-Space Database for External Beam Radiotherapy. Summary report of a consultants’ meeting. *INDC(NDS)*, 0484, 2006. (Cited on pages 141 and 143.)
- [36] J. R. Castro, J. M. Quivey, J. T. Lyman, G. T. Y. Chen, T. L. Phillips, C. A. Tobias, and E. L. Alpen. Current status of clinical particle radiotherapy at Lawrence Berkeley laboratory. *Cancer*, 46(4):633–641, 1980. (Cited on page 30.)
- [37] CERN. *Production and Test of an Aluminum Floating Strip Micromegas for Small Animal Proton Imaging*, 2022. (Cited on page 54.)
- [38] Chen KL, Bloch CD, Hill PM, and Klein EE. Evaluation of neutron dose equivalent from the Mevion S250 proton accelerator: measurements and calculations. *Phys. Med. Biol.*, 58:8709–8723, 2013. (Cited on page 59.)
- [39] S. E. Combs, A. Nikoghosyan, O. Jaekel, C. P. Karger, T. Haberer, M. W. Mütter, P. E. Huber, J. Debus, and D. Schulz-Ertner. Carbon ion radiotherapy for pediatric patients and young adults treated for tumors of the skull base. *Cancer*, 5(6):1348–1355, 2009. (Cited on page 31.)
- [40] A. M. Cormack. Early two-dimensional reconstruction and recent topics stemming from it. *Nobel Lecture*, 1(1), 1979. (Cited on page 33.)
- [41] G. Coutrakon, V. Bashkirov, F. Hurley, R. Johnson, V. Rykalin, H. Sadrozinski, and R. Schulte. Design and construction of the 1st proton CT scanner. *AIP Conference Proceedings*, 1525(1):327–331, 2013. (Cited on page 32.)
- [42] Cywicka-Jakiel T Stolarczyk L Swakon J Olko P; Waligórski M P R . Individual patient shielding for a proton eye therapy facility. *Radiation Measurements*, 2010. (Cited on page 59.)
- [43] D. Strickland, G. Mourou. Compression of Amplified Chirped Optical Pulses. *Opt. Commun.*, 56:219, 1985. (Cited on pages 2, 35, and 44.)
- [44] H. Daniel, B. Jianhui, S. Martin, A. Klaus, H. Jens, K. Christian, R. Enrico, O. T. M., and S. Jörg. Temporally Resolved Intensity Contouring (TRIC) for characterization of the absolute spatio-temporal intensity distribution of a relativistic, femtosecond laser pulse. *Scientific Reports*, 9(1):7697, 2019. (Cited on pages 45 and 165.)
- [45] De Smet V, Stichelbaut F, Vanaudenhove T, Mathot G., De Lentdecker G., Dubus A., Pauly N., and Gerardy I. Neutron H*(10) inside a proton therapy facility: comparison between Monte Carlo simulations and WENDI-2 measurements. *rapd*, 161(1-4):417–421, nov 2013. (Cited on page 65.)

- [46] J. Debus, T. Haberer, D. Schulz-Ertner, O. Jäkel, F. Wenz, W. Enghardt, W. Schlegel, G. Kraft, and M. Wannemacher. Bestrahlung von Schädelbasistumoren mit Kohlenstoffionen bei der GSI Erste klinische Ergebnisse und zukünftige Perspektiven. *Strahlentherapie und Onkologie*, 176(5):211–216, 2000. (Cited on page 31.)
- [47] W. Draxinger. Entwicklung und Charakterisierung eines Pixeldetektors für laserbeschleunigte Ionen. Master's thesis, LMU Munich, 2014. (Cited on pages 118 and 120.)
- [48] M. A. Dymova, S. Y. Taskaev, V. A. Richter, and E. V. Kuligina. Boron neutron capture therapy: Current status and future perspectives. *Cancer Communications*, 40(9):406–421, 2020. (Cited on page 16.)
- [49] A. Döpp, L. Hehn, J. Götzfried, J. Wenz, M. Gilljohann, H. Ding, S. Schindler, F. Pfeiffer, and S. Karsch. Quick x-ray microtomography using a laser-driven betatron source. *Optica*, 5:056703–8, 2018. (Cited on page 92.)
- [50] E. Esarey, C. B. Schroeder, W. P. Leemans. Physics of laser-driven plasma-based electron accelerators. *Review of modern physics*, 81:1229–1285, 2009. (Cited on pages 43 and 92.)
- [51] J. Eley, W. Newhauser, K. Homann, R. Howell, C. Schneider, M. Durante, and C. Bert. Implementation of an Analytical Model for Leakage Neutron Equivalent Dose in a Proton Radiotherapy Planning System. *Cancers*, page 427–438, 03 2015. (Cited on page 87.)
- [52] F. Englbrecht, F. Balling, T. F. Rösch, M. Würfl, F. H. Lindner, K. Parodi, and J. Schreiber. Characterization of online high dynamic range imaging for laser-driven ion beam diagnostics using visible light. *Current Directions in Biomedical Engineering*, 3:343–, 2017. (Cited on pages 127 and 129.)
- [53] F. S. Englbrecht. Experimental based Monte Carlo modeling of a clinical proton beam. *LMU Munich Master Thesis*, 2014. (Cited on pages 30, 41, 62, 98, and 144.)
- [54] F. S. Englbrecht, K. Parodi, A. Döpp, J. Hartmann, F. H. Lindner, H. F. Wirth, S. Karsch, J. Schreiber, K. Parodi, and G. Dedes. Monte Carlo model of the 3 PW CALA facility in Munich Radiation protection modeling for 3 petawatt-laser production of ultrashort X-ray, proton and ion bunches: Monte Carlo model of the Munich CALA facility. *Journal of Radiological Protection* 40, 4:1048–1073, 2020. (Cited on pages 93, 109, 111, and 113.)
- [55] F. S. Englbrecht, S. Trinkl, V. Mares, W. Rühm, M. Wielunski, J. J. Wilkens, M. Hillbrand, and K. Parodi. A comprehensive Monte Carlo study of out-of-field secondary neutron spectra in a scanned-beam proton therapy gantry room. *Zeitschrift für Medizinische Physik*, 31(2):215–228, 2021. Special Issue: Ion Beam Therapy, Part I. (Cited on pages 30 and 93.)
- [56] F. S. Englbrecht, M. Würfl, D. Haffa, C. Kreuzer, S. Reinhardt, J. Schreiber, and K. Parodi. Monte Carlo studies for the development of laser-driven proton radiography. *Annual conference of the German Society for Medical Physics*, 46(DGMP 2015), 2015. (Cited on pages 32, 33, 163, and 164.)
- [57] F. S. Englbrecht, M. Würfl, F. Olivari, A. Ficorella, C. Kreuzer, F. H. Lindner, M. D. Palma, L. Pancheri, G.-F. D. Betta, J. Schreiber, A. Quaranta, and K. Parodi. An Online, Radiation Hard Proton Energy-Resolving Scintillator Stack For Laser-Driven Proton Bunches. *Radiation Protection Dosimetry*, 180(1-4):291–295, 02 2018. (Cited on pages 122, 124, 125, 126, and 162.)
- [58] T. Esirkepov, M. Borghesi, S. V. Bulanov, G. Mourou, and T. Tajima. Highly Efficient Relativistic-Ion Generation in the Laser-Piston Regime. *Phys. Rev. Lett.*, 92:175003, Apr 2004. (Cited on page 40.)
- [59] C. et al. Particle therapy at the Heidelberg Ion Therapy Center (HIT) – Integrated research-driven university-hospital-based radiation oncology service in Heidelberg, Germany. *Radiotherapy, Oncology*, 95(1):41–44, 2010. (Cited on page 31.)
- [60] R. D. Evans. *The Atomic Nucleus*. AIP, 1955. (Cited on page 8.)
- [61] F. H. Lindner, J. H. Bin, F. Englbrecht, D. Haffa, P. R. Bolton, Y. Gao, J. Hartmann, P. Hilz, C. Kreuzer, T. M. Ostermayr, T. F. Rösch, M. Speicher, K. Parodi, P. G. Thirolf, J. Schreiber. A novel approach to electron data background treatment in an online wide-angle spectrometer for laser-accelerated ion and electron bunches. *Review of Scientific Instruments*, 89:013301, 2018. (Cited on pages 38, 44, 45, 92, 126, 140, 141, 142, and 165.)
- [62] B. Faddegon, J. Perl, and M. Asai. Monte Carlo simulation of large electron fields. *Physics in Medicine and Biology*, 53:1497–1510, 2008. (Cited on page 143.)

- [63] B. Faddegon, E. Schreiber, and X. Ding. Monte Carlo simulation of large electron fields. *Physics in Medicine and Biology*, page 741–753, 2005. (Cited on page 143.)
- [64] B. A. Faddegon, D. Sawkey, T. O’Shea, M. McEwen, and C. Ross. Treatment head disassembly to improve the accuracy of large electron field simulation. *Medical Physics*, 36(10):4577–4591, 2009. (Cited on page 143.)
- [65] U. Fano. Penetration of Protons, Alpha Particles, and Mesons. *Annual Review of Nuclear Science*, 13(1):1–66, 1963. (Cited on page 9.)
- [66] Farah J., Mares V., Romero-Expósito M., Trinkl S., Domingo C., Dufek V., Klodowska M., Kubancak J., Knežević Ž., Liszka M., Majer M., Miljanić S., Ploc O., Schinner K., Stolarczyk L., Trompier F., Wielunski M., Olko P., and Harrison R. M. Measurement of stray radiation within a scanning proton therapy facility: EURADOS WG9 intercomparison exercise of active dosimetry systems. *Med. Phys.*, 42(5):2572–2584, 2015. doi: 10.1118/1.4916667. (Cited on page 82.)
- [67] A. Fasso, A. Ferrari, S. Roesler, J. Ranft, P. Sala, G. Battistoni, M. Campanella, F. Cerutti, L. De Biaggi, E. Gadioli, et al. The FLUKA code: present applications and future developments. *arXiv preprint physics/0306162*, 2003. (Cited on pages 33 and 35.)
- [68] A. Fasso, A. Ferrari, S. Roesler, P. Sala, F. Ballarini, A. Ottolenghi, G. Battistoni, F. Cerutti, E. Gadioli, M. Garzelli, et al. The physics models of FLUKA: status and recent development. *arXiv preprint hep-ph/0306267*, 2003. (Cited on pages 33 and 35.)
- [69] E. Fermi and R. Richtmyer. Note on census-taking in Monte Carlo calculations. *The Los Alamos Archive.*, 1948. (Cited on page 34.)
- [70] A. Ferrari, E. Amato, and D. Margarone. Radiation field characterization and shielding studies. *AIP Conference Proceedings*, 1546(1):57–62, 2013. (Cited on page 47.)
- [71] A. Ferrari and P. Sala. The Physics of High Energy Reactions. In *Nuclear Reaction Data and Nuclear Reactors Physics, Design and Safety*, 1997. (Cited on pages 64 and 86.)
- [72] A. Ferrari, P. R. Sala, A. Fassó, and J. Ranft. FLUKA: a multi-particle transport code. *CERN-2005-10, INFN/TC_05/11, SLAC-R-773*, 2005. (Cited on pages 33, 34, and 61.)
- [73] J. Fontenot, P. Taddei, Y. Zheng, D. Mirkovic, T. Jordan, and W. Newhauser. Equivalent dose and effective dose from stray radiation during passively scattered proton radiotherapy for prostate cancer. *Physics in Medicine and Biology*, 53(6):1677, 2008. (Cited on page 59.)
- [74] Forster Ingenieurgesellschaft. www.forster-bau.de/referenzen.html, www.forster-bau.de/sandwich-construction.html, 1 July 2020. (Cited on page 91.)
- [75] E. R. Fossum et al. Charge transfer noise and lag in CMOS active pixel sensors. In *Proc. 2003 IEEE Workshop on CCDs and Advanced Image Sensors, Elmau, Bavaria, Germany*, page 11–13. Citeseer, 2003. (Cited on page 127.)
- [76] T. Freeman. Upright treatment could increase patient comfort, reduce proton therapy costs, 2020. (Cited on page 87.)
- [77] G., Dollinger and A., Bergmaier and V., Hable and R., Hertenberger and C., Greubel and A., Hauptner and P., Reichart. Nanosecond pulsed proton microbeam. *Nuclear Instruments and Methods in Physics Research Section B, Beam Interactions with Materials and Atoms*, 267(12-13):2008–2012, 2009. (Cited on page 26.)
- [78] Y. Gao. *High repetition rate laser driven proton source and a new method of enhancing acceleration*. PhD thesis, LMU Munich, July 2020. (Cited on page 121.)
- [79] Y. Gao, J. Bin, D. Haffa, C. Kreuzer, J. Hartmann, M. Speicher, F. H. Lindner, T. M. Ostermayr, P. Hiltz, T. F. Rösch, and et al. An automated, 0.5 Hz nano-foil target positioning system for intense laser plasma experiments. *High Power Laser Science and Engineering*, 5:e12, 2017. (Cited on pages 41, 42, 44, 121, 142, 165, and 166.)
- [80] P. Gibbon. Harmonic Generation by Femtosecond Laser-Solid Interaction: A Coherent “Water-Window” Light Source? *Phys. Rev. Lett.*, 76:50–53, Jan 1996. (Cited on page 40.)

- [81] H. Goebel. Dose Delivery System Of The Varian Probeam System With Continuous Beam. *Workshop On Innovative Delivery Systems In Particle Therapy*, 2017. (Cited on page 60.)
- [82] M. Goitein, A. J. Lomax, and E. S. Pedron. Treating cancer with protons. *Physics Today*, 55(9):45–50, 2002. (Cited on pages 27 and 28.)
- [83] A. J. Gonsalves, K. Nakamura, J. Daniels, C. Benedetti, C. Pieronek, T. C. H. de Raadt, S. Steinke, J. H. Bin, S. S. Bulanov, J. van Tilborg, C. G. R. Geddes, C. B. Schroeder, C. Tóth, E. Esarey, K. Swanson, L. Fan-Chiang, G. Bagdasarov, N. Bobrova, V. Gasilov, G. Korn, P. Sasorov, and W. P. Leemans. Petawatt Laser Guiding and Electron Beam Acceleration to 8 GeV in a Laser-Heated Capillary Discharge Waveguide. *Phys. Rev. Lett.*, 122:084801, Feb 2019. (Cited on page 43.)
- [84] B. Gottschalk. Physics of proton interactions in matter. *Proton Therapy Physics*, page 19–60, 2012. (Cited on pages 14 and 17.)
- [85] T. Graeve and G. P. Weckler. Application Note AN07: High-resolution CMOS imaging detector. In *SPIE Medical Imaging*, 2001. (Cited on pages 122 and 133.)
- [86] C. Grau, N. Defourny, J. Malicki, P. Dunscombe, J. M. Borrás, M. Coffey, B. Slotman, M. Bogusz, C. Gasparotto, Y. Lievens, A. Kokobobo, F. Sedlmayer, E. Slobina, K. Feyen, T. Hadjieva, K. Odrzaska, J. G. Eriksen, J. Jaal, R. Bly, B. Chauvet, N. Willich, C. Polgar, J. Johannsson, M. Cunningham, S. Margrini, V. Atkocius, M. Untereiner, M. Pirotta, V. Karadjinovic, S. Leverages, K. Skladowski, M. L. Trigo, B. Šegedin, A. Rodriguez, M. Lagerlund, B. Pastoors, P. Hoskin, J. Vaarkamp, and R. C. Soler. Radiotherapy equipment and departments in the European countries: Final results from the ESTRO-HERO survey. *Radiotherapy and Oncology*, 112:155–164, 2014. (Cited on page 1.)
- [87] H. Daido, M. Nishiuchi, A. S. Pirozhkov. Review of laser-driven ion sources and their applications. *Reports on progress in Physics*, 75:056401–72, 2012. (Cited on pages 35, 38, 40, 41, 42, 43, 44, 47, 52, and 92.)
- [88] H. Röcken, M. Abdel-Bary, E. Akçöltekin, P. Budz, T. Stephani, J. Wittschen. The VARIAN 250 MeV Superconducting Compact Proton Cyclotrons: Medical Operation of the 2nd Machine, Production and Commissioning Status of Machines No. 3 to 7. In *2nd Workshop on Hadron Beam Therapy of Cancer*, 2011. (Cited on pages 30 and 41.)
- [89] T. Haberer, W. Becher, D. Schardt, and G. Kraft. Magnetic scanning system for heavy ion therapy. *Nuclear Instruments and Methods in Physics Research Section A: Accelerators, Spectrometers, Detectors and Associated Equipment*, 330(1-2):296–305, 1993. (Cited on page 31.)
- [90] T. Haberer, J. Debus, H. Eickhoff, O. Jäkel, D. Schulz-Ertner, and U. Weber. The heidelberg ion therapy center. *Radiotherapy and Oncology*, 73:S186–S190, 2004. Carbon-Ion Therapy. (Cited on page 31.)
- [91] D. Habs, P. G. Thirolf, M. Gross, K. Allinger, J. Bin, A. Henig, D. Kiefer, W. Ma, and J. Schreiber. Introducing the fission–fusion reaction process: using a laser-accelerated Th beam to produce neutron-rich nuclei towards the N=126 waiting point of the r-process. *Applied Physics B*, 103:471–484, 2011. (Cited on page 49.)
- [92] D. Haffa. *Tailored Online Diagnostics for a Laser-driven Plasma Ion Source Prototype*. PhD thesis, LMU Munich, 2019. (Cited on pages 42, 44, and 165.)
- [93] D. Haffa, R. Yang, J. Bin, S. Lehrack, F.-E. Brack, H. Ding, F. S. Englbrecht, Y. Gao, J. Gebhard, M. Gilljohann, J. Götzfried, J. Hartmann, S. Herr, P. Hilz, S. D. Kraft, C. Kreuzer, F. Kroll, F. H. Lindner, J. Metzkes-Ng, T. M. Ostermayr, E. Ridente, T. F. Rösch, G. Schilling, H.-P. Schlenvoigt, M. Speicher, D. Taray, M. Würfl, K. Zeil, U. Schramm, S. Karsch, K. Parodi, P. R. Bolton, W. Assmann, and J. Schreiber. I-BEAT: Ultrasonic method for online measurement of the energy distribution of a single ion bunch. *Scientific Reports*, 9(1):6714–, 2019. (Cited on pages 45, 122, and 165.)
- [94] E. J. Hall. The impact of protons on the incidence of second malignancies in radiotherapy. *Technol Cancer Res Treat*, 2007. (Cited on page 19.)
- [95] J. Hartmann. From a Laser Focus to an Ion Focus. *LMU Munich Master Thesis*, 2017. (Cited on pages 44 and 165.)
- [96] J. Hartmann. Quantitative ion spectrometry. *LMU Munich PhD Thesis*, 2022. (Cited on pages 122 and 168.)

- [97] S. P. Hatchett, C. G. Brown, T. E. Cowan, E. A. Henry, J. S. Johnson, M. H. Key, J. A. Koch, A. B. Langdon, B. F. Lasinski, R. W. Lee, A. J. Mackinnon, D. M. Pennington, M. D. Perry, T. W. Phillips, M. Roth, T. C. Sangster, M. S. Singh, R. A. Snavely, M. A. Stoyer, S. C. Wilks, and K. Yasuike. Electron, photon, and ion beams from the relativistic interaction of Petawatt laser pulses with solid targets. *Physics of Plasmas*, 7(5):2076–2082, 2000. (Cited on page 39.)
- [98] E. Hecht. *Optics*. De Gruyter, 1974. (Cited on page 129.)
- [99] B. M. Hegelich, B. J. Albright, J. Cobble, K. Flippo, S. Letzring, M. Paffett, H. Ruhl, J. Schreiber, R. K. Schulze, and J. C. Fernández. Laser acceleration of quasi-monoenergetic MeV ion beams. *Nature*, 439(7075):441–444, 2006. (Cited on page 38.)
- [100] M. Hegelich. Teilchenbeschleunigung mit Lasern. *Physik in unserer Zeit*, 33(6):252–252, 2002. (Cited on page 38.)
- [101] A. Henig, S. Steinke, M. Schnürer, T. Sokollik, R. Hörlein, D. Kiefer, D. Jung, J. Schreiber, B. M. Hegelich, X. Q. Yan, J. M. ter Vehn, T. Tajima, P. V. Nickles, W. Sandner, and D. Habs. Radiation-Pressure Acceleration of Ion Beams Driven by Circularly Polarized Laser Pulses. *Phys. Rev. Lett.*, 103:245003, Dec 2009. (Cited on page 40.)
- [102] V. Highland. Some practical remarks on multiple scattering. *Nuclear Instruments and Methods*, page 497–499, 1975. (Cited on page 12.)
- [103] M. Hillbrand, D. Georg, H. Gadner, R. Pötter, and K. Dieckmann. Abdominal cancer during early childhood: A dosimetric comparison of proton beams to standard and advanced photon radiotherapy. *Radiotherapy and Oncology*, 89(2):141–149, 2009. (Cited on pages 28 and 59.)
- [104] P. Hilz, T. Ostermayr, A. Huebl, V. Bagnoud, B. Borm, M. Bussmann, M. Gallei, J. Gebhard, D. Haffa, J. Hartmann, et al. Isolated proton bunch acceleration by a petawatt laser pulse. *Nature communications*, 9(1):1–9, 2018. (Cited on pages 38 and 169.)
- [105] W. Hofmann and W. Dittrich. Use of Isodose Rate Pictures for the Shielding Design of a Proton Therapy Centre. In *Proc. of Shielding Aspects of Accelerators, Targets and Irradiation Facilities (SATIF 7)*, 2004. (Cited on page 62.)
- [106] Hohmann E; Safai S; Bula Ch. et al. Investigation of the neutron stray radiation field produced by irradiating a water phantom with 200-MeV protons. *Nuclear Technology*, 2011. (Cited on pages 60 and 70.)
- [107] R. M. Howell, S. F. Kry, E. Burgett, N. E. Hertel, and D. S. Followill. Secondary neutron spectra from modern Varian, Siemens, and Elekta linacs with multileaf collimators. *Medical Physics*, 36(9Part1):4027–4038, 2009. (Cited on page 16.)
- [108] Howell RM, Burgett EA, D Isaacs, et al. Measured Neutron Spectra and Dose Equivalents From a Mevion Single-Room, Passively Scattered Proton System Used for Craniospinal Irradiation. *Int J Radiat Oncol Biol Phys*, 1(95):249–284, 2016. (Cited on page 60.)
- [109] N. Hudobivnik, F. Schwarz, T. Johnson, L. Agolli, G. Dedes, T. Tessonier, F. Verhaegen, C. Thieke, C. Belka, W. H. Sommer, K. Parodi, and G. Landry. Comparison of proton therapy treatment planning for head tumors with a pencil beam algorithm on dual and single energy CT images. *Medical Physics*, 43(1):495–504, 2016. (Cited on page 32.)
- [110] A. Hupe O., Ambrosi P. Deficiencies of active electronic radiation protection doseimeters in pulsed fields. *Radiation Protection Dosimetry*, 135:149–153, 2009. (Cited on pages 25 and 89.)
- [111] R. A. Hälgl and U. Schneider. Neutron dose and its measurement in proton therapy—current State of Knowledge. *The British Journal of Radiology*, 93(1107):20190412, 2020. PMID: 31868525. (Cited on page 59.)
- [112] ICRP. The 2007 Recommendations of the International Commission on Radiological Protection. *Annals of the ICRP*, 37(103):2–4, 2007. (Cited on pages 15, 17, and 18.)
- [113] ICRU. International Commission on Radiation Units and Measurements. Quantities and Units in Radiation Protection Dosimetry. *International Commission on Radiation Units and Measurements Reports*, 1993. (Cited on page 17.)

- [114] ICRU. International Commission on Radiation Units and Measurements. Report 49: Stopping Powers and Ranges for Protons and Alpha Particles. *International Commission on Radiation Units and Measurements Reports*, 1993. (Cited on page 9.)
- [115] J. Schreiber, P. Bolton, K. Parodi. Invited Review Article: “Hands-on” laser-driven ion acceleration: A primer for laser-driven source development and potential applications. *Review of Scientific Instruments*, 87:071101, 2016. (Cited on pages 2, 36, 38, 40, 92, and 121.)
- [116] J. Schreiber, P. Bolton, K. Parodi. *Applications of Laser-Driven Particle Acceleration*. CRC Press, 2018. (Cited on pages 2, 37, 40, 42, 46, 50, and 52.)
- [117] Y. Junting, L. Binqiao, Y. Pingping, X. Jiangtao, and M. Cun. Two-dimensional pixel image lag simulation and optimization in a 4-T CMOS image sensor. *Journal of Semiconductors*, 31(9):094011, 2010. (Cited on page 127.)
- [118] S. Karsch. *High-intensity laser generated neutrons*. PhD thesis, LMU Munich, December 2002. (Cited on page 43.)
- [119] M. Kausch H Anjum N Chevolut Y Gupta B Léonard D Mathieu H J Pruitt L A Ruiz-Taylor L Scholz. *Radiation Effects on Polymers for Biological Use*. Springer, Berlin, Heidelberg, 2003. (Cited on page 20.)
- [120] K. Khrennikov, J. Wenz, A. Buck, J. Xu, M. Heigoldt, L. Veisz, and S. Karsch. Tunable all-optical quasimonochromatic thomson x-ray source in the nonlinear regime. *Phys. Rev. Lett.*, page 195003, May 2015. (Cited on page 43.)
- [121] M. Kis. High intensity pulsed proton beam detection with diamond membrane detectors. 2. *Annual Matter and Technologies Meeting*, 2016. (Cited on page 39.)
- [122] C. Kleffner, D. Ondreka, and U. Weinrich. The Heidelberg Ion Therapy (HIT) Accelerator Coming into Operation. *AIP Conference Proceedings*, 426(1):426–428, 2008. (Cited on page 31.)
- [123] F. Klitzner. *Development of novel two-dimensional floating strip micromegas detectors with an in-depth insight into the strip signal formation*. PhD thesis, LMU Munich, May 2019. (Cited on page 54.)
- [124] A. M. Koehler. Proton Radiography. *Science*, 160(3825):303–304, 1968. (Cited on pages 32 and 163.)
- [125] A. M. Koehler, R. J. Schneider, and J. M. Sisterson. Flattening of proton dose distributions for large-field radiotherapy. *Medical Physics*, 4(4):297–301, 1977. (Cited on pages 28 and 163.)
- [126] E. Kollitz, H. Han, K. CH, C. Kroll, M. Riboldi, W. Newhauser, G. Dedes, and K. Parodi. A novel hybrid model for out-of-field dose calculation in proton therapy treatment planning. *Int J Part Ther*, 6(4):285, 2020. (Cited on pages 59 and 87.)
- [127] E. Kollitz, H. Han, C. H. Kim, M. Pinto, M. Schwarz, M. Riboldi, F. Kamp, C. Belka, W. D. Newhauser, G. Dedes, and K. Parodi. A patient-specific hybrid phantom for calculating radiation dose and equivalent dose to the whole body. *Physics in Medicine & Biology*, 2021. (Cited on pages 59 and 87.)
- [128] A. Kraan. Range Verification Methods in Particle Therapy: Underlying Physics and Monte Carlo Modeling. *Frontiers in oncology*, 5:150, 07 2015. (Cited on pages 10, 12, 13, and 34.)
- [129] H. Krieger. *Strahlenphysik, Dosimetrie und Strahlenschutz*. G. B. Teuber Stuttgart, 1998. (Cited on pages 14, 15, 17, and 19.)
- [130] D. Krischel, C. Baumgarten, A. Geisler, A. Hobl, H. Klein, M. Poier, H. Rocken, M. Schillo, P. vom Stein, T. Stephani, J. H. Timmer, and C. Zimmer. Design Aspects and Operation Experience With a Novel Superconducting Cyclotron for Cancer Treatment. *IEEE Transactions on Applied Superconductivity*, 17:2307–2310, 2007. (Cited on pages 30 and 41.)
- [131] F. Kroll, F.-E. Brack, C. Bernert, S. Bock, E. Bodenstern, K. Brüchner, T. E. Cowan, L. Gaus, R. Gebhardt, U. Helbig, L. Karsch, T. Kluge, S. Kraft, M. Krause, E. Lessmann, U. Masood, S. Meister, J. Metzkes-Ng, A. Nossula, J. Pawelke, J. Pietzsch, T. Püschel, M. Reimold, M. Rehwald, C. Richter, H.-P. Schlenvoigt, U. Schramm, M. E. P. Umlandt, T. Ziegler, K. Zeil, and E. Beyreuther. Tumour irradiation in mice with a laser-accelerated proton beam. *Nature Physics*, 18(3):316–322, 2022. (Cited on page 21.)
- [132] S. Kundel. Towards a Beamline for Small Animal Irradiation at Clinical Proton Therapy Facilities. *LMU Munich Master Thesis*, 2019. (Cited on page 30.)

- [133] P. Kühnemann. Development of a self-calibrating energy measurement template for laser-driven protons. *LMU Munich Bachelor Thesis*, 2018. (Cited on page 167.)
- [134] L. D. Landau. “On the energy loss of fast particles by ionization. *J. Phys.*, page 201–205, 1944. (Cited on page 184.)
- [135] G. Landry and C. ho Hua. Current state and future applications of radiological image guidance for particle therapy. *Medical Physics*, 45(11):e1086–e1095, 2018. (Cited on page 31.)
- [136] K. Langer U W; Eley J G; Dong L; Langen. Comparison of multi-institutional Varian ProBeam pencil beam scanning proton beam commissioning data. *Radiation Oncology Physics*, 2017. (Cited on page 61.)
- [137] J. Lindhard, V. Nielsen, M. Scharff, and P. Thomsen. Integral equations governing radiation effects (Note on atomic collisions III). *Kgl. Danske Videnskab., Selskab. Mat. Fys. Medd.*, 1963. (Cited on page 10.)
- [138] F. Lindner. Online Diagnostics for Laser Accelerated Ions and Electrons. *LMU Munich Master Thesis*, 2015. (Cited on pages 38, 119, 120, 141, 148, and 149.)
- [139] F. Lindner, D. Haffa, J. Bin, F. Englbrecht, Y. Gao, J. Gebhard, J. Hartmann, P. Hilz, C. Kreuzer, S. Lehrack, T. Ostermayr, T. Rösch, M. Speicher, M. Würfl, K. Parodi, J. Schreiber, and P. Thirolf. Towards swift ion bunch acceleration by high-power laser pulses at the Centre for Advanced Laser Applications (CALA). *Nuclear Instruments and Methods in Physics Research Section B: Beam Interactions with Materials and Atoms*, 03 2017. (Cited on pages 38, 46, and 48.)
- [140] X. Llopart, R. Ballabriga, M. Campbell, L. Tlustos, and W. Wong. Timepix, a 65k programmable pixel readout chip for arrival time, energy and/or photon counting measurements. *Nucl. Instrum. Meth. A*, 581:485–494, 2007. [Erratum: *Nucl.Instrum.Meth.A* 585, 106–108 (2008)]. (Cited on page 118.)
- [141] A. Lomax. Intensity modulation methods for proton radiotherapy. *Physics in Medicine and Biology*, 44(1):185–205, jan 1999. (Cited on page 29.)
- [142] G. R. Lynch and O. I. Dahl. Approximations to multiple Coulomb scattering. *Nuclear Instruments and Methods in Physics Research Section B: Beam Interactions with Materials and Atoms*, 58(1):6–10, 1991. (Cited on page 12.)
- [143] W. S. M. Scholz, G. Kraft. RBE for carbon track-segment irradiation in cell lines of differing repair capacity. *International Journal of Radiation Biology*, 75(11):1357–1364, 1999. (Cited on page 20.)
- [144] W. Ma, V. Liechtenstein, J. Szerypo, D. Jung, P. Hilz, B. Hegelich, H. Maier, J. Schreiber, and D. Habs. Preparation of self-supporting diamond-like carbon nanofoils with thickness less than 5nm for laser-driven ion acceleration. *Nuclear Instruments and Methods in Physics Research Section A: Accelerators, Spectrometers, Detectors and Associated Equipment*, 655(1):53–56, 2011. Proceedings of the 25th World Conference of the International Nuclear Target Development Society. (Cited on page 38.)
- [145] A. Mairani, T. T. Böhlen, A. Schiavi, T. Tessonier, S. Molinelli, S. Brons, G. Battistoni, K. Parodi, and V. Patera. A Monte Carlo-based treatment planning tool for proton therapy. *Physics in Medicine and Biology*, 58(8):2471, 2013. (Cited on page 32.)
- [146] V. Mares, M. Romero-Expósito, J. Farah, S. Trinkl, C. Domingo, M. Dommert, L. Stolarczyk, L. V. Ryckeghem, M. Wielunski, P. Olko, and R. M. Harrison. A comprehensive spectrometry study of a stray neutron radiation field in scanning proton therapy. *Physics in Medicine and Biology*, 61(11):4127, 2016. (Cited on pages 60, 61, 70, 82, 83, and 86.)
- [147] J. Martinetti F Sayah R at al. Farah. Monte Carlo modeling of proton therapy installations: a global experimental method to validate secondary neutron dose calculations. *Physics in Medicine and Biology*, 2014. (Cited on pages 59 and 60.)
- [148] S. C. Mayo, P. R. Miller, S. W. Wilkins, T. J. Davis, D. Gao, T. E. Gureyev, D. Paganin, D. J. Parry, A. Pogany, and A. W. Stevenson. Quantitative X-ray projection microscopy: phase-contrast and multi-spectral imaging. *Journal of Microscopy*, 207(2):79–96, 2002. (Cited on page 169.)
- [149] N. Metropolis. The beginning of the Monte Carlo Method. *Los Alamos Science Special Issue*, 1987. (Cited on page 34.)
- [150] N. Metropolis and S. Ulam. The Monte Carlo Method. *Journal of the American Statistical*, 44, 335 (1949), 1949. (Cited on page 34.)

- [151] S. Meyer. *On the Clinical Potential of Ion Computed Tomography with Different Detector Systems and Ion Species*. PhD thesis, LMU Munich, 2019. (Cited on pages 30, 31, and 32.)
- [152] S. Meyer, J. Bortfeldt, P. Lämmer, F. S. Englbrecht, M. Pinto, K. Schnürle, M. Würll, and K. Parodi. Optimization and performance study of a proton CT system for pre-clinical small animal imaging. *Physics in Medicine & Biology*, 65(15):155008, aug 2020. (Cited on pages 30, 32, and 54.)
- [153] O. Mohamad, T. Tabuchi, Y. Nitta, et al. Risk of subsequent primary cancers after carbon ion radiotherapy, photon radiotherapy, or surgery for localised prostate cancer: a propensity score-weighted, retrospective, cohort study. *Lancet Oncol.*, 5:674–685, 2019. (Cited on page 59.)
- [154] G. Molière. Theorie der Streuung schneller geladener Teilchen II. Mehrfach- und Vielfachstreuung. *Zeitschrift für Naturforschung A*, Band 3a, 1948. (Cited on page 12.)
- [155] P. Mora. Plasma Expansion into a Vacuum. *Physical Review Letters*, 90:185002, May 2003. (Cited on page 140.)
- [156] W. D. Newhauser and M. Durante. Assessing the risk of second malignancies after modern radiotherapy. *Nature Reviews Cancer*, 11(6):438–448, 2011. (Cited on pages 19 and 59.)
- [157] W. D. Newhauser and R. Zhang. The physics of proton therapy. *Physics in Medicine and Biology*, 60(8):R155, 2015. (Cited on pages 11, 19, and 28.)
- [158] F. Olivari. Investigating two prototype detector systems for spectrometry of polyenergetic proton bunches. Master’s thesis, LMU Munich, 2017. (Cited on page 125.)
- [159] T. Ostermayr. *Relativistically Intense Laser–Microplasma Interactions*. PhD thesis, LMU Munich, 2019. (Cited on pages 170 and 171.)
- [160] T. M. Ostermayr, C. Kreuzer, F. S. Englbrecht, J. Gebhard, J. Hartmann, A. Huebl, D. Haffa, P. Hilz, K. Parodi, J. Wenz, M. E. Donovan, G. Dyer, E. Gaul, J. Gordon, M. Martinez, E. Mccary, M. Spinks, G. Tiwari, B. M. Hegelich, and J. Schreiber. Laser-driven x-ray and proton micro-source and application to simultaneous single-shot bi-modal radiographic imaging. *Nature Communications*, 11(1):6174, 2020. (Cited on pages 38, 43, 47, 50, 169, 170, 171, and 172.)
- [161] T. M. Ostermayr, C. Kreuzer, F. S. Englbrecht, J. Gebhard, J. Hartmann, A. Huebl, D. Haffa, P. Hilz, K. Parodi, J. Wenz, M. E. Donovan, G. Dyer, E. Gaul, J. Gordon, M. Martinez, E. Mccary, M. Spinks, G. Tiwari, B. M. Hegelich, and J. Schreiber. Supplementary Information: Laser-driven x-ray and proton micro-source and application to simultaneous single-shot bi-modal radiographic imaging. *Nature Communications*, 11(1):6174, 2020. (Cited on pages 170 and 171.)
- [162] A. Ottolenghi. ANDANTE - Multidisciplinary evaluation of the cancer risk from neutrons relative to photons using stem cells and the induction of second malignant neoplasms following pediatric radiation therapy, 2016. (Cited on page 59.)
- [163] H. Paganetti. Significance and Implementation of RBE Variations in Proton Beam Therapy. *Technology in Cancer Research & Treatment*, 2(5):413–426, 2003. PMID: 14529306. (Cited on page 20.)
- [164] H. Paganetti. Range uncertainties in proton therapy and the role of Monte Carlo simulations. *Physics in Medicine and Biology*, 57(11):R99, 2012. (Cited on page 32.)
- [165] M. D. Palma, S. Carturan, M. Degerlier, T. Marchi, M. Cinausero, F. Gramegna, and A. Quaranta. Non-toxic liquid scintillators with high light output based on phenyl-substituted siloxanes. *Optical Materials*, 42(Complete):111–117, 2015. (Cited on page 124.)
- [166] M. D. Palma, A. Quaranta, T. Marchi, G. Collazuol, S. Carturan, M. Cinausero, and F. Gramegna. Red Emitting Phenyl-Polysiloxane Based Scintillators for Neutron Detection. In *Red Emitting Phenyl-Polysiloxane Based Scintillators for Neutron Detection*, volume 61, page 1–7, 06 2013. (Cited on page 124.)
- [167] K. Parodi. *On the Feasibility of Dose Quantification with in Beam PET Data in Radiotherapy with ^{12}C and Proton Beams*. PhD thesis, HZDR, 2004. (Cited on page 31.)
- [168] K. Parodi. Heavy ion radiography and tomography. *Physica Medica*, 30(5):539–543, 2014. Particle Radiosurgery Conference. (Cited on page 32.)

- [169] K. Parodi, W. Assmann, C. Belka, J. Bortfeldt, D.-A. Clevert, G. Dedes, R. Kalunga, S. Kundel, N. Kurichiyanil, P. Lämmer, J. Lascaud, K. Lauber, G. Lovatti, S. Meyer, M. Nitta, M. Pinto, M. J. Safari, K. Schnürle, J. Schreiber, P. G. Thirolf, H.-P. Wieser, and M. Würfl. Towards a novel small animal proton irradiation platform: the SIRMIO project. *Acta Oncologica*, 0(0):1–6, 2019. PMID: 31271091. (Cited on pages 30, 32, 33, 132, and 136.)
- [170] K. Parodi, A. Mairani, S. Brons, B. G. Hasch, F. Sommerer, J. Naumann, O. Jäkel, T. Haberer, and J. Debus. Monte Carlo simulations to support start-up and treatment planning of scanned proton and carbon ion therapy at a synchrotron-based facility. *Physics in Medicine and Biology*, 57(12):3759, 2012. (Cited on pages 32 and 34.)
- [171] K. Parodi, H. Paganetti, E. Cascio, J. B. Flanz, A. A. Bonab, N. M. Alpert, K. Lohmann, and T. Bortfeld. PET/CT imaging for treatment verification after proton therapy: A study with plastic phantoms and metallic implants. *Medical Physics*, 34, 2007. (Cited on page 34.)
- [172] C. Patrignani. Review of Particle Physics. *Chinese Physics C*, 40(10):100001, oct 2016. (Cited on page 8.)
- [173] M. Pelliccioni. Overview of Fluence-to-Effective Dose and Fluence-to-Ambient Dose Equivalent Conversion Coefficients for High Energy Radiation Calculated Using the FLUKA Code. *Radiation Protection Dosimetry*, 88(4):279–297, 04 2000. (Cited on page 35.)
- [174] Physikalisch-Technische Bundesanstalt (PTB) der Bundesrepublik Deutschland. Dichte- und Gehaltsmeßgeräte - Flüssigkeits-Dichtemeßgeräte nach dem Schwingerprinzip. *PTB-Anforderungen*, PTB-A 13.6, 2004. (Cited on page 144.)
- [175] Pleora Technologies. *iPORT PT1000-LV Hardware Guide*, 2007. (Cited on page 120.)
- [176] PTCOG: Particle Therapy Co-Operative Group. Particle therapy facilities under construction , 2019. PTCOG Press Releases [Accessed: 11.04.2019]. (Cited on pages 1 and 60.)
- [177] A. Pérez-Andújar, W. D. Newhauser, and J. P. M. DeLuca. Neutron production from beam-modifying devices in a modern double scattering proton therapy beam delivery system. *Physics in Medicine and Biology*, 54(4):993, 2009. (Cited on page 59.)
- [178] Radeycon. Application Note AN04: Imaging with Pulsed X-Ray Sources . Technical report, Radeycon, 2001. (Cited on pages 128 and 133.)
- [179] Radeycon. Application Note AN06: Detector Lifetime and Radiation Damage . Technical report, Radeycon, 2002. (Cited on page 133.)
- [180] Radeycon. Application Note AN07: Scintillator Options for Shad-o-Box Cameras. Technical report, Radeycon, 2005. (Cited on pages 118 and 133.)
- [181] Radeycon. Application Note AN10: QE Measurement of the Radeye1 Image Sensor. Technical report, Radeycon, 2007. (Cited on pages 119, 132, 133, and 152.)
- [182] J. Ranft. DPMJET version II.5, code manual. <http://arxiv.org/abs/hep-ph/9911232>, 1999. (Cited on page 35.)
- [183] L. Rechner, E. JG, H. RM, R. Zhang, D. Mirkovic, and N. WD. Risk- optimized proton therapy to minimize radiogenic second cancers. *Phys. Med. Biol.*, 60:3999–4013, 2015. (Cited on pages 19 and 59.)
- [184] S. Reinhardt. *Detection of laser-accelerated protons*. PhD thesis, LMU Munich, 2012. (Cited on pages 41, 136, and 183.)
- [185] C. Richter, G. Pausch, S. Barczyk, M. Priegnitz, I. Keitz, J. Thiele, J. Smeets, F. V. Stappen, L. Bombelli, C. Fiorini, L. Hotoiu, I. Perali, D. Prieels, W. Enghardt, and M. Baumann. First clinical application of a prompt gamma based in vivo proton range verification system. *Radiotherapy and Oncology*, 118(2):232–237, 2016. (Cited on page 31.)
- [186] S. Roesler and G. R. Stevenson. deq99.f - A FLUKA user-routine converting fluence into effective dose and ambient dose equivalent. *CERN-SC-2006-070-RP-TN*, 809389, 2006. (Cited on page 35.)
- [187] M. Roth, A. Blazevic, M. Geissel, T. Schlegel, T. E. Cowan, M. Allen, J.-C. Gauthier, P. Audebert, J. Fuchs, J. M. ter Vehn, M. Hegelich, S. Karsch, and A. Pukhov. Energetic ions generated by laser pulses: A detailed study on target properties. *Phys. Rev. ST Accel. Beams*, 5:061301, Jun 2002. (Cited on page 162.)

- [188] S. G. Rykovanov, J. Schreiber, J. M. ter Vehn, C. Bellei, A. Henig, H. C. Wu, and M. Geissler. Ion acceleration with ultra-thin foils using elliptically polarized laser pulses. *New Journal of Physics*, 10(11):113005, nov 2008. (Cited on page 40.)
- [189] H. Ryu, E. Song, J. Lee, and J. Kim. Density and spatial resolutions of proton radiography using a range modulation technique. *Physics in Medicine and Biology*, 53(19):5461–5468, sep 2008. (Cited on page 32.)
- [190] T. F. Rösch, D. Haffa, J. H. Bin, F. Englbrecht, Y. Gao, V. Gisbert, J. Gebhard, D. Hahner, J. Hartmann, M. Haug, S. Herr, P. Hilz, C. Kreuzer, S. Lehrack, F. H. Lindner, T. M. Ostermayr, E. Ridente, S. Seufferling, M. Speicher, M. Würll, R. Yang, K. Parodi, and J. Schreiber. Laser-driven ION (LION) Acceleration at the Centre for Advanced Laser Applications (CALA). *2017 European Conference on Lasers and Electro-Optics and European Quantum Electronics Conference*, page JSIII_P_2, 2017. (Cited on pages 45 and 46.)
- [191] T. F. Rösch, Z. Szabó, D. Haffa, J. Bin, S. Brunner, F. S. Englbrecht, A. A. Friedl, Y. Gao, J. Hartmann, P. Hilz, C. Kreuzer, F. H. Lindner, T. M. Ostermayr, R. Polanek, M. Speicher, E. R. Szabó, D. Taray, T. Tőkés, M. Würll, K. Parodi, K. Hideghéty, and J. Schreiber. A feasibility study of zebrafish embryo irradiation with laser-accelerated protons. *Review of Scientific Instruments*, 91(6):063303, 2020. (Cited on pages 45 and 165.)
- [192] R. S. Engel and J. Ranft. The Monte Carlo event generator DPMJET-III. *Proceedings of the MonteCarlo 2000 Conference*, 2001. (Cited on page 35.)
- [193] S. Reinhardt, C. Granja, F. Krejci, W. Assmann. Test of pixel detectors for laser-driven accelerated particle beams. *Journal of Instrumentation*, 6:C12030, 2011. (Cited on pages 26, 118, 119, 133, 136, 167, 168, and 184.)
- [194] S. Reinhardt, W. Draxinger, J. Schreiber, W. Assmann. A pixel detector system for laser-accelerated ion detection. *Journal of Instrumentation*, 8:P03008, 2013. (Cited on pages 26, 118, 133, and 136.)
- [195] S.A. Gaillard, T. Kluge, K. A. Flippo, M. Bussmann, B. Gall, T. Lockard, M. Geissel, D. T. Offermann, M. Schollmeier, Y. Sentoku, T. E. Cowan. Increased laser-accelerated proton energies via direct laser-light-pressure acceleration of electrons in microcone targets. *Physics of Plasmas*, 18:056710, 2001. (Cited on pages 37, 92, and 93.)
- [196] R. Sarah. *Evaluations des doses dues aux neutrons secondaires reçues par des patients de différents âges traités par protonthérapie pour des tumeurs intracrâniennes*. PhD thesis, IRSN - Institut de Radioprotection et de Sécurité Nucléaire, 2013. (Cited on pages 60 and 82.)
- [197] J. M. Schippers and A. J. Lomax. Emerging technologies in proton therapy. *Acta Oncologica*, 50(6):838–850, 2011. (Cited on page 29.)
- [198] R. A. Schneider, L. Wisser, M. R. Arnold, C. Berchtenbreiter, H.-J. Borchert, D. E. Geismar, M. C. Loscar, M. Mayr, M. Wilms, and M. Herbst. Proton therapy with spot scanning: the Rinecker Proton Therapy Center in Munich. *Nowotwory Journal of Oncology*, 57(5), 2007. (Cited on pages 30, 59, and 62.)
- [199] U. Schneider, S. Agosteo, E. Pedroni, and J. Besserer. Secondary neutron dose during proton therapy using spot scanning. *Int J Radiat Oncol Biol Phys*, 53, 2002. (Cited on pages 59 and 60.)
- [200] U. Schneider, R. A. Hälgl, and T. Lomax. Neutrons in active proton therapy: Parameterization of dose and dose equivalent. *Zeitschrift für Medizinische Physik*, 27(2):113–123, 2017. (Cited on pages 59 and 60.)
- [201] W. Schneider, T. Bortfeld, and W. Schlegel. Correlation between CT numbers and tissue parameters needed for Monte Carlo simulations of clinical dose distributions. *Physics in Medicine and Biology*, 45(2):459–478, jan 2000. (Cited on page 9.)
- [202] Schneider U; Hälgl A; Baiocco G; Lomax T. Neutrons in proton pencil beam scanning: parameterization of energy, quality factors and RBE. *Physics in Medicine and Biology*, 2016. (Cited on pages 17 and 19.)
- [203] K. Schnürle. Integration mode imaging with a CMOS detector for a small animal proton irradiation: PhD Thesis in Preparation. *LMU Munich PhD Thesis*, 2022. (Cited on pages 33, 132, and 136.)
- [204] K. Schnürle, J. Bortfeldt, F. S. Englbrecht, C. Gianoli, J. Hartmann, P. Hofverberg, S. Meyer, K. Niepel, I. Yohannes, M. Vidal, G. Landry, J. Herault, J. Schreiber, K. Parodi, and M. Würll. Small Animal CMOS Integration Mode Proton Imaging at Different Treatment Facilities. In *Presentation at*

- the Seventh Annual Loma Linda Workshop on Particle Imaging and Radiation Treatment Planning*, 2022.
(Cited on pages 33, 132, 135, and 136.)
- [205] K. Schnürle, J. Bortfeldt, F. S. Englbrecht, C. Gianoli, J. Hartmann, P. Hofverberg, S. Meyer, K. Niepel, I. Yohannes, M. Vidal, G. Landry, J. Hérault, J. Schreiber, K. Parodi, and M. Würfl. Small Animal CMOS Integration Mode Proton Imaging at Different Treatment Facilities. In *Oral presentation at Applied Nuclear Physics Conference 2021*, 2021.
(Cited on pages 33, 132, and 136.)
- [206] K. Schnürle, J. Bortfeldt, F. S. Englbrecht, C. Gianoli, J. Hartmann, P. Hofverberg, S. Meyer, M. Vidal, J. Hérault, J. Schreiber, K. Parodi, and M. Würfl. Feasibility study of correlated Bragg peak localization via ultrasound and ionoacoustics in an abdominal imaging phantom. In *Poster at the Joint Conference of the ÖGMP, DGMP and SGSMP, Dreiländertagung der Medizinischen Physik*, 2021.
(Cited on pages 33, 132, and 136.)
- [207] K. Schnürle, J. Bortfeldt, F. S. Englbrecht, C. Gianoli, J. Hartmann, P. Hofverberg, S. Meyer, M. Vidal, J. Schreiber, K. Parodi, and M. Würfl. Development of integration mode proton imaging with a single CMOS detector for a small animal irradiation platform. In *Presentation at the Third European Congress of Medical Physics*, 2021.
(Cited on pages 33, 132, and 136.)
- [208] K. Schnürle, J. Bortfeldt, F. S. Englbrecht, C. Gianoli, J. Hartmann, S. Meyer, K. Niepel, G. Landry, I. Yohannes, J. Schreiber, and K. P. M. und Würfl. Entwicklung von Protonenbildgebung mit einem einzelnen integrierenden CMOS-Detektor für eine Kleintierbestrahlungsanlage. In *Präsentation auf der 51. Jahrestagung der Deutschen Gesellschaft für Medizinische Physik*, 2020.
(Cited on pages 33, 132, and 136.)
- [209] J. Schreiber, F. Bell, F. Grüner, U. Schramm, M. Geissler, M. Schnürer, S. Ter-Avetisyan, B. Hegelich, J. Cobble, E. Brambrink, J. Fuchs, P. Audebert, and D. Habs. Analytical Model for Ion Acceleration by High-Intensity Laser Pulses. *Physical Review Letters*, 97:045005, 08 2006. (Cited on page 140.)
- [210] D. Schulz-Ertner, A. Nikoghosyan, B. Didinger, and J. Debus. Carbon ion radiation therapy for chondromas and low grade chondrosarcomas-current status of the clinical trials at GSI. *Radiotherapy and Oncology*, page S53–S56, 2004. (Cited on page 31.)
- [211] H. Schwoerer, B. Liesfeld, H.-P. Schlenvoigt, K.-U. Amthor, and R. Sauerbrey. Thomson-Backscattered X Rays From Laser-Accelerated Electrons. *Phys. Rev. Lett.*, 96:014802, Jan 2006. (Cited on page 38.)
- [212] S. M. Seltzer and M. J. Berger. Procedure for calculating the radiation stopping power for electrons. *The International Journal of Applied Radiation and Isotopes*, 33(11):1219–1226, 1982. (Cited on page 10.)
- [213] R. A. Snavely, M. H. Key, S. P. Hatchett, T. E. Cowan, M. Roth, T. W. Phillips, M. A. Stoyer, E. A. Henry, T. C. Sangster, M. S. Singh, S. C. Wilks, A. MacKinnon, A. Offenberger, D. M. Pennington, K. Yasuike, A. B. Langdon, B. F. Lasinski, J. Johnson, M. D. Perry, and E. M. Campbell. Intense High-Energy Proton Beams from Petawatt-Laser Irradiation of Solids. *Physical Review Letters*, 85:2945–2948, Oct 2000. (Cited on pages 37, 38, and 39.)
- [214] M. Sng. Characterisation of the CM49 CMOS detector for laser-driven ion acceleration. *LMU Munich Master Thesis*, 2019. (Cited on pages 135, 183, and 184.)
- [215] M. Speicher, D. Haffa, M. Haug, J. Bin, Y. Gao, J. Hartmann, P. Hilz, C. Kreuzer, F. Lindner, T. Ostermayr, T. Rösch, R. Yang, and J. Schreiber. Integrated double-plasma-mirror targets for contrast enhancement in laser ion acceleration. *Journal of Physics: Conference Series*, 1079:012002, 08 2018. (Cited on pages 38, 44, 45, 140, and 165.)
- [216] Statistisches Bundesamt. Bevölkerungsstand am 30. September 2020, 2020. (Cited on page 1.)
- [217] V. W. Steward and A. M. Koehler. Proton Beam Radiography in Tumor Detection. *Nature*, 245, 1973. (Cited on pages 32 and 33.)
- [218] V. W. Steward and A. M. Koehler. Proton Radiographic Detection of Strokes. *Nature*, 245(5419):38–40, 1973. (Cited on page 32.)
- [219] T. F. Rösch, P. Hilz, J. Bin, F. Englbrecht, Y. Gao, D. Haffa, J. Hartmann, S. Herr, S. Lehrack, F. H. Lindner, M. Speicher, M. Würfl, K. Parodi, J. Schreiber. Considerations on employing a PMQ-doublet for narrow and broad proton energy distributions. *Submitted*, 3:339, 2019. (Cited on pages 43, 45, 165, and 179.)

- [220] T. Tajima, J. M. Dawson. Laser Electron Accelerator. *Physical Review Letters*, 43:268, 1979. (Cited on pages 2 and 35.)
- [221] Taddei P J; Fontenot J D; Zheng Y et al. Reducing stray radiation dose to patients receiving passively scattered proton radiotherapy for prostate cancer. *Physics in Medicine and Biology*, 2008. (Cited on pages 59 and 60.)
- [222] M. Tampo, S. Awano, P. Bolton, K. Kondo, K. Mima, Y. Mori, H. Nakamura, M. Nakatsutsumi, R. Stephens, K. Tanaka, T. Tanimoto, T. Yabuuchi, and R. Kodama. Correlation between laser accelerated MeV proton and electron beams using simple fluid model for target normal sheath acceleration. *Physics of Plasmas*, 17:073110, 07 2010. (Cited on page 140.)
- [223] M. Tanabashi et al. *Review of Particle Physics*, volume 98. APS Physics, August 2018. (Cited on page 8.)
- [224] Tayama R; Handa H; Hayashi K et al. Benchmark calculations of neutron yields and dose equivalent from thick iron target for 52–256 MeV protons. *Nuclear Engineering and Design*, 2002. (Cited on page 59.)
- [225] Teledyne DALSA. CM49 DST CMOS Image Sensor Product Specification Data Sheet. Technical report, Teledyne, 2014. (Cited on page 133.)
- [226] Teledyne DALSA. CMOS X-RAY DETECTORS for Industrial Non-Destructive Testing. Technical report, Teledyne, 2017. (Cited on page 133.)
- [227] Teledyne DALSA. Shad-o-Box HS Product Family Datasheet. Technical report, Teledyne, 2021. (Cited on page 183.)
- [228] The Geant4 Collaboration. Physics Lists EM constructors in Geant4 10.1, 2015. (Cited on page 65.)
- [229] The International atomic energy agency IAEA. Technical reports series No. 398: Absorbed dose determination in external beam radiotherapy: an international code of practice for dosimetry based on standards of absorbed dose to water. Technical report, International Atomic Energy Agency, 2000. (Cited on page 145.)
- [230] The International atomic energy agency IAEA. *Radiation Oncology Physics: A Handbook for Teachers and Students*. The International atomic energy agency IAEA, 2005. (Cited on page 26.)
- [231] M. Tisi, V. Mares, J. Schreiber, F. S. Englbrecht, and W. Rühm. Geant4 Monte Carlo simulation study of the secondary radiation fields at the laser-driven ion source LION. *Scientific Reports*, 11(1):24418, 2021. (Cited on pages 113 and 115.)
- [232] Titt U; Newhauser W D. Neutron shielding calculations in a proton therapy facility based on Monte Carlo simulations and analytical models: criterion for selecting the method of choice. *Radiation Protection Dosimetry*, 2005. (Cited on page 59.)
- [233] C. A. Tobias, J. H. Lawrence, J. L. Born, R. K. McCombs, J. E. Roberts, H. O. Anger, B. V. A. Low-Beer, and C. B. Huggins. Pituitary Irradiation with High-Energy Proton Beams A Preliminary Report. *Cancer Research*, 18(2):121–134, 1958. (Cited on page 1.)
- [234] S. Trinkl, V. Mares, F. Englbrecht, J. Wilkens, M. Wielunski, K. Parodi, W. Rühm, and M. Hillbrand. Systematic out-of-field secondary neutron spectrometry and dosimetry in pencil beam scanning proton therapy. *Medical Physics*, 44(5):1912–1920, 2017. (Cited on pages 19, 30, 60, 61, 62, 64, 65, 66, 71, 72, and 82.)
- [235] U. Linz and J. Alonso. Laser-driven ion accelerators for tumor therapy revisited. *Phys. Rev. Accel. Beams*, 19:124802–124810, 2016. (Cited on pages 42 and 43.)
- [236] P. UNTORO. RISIKO PLTN DI INDONESIA, 2018. (Cited on page 36.)
- [237] J. Valentin. Relative biological effectiveness (RBE), quality factor (Q), and radiation weighting factor (w_R): ICRP Publication 92: Approved by the Commission in January 2003. *Annals of the ICRP*, 33(4):1–121, 2003. (Cited on pages 18 and 19.)
- [238] S. van de Water, S. Safai, J. M. Schippers, D. C. Weber, and A. J. Lomax. Towards FLASH proton therapy: the impact of treatment planning and machine characteristics on achievable dose rates. *Acta Oncologica*, 0(0):1–7, 2019. PMID: 31241377. (Cited on page 21.)
- [239] Varian Medical Systems. <http://newsroom.varian.com/index.php?s=31899&cat=2479&mode=gallery>, 2014. (Cited on pages 29 and 63.)

- [240] W. Lu, M. Tzoufras, C. Joshi, F. S. Tsung, W. B. Mori, J. Vieira, R. A. Fonseca, L. O. Silva. Generating multi-GeV electron bunches using single stage laser wakefield acceleration in a 3D nonlinear regime. *Phys. Rev. ST Accel. Beams*, 10:061301, 2007. (Cited on pages 43 and 92.)
- [241] F. Wagner, O. Deppert, C. Brabetz, P. Fiala, A. Kleinschmidt, P. Poth, V. A. Schanz, A. Tebartz, B. Zielbauer, M. Roth, T. Stöhlker, and V. Bagnoud. Maximum Proton Energy above 85 MeV from the Relativistic Interaction of Laser Pulses with Micrometer Thick CH₂ Targets. *Physical Review Letters*, 116:205002, May 2016. (Cited on page 37.)
- [242] Wenz J., Döpp A., Khrennikov K., Schindler S., Gilljohann M. F., Ding H., Götzfried J., Buck A., Xu J., Heigoldt M., Helml W., Veisz L., and Karsch S. Dual-energy electron beams from a compact laser-driven accelerator. *Nature Photonics*, 13(4):263–269, 2019. (Cited on pages 43 and 49.)
- [243] Wenz J., Schleede S., Khrennikov K., Bech M., Thibault P., Heigoldt M., Pfeiffer F., and Karsch S. Quantitative X-ray phase-contrast microtomography from a compact laser-driven betatron source. *Nature Communications*, 6(1):7568, 2015. (Cited on pages 43, 49, and 170.)
- [244] W. Weyrather and G. Kraft. RBE of carbon ions: experimental data and the strategy of RBE calculation for treatment planning. *Radiotherapy and Oncology*, 73(2):S161–S169, 2004. (Cited on page 30.)
- [245] S. C. Wilks, A. B. Langdon, T. E. Cowan, M. Roth, M. Singh, S. Hatchett, M. H. Key, D. Pennington, A. MacKinnon, and R. A. Snavely. Energetic proton generation in ultra-intense laser–solid interactions. *Physics of Plasmas*, 8(2):542–549, 2001. (Cited on pages 39 and 44.)
- [246] R. R. Wilson. Radiological Use of Fast Protons. *Radiology*, 47(5):487–491, 1946. (Cited on page 1.)
- [247] M. Würfl. PET activation studies at a cyclotron-based proton therapy facility. *LMU Munich Master Thesis*, 2014. (Cited on page 12.)
- [248] M. Würfl. *On the Spectrometry of Laser-Accelerated Particle Bunches and Laser-Driven Proton Radiography*. PhD thesis, LMU Munich, 2018. (Cited on pages 27, 33, 55, and 162.)
- [249] M. Würfl, F. Englbrecht, K. Parodi, and M. Hillbrand. Dosimetric impact of the low-dose envelope of scanned proton beams at a ProBeam facility: comparison of measurements with TPS and MC calculations. *Physics in Medicine and Biology*, 61(2):958, 2016. (Cited on pages 13, 27, 30, 62, and 66.)
- [250] M. Würfl, F. S. Englbrecht, S. Lehrack, C. Gianoli, F. H. Lindner, T. F. Rösch, D. Haffa, F. Olivari, M. Petasecca, M. L. F. Lerch, A. Pogosso, L. T. Tran, W. Assmann, J. Schreiber, A. B. Rosenfeld, and K. Parodi. Time-of-flight spectrometry of ultra-short, polyenergetic proton bunches. *Review of Scientific Instruments*, 89(12):123302, 2018. (Cited on pages 26, 27, 42, 45, 55, 140, 162, and 184.)
- [251] M. Würfl, C. Gianoli, F. Englbrecht, J. Schreiber, and K. Parodi. A Monte Carlo feasibility study on quantitative laser-driven proton radiography. *Zeitschrift für Medizinische Physik*, 2020. (Cited on page 122.)
- [252] Yan X, Nill S, Newhauser W D, Titt U, Dexheimer D. Neutron shielding verification measurements and simulations for a 245-MeV proton therapy center. *Nuclear Instruments and Methods in Physics Research Section A*, 2002. (Cited on page 60.)
- [253] M. Yang, X. R. Zhu, P. C. Park, U. Titt, R. Mohan, G. Virshup, J. E. Clayton, and L. Dong. Comprehensive analysis of proton range uncertainties related to patient stopping-power-ratio estimation using the stoichiometric calibration. *Physics in Medicine and Biology*, 57(13):4095–4115, jun 2012. (Cited on page 32.)
- [254] E. M. Zeman, E. C. Schreiber, and J. E. Tepper. Basics of Radiation Therapy. In J. E. Niederhuber, J. O. Armitage, J. H. Doroshow, M. B. Kastan, and J. E. Tepper, editors, *Abeloff's Clinical Oncology (Fifth Edition)*, volume Fifth Edition, page 393–422.e3. Churchill Livingstone, Philadelphia, fifth edition edition, 2014. (Cited on page 26.)
- [255] Y. Zheng, J. Fotenot, P. Taddei, D. Mirkovic, and W. Newhauser. Monte Carlo simulations of neutron spectral fluence, radiation weighting factor and ambient dose equivalent for a passively scattered proton therapy unit. *Phys. Med. Biol.*, 53:187–201, 2008. (Cited on page 19.)
- [256] Zheng Y, Newhauser W, Fotenot J, Taddei P, Mohan R. Monte Carlo study of neutron dose equivalent during passive scattering proton therapy. *Phys Med Biol*, 52(14), 2007. (Cited on page 60.)

- [257] D. Zheng Y; Newhauser W; Klein E; Low. Monte Carlo simulation of the neutron spectral fluence and dose equivalent for use in shielding a proton therapy vault. *Physics in Medicine and Biology*, 2009.
(Cited on page 60.)
- [258] J. F. Ziegler, U. Littmark, and J. P. Biersack. *The stopping and range of ions in solids* / J.F. Ziegler, J.P. Biersack, U. Littmark. Pergamon New York, 1985.
(Cited on page 10.)
- [259] P. Zygmanski, K. P. Gall, M. S. Rabin, and S. J. Rosenthal. The measurement of proton stopping power using proton-cone-beam computed tomography. *Physics in Medicine & Biology*, 45(2):511, 2000.
(Cited on page 32.)